Scuola Internazionale Superiore di Studi Avanzati - Trieste

Area of Physics
Ph.D. in Astrophysics

Investigating Quasar Outflows at High Redshift.

Candidate
Serena Perrotta

Supervisors
Dr. Valentina D'Odorico
Prof. Stefano Cristiani
Dr. Francesca Perrotta

Thesis submitted in partial fulfillment of the requirements
for the degree of Doctor Philosophiae Academic Year 2015/2016

SISSA - Via Bonomea 265 - 34136 TRIESTE - ITALY

To the memory of my parents.

Foreword

The work presented in this thesis is based on the following publication Perrotta et al. (2016):

- *"Nature and statistical properties of quasar associated absorption systems in the XQ-100 Legacy Survey"*,
  S. Perrotta, V. D'Odorico, J.X. Prochaska, S. Cristiani, G. Cupani, S. Ellison, S. López, G.D. Becker, T.A.M. Berg, L. Christensen, K. Denney, F. Hamann, I. Paris, M. Vestergaard, G. Worseck.
  MNRAS, accepted
  arXiv:1605.04607.

- *"Probing NV Narrow Absorption Lines using stacked spectra of Lyman-α forest of the XQ-100 Legacy Survey"*,
  S. Perrotta, V. D'Odorico, J.X. Prochaska, S. Cristiani, G. Cupani, S. Ellison, S. López, G.D. Becker, T.A.M. Berg, L. Christensen, K. Denney, F. Hamann, M. Vestergaard, G. Worseck.
  In preparation.

Abstract

In this thesis, I present my work on the characterization of quasar outflows which I carried out using the statistics and the ionization properties of Narrow Absorption Lines (NALs). The study is based on a new sample of intermediate resolution spectra of 100 high-redshift quasars ($z_{em} \approx 3.5 - 4.5$), obtained with X-shooter at the European Southern Observatory Very Large Telescope, in the context of the XQ-100 Legacy Survey (Lopez et al., 2016). The combination of high signal-to-noise ratio (S/N), wide wavelength coverage and moderate spectral resolution of this survey have allowed me to look for empirical signatures to distinguish between two classes of absorbers: intrinsic (produced in gas that is physically associated with the quasar) and intervening, without taking into account any a priori definition or velocity cut-off. Previous studies have shown that NALs tend to cluster near the quasar emission redshift, at $z_{abs} \approx z_{em}$. I detect a significant excess of absorbers over what is expected from randomly distributed intervening structures. This excess does not show a dependence on the quasar bolometric luminosity and it is not due to the redshift evolution of NALs. Most interestingly, it extends far beyond the standard 5000 $\mathrm{km\,s^{-1}}$ cut-off traditionally defined for *associated* absorption lines. I take advantage of the large spectral coverage (from the UV cutoff at 300 nm to 2.5 μm) of the XQ-100 spectra to study the relative numbers of NALs in different transitions, indicative of the ionization structure of the absorbers and their locations relative to the continuum source. Among the ions examined in this work, NV is the ion that best traces the effects of the quasar ionization field, offering an excellent statistical tool to identify intrinsic systems and derive the fraction of quasar driving outflows. I also test the robustness of the use of NV as additional criterium to select intrinsic NALs, performing a stack analysis of the Lyα forest of the XQ-100 sample, to search for NV signal at large velocity offsets. Lastly, I compare the properties of the material along the quasar line of sight, derived from my sample, with results based on close quasar pairs investigating the transverse direction. I find a deficiency of cool gas (traced by CII) along the line of sight connected to the quasar host galaxy, in contrast with what is observed in the transverse direction in agreement with the predictions of the AGN unification models.

Contents

List of Figures

List of Tables

Motivations

Supermassive black holes (SMBHs) are ubiquitous at the center of stellar spheroids. Moreover, their mass is tightly related to global properties of the host galaxy (e.g., Kormendy and Ho, 2013; McConnell and Ma, 2013; Ferrarese and Merritt, 2000). Despite this close interplay between SMBHs and their host systems, several compelling questions remain unanswered. Hence, a full description of why, how, and when black holes alter the evolutionary pathways of their host systems remain key questions in galaxy formation. High velocity quasar outflows appear to be a natural byproduct of accretion onto the SMBH and have therefore attracted much attention as a mechanism that can physically couple quasars to the evolution of their host galaxies.

Simulations of galaxy evolution (e.g., Booth and Schaye, 2009; Sijacki et al., 2015; Schaye et al., 2015) suggest that feedback from active galactic nuclei (AGN) plays a crucial role in heating the interstellar medium (ISM), quenching star formation and preventing massive galaxies to over-grow. As a consequence, the colors of the host galaxies evolve quickly and become red, in agreement with the observed color distribution of nearby galaxies. Quasar outflows may also contribute to the blowout of gas and dust from young galaxies, and thereby provide a mechanism for enriching the intergalactic medium (IGM) with metals and reveal the central accreting SMBH as an optically visible quasar (Silk and Rees, 1998; Moll et al., 2007). Several mechanisms have been proposed that could produce the force accelerating disk winds in AGN, including gas/thermal pressure (e.g., Weymann et al., 1982; Krolik and Kriss, 2001), magnetocentrifugal forces (e.g., Blandford and Payne, 1982; Everett, 2005) and radiation pressure acting on spectral lines and the continuum (e.g., Murray and Chiang, 1995; Proga, 2000). In reality, these three forces may co-exist and contribute to the dynamics of the outflows in AGN to somewhat different degrees.

Some immediate questions on quasar outflows spring to mind about: 1) Their Nature. What are they? Which conditions trigger them? What powers them? How energetic are they? Are they relatively quiescent or explosive? What mass, momentum, energy, and metals do they transport? How far? 2) Their Frequency of Occurrence. How common were they in the past and are they now? What is

their duty cycle? When did they begin to blow? 3) Their Impact. How important are they? What impact do they have on the nucleus, bulge, disk, halo, and dark matter of the host galaxy? Are they the dominant source of feedback in galaxy evolution? How do they influence the intergalactic environment? What are their fossil signatures?

These are questions so complex, that an answer to each of them is likely not to be found in a single lifetime. This thesis seeks to shed light on one particular aspect: how common this phenomenon is.

A key piece of information to understand if outflow feedback can affect the host galaxy evolution, is the fraction of quasars driving outflows, as well as their energetics. The latter quantity can be inferred from the velocity, column density, and global covering factor of the outflowing gas. Observations of outflows are mainly carried out in absorption against the central compact UV/X-ray continuum. Quasar narrow absorption lines (NALs) with velocity widths less than 500 $km\,s^{-1}$ and broad absorption lines (BALs), with velocity widths greater than a few thousand $km\,s^{-1}$, are examples of these potential outflow signatures. Therefore, absorption line studies of high-z quasars is a powerful tool to search for distant galactic outflows and to constrain their environmental impact.

To build a more complete picture of quasar outflows, and explore what effects do they have on their surrounding host galaxy, we need better observational constraints on the physical properties of each outflow type. Better are the estimates of the detection rate of the absorbers, stronger are the constraints on the theoretical models. Indeed, the intrinsic fraction of absorption line quasars is important in constraining geometric and evolutionary models of quasars. In this context, large spectroscopic surveys provide a statistical means of measuring the frequency with which outflows are observed, but we must carefully select systems that truly sample outflowing gas.

With this short teaser in mind, we can start digging into the details of this work.

Chapter 1

1 Introduction

It has been nearly a century since it was realized that the Universe was not confined to our own galaxy, the Milky Way. Hubble (1925) demonstrated that the Andromeda nebula is a vast "island universe" of stars similar to our own galaxy. This breakthrough in our cosmological understanding — to paraphrase Christopher Marlowe — "launched a thousand exploratory studies" beyond the edges of the Milky Way. As we looked farther away, we made more and more puzzling discoveries: violent galactic collisions, powerful explosions of stars, and super massive black holes (SMBHs) feeding on surrounding gas.

Early suggestions about unusual activity in the nuclei of galaxies go back to the work of Sir James Jeans (1929). But, the modern understanding of the important role of galactic nuclei probably began with the famous paper by Seyfert (1943), who reported the presence of broad strong emission lines in the nuclei of seven spiral nebulae. Although Seyfert's name ultimately became attached to the general category of galaxies with broad nuclear emission lines associated with highly ionized elements, his 1943 paper apparently went unnoticed until Baade and Minkowski (1954) drew attention to the similarity between the optical emission line spectrum of the galaxies studied by Seyfert and that of the galaxy they had identified with the Cygnus A radio source.

During the following years many radio galaxies were identified. The paradigm which had previously considered all discrete radio sources as galactic stars quickly changed to one where most high latitude sources were assumed to be extragalactic.

Although the extragalactic nature of 3C 48 and of other quasi stellar radio sources was already discussed in 1960 by John Bolton and others, it was initially rejected largely because the derived radio and optical luminosities appeared to be unrealistically high. Not until the 1962 occultations of the strong radio source 3C 273 at Parkes Radio Telescope, which led Maarten Schmidt to recognize that the spectrum of the identified 13th magnitude apparently stellar object could be most easily interpreted assuming a redshift of 0.158. Successive radio and optical observations quickly led to increasingly large measured redshifts and the recognition of the broad class of active galactic nuclei (AGN) of which quasars occupy the high luminosity end (see Kellermann, 2014, for an historical review of the road to quasars).

Although other radio sources had been identified with distant galaxies, before the discovery of quasars there was great confusion as to the origin of this very large-scale radio emission which had no obvious connection with the galactic nuclei. It is beyond the scope of this thesis to review the twists and turns that finally led to the consensus that all these quasi-stellar objects (QSOs) were the extremely luminous active nuclei of distant galaxies.

For most of the past five decades the communities that studied galaxies and AGN remained largely disconnected. AGN were studied primarily as laboratories in which to probe exotic high-energy processes. There was some effort to understand the role that the environment might play in triggering or fueling the AGN (e.g., see the ancient review by Balick and Heckman, 1982) but there was almost no idea that AGN played a prominent role in the evolution of galaxies. Things are very different today. The notion of the co-evolution of galaxies and AGN has become inextricably engrained in our current cosmogony.

The reasons for this change are easy to see. First came the realization that powerful AGN (as represented by Quasars) were only the tip of the iceberg. Astronomers have put enormous effort into compiling large surveys of AGN in the radio, optical, and X-ray domains, revealing that a significant fraction of nearby galaxies exhibits signs of unusual activity in their nuclei unrelated to normal stellar processes. It has been established that evidence of weak level activity were commonplace in the nuclei of early-type galaxies (e.g., Ho, 2008). This strongly suggested that the AGN phenomenon — rather than being simply a rare and exotic event — was a part of the lifecycle of typical galaxies. A second reason followed from the remarkable agreement between the inferred cosmic histories of SMBH growth (traced by AGN) and stellar mass growth (tracing the populations of galaxies). The evolution of the two populations is strikingly similar: a steep rise in both the star formation rate (SFR) and SMBH growth rate by about a factor of 10 from redshift $z = 0$ to 1, a broad maximum in both rates at $z \sim 2$ to 3 and then a relatively steep decline at higher redshifts (see Fig. 1.1; Shankar et al., 2009 and references therein).

For at least the last ~ 11 Gyr of cosmic history the ratio of these two growth rates has remained roughly constant with a value of order 10^3, suggesting that the two processes are intimately linked somehow.

Finally, stellar/gas dynamics and photometric observations over the past decade have not only established that SMBH exist in the nuclei of almost all galactic bulges, they have shown that the BH mass, M_{BH}, correlates strongly with physical properties of the host galaxy (see Kormendy and Ho, 2013 for a recent review). In addition to the accumulating observational evidence for the co-evolution of galaxies and SMBHs at their centers, a considerable theoretical argument to invoke this

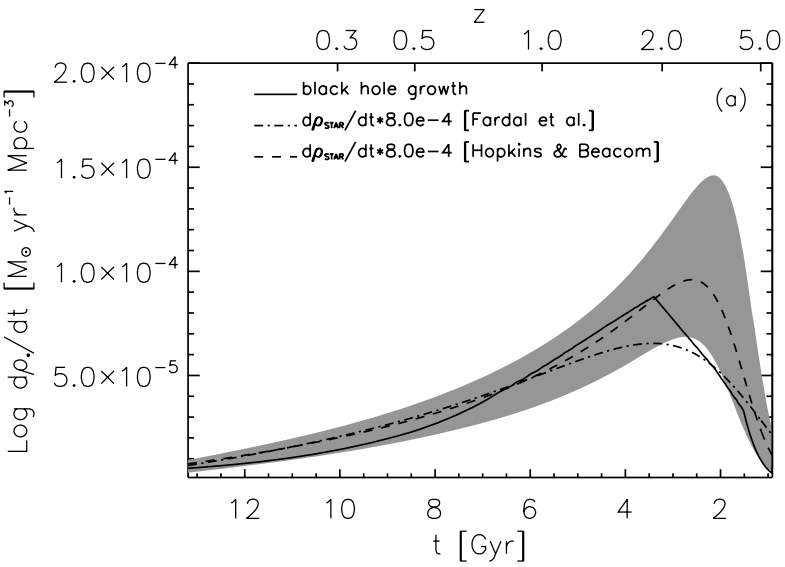

Figure 1.1: Average BH accretion rate compared to the SFR as a function of redshift, the latter is given by Hopkins and Beacom, 2006 and Fardal et al., 2007, scaled by the factor $M_\bullet/M_\star = 0.8 \times 10^{-3}$. The shaded grey area shows the 3σ uncertainty region from Hopkins and Beacom, 2006. Figure from Shankar et al., 2009.

linkage has developed as well. The current paradigm for AGN phenomenon is a central engine that consists of a hot accretion disk surrounding a BH. In this context, the accretion of matter on the central BH triggers a release of energy on the surrounding interstellar medium (ISM), which controls the evolution of the host galaxy. This is called AGN feedback. The impact of the AGN feedback can dramatically affects the properties of massive galaxies, inducing a cut-off similar to that observed at the bright end of the galaxy luminosity function, and bringing colours, morphologies and stellar ages into much better agreement with observation than is the case for models without such feedback (e.g., Granato et al., 2004; Croton et al., 2006, but also see Fabian, 2012 for a review). In conclusion, while the evidence to date remains indirect, it is hard not to infer that the cosmic evolution of galaxies and of SMBHs have seemingly been driven by a suite of inter-linked physical processes.

1.1 The Central Engine

In the AGN paradigm, the energy is generated by gravitational infall of material which is heated in a dissipative accretion disk. We can consider a simple spherical model in which a central source with luminosity L is surrounded by gas with density distribution $\rho(r)$. The flux at a radius r from the source is $L/(4\pi r^2)$ and

the radiation pressure is

$$P_{rad}(r) = \frac{L}{4\pi r^2 c} \tag{1.1}$$

For simplicity, we can consider the case of a completely ionized hydrogen gas. So, the pressure force on a unit volume of gas due to the scattering of photons by electrons is

$$F_{rad} = \sigma_T P_{rad}(r) n_e(r) \hat{r} \tag{1.2}$$

where σ_T is the Thomson scattering cross-section, $n_e(r)$ is the electron density at radius r, and $\hat{r}$ is a dimensionless unit vector in the radial direction. The gas is not dispersed quickly if the pressure force is smaller than the gravitational force of the gas, i.e.

$$|F_{rad}| \leq F_{grav} = \frac{GM_{BH}\rho(r)}{r^2}. \tag{1.3}$$

This defines the largest possible luminosity of a source of mass M_{BH} that can be achieved by spherical accretion, the Eddington luminosity:

$$L_{Edd} \equiv \frac{4\pi G c m_p}{\sigma_T} M_{BH} \approx 1.28 \times 10^{46}\ \mathrm{M_8\,erg\,s^{-1}} \qquad (\mathrm{M_8} \equiv \mathrm{M_{BH}}/10^8\,\mathrm{M_\odot}) \tag{1.4}$$

where m_p is the mass of the proton, G is the gravitational constant, and c is the speed of light. The above relation can be inverted to give a minimum central mass required to achieve a given luminosity:

$$M_{Edd} = 8 \times 10^7\,\mathrm{L_{46}\,M_\odot} \qquad [\mathrm{L_{46}} \equiv \mathrm{L}(10^{46}\ \mathrm{erg\,s^{-1}})]. \tag{1.5}$$

A bright quasar with luminosity $L \sim 10^{46}\ \mathrm{erg\,s^{-1}}$ may be powered by a BH with a mass $M_{BH} \sim 10^8\,\mathrm{M_\odot}$. The fundamental process at work in an AGN is the conversion of mass to energy. Under the assumption that the luminosity is powered by the gravitational potential of the central BH, the accretion luminosity can be written as

$$L = \frac{GM_{BH}}{r}\dot{M}_{BH}, \tag{1.6}$$

where $\dot{M}_{BH}$ is the mass accretion rate, i.e. the rate at which mass crosses a shell of radius r. From the previous relation we see that the efficiency at which the rest mass of accreted material is converted into radiation is

$$\eta \equiv \frac{L}{\dot{M}_{BH}c^2} = \frac{1}{2}\frac{r_S}{r} \tag{1.7}$$

where r_S is the Schwarzschild radius of a BH with mass M_{BH}, i.e.

$$r_S = \frac{2GM_{BH}}{c^2} \approx 10^{-2}\,\mathrm{M}_8 \;\; \mathrm{light-days}. \tag{1.8}$$

If we ignore relativistc effects, the energy available from a particle of mass m falling to within $5\,r_S$, which is about where most of the optical/UV continuum radiation is expected to originate, is $\sim GM_{BH}m/5\,r_S = 0.1m\,c^2$. This oversimplified calculation suggests that $\eta \approx 0.1$. This is a very high efficiency, much higher than the efficiency with which hydrogen is burned into helium in stars, which is only ~ 0.007. For $\eta = 0.1$ an accretion rate of $\dot{M} \sim 2\,\mathrm{M}_\odot\,\mathrm{yr}^{-1}$ is required to power a bright quasar with luminosity $L = 10^{46}\,\mathrm{erg\,s}^{-1}$. The Eddington luminosity defined in Eq. 1.4 corresponds to a mass accretion rate

$$\dot{M}_{Edd} = \frac{L_{Edd}}{\eta c^2} \approx 2.2\,M_8 \left(\frac{\eta}{0.1}\right)^{-1} \mathrm{M}_\odot\,\mathrm{yr}^{-1}. \tag{1.9}$$

This critical rate can easily be exceeded, however, with models that are not spherically symmetric. For example, the Eddington rate can be exceeded if the mass accretion occurs primarily equatorially in a disk, while the radiation escapes from the polar zones.

1.2 The Unified Model for AGN

Although different classes of AGN appear quite differently, many of them have properties in common. For example, radio-quiet quasars (RQQs) and radio-loud quasars (RLQs) have very different radio properties, but their emission line properties are very similar. Unified models of AGN propose that different observational classes of AGN are a single type of physical object observed under different conditions. The currently favored unified model is a "orientation-based unified model", where the apparent differences amongst AGN arise because of their different orientations to the observer (Antonucci, 1993; Padovani and Giommi, 1995). Fig. 1.2 shows the AGN components according to the picture offered by the unification model:

(1) The SMBH at the very heart of the quasar surrounded by the accretion disc. Hurled away from the plane of the disc are jets of matter, moving at velocities close to the speed of light. This region is typically a few light-days across. (2) The broad line region (BLR) at about 100 light days from the central source. Some of its properties will be described in section § 1.5.2. (3) The molecular torus at about 100 light years across. This "doughnut" is made up of many clouds of dusty gas. The torus is optically thick, so if the torus is edge-on, the central regions will

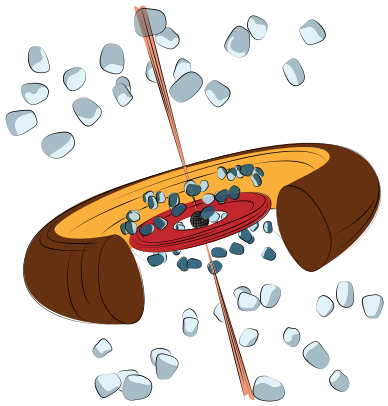

Figure 1.2: Artist's view of an AGN. The black core represents the accreting BH, and the red ring the accretion disk. The jets are colored in salmon. Grey clouds close to the accretion disk represent the Broad Line Region, while the most outer clouds are the Narrow Line Region. The dusty torus is represented in brown/yellow.

be blocked out and the AGN will look different according to the angle at which it lies. (4) The narrow line region (NLR) is outer region (see section § 1.5.2 for more details). It is similar to the BLR, but it has a lower density and the clouds move with a lower velocity. Clouds that are in the cone of light from the inner nucleus are more ionized than those that lie in the shadow of the torus.

1.3 Coevolution of SMBHs and Host Galaxies

After decades of indirect and circumstantial evidence, stellar and gas dynamical studies in an ever increasing number of galaxies have established that many — and perhaps all — luminous galaxies contain central SMBHs (e.g., Kormendy and Richstone, 1995; Ferrarese and Merritt, 2000). While efforts to build ever larger sample continued, we have moved from debating the existence of SMBHs to asking what regulates their formation and evolution and how their presence influences, and is influenced by, their host galaxies.

AGN feedback features in many theoretical, numerical and semi-analytic simulations of galaxy growth and evolution. These works have greatly improved our understanding of the physics of galaxy formation and evolution and are widely used to guide the interpretation of observations and the design of new observational campaigns and instruments. Observations, on the other hand, can provide direct constraints on how BHs and galaxies co-evolve by probing the scaling relations over cosmic time. Such an empirical evidence is essential to determine the underlying fundamental physical processes at work and to constrain models.

In the following sections I will briefly summarize the main evidences for the co-evolution of galaxies and SMBHs as derived from observations (§ 1.3.1) and models (§ 1.3.2). A comprehensive review of these two fascinating subjects is beyond the scope of this work.

1.3.1 Observational evidences

The Hubble Space Telescope revolutionized BH research by advancing the subject from its proof-of-concept phase into quantitative studies of BH demographics. Consequently, empirical correlations between the masses of SMBHs, $M_\bullet$, and numerous properties of their host galaxies have been explored in the past decade.

These include scaling relations between $M_\bullet$ and stellar velocity dispersion, σ (e.g., Ferrarese and Merritt, 2000; Gebhardt et al., 2000; Merritt and Ferrarese, 2001; Tremaine et al., 2002; Hu, 2008; Gültekin et al., 2009; Schulze and Gebhardt, 2011; McConnell et al., 2011; Graham et al., 2011; Beifiori et al., 2012; McConnell and Ma, 2013; Ho and Kim, 2014) and between $M_\bullet$ and the stellar mass of the bulge (e.g., Kormendy and Richstone, 1995; Magorrian et al., 1998; Marconi and Hunt, 2003; Häring and Rix, 2004; Sani et al., 2011; Beifiori et al., 2012; McConnell and Ma, 2013). Various scaling relations between $M_\bullet$ and the photometric properties of the galaxy have also been examined: bulge optical luminosity (e.g., Kormendy and Richstone, 1995; Kormendy and Gebhardt, 2001; Gültekin et al., 2009; Schulze and Gebhardt, 2011; McConnell et al., 2011; Beifiori et al., 2012), bulge near-infrared luminosity (e.g., Marconi and Hunt, 2003; McLure and Dunlop, 2002; Graham and Driver, 2007; Sani et al., 2011), total luminosity (e.g., Kormendy and Gebhardt, 2001; Beifiori et al., 2012; Kormendy and Bender, 2011), and bulge concentration or Sérsic index (e.g., Graham et al., 2001; Graham and Driver, 2007; Beifiori et al., 2012).

On a larger scale, correlations between $M_\bullet$ and the circular velocity or dynamical mass of the dark matter halo have been reported as well as disputed (e.g., Ferrarese, 2002; Baes et al., 2003; Zasov et al., 2005; Kormendy and Bender, 2011; Volonteri et al., 2011; Beifiori et al., 2012). More recently, $M_\bullet$ has been found to correlate with the number and total mass of globular clusters in the host galaxy (e.g., Burkert and Tremaine, 2010; Harris and Harris, 2011; Sadoun and Colin, 2012). In early-type galaxies with core profiles, Lauer et al. (2007) and Kormendy and Bender (2009) have explored correlations between $M_\bullet$ and the core radius, or the total "light deficit" of the core relative to a Sérsic profile.

The existence of the $M_\bullet$ scaling relations supports the idea that the host galaxies and their SMBHs form and grow in a coordinated way by a common physical mechanism.

These relations are established based on $M_\bullet$ measurements from spatially resolved kinematic of stars, gas or maser around BH's sphere of influence. $M_\bullet$ estimates have become available for AGN through methods such as reverberation mapping and single-epoch spectroscopy of broad emission lines (e.g., Peterson, 1993; Merloni et al., 2010; Woo et al., 2013). Recent and ongoing data and modeling efforts have substantially expanded the various samples used in all of the studies above, allowing to derive more robust correlations and to better understand the systematic effects in their scatter.

Perhaps the most commonly used relation — due to the small level of scatter ($\sim$ 0.3 dex) — is the $M_\bullet - \sigma$ relation.

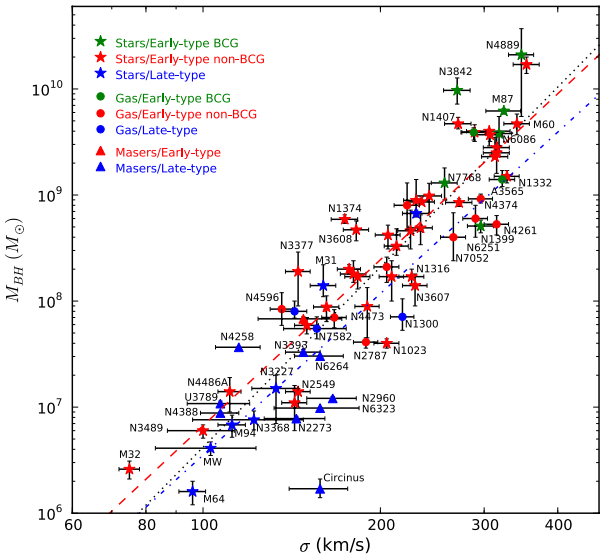

Figure 1.3: $M_\bullet - \sigma$ relation for 72 galaxies from McConnell and Ma (2013). Brightest cluster galaxies that are also the central galaxies of their clusters are plotted in green, other elliptical and S0 galaxies are plotted in red, and late-type spiral galaxies are plotted in blue. The BH masses are measured using the dynamics of masers (triangles), stars (stars), or gas (circles). Error bars indicate 68% confidence intervals. The black dotted line shows the best-fitting power law for the entire sample, while the red dashed and blue dot-dashed lines represent the fits for early-type and late-type galaxies, respectively. Figure from McConnell and Ma (2013).

In the literature, the exact value of the $M_\bullet - \sigma$ slope has been much debated by observers and regarded by theorists as a key discriminator for models of the assembly and growth of SMBHs and their host galaxies.

Comparison of works on this relation with each other is trickier than it sounds. Among the reasons: (1) some them include $M_\bullet$ based on kinematics of ionized gas but it has been shown that emission-line rotation curves underestimate $M_\bullet$ unless broad line widths are taken into account; (2) some include NGC 1316 or

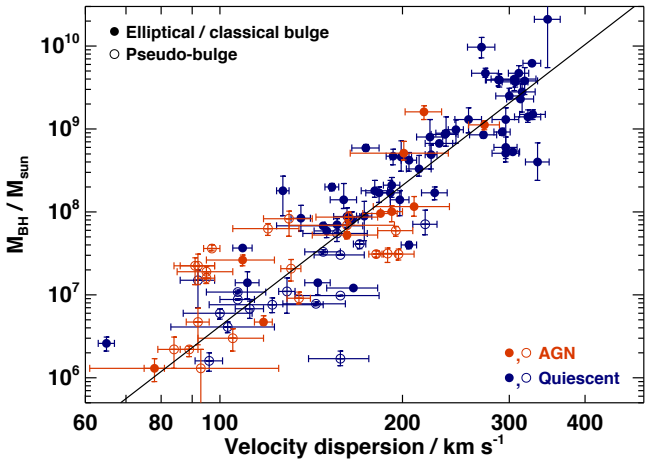

Figure 1.4: The $M_\bullet - \sigma$ relation of local galaxies with direct M_{BH} measurements (data from Woo et al., 2013 and references therein). Both AGN (the color-coding includes both radiative-mode and jet-mode AGN) and quiescent galaxies are consistent with the McConnell and Ma (2013) relation, shown by the solid line. Figure from Woo et al. (2013).

NGC 5128, which have low BH masses for their high bulge masses; (3) studies before 2011 have few or no BH masses that have been corrected upward as a result of the inclusion of dark matter in dynamical models; some do not include pseudobulges since they do not satisfy the same tight $M_\bullet$−host galaxy correlations as classical bulges and ellipticals; (5) even later studies do not generally have all the extraordinarily high-$M_\bullet$ objects published by McConnell, Gebhardt, Rusli, and collaborators.

McConnell and Ma (2013) presented revised fits for the $M_\bullet - \sigma$ relation (see Fig. 1.3), for a sample of 72 BHs and their host galaxies. The black dotted line shows the best-fitting power law for the entire sample: $log_{10}\,(M_\bullet/M_\odot) = 8.32 + 5.64\,log_{10}\,(\sigma/200\,\mathrm{km\,s^{-1}})$. When early-type and late-type galaxies are fit separately they obtain slightly shallower slopes: $\beta = 5.20 \pm 0.36$ for early types (red dashed line in Fig. 1.3) and $\beta = 5.06 \pm 1.16$ for late types (blue dot-dashed line). The late-type galaxies have a significantly lower intercept: $\alpha = 8.39 \pm 0.06$ versus 8.07 ± 0.21. The authors find a steeper power law than previous works also including to their analysis 92 upper limits on $M_\bullet$ from Beifiori et al. (2012). They argued that the individual observed $M_\bullet - \sigma$ relations for the early- and late-type galaxies provide more meaningful constraints on theoretical models than the global relation. After all, these two types of galaxies are formed via different processes.

In addition, Woo et al. (2013) concluded that the relationship between $M_\bullet$ and σ is consistent between samples of quiescent galaxies (from McConnell and Ma, 2013) and AGN (see Fig. 1.4). This result was reinforced by an investigation of powerful

AGN with more massive BHs by Grier et al. (2013).

We will not attempt to describe the large amount of detailed studies aimed at constraining the scatter in $M_\bullet$. The overall message is that the discovery that SMBHs are tightly related to the large-scale properties of their host galaxies allows us to tackle cardinal questions like: how did SMBHs form, how do they accrete, how do they evolve, and what role do they play in the formation of cosmic structure? All of the empirical relations above can be, and indeed must be, used to constrain any complete theory or model of galaxy/SMBH coevolution.

There are now many direct observations that are consistent with AGN feedback in action. Perhaps, the clearest observational evidence is found in the most massive galaxies known, Brightest Cluster Galaxies in individual giant ellipticals, groups and clusters of galaxies. These objects contain large amounts of hot, X-ray-emitting gas, often showing X-ray cavities or "bubbles" that are believed to be inflated by AGN jets. This subject is reviewed by McNamara and Nulsen (2007, 2012) and Fabian (2012).

Furthermore, some bright quasars show blue-shifted X-ray spectral absorption lines interpreted as coming from winds with velocities $v \gtrsim 0.1\,c$ and with mass loss rates of one to tens of $\mathrm{M}_\odot\,\mathrm{yr}^{-1}$ (e. g., Pounds and Page, 2006; Reeves et al., 2009; Tombesi et al., 2012. Nonrelativistic outflows are also seen (Cano-Díaz et al., 2012 and references therein). Maiolino et al. (2012) report on a quasar at $z = 6.4$ with an inferred outflow rate of $> 3500\,M_\odot\,\mathrm{yr}^{-1}$. Such an outflow can clean a galaxy of cold gas in a single AGN episode.

Some powerful radio galaxies at $z \sim 2$ show ionized gas outflows with velocities of $\sim 10^3$ km s^{-1} and gas masses of $\sim 10^{10}$ $\mathrm{M}_\odot$. Kinetic energies of ~ 0.2 % of BH rest masses are one argument among several that the outflows are driven by the radio sources and not by star formation (Nesvadba et al., 2006, 2008). Molecular gas outflows are also detected (e.g., Nesvadba et al., 2010; Cicone et al., 2014).

We will accurately discuss observations of quasar winds carried out in absorption against the central compact UV/X-ray continuum in section § 2.2.

1.3.2 Theoretical models

In a series of seminal theoretical papers (Silk and Rees, 1998; Haehnelt et al., 1998; Fabian and Iwasawa, 1999; King, 2003) principal ideas have been developed to explain the possible mutual feedback between galaxies and their central BHs, motivated by the observational evidences outlined in the previous section (e.g., Magorrian et al., 1998; Ferrarese and Merritt, 2000; Tremaine et al., 2002; McConnell

and Ma, 2013; Kormendy and Ho, 2013). However, the exact mechanisms leading to the observed tight coupling are not yet fully understood.

The overall picture in terms of energetics is fairly straightforward. It is easy to see that the growth of the central BH by accretion can have a profound effect on its host galaxy. The mass of the BH is typically observed to be $M_{BH} \approx 1.4 \times 10^{-3}\, M_b$, where M_b is the mass of the galaxy bulge (e.g., Kormendy and Ho, 2013). Accretion of matter onto central BHs, accompanied by the release of a fraction of the rest-mass energy of the fuel, has long been recognized as one of the most likely mechanisms powering the engines of AGN (Salpeter, 1964; Lynden-Bell, 1969; Rees, 1984). An estimate of the released energy is: $E_{BH} = \eta\, M_{BH}\, c^2 \sim 2 \times 10^{61}\, \mathrm{M_8\, erg}$, assuming a radiative efficiency for the accretion process of $\eta \sim 10\%$ (see section § 1.1).

The binding energy of the galaxy bulge is $E_b \sim M_b\, \sigma^2 \sim 8 \times 10^{58}\, \mathrm{M_8}\, \sigma^2_{200}$ erg, where σ is the velocity dispersion of the host galaxy's central bulge in unit of $200\ \mathrm{km\, s^{-1}}$. The energy produced by the growth of the BH therefore exceeds the binding energy by a large factor, $E_{BH}/E_b \sim 250$. If even a small fraction of the energy is transferred to the gas, then an AGN can play a major role on the evolution of its host galaxy. However, the details of the mechanism responsible for coupling the quasar radiation with the galactic ISM are still being debated.

Theoretical models of galaxy formation have found it necessary to implement AGN feedback processes, during which AGN activity injects energy into the gas in the larger-scale environment, in order to reproduce the properties of local massive galaxies, intracluster gas and the intergalactic medium (e.g., $M_{BH} - M_b$ relationship; the sharp cut-off in the galaxy luminosity function; colour bi-modality; metal enchrichment; X-ray temperature-luminosity relationship). Several of these models invoke a dramatic form of energy injection (sometimes called the "quasar-mode") where AGN drives galaxy-wide (i.e. $\gtrsim$ 0.1-10 kpc) energetic outflows that expel gas from their host galaxies, eventually clear the galaxy of its cold gas reservoir and consequently this shuts down future BH growth and star formation and/or enriches the larger-scale environment with metals (e.g., Silk and Rees, 1998; Fabian, 1999; Benson et al., 2003; King, 2003; Granato et al., 2004; Di Matteo et al., 2005; Springel et al., 2005; Hopkins et al., 2006, 2008; Booth and Schaye, 2010; Debuhr et al., 2012). This is in contrast to the "maintenance mode" feedback where radio jets, launched by the AGN, control the level of cooling of the hot gas in the most massive halos (see Bower et al., 2012; Harrison et al., 2014 for a discussion on the two modes).

Two main theoretical approaches have been developed to try and understand how the complex and non-linear physics of the baryons leads to galaxies with the properties observed in the real Universe: (i) semi-analytical modelling (SAM,

e.g., Monaco et al., 2000; Kauffmann and Haehnelt, 2000; Volonteri et al., 2003; Granato et al., 2004; Menci et al., 2006; Croton et al., 2006; Bower et al., 2006; Malbon et al., 2007; Somerville et al., 2008; Lacey et al., 2015), in which simplified mathematical descriptions are adopted for the baryonic processes, which are then applied to evolving dark matter halos calculated from N-body simulations or by Monte Carlo methods; (ii) fully hydrodynamic simulations (e.g., Di Matteo et al., 2003; Sijacki et al., 2007; Colberg and Di Matteo, 2008; Booth and Schaye, 2009; Sijacki et al., 2015) which follow the gas dynamics in more detail, and try to model the physical processes in a more finegrained way.

Both SAMs and hydrodynamic simulations of full cosmological volumes, have showed that the inclusion of AGN physics into galaxy formation models allows to match many of the observed properties of galaxies in the local universe.

For example, Croton et al. (2006) shows that incorporating AGN feedback into semi-analytic models of galaxy formation has a dramatic effect on the bright end of the galaxy luminosity function. Fig. 1.5 represents K- and b_J-band luminosity functions (left and right panels respectively) with and without AGN feedback (solid and dashed lines respectively). The luminosities of bright galaxies are reduced by up to two magnitudes when the feedback is switched on, and this induces a relatively sharp break in the luminosity function which matches the observations quite well. This model also indicates that feedback from AGN is necessary in order to build up a red-sequence of galaxies. Fig. 1.6 shows the B-V colour distribution as a function of stellar mass, with and without the central heating source (top and bottom panels respectively). Here the galaxy population is colour-coded by morphology as estimated from bulge-to-total luminosity ratio (split at $L_{bulge}/L_{total} = 0.4$). It is worth noting the bimodal distribution in galaxy colours, with a well-defined red sequence of appropriate slope separated cleanly from a broader blue cloud. It is significant that the red sequence is composed predominantly of early-type galaxies, while the blue cloud is comprised mostly of disk-dominated systems.

By comparing the upper and lower panels in Fig. 1.6 one can see how AGN feedback modifies the luminosities, colours and morphologies of high mass galaxies. The brightest and most massive galaxies are also the reddest and are ellipticals when cooling flows are suppressed, whereas they are brighter, more massive, much bluer and typically have disks if cooling flows continue to supply new material for star formation. AGN heating cuts off the gas supply to the disk from the surrounding hot halo, truncating star formation and allowing the existing stellar population to redden. These are only a couple of possible examples of how theoretical models suggest that AGN feedback plays a fundamental role in heating the ISM, quenching the star formation, preventing massive galaxy to overgrow.

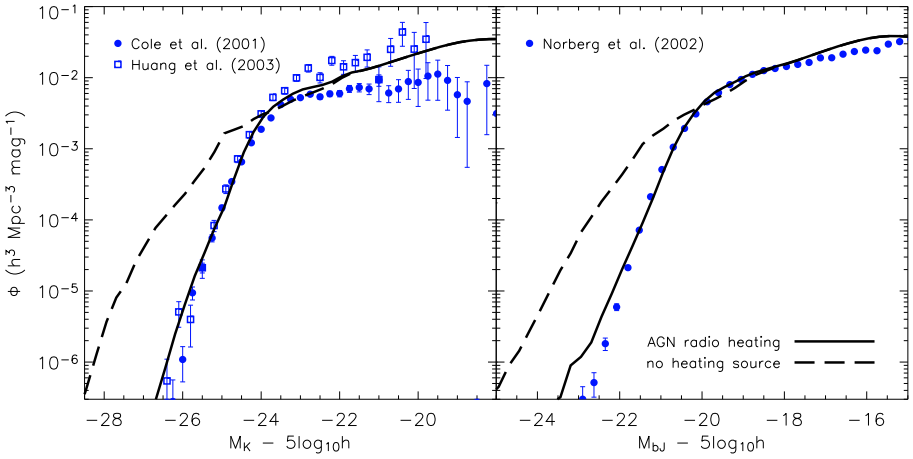

Figure 1.5: Galaxy luminosity functions in the K (left) and J (right) photometric bands, plotted with and without radio mode feedback (solid and long dashed lines respectively). Symbols indicate observational results as listed in each panel. As can be seen, the inclusion of AGN heating produces a good fit to the data in both colours. Without this heating source our model overpredicts the luminosities of massive galaxies by about two magnitudes and fails to reproduce the sharp bright end cut-offs in the observed luminosity functions. Figure from Croton et al. (2006).

Both approaches, SAMs and hydrodynamical simulations, have advantages and disadvantages. The semi-analytical approach is fast and flexible, allowing large parameter spaces to be explored, and making it easy to generate mock catalogues of galaxies over large volumes, which on the one hand can be compared to observational data to test the model assumptions and constrain the model parameters, and on the other hand, can be used to interpret large observational surveys. Hydrodynamical simulations can calculate the anisotropic distribution and flows of gas in much more detail and with fewer approximations, and provide detailed predictions for the internal structure of halos and galaxies, rather than just global properties.

To adequately model AGN feedback it is necessary to resolve spatial scales ranging from $\gtrsim 0.001\,\mathrm{pc}$ where energy is released from the accretion disc that feeds the SMBH, all the way to galactic (kpc) scales at which the large-scale outflow sweeps across the galaxy and the surrounding halo. Due to current computational limitations and to our lack of understanding of the nature of accretion, numerical implementations of AGN feedback always rely on subgrid models that attempt to mimic the effects of unresolved outflow physics (see e.g., Wurster and Thacker, 2013, for a comparison of several widely used AGN feedback models). These subgrid approximations, whose form is phenomenological, contain various free parameters, which are then adjusted so that, by analogy with SAMs, the predictions from the simulation agree with a predetermined set of observed properties. The use of these

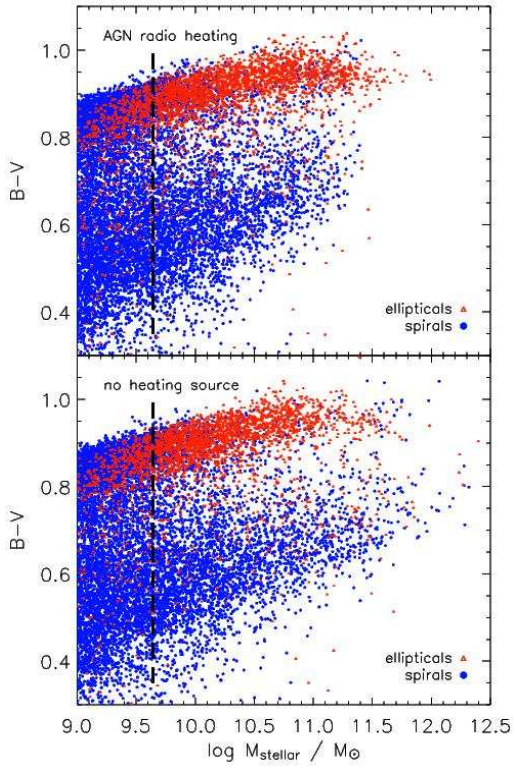

Figure 1.6: The B-V colours of model galaxies plotted as a function of their stellar mass with (top) and without (bottom) 'radio mode' feedback. A clear bimodality in colour is seen in both panels, but without a heating source the most massive galaxies are blue rather than red. Only when heating is included are massive galaxies as red as observed. Triangles (red) and circles (blue) correspond to early and late morphological types respectively, as determined by bulge-to-total luminosity ratio. The thick dashed lines mark the resolution limit to which morphology can be reliably determined in the Millennium Run. Figure from Croton et al. (2006).

subgrid models in simulations is thus closely analogous to the approach in SAMs, albeit on a smaller spatial scale.

The primary difference between the state-of-the-art simulations is a different parametrization of many important physical processes for the baryons (e.g., effective equation of state of the cold ISM, star formation, gas accretion on to BHs and feedback from both stars and AGN). As demonstrated by Wurster and Thacker (2013), AGN growth and star formation history could differ by orders of magnitudes depending on the type of feedback implementation. The subgrid modelling of gas accretion on to BH is discussed widely. In large scale simulations a spherical accretion onto a compact object traveling through the ISM (Bondi accretion model) can be assumed (in this case the energy is restricted by the Eddington limit, see section § 1.1). Angular momentum of in-falling gas has been accounted in newer prescription in isolated galaxies (Debuhr et al., 2010; Power et al., 2011). Another

area of uncertainty is the physical model for AGN feedback mechanism. Feedback has been modelled as direct thermal heating or in the form of radiative, mechanically driven winds (e.g., Faucher-Giguère and Quataert, 2012). Furthermore, the extent and the ways in which feedback energy is coupled to the surrounding gas are unknown. Some authors opt for deposit feedback energy within a given radius (fixed volume; e.g., Booth and Schaye, 2009; Dubois et al., 2012). Or in the case of Smoothed-particle hydrodynamics (SPH), energy is deposited to a fixed number of particles (fixed mass) near the BH (e.g., Springel et al., 2005; Okamoto et al., 2008).

Many efforts have been done to improve realism in drawing the AGN feedback, however, both theoretical understanding and numerical implementations have several challenges to tackle.

1.4 Quasar Outflows

Galaxy-scale outflows driven by quasars are thought to play a crucial role in galaxy formation, since they provide a mechanism for the central BH to possibly regulate star formation in the host galaxy. This mechanism can potentially explain the relation between the M_{BH} and the galaxy bulge properties and why star formation appears to be suppressed in massive galaxies (see section § 1.3.1). Quasar outflows may also contribute to the blowout of gas and dust from young galaxies, helping to enrich the intergalactic medium (IGM) with metals.

In recent years, multiple studies have presented observational evidence for the existence of such quasar-driven galaxy-scale outflows (e.g., Nesvadba et al., 2006, 2011; Greene et al., 2011; Rupke and Veilleux, 2011; Sturm et al., 2011; Maiolino et al., 2012; Arav et al., 2013; Cicone et al., 2014; Harrison et al., 2014). However, the physics which govern the dynamics of these large-scale outflows is still debated. A crucial question that then arises is how these outflows interact with the host galaxy and affect its gas content, star formation rate and morphology. The quasar-driven outflows are sufficiently energetic that they may heat and unbind a large fraction of the gas in a galaxy (Silk and Rees, 1998; Fabian, 1999; King, 2005), ridding the galaxy of its star formation reservoir and leading to the shutting off of star formation and quenching. On the other hand, it is possible that the outflows launched by the central engine cannot effectively couple with the surrounding dense interstellar medium and instead leave the host galaxy without causing major disruption to the ISM (Debuhr et al., 2012; Bourne et al., 2014; Roos et al., 2015) or they may even lead to shock-induced star formation bursts (Silk, 2013).

The approaches to include AGN feedback in numerical simulations, can vary widely, in both physics and numerical implementation. Pheraps one of the most relevant model for the Quasar winds has been proposed by King (2003, 2005). This model describes the interaction of a subrelativistic accretion disc wind with the ISM surrounding the accreting BH, which is assumed to lie at the centre of the galactic halo.

The structure of the shock pattern that ensues is qualitativey identical to that resulting from the interaction between a fast stellar wind and the surrounding interstellar gas (see e.g., Weaver et al., 1977; Dyson and Williams, 1997). The inner wind drives a forward shock wave that acts like a piston, sweeping up the host ISM, while the inner wind itself must decelerate strongly in an inner reverse shock facing towards the BH. Thus, in order of increasing distance from the AGN, the flow pattern consists of four zones (see Fig. 1.7): (a) the unshocked highly supersonic inner wind; (b) the shocked inner wind material that has crossed the reverse shock; (c) a shell of interstellar gas swept up by the forward shock and (d) the unperturbed ambient ISM.

The nature of this shock differs sharply depending on whether or not some form of cooling (typically radiation) removes a significant amount of energy from the hot shocked gas on a timescale shorter than its flow time. In other words, it is the cooling of region (b) that determines whether the outflowing shell in region (c) is energy- or momentum-driven.

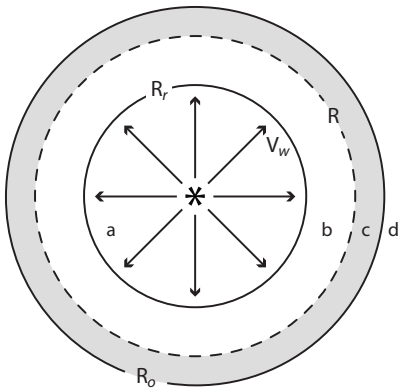

Figure 1.7: The shock pattern resulting from the collision of a fast inner AGN wind with the surrounding ISM. In order of increasing distance from the AGN, the flow pattern consists of four zones: (a) the unshocked highly super-sonic inner wind; (b) the shocked inner wind material that has crossed the reverse shock ; (c) a shell of interstellar gas swept up by the forward shock and (d) the unperturbed ambient ISM. Figure from Costa et al. (2014).

A momentum-driven outflow (shown in Fig. 1.8 on the left) occurs when the reverse shock cools efficiently. The shocked inner wind gas in region (b) traverses a radiative

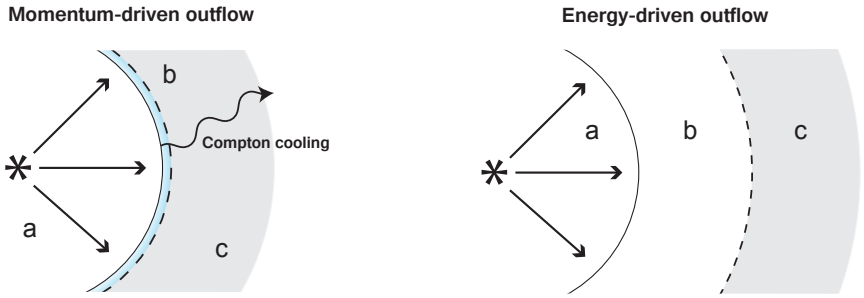

Figure 1.8: Momentum and energy-driven AGN outflows. A momentum-driven outflow (shown on the left) occurs when the reverse shock (region (b)) cools efficiently. An energy-driven outflow (shown on the right) happens when no substantial cooling losses are sustained. Figure from Costa et al. (2014).

region with a size of the order of the cooling length l_{cool} until its temperature returns to its pre-shock value at a radius $\approx R_r + l_{cool}$. Where R_r is the radius that delimits the region (a). The resulting (isothermal) shock consists of an initially adiabatic shock followed by a region where radiative cooling dominates (shown in light blue). The loss of thermal energy results in a drop of pressure support and causes region (b) to be very thin.

An energy-driven outflow (shown in Fig. 1.8 on the right) results when the energy injected by the inner wind (region (a)) is fully conserved throughout the outflow, i.e. no substantial cooling losses are sustained. Region (c) is driven out as the now hot and thick region (b) expands adiabatically. The question of how efficiently region (c) cools does not determine whether the outflow is energy- or momentum-driven.

The very rapid cooling means that the shocked wind gas is highly compressed, making the post-shock region geometrically narrow (shown in light blue, in Fig. 1.8, left). This region is often idealized as a discontinuity, know as an 'isothermal shock' (cfr. Dyson and Williams, 1997). As momentum must be conserved, the post-shock gas transmits just its ram pressure to the host ISM. In other words, in the momentum-driven limit, the energy injected into the bulge ISM, E_{mom}, is $E_{mom} \sim 0.1\, E_{gas}$, where E_{gas} is the gravitational binding energy of the bulge gas (we refer to King and Pounds, 2015 for a complete derivation of this energy limit). Thus momentum-driven flows do not threaten the bulge's integrity. A momentum-driven regime is a stable environment for M_{BH} growth. In the opposite limit where cooling is negligible, the post-shock gas retains all the mechanical luminosity thermalized in the shock, and instead expands adiabatically into the ISM. The available BH wind mechanical energy, E_{wind}, is in this case $E_{wind} \backsimeq 100\, E_{gas}$ (see King and Pounds, 2015). The post-shock gas is now geometrically extended (see Fig. 1.8, right), unlike the momentum-driven case. This energy-driven flow is much more violent than the momentum-driven flow.

Given these starkly different outcomes we must understand under what conditions we have momentum- or energy-driven outflows. Simple estimates immediately show that ordinary atomic two-body processes have no significant effect in cooling the wind shock. But the wind shock is exposed to the radiation field of an Eddington-accreting SMBH. This has a characteristic temperature of no more than $\sim 10^7$ K, far lower than the wind's immediate post-shock temperature of $\sim 10^{10} - 10^{11}$ K. Electrons in the post-shock gas lose energy to these photons through the inverse Compton effect (cfr. Ciotti and Ostriker, 1997), at a rate dependent on the radiation density. For wind shocks close to the SMBH, the accretion radiation field is intense enough that this effect cools the post-shock wind gas in less than the momentum-driven flow time $\sim R/\sigma$, and we are self-consistently in the momentum-driven regime, provided that the post-shock gas is in equipartition, i.e. that electron and ion temperatures remain effectively equal. For shocks at larger radii R the radiation energy density decreases as R^2, increasing the cooling time as R^2. The flow time increases only as R, so for R greater than the critical cooling radius

$$R_C \sim 500 M_8^{1/2} \sigma_{200}\,\mathrm{pc} \tag{1.10}$$

(King, 2003, 2005; King et al., 2011; Zubovas and King, 2012) the cooling time is longer than the flow time, and the flow must be energy-driven. So we have the general result that momentum-driven flows are confined to a small region $R < R_C$, while energy-driven flows must be large-scale. This is just as one would expect, given that a momentum-driven flow allows stable BH mass growth, while an energy-driven one is likely to expel most of the bulge gas. Therefore, it seems reasonable that the shock interaction characterizing the BH wind feedback changes from momentum-driven, acting on small spatial scales near the BH, to energy-driven, instead acting globally on the whole galaxy bulge and producing a high-energy clear out of its gas.

A separate class of models for AGN feedback envisages that AGN-driven outflows are driven by direct radiation pressure on dust grains embedded in the ISM of the galaxy (Fabian, 1999; Murray et al., 2005; Debuhr et al., 2011). In this scenario, interstellar gas is pressurised by the radiation field of the AGN rather than by a shocked AGN inner wind as in King (2003, 2005).

1.5 Quasar spectrum

1.5.1 The Continuum

Quasars show an intense continuum emission ranging from X-rays to radio. Due to the high luminosity of the nucleus and the large distance, the underlying galaxy, the host galaxy, is normally not seen; hence their stellar appearance. The mean spectral energy distribution (SED) for quasars is shown in Fig. 1.9.

The X-ray spectrum, which contributes approximately 10% to the bolometric luminosity of AGN, consists of several components. These include a power law continuum, a "soft excess" below X-ray energies of 1 keV (Arnaud and Rothenflug, 1985), and a "reflection hump" between 10 and 30 keV (George and Fabian, 1991). Photon energies extend to several GeV and, in some objects, even to γ-rays with energies in the TeV region (Horan and Weekes, 2004). For photon energies from 1 to 10 keV, the continuum can be represented by a power law $F\nu \propto \nu^{\alpha}$, with $\alpha \sim -0.8$ (Nandra and Pounds, 1994; Tozzi et al., 2006). The spectrum is by consequence not that of thermal emission, i.e. not a blackbody spectrum. It results from inverse Compton scattering in the hot corona above the accretion disk (Liang, 1979; Torricelli-Ciamponi et al., 2005). Due to the generation of the emission close to the nucleus, it often shows variations on timescales of weeks or days.

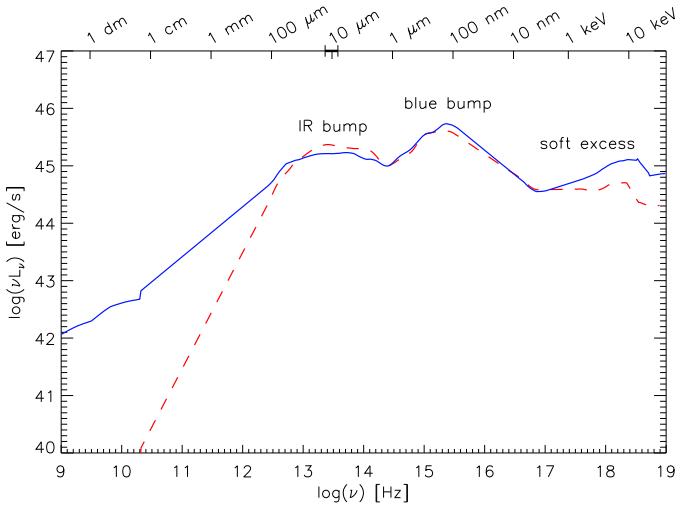

Figure 1.9: Mean quasar spectral energy distribution for radio-loud (blue line) and radio-quiet (red dashed line) quasars. The energy distribution is adapted from Elvis et al., 1994).

Between 10 and 400 nm, the spectrum shows another local maximum, the blue bump. This bump is of thermal nature. Generally, it is attributed to thermal radiation at temperatures of 10^4 to 10^5 K, albeit its origin is not entirely clear.

The emission might be caused either by optically thick, hot gas, i.e. blackbody radiation, or by free-free emission of optically thin gas (Barvainis, 1993). The most favoured understanding is that the emission originates from the supposed accretion disk (Shields, 1978; Malkan and Sargent, 1982; Shang et al., 2005). In the infrared, the continuum radiation of active galactic nuclei shows a thermal peak at wavelengths between 2 and 300 μm. This smooth bump, separated from the blue bump by a local minimum at ~ 1 μm, is frequently referred to as the infrared bump. Because of its thermal spectrum, the infrared bump is mainly ascribed to the emission from dust with temperature $T \lesssim 1500$ K (Rees et al., 1969; Lebofsky and Rieke, 1980; Barvainis, 1987). This dust is associated with the dusty torus. Depending on whether the AGN is radio-loud or radio-quiet, the emission in the radio regime is more or less pronounced. The radio spectrum is non-thermal and the spectral intensity follows a power law $F(\nu) \propto \nu^{\alpha}$. The radiation is due to synchrotron emission of relativistic electrons in the jets or extended emission lobes.

1.5.2 The Emission Lines

An important characteristic of AGN spectra is the presence of strong broad and narrow emission lines produced by the transitions of excited atoms. They can be used to infer both the physical conditions of the emitting gas (such as density, temperature, chemical composition, ionization state and turbulent motion) and the properties of the ionization sources.

We deal with two fundamental categories of emission lines: those produced by decays occurring during ionic recombination following ionization, and those produced by decays following collisional excitations by other particles in the gas. The observed emission lines are generally divided into two classes, permitted lines and forbidden lines (denoted by square brackets), according to the rate of spontaneous transition between the energy levels responsible for the emission. In general, forbidden transitions have lower probability than permitted ones. Because of the low transition probability, forbidden lines are not expected from gas with high density, where relevant ions can be removed quickly from the excited state by collisions with electrons before they have a chance to make the forbidden transition. On the other hand, permitted lines are expected in both high- and low-density gas.

One important application of emission line spectra is to use line ratios to separate AGN from star-forming galaxies whose spectra also contain emission lines due to the HII regions generated by young massive stars. As far as emission lines are concerned, the main difference between an AGN and a star-forming galaxy is in the level of ionization and temperature of the emitting gas, both expected to be higher

in an AGN due to the stronger UV flux involved. In addition, the radiation field in an AGN is also 'harder', i.e. contains a larger fraction of high-energy photons. These photons have a larger mean free path in a neutral medium, and can therefore penetrate farther to give rise to a larger partially ionized zone.

A further classification of the emission lines observed in Quasar spectra is between the *broad* lines with full width at half maximum (FWHM) of the order of 1000 to 5000 km s^{-1} and *narrow* lines with FWHM of the order of 500 km s^{-1}.

Forbidden transitions are only found as narrow lines whereas permitted lines may have both broad and narrow components. Lines that are collisionally excited and then decay radiatively have intensities that are proportional to the square of the density as do recombination lines. However, if a collisionally excited line normally decays by collisional de-excitation and only occasionally by radiative de-excitation (so the level population tends towards its Boltzmann equilibrium value), the intensity of the line will only be proportional to the density. Hence, at high densities, forbidden lines are weak compared with both permitted collisionally excited lines and recombination lines. All this implies that narrow lines in AGN come from a lower velocity and density region than the broad lines.

Broad-Line Region — The optical spectra of Seyfert 1 galaxies and quasars contain strong emission lines with velocity widths $\sigma_v > 1000$ km s^{-1}. If these velocity widths are due to the gravitational motion in the vicinity of the central BH, the sizes of the broad-line regions should be of the order

$$R \sim \frac{GM}{\sigma_v} \lesssim 0.5\, M_8 \left(\frac{\sigma_v}{1000\,\mathrm{km\,s^{-1}}}\right)\ pc. \tag{1.11}$$

This argument suggests that the broad lines are produced in a small inner region surrounding the accretion disk. Direct imaging of the broad-line region has not yet been possible, but the observed variabilities of broad lines suggest a typical size of $\lesssim 0.5$ 1 light-year (~ 0.3 pc), consistent with that based on the velocity width. Broad forbidden lines (such as [OIII]) are not observed, indicating that the electron density of the gas producing the broad lines is very high. Detailed photoionization models of the broad-line spectra give a representative density of about 10^9 cm^{-3} and gas temperatures $\sim 2 \times 10^4$ K.

Narrow-Line Region — The optical spectra of many AGN reveal strong narrow lines with velocity widths $\sigma_v \sim 100$ km s^{-1}. From Eq. 1.11 we see that such lines may be produced in a region of size ~ 50 pc around the central engine. Because of their relatively large sizes, narrow-line regions in nearby AGN can be spatially resolved even with ground-based observations. The observed sizes range from

$\sim$ 10 pc to $\sim$ 100 pc, again in good agreement with the sizes inferred from the velocity widths. Since forbidden [OIII] lines are usually observed, the density of the narrow-line gas must be $\lesssim 0.5{\times}10^6$ cm^{-3}. Detailed modeling of the narrow-line spectra yields densities in the range $(10^4 - 10^6)$ cm^{-3}. This relatively large range is also required within individual AGN to explain the observed line ratios, indicating that the gas within a narrow-line region is highly inhomogeneous. The gas is mainly photoionized by the central source, although collisional ionization may also be involved in some cases. The temperature of the gas is in the range $1 - 2 \times 10^4$ K.

Chapter 2

2 Quasar Absorption Spectra

Absorption features in quasar spectra provide a unique tool for probing the gas content of foreground galaxies and of the intergalactic medium IGM. It is well known that information about their temperature, density, chemical abundances and kinematics can be extracted from the analysis of these absorption lines. For instance, a detailed insight into the physical state of the IGM is provided by the analysis of the absorption lines found in the spectra of distant quasars (see e.g. Hu et al., 1995; Kim et al., 1997, 2001, 2002; McQuinn, 2015 and references therein).

Knowledge about the actual physical state of these systems can be obtained basically from the line profiles. Both line counting and line profile measurement are tricky tasks though, since the accuracy with which they can be performed highly depends on the resolution of the observed spectra.

For instance, depending on the spatial distribution of the absorbing systems, lines can appear very close to each other or even superposed (line blending), and a low spectral resolution may lead to the misidentification of the resulting composite profile as being a single, complex one. Because of this same reason, the determination of the exact shape of each individual absorption profile is far from being trivial, and misidentified profiles may lead to wrong conclusions about the properties of the absorbing systems.

In this chapter, I summarize a few basic and classical definitions on the formation and characteristics of absorption lines (section §2.1), that are important to keep in mind when discussing the results of this work in the following chapters. Finally, I introduce the standard classification for quasar absorption lines (section §2.2). Throughout this manuscript, I adopt a ΛCDM cosmology with $\Omega_M = 0.315$, $\Omega_\Lambda = 0.685$, and $H_0 = 67.3\,\mathrm{km\,s^{-1}Mpc^{-1}}$ (Planck Collaboration et al., 2014).

2.1 Absorption Lines

Absorption processes and their signatures imprinted on the spectra of bright background sources (quasars, Gamma-ray burst, etc.) are one of the main sources

of information about the physical and chemical properties of intervening systems and of the IGM. To gain informations from absorption lines, it is necessary to model them with some analytical profile whose parameters are related to the physical properties of the gas from which lines originated.

As the radiation propagates through the medium, the energy intensity of radiation, I_ν, evolves according to the equation of *radiative transfer*:

$$dI_\nu = -I_\nu \kappa_\nu \, dx + j_\nu \, dx, \tag{2.1}$$

where κ_ν is the attenuation coefficient at frequency ν, with dimensions of 1/length, and j_ν is defined as the emissivity at frequency ν, with dimensions of power per unit volume per unit frequency per unit solid angle. The term $-I_\nu \kappa_\nu dx$ is the net change in I_ν due to absorption and stimulated emission, and $j_\nu dx$ is the change in I_ν due to spontaneous emission by the material in the path crossed. Eq. 2.1 can be written, as

$$\begin{aligned} \frac{dI_\nu}{\kappa_\nu \, dx} &= -I_\nu + \frac{j_\nu}{\kappa_\nu} \\ \frac{dI_\nu}{d\tau_\nu} &= -I_\nu + S_\nu(\tau), \end{aligned} \tag{2.2}$$

where $d\tau_\nu = \kappa_\nu \, dx$ defines the *optical depth* through the pathlength and $S_\nu(\tau)$ is the source function. Since we are concerned only with absorption lines, we can set $S_\nu(\tau) = 0$ and thus easily solve Eq. 2.2 as

$$I_\nu = I_0 \, e^{-\tau_\nu}. \tag{2.3}$$

Suppose that we observe a bright continuum source behind a foreground cloud of gas, and we measure the energy *flux density* F_ν as a function of ν. We observe the source using an aperture of solid angle $\Delta\Omega$, and we assume that the properties of the foreground gas are essentially uniform over $\Delta\Omega$. If we integrate Eq. 2.3 over the solid angle $\Delta\Omega$ of our spectrometer aperture, we obtain the flux density at the observer

$$F_\nu = F_\nu(0) \, e^{-\tau_\nu}, \tag{2.4}$$

where $F_\nu(0)$ is the flux density from the source in the absence of absorption. We can interpolate to estimate the quasar continuum flux $F_\nu(0)$ even at the frequencies

where absorption is present, and we can evaluate the dimensionless *equivalent width*

$$W_{obs} = \int \frac{d\nu}{\nu_0} \left[1 - \frac{F_\nu}{F_\nu(0)}\right] = \int \frac{d\nu}{\nu_0}(1 - e^{-\tau_\nu}). \tag{2.5}$$

We can also define the wavelength equivalent width

$$W_{obs}(\lambda) = \int d\lambda\,(1 - e^{-\tau_\lambda}). \tag{2.6}$$

The integrals in Eqs. 2.5 and 2.6 extend only over the absorption feature, with the integrand $\propto [1 - F_\lambda/F_\lambda(0)] \to 0$ on either side of the feature. It is important to note that W_{obs} (or $W_{obs}(\lambda)$) can be measured even if the absorption line is not resolved, i.e. the equivalent width is just proportional to the total missing power that has been removed by the absorption line. For redshifted absorption lines, $W_{obs} = W_r \times (1 + z_{abs})$, where W_r is the equivalent width at rest frame and z_{abs} is the redshift of the absorption line.

The observed line profile results from the combination of different broadening mechanisms.

(1) **The Doppler broadening** is due to the motion of individual absorbing atoms. We can characterizes this effect with a function describing the broadening due to the distribution of atomic velocities (generally assumed to be Maxwellian with temperature T),

$$\phi(\nu) = \frac{1}{\sqrt{\pi}\Delta\nu_D}\, e^{-(\Delta\nu/\Delta\nu_D)^2} \tag{2.7}$$

with the *Doppler width*

$$\Delta\nu_D = \frac{\nu_0}{c}\sqrt{\frac{2kT}{m}} = \frac{\nu_0}{c}\, b_{th} \tag{2.8}$$

where ν_0 is the frequency of the line centre, $b_{th} = \sqrt{2kT/m}$ is the thermal Doppler parameter, and m is the mass of the atoms forming the pierced gas.

In addition to the thermal velocity field, the atoms in the gas may experience motion due to turbulence. If the turbulence can be modeled as a Gaussian velocity distribution with quadratic mean velocity $\sqrt{\frac{3}{2}}\,V$ and mean velocity $2V/\sqrt{\pi}$, then the resulting profile is still given by Eq. 2.7, but with Doppler parameter $b_{tot}^2 = b_{th}^2 + V^2$.

(2) **The natural and pressure line broadening**. Every spectral line has an intrinsic width due to the fact that excited states have in general very short lifetimes and by Heisenberg's uncertainty principle, $\Delta E \Delta t \sim h/2\pi$, so there will be a spread in energy level. The pressure or collisional broadening is the effect of deexcitation of the upper level caused by interactions with other particles. The two effects give

a similar line shape, the so called *Lorentzian* profile

$$\phi(\nu) = \frac{\Gamma}{4\pi^2} \frac{1}{(\nu - \nu_0)^2 + (\frac{\Gamma}{4\pi})^2} \tag{2.9}$$

where the Lorentzian width Γ is the sum of the collisional and natural line widths, and ν_0 is the central frequency of the transition. The global line profile always contains both components. The line centre is dominated by the Doppler profile, while the collisional/natural component is dominating the wings of the line. The convolved profile is called Voigt profile, and is given by

$$\phi(\nu) = \frac{a}{\pi^{3/2}\Delta\nu_D} \int_{-\infty}^{\infty} \frac{e^{-y^2}}{(x-y)^2 + a^2}\, dy \tag{2.10}$$

where $a = \Gamma/(4\pi\Delta\nu_D)$ is the ratio of the damping width to the Doppler width. It has been defined the Doppler frequency, $\Delta\nu_D$,

$$\Delta\nu_D = \frac{1}{\lambda_0}\sqrt{\frac{2kT}{m}} \tag{2.11}$$

which is the central frequency of the Lorentzian of an atom with the RMS velocity of the Maxwellian. The dimensionless frequency x is

$$x = \frac{\nu - \nu_0}{\Delta\nu_D} = \frac{\lambda - \lambda_0}{\Delta\lambda_D} \tag{2.12}$$

the difference between the frequency or wavelength and the line center in units of the Doppler frequency or Doppler wavelength,

$$\Delta\lambda_D = \frac{\lambda_0^2}{c}\Delta\nu_D = \frac{\lambda_0}{c}\sqrt{\frac{2kT}{m}}. \tag{2.13}$$

The resonance line scattering cross section is defined as

$$\sigma_\nu = a_{\nu_0} H(a, x) \tag{2.14}$$

where $H(a, x)$ is the *Voigt-Hjerting* function (Hjerting, 1938)

$$H(a, x) = \frac{a}{\pi} \int_{-\infty}^{\infty} \frac{e^{-y^2}}{(x-y)^2 + a^2}\, dy \tag{2.15}$$

and

$$a_{\nu_0} = \frac{\sqrt{\pi}e^2}{m_e c} \frac{f}{\Delta\nu_D} \tag{2.16}$$

where f is the oscillator strength.

If we assume that the absorbing atoms have a gaussian velocity distribution of mean v_0 relative to the referential R, then it is possible to estimate the optical depth as sees by an observer in R. An atom with velocity v absorbs a photon of frequency ν in R with a cross-section $\sigma(\nu^{'})$ where $\nu^{'} = v/(1 - v/c)$, v taken to be positive for an atom that goes away from the observer and,

$$\tau(\nu) = N\frac{1}{\sqrt{\pi}b}\int_{-\infty}^{+\infty}\sigma(\nu^{'})e^{-\frac{(\nu-\nu_0)^2}{b^2}}dv \tag{2.17}$$

where N is the column density, the total number of atoms along the line of sight in a cylindric volume of unitary base, b is the Doppler parameter (see the definition of b_{tot}).

The cross-section in turn can be expressed as the product of the line profile and a constant for a particular line

$$\sigma_\nu = \sigma_{\nu_0}\,\phi(\nu) \tag{2.18}$$

where the line profile is normalized so $\int \phi(\nu)\,d\nu = 1$.

One can show that the cross-section σ_{ν_0} [cm^{-3}] at line center for absorption is

$$\sigma_{\nu_0} = \frac{\sqrt{\pi}e^2}{m_e c}\frac{f}{\Delta\nu_D} \tag{2.19}$$

where f is the oscillator strength. Therefore, switching from frequency to wavelength, Eq. 2.17 reduces to

$$\tau(\lambda) = 1.498\times10^{-2}\,\frac{Nf\lambda}{b}\,H(a,x) \tag{2.20}$$

The observed line profile depends on the dimensionless optical depth at the line center, τ_{ν_0}, which is

$$\tau_{\nu_0} = \int n\,\sigma_{\nu_0}dl \tag{2.21}$$

where the right hand side is the integral through absorbing cloud of the volume density n [cm^{-3}] times the cross-section σ_{ν_0}. If the volume density n is uniform, it is possible to write

$$\tau_{\nu_0} = 1.498\times10^{-15}\,\frac{fN(\mathrm{cm}^{-2})\lambda_0(\text{Å})}{b(\mathrm{km\,s}^{-1})}. \tag{2.22}$$

2.1.1 The curve of growth

If the spectral resolution of the data is not good enough to resolve the intrinsic line profiles, we can still learn a lot by measuring the equivalent width of the absorption line, which is defined as the width of the rectangular line with area equal to the absorbed area of the actual line. From Eq. 2.6, 2.15 and 2.20 it is possible to connect the equivalent width to the column density for different values of the Doppler parameter. The function that gives this relation is called *curve of growth*. Fig 2.1 shows an example corresponding to the HI Lyα transition for b = 5, 10, 20 and 30 km s^{-1} (Petitjean, 1998). Three distinct regimes can be identified:

(1) On the linear part of the curve of growth, the equivalent width increases linearly with increasing column density. When the column density is small ($\tau_0 < 0.1$), the absorption line is optically thin, the Voigt function reduces to a Gaussian profile and the equivalent width does not depend on b. In this condition the determination of N from w is easy and reliable. For any transition,

$$N(\mathrm{cm}^{-2}) = 1.13 \times 10^{20} \frac{W_r\,(\text{Å})}{\lambda_0^2\,(\text{Å}) f} \tag{2.23}$$

(2) On the logarithmic or flat part of the curve of growth, the equivalent width is insensitive to column density but has some sensitivity to temperature, or equivalently, the b-value of the line. In this regime N is largely dependent on b at a given W. Thus, the determination of b and N are very uncertain except when various lines of the same ion are used. From Eq. 2.22 we can see that equivalent width and optical depth at the center of the line are related by

$$\frac{W}{\lambda_0} = 2\,\frac{b}{c}\sqrt{ln(\tau_0)} \tag{2.24}$$

(3) On the saturated part of the curve of growth the lines are characterized by prominent damping wings. The equivalent width does not depend on b and the column density can be accurately determine from measurement of W or fitting the wings. From Eq. 2.22 and 2.15

$$\frac{W}{\lambda_0} = 2.64 \frac{b\sqrt{a}}{c} \times \sqrt{\tau_0} \tag{2.25}$$

and for HI λ 1215.67, $\gamma = 6.265 \times 10^8\,\mathrm{s}^{-1}$ (Morton, 2003), and:

$$N(\mathrm{cm}^{-2}) = 1.88 \times 10^{18}\, W_r(\text{Å}) \tag{2.26}$$

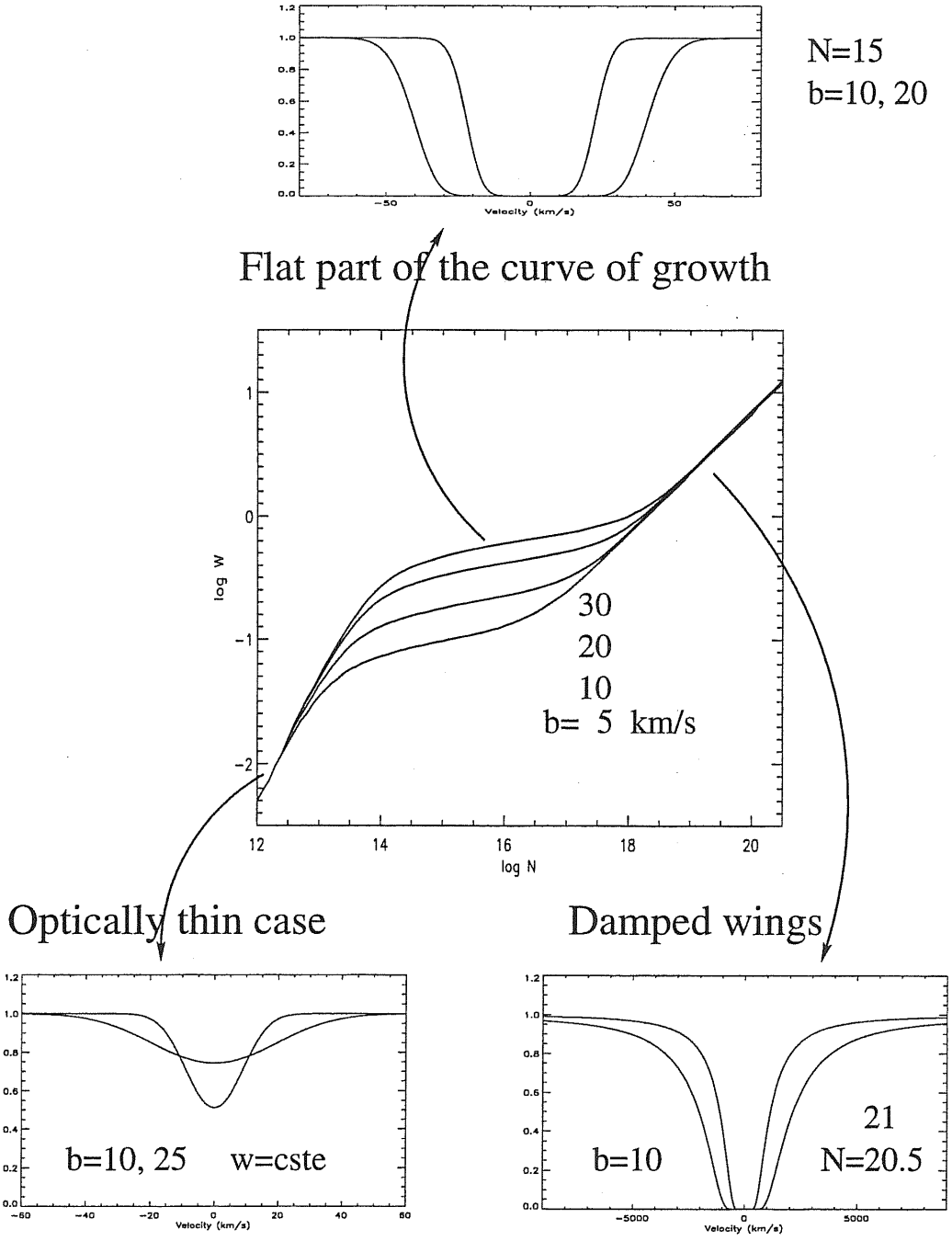

Figure 2.1: Curve of growth: logarithm of the equivalent width (in Å) versus logarithm of the column density (in cm^{-2}) for different values of the Doppler parameter (in km s^{-1}). The curves are calculated for HI Lyα1215. The figure shows the three characteristic regimes (see the text). Figure from Petitjean (1998).

In those cases in which one wants to determine both the column density and the Doppler parameter it is necessary to use multiple lines due to the same ion. Doublets (two components of a fine structure) are often exploit because they unambiguously identify redshift systems with two lines. Let (H) be the shorter

wavelength member of the doublet with an f-value which is twice the f-value of the longer wavelength member (K) of the doublet. In the optically thin limit, the ratio of the equivalent widths of the two lines will be exactly the ratio of the f-values, or 2. In this case, one can derive the column density from the equivalent width of either line, but not the b-value. Now consider the effects of increasing column density. The K line will become optically thick first. If the H line is still on the linear part of the curve of growth, then the ratio of the equivalent width will be between 1 and 2. The column density may be derived from the equivalent width of the H line, ad the b-value from the equivalent width of the K line. At still higher column density, both H and K are saturated.

2.1.2 Voigt profile decomposition

The introduction of echelle spectrographs on 4m telescopes has allowed the observation to obtain high resolution spectra (spectral resolution $\mathfrak{R} = \lambda/\Delta\lambda > 20,000$). With this resolution narrow absorption lines can be observed with an instrumental FWHM lower than their intrinsic width. This makes it possible to independently derive the column density and Doppler parameter from line profile fitting, rather than from the curve of growth analysis. The fit of heavy element systems may require the simultaneous fit of different lines spread all over the spectrum. For these lines, it is often necessary to test different configurations (i.e. number of components and constraints on them) before satisfying fit is achieved. In the analysis of the Lyman-α forest (see section § 2.2.1), on the contrary, hundreds of independent lines are fitted. Even if, for strong Lyα lines the higher order Lyman lines can provide additional constraints when fitted simultaneously. The standard approach to this problem (Webb, 1987; Carswell and Rees, 1987) relies on χ^2 minimization to achieve a complete decomposition of the spectrum into as many independent Voigt profile components as necessary to make the χ^2 probability consistent with random fluctuations.

If one assumes that the physical state of the absorbing medium is uniquely defined by its temperature and column density, single absorption line profiles are ideally described by Voigt profiles. The fit of a single absorption feature with several components is most often not unique; the different solutions can yield column densities differing by an order of magnitude. When several transitions from the same ion are used, better significance is achieved. The Voigt profile model for spectral lines is based on the assumption that absorbing atoms have a purely Gaussian velocity dispersion (a thermal Maxwell-Boltzmann distribution, plus any Gaussian contributions from turbulence).

Unfortunately, in most more realistic models of the absorbing gas, finite velocity and density gradients invalidate the assumptions, and the line parameters may have less immediate physical meaning.

Departures of the absorption line shape from a Voigt profile may contain valuable information about the underlying nature of the absorption systems, and different scenarios may have quite different observational signatures.

Rotational motion (Weisheit, 1978; Prochaska and Wolfe, 1997), gravitational collapse (McGill, 1990; Meiksin, 1994; Rauch et al., 1996), and galactic outflows (Fransson and Epstein, 1982; Wang, 1995) have been discussed in terms of the likely absorption line shapes they produce. As yet, the quantitative application of these results has proven difficult because of the lack of realistic prototypical models for the actual line formation, the rather subtle departures from Voigt profiles expected, and the wide variety of profiles actually encountered. Non-Voigt profiles can still be fitted as blends of several Voigt profiles, but the information about the nonthermal motion is encoded in the spatial correlations between the individual profiles (Rauch et al., 1996). Also, there is no guarantee that the number of components necessary for a good fit converges with increasing signal to noise ratio (S/N).

2.1.3 Apparent Optical Depth Method

The apparent optical depth (AOD) method (Savage and Sembach, 1991a; Sembach and Savage, 1992), provides a quick and convenient way to convert velocity-resolved flux profiles into reliable column density measurements for intergalactic absorption lines, without the need to follow a full curve of growth analysis or detailed component fit and without requiring prior knowledge of the component structure. The latter aspect is particularly important when high resolution data are not available.

An absorption line having optical depth, $\tau(\lambda)$, as a function of wavelength, λ, will appear in the spectrum of a quasar and can be described by Eq. 2.3

$$I(\lambda) = I_0(\lambda)\, exp[-\tau(\lambda)], \tag{2.27}$$

where $I(\lambda)$ and $I_0(\lambda)$ are the intensities with and without the absorption, respectively. When an absorption is recorded with an instruments having a finite resolution defined by its instrumental spectral spread function, $\phi_I(\Delta\lambda)$, the spectrum is a convolution of the intrinsic spectrum and the spread function,

$$I_{obs}(\lambda) = \{I_0(\lambda)\, exp[-\tau(\lambda)]\} \otimes \phi_I(\Delta\lambda). \tag{2.28}$$

It is reasonable to expect that the intensity of the quasar spectrum, $I_0(\lambda)$, changes slowly over the width of the spread function, and Eq. 2.28 becomes

$$I_{obs}(\lambda) = I_0(\lambda)\{exp[-\tau(\lambda)]\} \otimes \phi_I(\Delta\lambda)\}. \tag{2.29}$$

From Eq. 2.27 and 2.29 we can define two kinds of optical depth,

$$\tau(\lambda) = ln[I_0(\lambda)/I(\lambda)], \tag{2.30}$$

and

$$\tau_a(\lambda) = ln[I_0(\lambda)/I_{obs}(\lambda)]. \tag{2.31}$$

The optical depth, $\tau(\lambda)$, obtained from Eq. 2.30 is the *true* optical depth as determined from the true line profile. The optical depth, $\tau_a(\lambda)$, derived from Eq. 2.31 is hereafter referred to as *apparent* optical depth. The apparent optical depth is an instrumental blurred version of the true one. From Eq. 2.29 we can derive the apparent optical depth

$$\tau_a(\lambda) = ln[1/\{exp[-\tau(\lambda)] \otimes \phi_I(\Delta\lambda)\}]. \tag{2.32}$$

If the instrumental resolution is high compared to the line width (i.e., FWHM[line] $\gg$ FWHM[ϕ_I], where FWHM[line] and FWHM[ϕ_I] refer to the full widths at half-maximum intensity of the absorption line and the instrumental spread function, respectively), then $\tau_a(\lambda)$ will be a good representation of $\tau(\lambda)$ as long as the data have high S/N and the continuum level is well defined.

In the AOD method, a velocity-resolved flux profile $F(v)$ is converted to an apparent optical depth profile $\tau_a(v)$ using the relation Eq. 2.31.

There is a connection between the optical depth and the column density, Eq. 2.20. Therefore, the apparent optical depth profile can be converted into an apparent column density profile according to

$$N_a(v) = 3.768 \times 10^{14}\,(f\lambda)^{-1}\,\tau_a(v)\ \mathrm{cm}^{-2}\,(\mathrm{km\,s}^{-1})^{-1}, \tag{2.33}$$

where f is the oscillator strength of the transition, the column density is expressed here per unit velocity, and λ is the transition rest frame wavelength in Å (Savage and Sembach, 1991a). The total apparent column density is then

$$N_a = \int_{v_-}^{v^+} N_a(v)\,dv \tag{2.34}$$

where v_- and v^+ are the velocity limits of the line. This technique offers excellent results if applied to spectra with S/N $\gtrsim$ 20 (Fox et al., 2005). When two lines of different strength of the same ionic species are available, the AOD method allows to assess and correct for the level of saturation in the data by comparing the apparent column density derived from the stronger line with that derived from the weaker one (Savage and Sembach, 1991a; Jenkins, 1996). Therefore, we can take advantage of this method to correct the column density of doublets when the stronger member is saturated.

This method makes no a priori assumptions regarding the velocity distribution of the absorbing gas and permits a study of the full velocity dependence of the absorption and how it changes from ion to ion. The AOD method may have a number of advantages over the standard curve of growth and detailed profile fitting methods used for deriving column densities from absorption line measurements: (1) is computationally simple to derive column densities and error estimates; (2) provides significant empirical information about the velocity dependence of line saturation; (3) is more easily applicable when multiple component absorptions are involved; (4) where many absorption lines for a given species exist, a complete column density profile spanning several decades in $N_a(v)$ can be constructed by combining $N_a(v)$ profiles for weak and strong lines (see Savage and Sembach, 1991a, for a more detailed discussion about all the possible advantages of this method).

However, if one is more interested in obtaining the shape of the line profile (when it is reasonable to assume that the absorption line is fully resolved) than to obtain an accurate column density, a detailed line profile fitting is necessary.

The AOD technique, while an excellent tool when applied to data with good S/N, will likely overestimate the true column densities when applied to data with low S/N. This overestimation results from the nonlinear relationship between the flux falling on a given detector pixel and the apparent optical depth in that pixel.

The nonlinear distortion of the $N_a(v)$ profile and resulting overestimate of $N_a(v)$ become worse as the S/ N decreases (Fox et al., 2005). Rebinning the spectrum before measurement can lessen the distortion, since the rebinning process increases the effective S/N. Once the data are rebinned to a level coarser than the resolution element, the gain in the $N_a(v)$ accuracy is made at the expense of resolution, so that kinematic information is given up. However, if the absorption line before rebinning is fully or marginally resolved, and if one is more interested in obtaining an accurate column density than in obtaining knowledge about the detailed shape of the line profile, then overbinning is justified at low S/N.

For marginally resolved lines, the $N_a(v)$ tends to underestimate the true column

density at high line depths (Fox et al., 2005), since the high optical depth points are smoothed out to lower apparent optical depths by the instrumental blurring. This effect therefore works in the opposite sense to the S/N effect. The more unresolved the line is, the worse this effect becomes.

For a given S/N and line width, the overestimation factor is worse for shallow lines than for deep lines. This is because the noise is Poissonian, so a pixel with low optical depth (shallow) has a higher error on the flux than a pixel with high optical depth (deep).

I refer to Fox et al. (2005) for a detailed discussion about the accuracy of $N_a(v)$ determinations as a function of line depth and S/ N, together with the separate effects of line width and rebinning.

2.2 The classification of Quasar Absorption Lines

2.2.1 Lymanα Forest

The discovery of quasars in the sixties opened the study of the IGM (Schmidt, 1963). Looking at the absorption spectra of these objects people realized the presence of an extraordinary amount of absorption features, in particular a "forest" of absorption lines blue-ward of the Lyman-α (Lyα) emission, much more numerous than in the region red-ward of the Lyα emission. Most of the lines in the forest were proven to be due to the Lyα resonant transition in neutral hydrogen (Gunn and Peterson, 1965; Bahcall and Salpeter, 1965; Burbidge et al., 1966). With the acquisition of more and more data, the number of HI Lyα lines strongly supported the idea that galactic and intergalactic gas, and not only material intrinsic to the quasar, was the source of most quasar absorptions (Lynds, 1971; Oemler and Lynds, 1975; Young et al., 1979). Since neutral hydrogen clouds at different positions along this line of sight see the photons at different wavelengths (due to the redshift), each individual cloud leaves its fingerprint as an absorption line at a different position in the observed spectrum blue-ward of the Lyα emission line of the quasar. For a comprehensive review of the Lyα forest, which considers both theoretical and observational aspects, see McQuinn (2015).

The pattern of absorption lines imprinted on the spectra of distant objects by neutral hydrogen in the IGM, is one of the most fundamental probes of cosmic structure. The characteristics of this absorption reflect the density distribution, ionization state, and temperature of the intergalactic gas. The gas, in turn, closely traces the underlying distribution of dark matter, albeit with significant deviations

arising from hydrodynamics coupled to the radiative and mechanical feedback from galaxies and AGN. Consequently, the Lyα forest allows to probe the baryon physics connecting the evolution of large-scale structure to the highly non-linear processes driving galaxy formation.

Most of the Lyα forest is associated with moderate overdensities and traces filamentary structure on large scales, but strong forest absorbers along with Lyman limit systems and damped Lyman-α systems (DLAs) are thought to be associated with galaxies and the circumgalactic medium (e.g. Fumagalli et al., 2011).

Metals have been observed associated with the high-redshift Lyα forest. In particular, CIV (e.g., Meyer and York, 1987; Cowie et al., 1995; Songaila and Cowie, 1996; Ellison et al., 2000; Schaye et al., 2003; Pieri et al., 2006) and OVI (e.g., Schaye et al., 2000; Pieri and Haehnelt, 2004; Simcoe et al., 2004; Bergeron and Herbert-Fort, 2005; Aguirre et al., 2008; Frank et al., 2010; Pieri et al., 2010) provide prominent absorbers and are commonly measured. Other detected species seen are SiIV, SiIII, CIII, and NV (e.g., Schaye et al., 2003; Aguirre et al., 2004; Fechner and Richter, 2009). These measurements provide some indications of the regions of the universe affected by mechanical feedback, but they can also provide a useful probe of the ionization properties of the medium (and so the physical

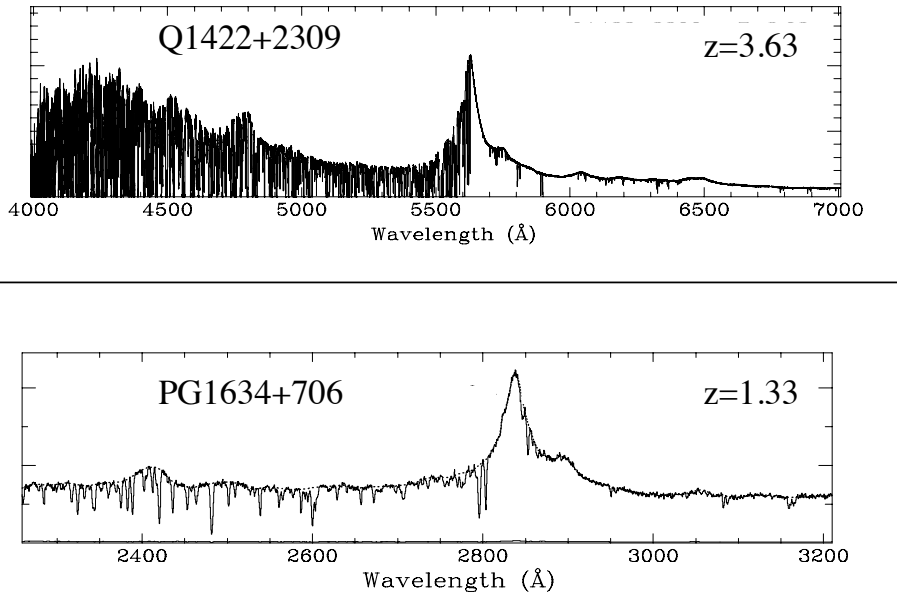

Figure 2.2: Illustration of structure evolution of intergalactic gas from high to low redshift. The upper spectrum of a $z = 3.6$ quasar is a Keck/HIRES observation, while the lower spectrum is a FOS/HST observations of a $z = 1.3$ quasar. Higher redshift quasars show a much thicker forest of Lyα lines. Figure from Charlton and Churchill (2000).

conditions of the gas), and the abundance pattern. Many other weak lines are challenging to detect, but progress has been made towards this goal (Pieri et al., 2010) by stacking Lyα forest lines in Sloan Digital Sky Survey II Data Release 5 (SDSS-II DR5; York et al., 2000) quasar spectra (see also Harris et al., 2016).

The appearance of the Lyα forest region in quasar spectra is strongly dependent on the emission redshift of the forest itself. Fig. 2.2 is a clear example of the observed evolution of the Lyα forest and of the environment that hosts the quasar. Qualitatively, the evolution can be understood in terms of two main factors. The UV radiation field is expected to decrease from $z \sim 2$ to $z = 0$, whether it is comprised of photons from quasars or starforming galaxies. Thus as the UV field decreases the neutral fraction increases and the number of detected lines should increase. This tendency is balanced and overcome by a second effect: as cosmic expansion proceeds, the density of the gas decreases and even if the photoionizing UV field was constant, the neutral fraction would decrease and the number of Lyα lines detected would decrease.

2.2.2 Metal Absorption Lines

The spectrum of a $z_{em} \sim 3$ quasar is shown in Fig. 2.3. The broad emission line at $\lambda_{obs} = 5000$ Å is the Lyα emission associated with the quasar. The broad feature just short of 5000 Å is a DLA absorption arising from an intervening absorber, which also causes the observed continuum of the quasar to go to zero at the Lyman limit.

Many absorption features due to ionic transitions in chemical elements heavier than He ("metals") are clearly present red-ward of the Lyα emission. These absorbers are generally associated with the strongest Lyα absorptions ($N_{HI} \gtrsim 10^{14}\,\mathrm{cm}^{-2}$; e.g. Cowie and Songaila, 1998; Lu et al., 1998; Ellison et al., 2000; Lopez et al., 2004; Lopez, 2006; D'Odorico et al., 2010; Boksenberg and Sargent, 2015; D'Odorico et al., 2016; Kim et al., 2016). Some of them are associated with the quasar itself but the majority are tracers of intervening metals belonging to structures of different nature, from diffuse gas to galaxies.

Absorption lines are usually classified based on the full width at half maximum (FWHM) of their profiles. The broad absorption lines (BALs) display deep, broad and typically smooth absorption troughs with velocity width larger than a few thousand km s^{-1} (Weymann et al., 1981; Turnshek, 1984; Weymann et al., 1991; Reichard et al., 2003; Trump et al., 2006). The narrow absorption lines (NALs), on the other hand, have relatively sharp profiles with FWHM $\lesssim$ 300 km s^{-1} so that important UV doublets, such as CIV $\lambda\lambda$ 1548, 1550 Å, are discernible. Since

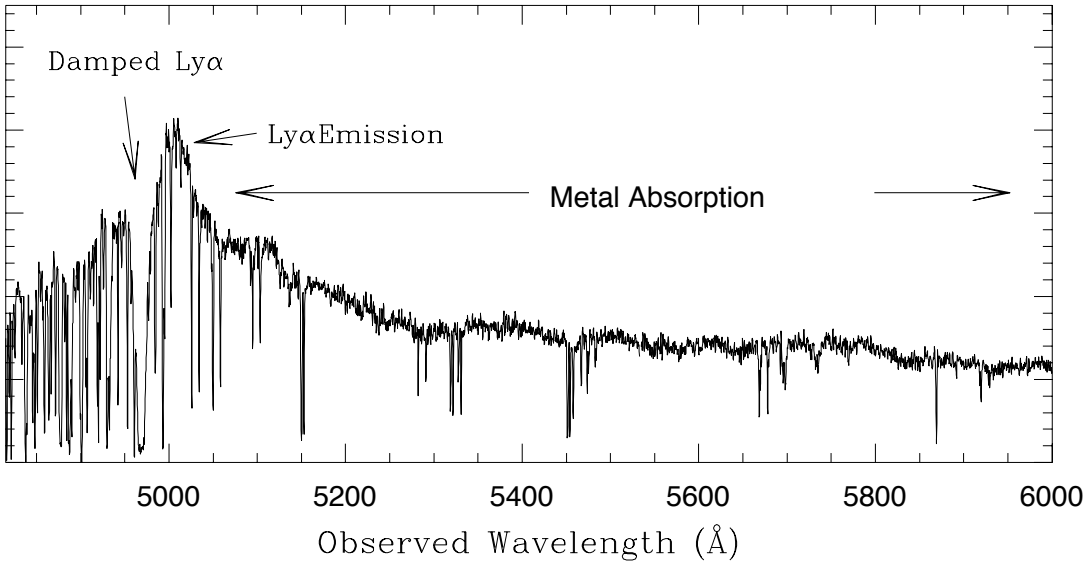

Figure 2.3: High resolution spectrum of the quasar Q 0420-388 at $z_{em} = 3.12$ obtained with the Las Campanas echelle spectrograph, by the author and S. A. Shectman. Prominent features are indicated. Figure from Bechtold (2001).

there is a whole continuum of velocity widths, this has led to an in-between class known as mini-BALs (e.g., Hamann et al., 1997c; Churchill et al., 1999).

Outflows are most commonly indentified through absorption lines against the central compact UV/X-ray continuum. NAL, BAL and mini-BAL absorption features represent the potential fingerprints of these outflows imprinted on quasar spectra.

A central problem is our poor understanding of the physical relationships between BAL, NAL and mini-BAL outflows. One possibility is that the different line types are simply different manifestations of a single outflow phenomenon viewed at different angles. For example, it is often supposed that BALs form in the main body of the outflow near the accretion disc plane, while NALs and mini-BALs form along sightlines that skim the edges of the BAL flow at higher latitudes above the disc (Ganguly et al., 2001; Chartas et al., 2009). There could also be evolutionary effects. For example, NALs and mini-BALs might represent the tentative beginning or end stages of a more powerful BAL outflow phase (Hamann et al., 2008). There is some evidence for outflow evolution, a particular variety of low-ionization BALs (the so-called FeLoBALs) is found preferentially in dusty young host galaxies with high star formation rates (Farrah et al., 2007). Variability studies have shown further that BALs and mini-BALs in quasar spectra can appear, disappear or swap identities (where a BAL becomes a mini-BAL or vice versa) on time-scales of months to years in the quasar rest frame (Gibson et al., 2008, 2010; Hamann

et al., 2008; Leighly et al., 2009; Capellupo et al., 2010; Rodríguez Hidalgo et al., 2011). The true relationship between outflow NALs, BALs and mini-BALs probably involves a combination of orientation and time-dependent effects.

A major challenge is to understand how NALs, BALs, and mini-BALs fit together into an single paradigm of quasar outflows. Whether these outflows, which are observed as different types of absorption lines, are a different manifestation of the same physical process or a completely different phenomenon remains unknown. As unification theories dictate, the geometry and flow structure of these outflows might be directly related to their observed frequency. In fact, in its most basic interpretation, the observed frequency of outflows can be equated with the fraction of solid angle (from the viewpoint of the central black hole) subtended by outflowing gas. This interpretation assumes that all AGNs feature outflows and that not all sight lines to the emitting regions are occulted by the outflow. Indeed, the outflows might be ubiquitous in AGN if, as expected, the absorbing gas subtends only part of the sky as seen from the central continuum source.

Although several geometrical models have been proposed (e.g., Elvis, 2000; Ganguly et al., 2001), the diversity of quasar outflows and the lack of a complete account of the frequency of every different outflow class have made this task quite difficult and have resulted in disparities between these models. For example, in the Elvis (2000) model, NALs are the observation of the same streams that produce the BALs but viewed at inclination angles closer to the accretion disk plane, thus intersecting a narrower portion of the outflowing stream. In the Ganguly et al. (2001) picture, NALs are clumps of gas viewed at smaller inclination angles than BAL quasars (nearer the disk's polar axis).

Fig. 2.4 shows how these features might coexist in a single outflow geometry (Hamann et al., 2012). There surely are strong orientation effects in quasar outflows, probably resembling Fig. 2.4 (see also Proga et al., 2012), and it seems natural to attribute the small structures that produce NALs and mini-BALs to the ragged edges of a massive BAL outflow. In this picture, different sightlines through this flow (dashed lines) produce BALs, mini-BALs, or outflow NALs in quasar spectra. The trend is for narrower/weaker absorption lines, smaller outflow column densities, and weaker X-ray absorption at higher latitudes above the disk plane. The percent ranges in parentheses are detection frequencies of BALs, mini-BALs, and outflow NALs in quasar spectra (circled values are favored, see sections § 2.2.3 and § 2.2.4), which might correspond to opening angles for the different outflow types. A better characterization of every outflow type is needed in order to develop a coherent picture.

Alternatively (and equally simplistic), the observed frequency can be interpreted

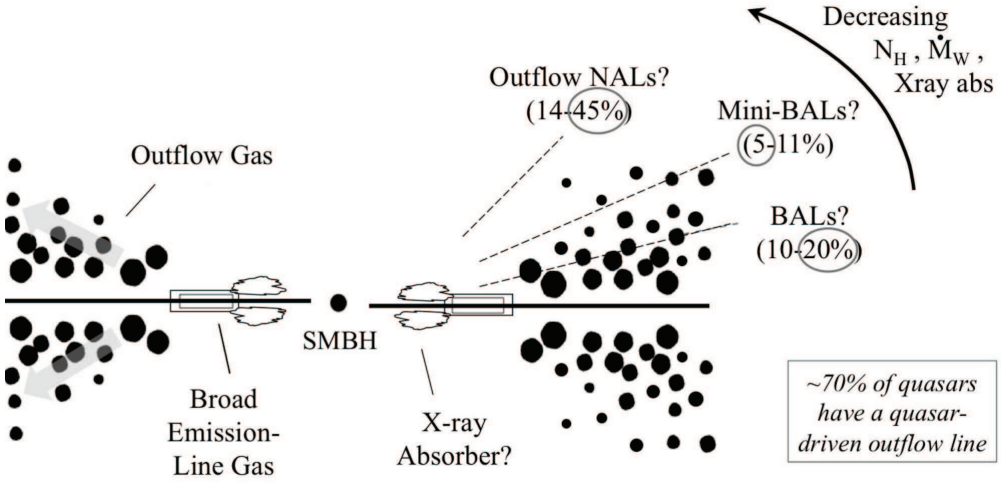

Figure 2.4: A plausible geometry for quasar accretion disk winds. The disk is shown edge-on as a bold horizontal line around the central SMBH. The highly ionized X-ray absorber (white clouds above and below the disk) resides somewhere near the base of the outflow (black circles farther out). Different sightlines through this flow (dashed lines) produce BALs, mini-BALs, or outflow NALs in quasar spectra. Figure from Hamann et al. (2012).

as the fraction of the duty cycle over which AGNs feature outflows (assuming the outflow subtends 4 π sr). The actual conversion of the fraction of AGNs featuring spectroscopic evidence of outflow to the solid angle subtended by such outflows has been treated by Crenshaw et al. (1999, 2003). This computation involves further knowledge of the line-of-sight covering factor (that is, the fraction of lines of sight that reach the observer that are occulted by the outflow) as well as an understanding of the range of solid angles sampled by the AGNs used (e.g., type 1 vs. type 2 AGNs).

A key piece of information to understand if outflow feedback can affect the host galaxy evolution, is the fraction of quasar driving outflows, as well as their energetics. The latter quantity can be inferred from the velocity, column density, and global covering factor of the outflowing gas. Therefore, to build a more complete picture of quasar outflows, and explore what impact do they have on their surrounding host galaxy, we need better observational constraints on the physical properties of each outflow type. So in this context, large spectroscopic surveys provide a statistical means of measuring the frequency with which outflows are observed, but we must carefully select systems that truly sample outflowing gas. In the next two sections I will briefly review results from previous studies on the observed frequency of each class of absorbers.

2.2.3 Broad Absorption Lines and mini-BALs

As mentioned in the previous section, BALs show typical widths of several thousands of km s^{-1}. They clearly identify powerful outflows with typical velocities of order 20,000 to 30,000 km s^{-1}, although velocities reaching 60,000 km s^{-1} have also been measured (Jannuzi et al., 1996; Hamann et al., 1997c). They are thought to be intrinsic, since only the SMBH can feasibly generate the high-velocity outflows of gas responsible for the absorption (e.g., Crenshaw et al., 2003).

BALs are detected almost exclusively in the most luminous radio-quiet quasars (RQQs) at a frequency of 12 - 23 percent (Hamann et al., 1993; Hewett and Foltz, 2003; Reichard et al., 2003; Ganguly et al., 2007; Rodríguez Hidalgo et al., 2011). Several studies (e.g., Brotherton et al., 1998) have dismantled the myth that BALs are only observed in formally radio-quiet (i.e. $f_\nu(5GHz)/f_\nu$ (3000 Å) < 10) objects, although their frequency does significantly decrease among the most radio-loud quasars (Becker et al., 2001; Gregg et al., 2006).

Previous surveys of BALs (e.g., Reichard et al., 2003; Trump et al., 2006) have focused on classifying them based on integrated measurements of the total broad absorption present in their spectra: i.e. Balnicity Index (BI - Weymann et al., 1991) and Absorption Index (AI -Hall et al., 2002; Trump et al., 2006). The Balnicity Index is defined as:

$$BI = \int_{3000}^{25000} [1 - f(v)/0.9] C dv, \tag{2.35}$$

where $f(v)$ is the normalized flux as a function of velocity displacement from the emission redshift z_{em}, and C is a parameter initially set to 0 and reset to 1 whenever the quantity in brackets has been continuously positive over an interval of 2000 km s^{-1}, a value arbitrarily chosen to avoid narrow absorption. The lower limit of the integral (v = 3000 km s^{-1}) was set to avoid counting associated absorption. BAL quasars are defined to have $BI > 0$. While the use of BI to define samples of BAL quasars has utility, especially in comparing results between data sets of varying quality, it excludes some fraction of real high-velocity dispersion outflows that qualitatively appear to be BAL quasars but just fail to have positive BI. An improvement on the BI, termed the AI index , was developed by Hall et al. (2002) to alleviate the inadequacies of BI in selecting objects where high-velocity outflows were clearly observed but were not included as BAL quasars by the BI criteria.

Hall et al. (2002) defined AI to be a less restrictive measurement of any kind of intrinsic absorption, not only BALs, and attempted to exclude intervening absorption lines. Hall et al. (2002) proposed a definition, that was reviewed in

Trump et al. (2006):

$$AI = \int_0^{29000} [1 - f(v)]C' dv, \tag{2.36}$$

with the same definition for $f(v)$ but with a C' that, also initially set to 0, becomes 1 in continuous troughs that exceed the minimum depth (10%) and the minimum width (1000 km s^{-1}). The AI was designed to be more flexible and inclusive and has been very useful in its application to newer and better quality data sets like the Sloan Digital Sky Survey (SDSS). This flexibility, while good at including objects not previously selected by BI, has increased the contamination of samples of intrinsic absorption while still not including other forms of intrinsic absorption (e.g., Ganguly et al., 2007).

The incidence of BALs has primarily been determined using optical spectra where, historically, large samples of high-redshift quasars (to get rest-frame UV coverage) could efficiently be selected (e.g., with color selection). In such surveys (Hewett and Foltz, 2003; Reichard et al., 2003; Trump et al., 2006; Ganguly et al., 2007), roughly $10\% - 25\%$ of objects are observed to host BALs. An issue with optical/UV surveys, however, is potential biases in the selection of quasars against those hosting BALs due to the fact that much of the continuum is absorbed (e.g., Goodrich and Miller, 1995; Goodrich, 1997; Krolik and Voit, 1998) and intrinsically reddened (e.g., Reichard et al., 2003). Using the Large Bright Quasar Survey (Foltz et al., 1987, 1989; Hewett et al., 1991, 1995), where the observed frequency of BAL quasars in the redshift range $1.5 \leq z \leq 3$ is 15% using a BIcriterion, Hewett and Foltz (2003) estimated a true BAL frequency of 22% from comparisons in the k-corrections of BAL and non-BAL quasars. The catalog of BAL quasars using an AI criterion from Trump et al. (2006) found a BAL frequency of 26% (in the redshift range $1.7 \leq z \leq 4.38$).

To avoid possible selection biases in the optical, one can examine quasar catalogs selected in other bands. Becker et al. (2000) examined radio-selected quasars from the FIRST Bright Quasar Survey and found a BAL quasar frequency of about 18% (although it is only 14% if only $BI > 0$ objects are counted, comparable to other estimates based on optical selection), for objects at $z > 1.7$.

In addition to radio selection, one can examine the frequency of BAL quasars from infrared selection. Dai et al. (2008) compared the catalog of BAL quasars (Trump et al., 2006) from the Third Data Release (DR3) of SDSS and the parent sample of DR3 quasars (Schneider et al., 2005) with the Two Micron All-Sky Survey (2MASS; Skrutskie et al., 2006) Point-Source Catalog (PSC). With some variation with redshift, they reported an overall true BAL quasar fraction of $43\% \pm 2\%$, considerably higher than estimates based on UV/optical data alone.

Presumably, this difference accounts for the effects of dust and absorption that may bias UV/optical selection techniques against find BAL quasars. This estimate relies heavily on the automated techniques employed in finding BAL quasars in a large data set such as SDSS. From a critical look at 5088 $1.7 < z < 2$ quasars from SDSS DR2, Ganguly et al. (2007) noted several instances of false (and missed) classifications in the Trump et al. (2006) catalog. A comparison of the Ganguly et al. (2007) sample with the 2MASS PSC reveals a BAL fraction of 66/287 (23%), completely consistent with the analysis of Hewett and Foltz (2003). Blindly using the Trump et al. (2006) catalog yields a BAL fraction of 96/287 (33%), consistent with the $z < 2$ points from Dai et al. (2008) (see their Figure 4). At face value, this implies that nearly 30% of the Trump et al. (2006)-2MASS cross matched sample consists of false positives.

Absorption lines with intermediate widths, called mini-BALs, have been found at a variety of velocities but only in a handful of quasars (i.e. Turnshek, 1988; Jannuzi et al., 1996; Hamann et al., 1997b; Churchill et al., 1999; Narayanan et al., 2004; Misawa et al., 2007). Most mini-BALs are believed to be outflows because they show some of the typical outflow signatures, such as variability (Narayanan et al., 2004; Misawa et al., 2007) and smoot profiles at high resolution, which suggests that they are not blends of many NALs (Barlow and Sargent, 1997; Hamann et al., 1997a).

2.2.4 Narrow Absorption Lines

NALs, unlike their very broad kin, are generally not blended and, therefore, offer a means to determine ionization levels and metallicities using absorption-line diagnostics. In addition, they are found with greater ubiquity, and detected (with varying frequency) in all AGN subclasses from Seyfert galaxies (e.g., Crenshaw et al., 1999) to higher luminosity quasars (e.g., Ganguly et al., 2001; Vestergaard, 2003; Misawa et al., 2007) and from steep to flat radio spectrum sources (Ganguly et al., 2001; Vestergaard, 2003), although the strongest ones appear preferentially in RLQ spectra (Foltz et al., 1986; Anderson et al., 1987). Thus, NALs are more useful as probes of the physical conditions of outflows and provide an important tool to investigate the quasar environment. They may give us access to a different fraction, a different phase or different directions through the outflow with respect to BALs (e.g., Hamann and Sabra, 2004).

The limitation of NALs is that they arise from a wide range of environments, from high speed outflows, to halo gas, to the unrelated gas or galaxies at large distances from the AGN. Because some of the gas intrinsic to the quasar may have similar

ionization parameter to that of the intervening gas, the absorption signatures may be similar, complicating or even hindering a secure identification of its origin. While the gas intrinsic to the quasar is subjected to a stronger radiation field, it is often also denser (resulting in a similar ionization parameter) and can be moving at high velocities owing to the strong radiation field. This can place the intrinsic absorption line at a wavelength indistinguishable from the intervening absorption lines. While intervening absorbers typically have equivalent widths below 1 Å, for the reasons outlined, some absorbers associated with the quasar may be of similar strength. This difficulty of separating intrinsic and intervening absorbers is the reason that many studies typically ignored absorbers below 1 Å.

The outflow/intrinsic origin of individual NALs can be inferred from: i) time-variable line-strengths, ii) resolved absorption profiles that are significantly broader and smoother compared with the thermal line widths, iii) excited-state absorption lines that require high gas densities or intense radiation fields, iv) line strength ratios in multiplets that reveal partial coverage of the background light source, v) higher ionization states than intervening absorbers. Nonetheless, NALs can still be connected to the quasar host without exhibiting such properties (Hamann et al., 1997c).

Previous studies have shown that NALs tend to cluster near the emission redshift, at $z_{abs} \approx z_{em}$. A significant excess of absorbers over what is expected from randomly distributed intervening structures was measured by Weymann et al. (1979), with a distribution of intrinsic CIV NALs extending up to $v \sim 18,000\ \mathrm{km\,s^{-1}}$. Foltz et al. (1986) confirmed such a statistical excess within $\sim 5000\ \mathrm{km\,s^{-1}}$ of z_{em}. However, other studies failed to confirm any peak in the distribution of CIV absorption systems close to the emission redshift (Young et al., 1982; Sargent et al., 1988). After the work by Foltz et al. (1986), it has been traditionally assumed that NALs at less than $5000\ \mathrm{km\,s^{-1}}$ from the systemic redshift of the quasar are likely intrinsic and directly influenced by quasar radiation. These systems have been commonly defined as *associated* absorption lines (AALs) and those with velocity displacements greater than $5000\ \mathrm{km\,s^{-1}}$, as *intervening* systems. Despite the commonly adopted threshold of $5000\ \mathrm{km\,s^{-1}}$ to distinguish intervening and associated absorbers, there is some evidence of a statistically significant excess of NALs extending to somewhat larger velocities (Misawa et al., 2007; Nestor et al., 2008; Tripp et al., 2008; Ganguly et al., 2013).

Ganguly and Brotherton (2008) provide a review of the recent literature regarding the frequency of outflows, finding that, almost independently of luminosity, about 60 percent of AGNs show outflows in absorption (considering both BALs and NALs; see also Hamann et al. (2012). However, this estimate is based on several simplifying

assumptions and is affected by large uncertainties due to the inhomogeneity of the samples under consideration. In the case of NALs, the estimate of the frequency of outflows (based on the identification of intrinsic systems) has been carried out mainly in two ways: (1) with small samples of high redshift spectra, identifying intrinsic systems using mainly the partial coverage effect (Ganguly et al., 2001; Misawa et al., 2007; Ganguly et al., 2013). In particular, Ganguly et al. (2013) found a possible evidence of redshift evolution of the fraction of outflows with $9-19$ percent at $0<\mathrm{z}<0.7$, $14-29$ percent at $0.8<\mathrm{z}<2$ and $43-54$ percent at $2<\mathrm{z}<4$ (Misawa et al., 2007). In a survey of $1.8<z<3.5$ SDSS sources, Rodriguez Hidalgo et al. (2007) find about 12% of quasars have high-velocity NALs in the velocity range $5000-50,000$ km s^{-1} and $\sim 2.3\%$ in the velocity range $25,000-50,000$ km s^{-1}. This latter velocity range is often missed by surveys due purely to observational cutoffs. (2) with very large samples at low resolution (based on SDSS) where the incidence of intrinsic systems is determined statistically by modeling the velocity offset distribution of absorbers (Nestor et al., 2008; Wild et al., 2008; Bowler et al., 2014). In particular, Nestor et al. (2008) found a fraction of outflows of ~ 14 percent (for $0<\mathrm{v}<12,000\,\mathrm{km\,s^{-1}}$) which should be considered as a lower limit due to the uncertainties related with the low resolution and S/N of the spectroscopic sample.

Chapter 3

3 Nature and statistical properties of quasar NALs

In this chapter, I present my work on the statistical analysis of the properties of a sample of narrow metal absorptions. The observations have been carried out with VLT/X-shooter in the context of the XQ-100 Legacy Survey. The combination of high S/N, large wavelength coverage and intermediate resolution makes XQ-100 a unique dataset to study NALs of high-z quasars in a single, homogeneous and statistically significant sample Lopez et al. (2016) provides details on the survey design.

The chapter is organized as follows: §3.1 describes the properties of the quasar sample and briefly summarizes the observations; §3.2 describes my methodology for identifying NALs. The results of this work are presented in §3.3 and their implications to determine additional criteria that can be used to disentangle between intrinsic and intervening NALs are discussed in §3.4.

3.1 XQ-100 Legacy Survey

The quasars in my sample have been originally selected and observed in a new Legacy Survey, hereafter "XQ-100", of 100 quasars at emission redshift $z_{em} = 3.5-4.5$ (ESO Large Programme 189.A-0424). The observations have been carried out with X-shooter/VLT (Vernet et al., 2011). The released spectra provide a complete coverage from the atmospheric cutoff to the NIR with a spectral resolution $\mathfrak{R} \approx 6000-9000$ depending on wavelength, and a median signal-to-noise ratio S/N $\sim$ 30 at the continuum level. XQ-100 provides the first large intermediate-resolution sample of high-redshift quasars with simultaneous rest-frame UV/optical coverage. A full description of the target selection, observations, and data reduction process is presented by Lopez et al. (2016). The distribution of quasar emission redshifts is shown in Fig. 3.1 compared with those of other relevant works.

XQ-100 was designed to address a wide range of high-redshift science (for an extensive list, see Lopez et al., 2016). The targets were not selected on account

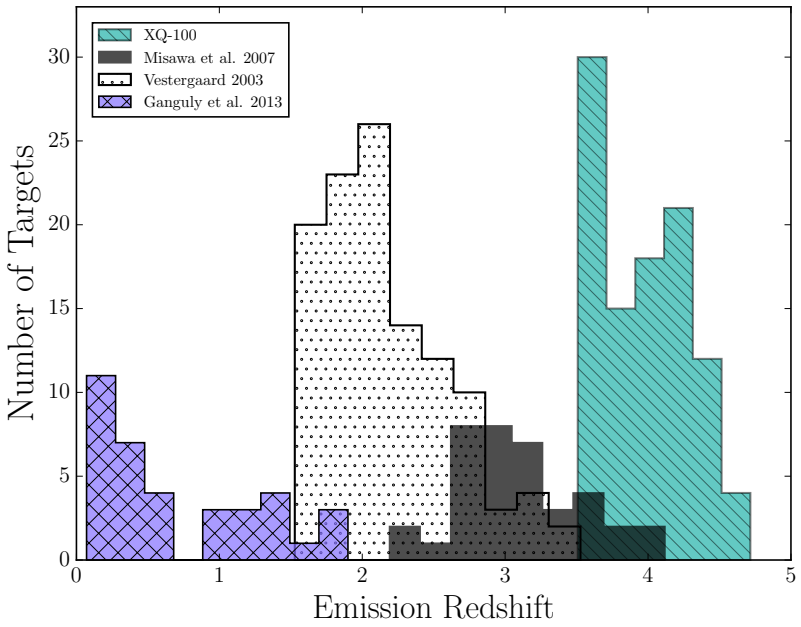

Figure 3.1: Redshift distribution of my quasar sample (diagonal filled histogram), compared with previous works: Vestergaard (2003; open dotted histogram); Misawa et al. (2007; dark shaded histogram); Ganguly et al. (2013; diamond filled histogram). XQ-100 enlarge the studied redshift range to higher values.

of the presence of absorption lines in their spectra, although BAL quasars were avoided, so the sample is relatively unbiased with respect to the properties of NALs. Therefore, XQ-100 represents a unique dataset to study the rest-frame UV and optical of high-z quasars in a single, homogeneous and statistically significant sample.

The bolometric luminosities L_{bol} of all the quasars in my sample are estimated based on the observed flux at $\lambda = 1450$ Å and using a bolometric correction factor $L = 4.2\ \lambda\ L_{\lambda}$ (Runnoe et al., 2012).

An important point for my study is to obtain accurate systemic redshift for the quasars in order to determine the relative velocity/location of the absorbers. This is crucial especially for the associated systems. The quasar emission redshifts of my sample have been obtained from a Principal Components Analysis (PCA; see e.g., Suzuki et al., 2005). For a complete description of the procedure, see Lopez et al. (2016).

3.1.1 Radio properties

Previous studies have shown that there is a possible dependence of the presence of associated systems on the radio properties of the inspected quasars (Baker

et al., 2002; Vestergaard, 2003). For this reason, I have also investigated the radio properties of the XQ-100 sample.

Matching my sample with the FIRST catalogue (Becker et al., 1995), I have found radio information for 67 over 100 quasars. According to my determination of the radio-loudness parameter, 12 objects are radio-loud and 55 are radio-quiet. Most likely the objects which are not in the FIRST catalogue are also radio-quiet. As a consequence, I will consider the XQ-100 sample as a substantially radio-quiet sample.

The radio-loudness of a quasar is typically parametrized by the ratio between the rest-frame flux densities at 5 GHz and 2500 Å, i.e., $R = f_\nu(5\ GHz)/f_\nu(2500)$ Å (Sramek and Weedman, 1980). I compute the radio flux density at rest-frame 5 GHz, $f_\nu^{rest}(5\ \mathrm{GHz})$, from the observed flux density, $f_\nu^{obs}(\nu)$, at observed frequency ν:

$$\begin{aligned} log\ f_\nu^{rest}(5\ \mathrm{GHz}) = log\ f_\nu^{obs}(\nu) + \alpha_r log(5\mathrm{GHz}/\nu) \\ - (1+\alpha_r)\ log\ (1+z_{em}), \end{aligned} \tag{3.1}$$

where α_r is the spectral index, $f_\nu \sim \nu^\alpha$. I assume $\alpha_r = -0.5$ (e.g., Ivezic et al. 2004). The flux density $f_\nu^{rest}(2500)$ Å, is derived from a power-law fit to my own data.

Following Ganguly et al. (2013), I adopt $R \geq 23$ as the criterion for radio loudness.

The most important properties of the quasars in my sample are summarized in the Table A.1 in the Appendix. Columns (1) and (2) of the Table A.1 give the quasar name and emission redshift, column (3) the bolometric luminosity and column (4) quasar radio type.

3.2 Sample of NAL Systems

3.2.1 Identification and measurement of CIV absorbers

With the aim of mapping the incidence of NALs in quasar rest-frame velocity space, I produce a catalog of the ultraviolet doublet CIV $\lambda\lambda$ 1548.204, 1550.78[1] Å. Since I do not impose an a priori velocity definition of associated system, I look for any CIV absorber outside the Ly-α forest in each spectrum.

[1] Wavelengths and oscillator strengths used in this work are adopted from Morton (2003).

Although continuum estimates are available for the XQ-100 public data release, I elect to perform my own continuum fits, due to the sensitive nature of accurate continuum placement close to the quasar emission lines. For each target the continuum level is determined by fitting with a cubic spline the portions of the spectrum free from evident absorption features in the region red-ward of the Ly-α emission of the quasar. I then normalize the flux and flux error arrays by the modelled continuum level. I visually inspect all the quasar spectra looking for CIV doublets using the LYMAN context of the MIDAS reduction package (Fontana and Ballester, 1995). I select all the candidate λ1548 and λ1550 transitions with matching kinematic profiles. I make use of the TELLURIC task of the Image Reduction and Analysis Facility package (IRAF; Tody, 1986) to apply appropriate corrections to each spectrum in the spectral regions affected by the telluric bands. This latter step allows me to remove telluric features and to have a more firm identification of the lines. Initially, absorption troughs that are separated by unabsorbed regions are considered to be separate lines. In this manner, 1098 CIV doublets are identified.

The rest-frame equivalent width (W_0) and its measurement error are measured for each line by integrating across the flux density and flux error array, respectively, over a user-defined interval. The interval extremes are defined by the wavelengths where the flux matches again the level of the continuum to within the values of the flux error array. For the statistical analysis I include in my sample of NALs only doublet lines whose weaker member is detected at a confidence level greater than $3\,\sigma$ i.e., each W_{1550} is larger than the detection limit, given by:

$$W_{lim} = n_\sigma \frac{FWHM}{(1+z_{abs})\ S/N} \tag{3.2}$$

where, n_σ is equal to 3, $FWHM$ is computed as the ratio of the observed wavelength λ and the spectral resolution $\mathfrak{R}$[2], z_{abs} is the absorption redshift of the line and S/N is the signal to noise ratio per pixel at the relevant wavelength.

The NAL sample defined by this limit contains 1075 CIV doublets. Furthermore, as CIV absorption is relatively common in quasar spectra, blending of systems at similar redshifts could be a problem. Therefore, when either the λ1548 or the λ1550 CIV component is blended with other transitions I include the doublet in the complete sample only if the doublet ratio, defined as the ratio of equivalent widths of the stronger to the weaker component, is in the range $0.8 - 2.2$. The theoretical ratio for this doublet is 2, so the above mentioned interval is adopted to account for blending effects and is determined from CIV narrow absorption doublets clearly

[2]The mean spectral resolution in the optical wavelength range is 8800.

not affected by blending. Adopting this criterion the sample is reduced to 1060 doublets.

To refine my sample for statistical analysis, I combine NALs that lie within 300 km s^{-1} of each other into a single *system*. This makes the sample homogeneous. This clustering velocity is chosen considering the largest velocity extent of an absorber in my sample for which it is not possible to discern the individual components. Therefore, I take 300 km s^{-1} as the minimum velocity separation for which two absorbers are counted separately. To identify CIV systems, I proceed in the following way: for each list of CIV components corresponding to a single quasar the velocity separations among all the lines are computed and sorted in ascending order. If the smallest separation is less than dv_{min} = 300 km s^{-1} the two lines are merged into a new line with equivalent width equal to the sum of the equivalent widths, and redshift equal to the average of the redshifts weighted with the equivalent widths of the components. The velocity separations are then computed again and the procedure is iterated until the smallest separation becomes larger than dv_{min}.

The absorber velocity with respect to the quasar systemic redshifts is conventionally defined as $v_{abs} = \beta\, c$, I compute it by the relativistic Doppler formula (e.g., see Vestergaard (2003)),

$$\beta \equiv \frac{v_{abs}}{c} = \frac{(1+z_{em})^2 - (1+z_{abs})^2}{(1+z_{em})^2 + (1+z_{abs})^2} \tag{3.3}$$

where z_{em} and z_{abs} are the emission redshift of the quasar and the absorption redshift of the line, respectively and c is the speed of light. Our final sample consists of 986 CIV doublets with $-1000 < v_{abs} < 73,000$ km s^{-1} and equivalent widths 0.015 Å $< W_0 <$2.00 Å.

I finally measure the column densities (N) of the lines with the AOD method (Savage and Sembach, 1991a; Sembach and Savage, 1992; see section § 2.1.3). I take advantage of this method to correct the column density of the CIV doublets when the stronger member is saturated. I define as saturated lines those which have flux density levels at the wavelength of peak absorption of less than 0.2 in the normalized spectra (Krogager et al., 2016).

3.2.2 Identification of other species

The detection of a single species in a single ionization state substantially limits the information on the nature and the physical properties of the studied absorbers.

Table 3.1: Number and fraction of CIV systems with detected NV, SiIV and CII.

	$-0.1 < v^a_{abs} < 0.25$	$0.25 < v^a_{abs} < 0.55$	$v^a_{abs} < 0.5$
CIV	72	68	122
NV	34; 47%	12; 18%	43; 35%
SiIV	26; 36%	27; 40%	46; 53%
CII	7; 10%	10; 15%	16; 13%

[a] v_{abs} is measured in unity of 10^4 km s^{-1}.
Note: the bin in the second column is extended to 5500 km s^{-1} to include all the NV absorptions detected. The third column shows the number and fraction of associated CIV systems with other detected ions.

The quality and wavelength extent of my spectra give me the possibility to search for other common ions (NV, SiIV and CII) related to each detected CIV absorber. Furthermore, for the ions mentioned above, I search for absorption lines not related to the identified CIV, but I do not find any.

I identify NV, SiIV doublets and CII in the following regions:

1. NV $\lambda\lambda$1238.821, 1242.804 Å absorption doublets: from -1000 to 5500 km s^{-1} with respect to the quasar's NV emission line. The velocity range is relatively narrow for this transition because contamination by the Ly-α forest prevents me from searching for NV NALs at larger velocity offsets;
2. SiIV $\lambda\lambda$1393.760, 1402.772 Å absorption doublets: from -1000 to 45,000 km s^{-1} with respect to the quasar's SiIV emission line;
3. CII λ1334.532 Å absorption: from -1000 to 10,000 km s^{-1} with respect to the quasar's CII emission line.

The same procedures of analysis described above for CIV are applied to NV, SiIV and CII as well. In particular, I require the detection level for the weaker member of the doublets to be 3σ, and 5σ for single absorption lines. The final sample includes 574 SiIV (234 detections, 340 upper limits), 140 NV (46 detections, 94 upper limits) and 142 CII (28 detections, 114 upper limits). See Table 3.1 for more details on the associated region. The non-detections are reported as upper limits. They are calculated by integrating across the expected location of each species in the spectrum, over a velocity interval similar to that of the corresponding CIV absorber. This procedure is actuated when spurious absorption lines are not present in the considered portion of the spectra.

For the remainder of the paper, W_0 represents the rest frame equivalent width of the stronger member of a given doublet. Columns (7) and (8) of Table A.1 in the

Appendix report the apparent column density of the absorbers and the equivalent width of the lines combined into single *systems* within 300 km s^{-1}, respectively. Examples of the identified absorbers are reported in the appendix.

3.2.3 Completeness Limits

In order to estimate the completeness of my sample, I test the detection sensitivity of the whole dataset. I compute the cumulative distributions of the number of quasars with W_{lim} larger than a given value of W_{1548} and within a given velocity separation from the quasar emission redshift. W_{lim} is measured from Eq. 3.2, for various absorber velocities (parametrized by β) in the spectra of all quasars. The results are shown in Fig. 3.2.

The black solid line and the dot-dashed one represent the distributions for $\beta = 0.0$ and $\beta = 0.1$, respectively. The lines corresponding to the cumulative distributions

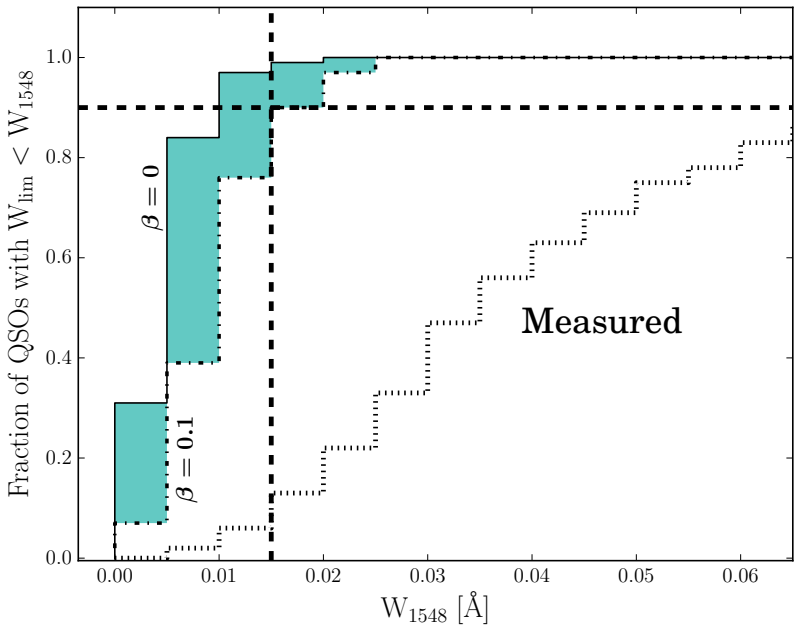

Figure 3.2: Cumulative distribution of the number of quasars with 3σ rest-frame W_{lim} detection limit smaller than a given W_{1548} value and for several β-values. The black solid line represents the distribution for $\beta = 0.0$, the dot-dashed one represents the $\beta = 0.1$ distribution. The cumulative distributions for $\beta > 0.1$ overlap with the $\beta = 0.1$ distribution and are not marked. The cumulative distribution of the number of quasars showing at least one detected absorber with W_{1548} larger than a given threshold is reported for comparison (dotted line, labeled "Measured"). The 90 percent completeness level is marked by the dashed horizontal line. The 3σ detection limit measured to a completeness level of ~ 90 percent is $W_{1548} = 0.015$ Å (dashed vertical line).

Table 3.2: Results of the completeness test for various absorber velocities, parametrized by β.

	Cumulative fraction of quasars with W_{lim} [Å] up to						
	0.005	0.01	0.015	0.02	0.025	0.03	0.035
$\beta = 0.00$	0.31	0.84	0.97	0.99	1.00	1.00	1.00
$\beta = 0.01$	0.21	0.69	0.90	0.97	1.00	1.00	1.00
$\beta = 0.02$	0.12	0.57	0.86	0.93	0.98	1.00	1.00
$\beta = 0.03$	0.08	0.49	0.79	0.91	0.96	0.99	1.00
$\beta = 0.04$	0.07	0.42	0.77	0.89	0.97	0.99	0.99
$\beta = 0.10$	0.07	0.39	0.76	0.90	0.97	1.00	1.00

relative to values of β between $\beta = 0$ and $\beta = 0.1$ span the shaded area in the plot. For increasing β-values, the cumulative distributions overlap the one with $\beta = 0.1$.

The cumulative distributions show that in my sample the CIV detection sensitivity drops below 90 percent at $W_{1548} \approx 0.015$ Å for $\beta \geq 0.1$ (vertical and horizontal dashed lines in Fig. 3.2). This is explained by the identical spectral coverage and the uniformity in S/N of the spectra in my sample. More explicitly, at $\beta = 0.02$ (0.10), corresponding to 6000 km s^{-1} (30000 km s^{-1}), the completeness level of $W_{lim} \geq 0.015$ Å absorbers is ≥ 93 percent (≥ 90 percent). Part of the cumulative distribution of the number of quasars with at least one identified CIV line stronger than a given threshold is also shown in Fig. 3.2 for comparison (dotted line). It is noticeable from the plot that more than 87 percent of the quasars in my sample have at least one CIV detection with W_{1548} above the 0.015 Å completeness limit. The results of the completeness test are collected in Table 3.2.

3.3 Statistics of NAL Systems

Using the complete CIV sample described in the previous section, I first investigate the equivalent width distribution and the number density of absorbers per unit of velocity interval as a function of the velocity separation from the quasar, i.e., the velocity offset distribution, $dn/d\beta = c\,dn/dv$, where β is computed in Eq. 3.3. Then, I examine the relative number of NALs in different transitions and their velocity offset distributions. The goal is to investigate the ionization structure of the absorbers and their locations relative to the continuum source. I also estimate the number of intrinsic NALs per quasar, and the fraction of quasars hosting

intrinsic NALs. These values can be used to study the geometry of absorbing gas around the quasar.

To further characterize the metal absorptions associated to galaxies hosting $z \sim 4$ quasars, I examine the distributions of the covering fractions. Finally, I briefly look for dependencies of the NAL properties relative to those of their quasar hosts. I choose to show the plots of this section in equivalent width and not in column density to better compare my results with previous works present in the literature. The statistical significance of the results remains the same using column density.

3.3.1 Equivalent Width Distribution

The distribution of rest-frame equivalent widths of the CIV absorbers is shown in Figure 3.3 (light shaded histogram). It rises steeply towards the detection limit of 0.015 Å, marked in the diagram by the dashed line.

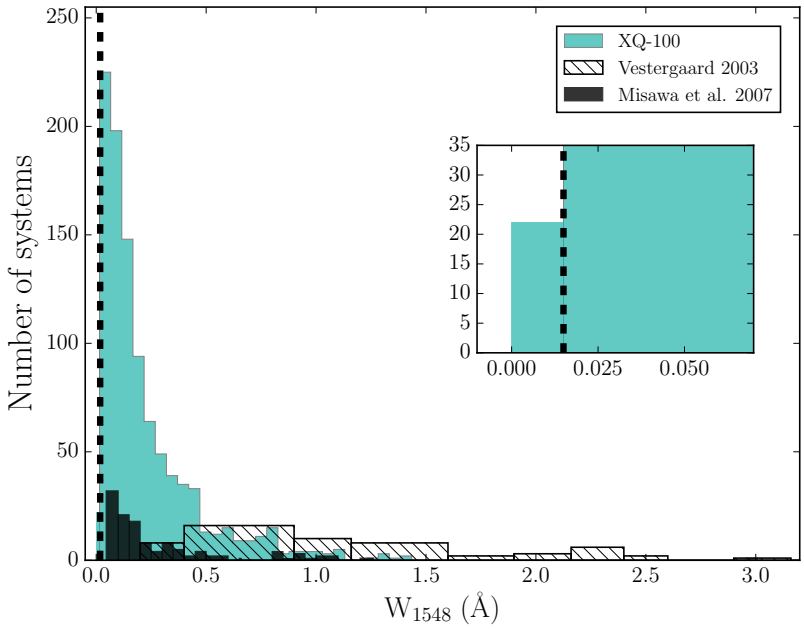

Figure 3.3: The rest-frame equivalent width distribution of all CIV systems in my sample (light shaded histogram). The vertical dashed line marks my detection limit of 0.015 Å. Distributions measured by previous works are also shown: Vestergaard (2003; diagonal filled histogram) and Misawa et al. (2007; dark shaded histogram). The insert shows the details of the bottom left region of the histogram.

It is evident from the insert of Figure 3.3 that very few of the identified lines are excluded from the analysis because they are weaker than the detection level required. We can also note that more than half of the absorbers ($\sim$ 63 percent)

have $W_{1548} < 0.2$ Å. Thanks to the intermediate resolution of X-shooter and to the high S/N level of the XQ-100 sample, I am probing much weaker lines than previous works at lower spectral resolution. For example, in the study of Weymann et al. (1979) the rest-frame equivalent width limit was about 0.6 Å, while Young et al. (1982), Foltz et al. (1986) and Vestergaard (2003) reach a limit of about 0.3 Å, larger than 91 percent and 76 percent of the CIV lines in my sample, respectively. Also Misawa et al. (2007), a study based on data at larger resolution than mine, obtain a detection limit of ~ 0.056 Å, larger than 17 percent of NALs detected in my sample, due to the lower S/N of their spectra.

Equivalent width distributions from Vestergaard (2003; diagonal filled histogram) histogram and Misawa et al. (2007; dark shaded histogram) are also shown in Fig. 3.3 for comparison. The XQ-100 survey data can better detect and resolve weak lines with respect to Vestergaard (2003). The comparison with Misawa et al. (2007) illustrates that high resolution data, able to detect and better resolve weak lines, are usually based on less statistically significant samples.

Dependence on radio properties

I investigate possible differences between RLQs and RQQs with respect to the NAL properties and I do not find any. A direct comparison of the incidence of the absorbers with previous works is non-trivial. The aspects that play a crucial role are the spectral resolution and the different properties of the targets. Two different samples can have: i) differences in the radio properties and intrinsic luminosities of the targets, ii) different ranges in W_{1548} of the detected absorbers, iii) different number of targets with a full coverage of the associated region.

With the aim of comparing the equivalent width distribution in my analysis with previous studies, I focus on systems with $W_{1548} > 1.5$ Å following Vestergaard (2003) who claimed the strongest systems are likely intrinsic candidates. The Vestergaard sample has 66 RLQs and 48 RQQs, nearly the same number, unlike mine, in which only 17 percent (12/67) of the targets for which I have information about radio properties, are radio-loud. If I consider separately the radio-loud and radio-quiet objects in the Vestergaard sample, only 5/66 and 1/48 quasars exhibit at least one CIV NAL with $W_{1548} > 1.5$ Å, respectively. Thus, a weighted prediction based on the fraction of RQQ and RLQ in my sample on the number of very strong CIV NALs is that two should be detected. Indeed, I do detect exactly two such absorbers with $W_{1548} > 1.5$ Å. The fraction of radio-loud quasars in my sample (17 percent) is only slightly larger than the general population (~ 10 percent). As a consequence, I do not expect to be biased toward strong NALs in RLQs, unlike

Vestergaard (2003) whose sample was formed by more than 50% RLQs since the aim was to compare the NALs in RLQs and RQQs. The distribution of weaker lines is considered in the next sections.

3.3.2 Velocity Offset Distributions

The velocity offset distributions of the number density of CIV and SiIV NALs in my study are presented in Fig. 3.4, upper and lower panels, respectively. In both diagrams the upper panel shows the distribution of the whole sample while in the bottom one the sample is split in two according to the strength of the NALs' equivalent widths: the color-shaded histogram represents the weak lines ($W_0 < 0.2$ Å) and the black hashed histogram the strong lines ($W_0 > 0.2$ Å). Error bars indicate the propagation of Poissonian uncertainties. The zero velocity corresponds to the emission redshift of the quasar. The observed distributions include contributions from: i) intervening systems; ii) environmental absorption which arises either in the interstellar medium of the AGN host galaxy or in the IGM of the galaxy's group or cluster; and iii) outflow systems that are ejected from the central AGN.

I do find an excess of the number density of NALs within 10,000 km s^{-1} of the emission redshift. The excess is clearly detected in both the velocity offset distributions of CIV and SiIV NALs within the first two bins, starting from $v_{abs} = -1000$ km s^{-1}. Since there is not a sizeable change in sensitivity to finding absorbers as a function of velocity, as shown in § 3.2.3, and my spectra have all the same wavelength coverage, beyond the first two bins I see an approximately constant value expected for intervening systems.

To assess whether the detected excess is statistically significant over random incidence or not, I firstly compute the average occurrence of CIV absorption in bins of 5000 km s^{-1} at large velocity separation ($v_{abs} > 5 \times 10^4$ km s^{-1}) from z_{em}, where I am more confident that systems are intervenings. The average number density of CIV expected for the whole sample is 31 ± 4 per $dv = 5000$ km s^{-1} bin, to be compared with $dn/d\beta = 59$ and 64 that I find at velocity separations of $-1000 < v_{abs} < 5000$ km s^{-1} and $5000 < v_{abs} < 10,000$ km s^{-1}, respectively. This corresponds to a $\sim 8\,\sigma$ excess in the first two bins. This result does not significantly change if a different bin size is considered (e.g. 2000 km s^{-1}). The extension of the first bin to -1000 km s^{-1} is justified and motivated by the need to take into account uncertainties in the systemic redshift and to consider possible inflows. I also compute the average occurrence of CIV absorptions in bins of 5000 km s^{-1} excluding only the first two velocity bins, obtaining 37 ± 5, and the excess

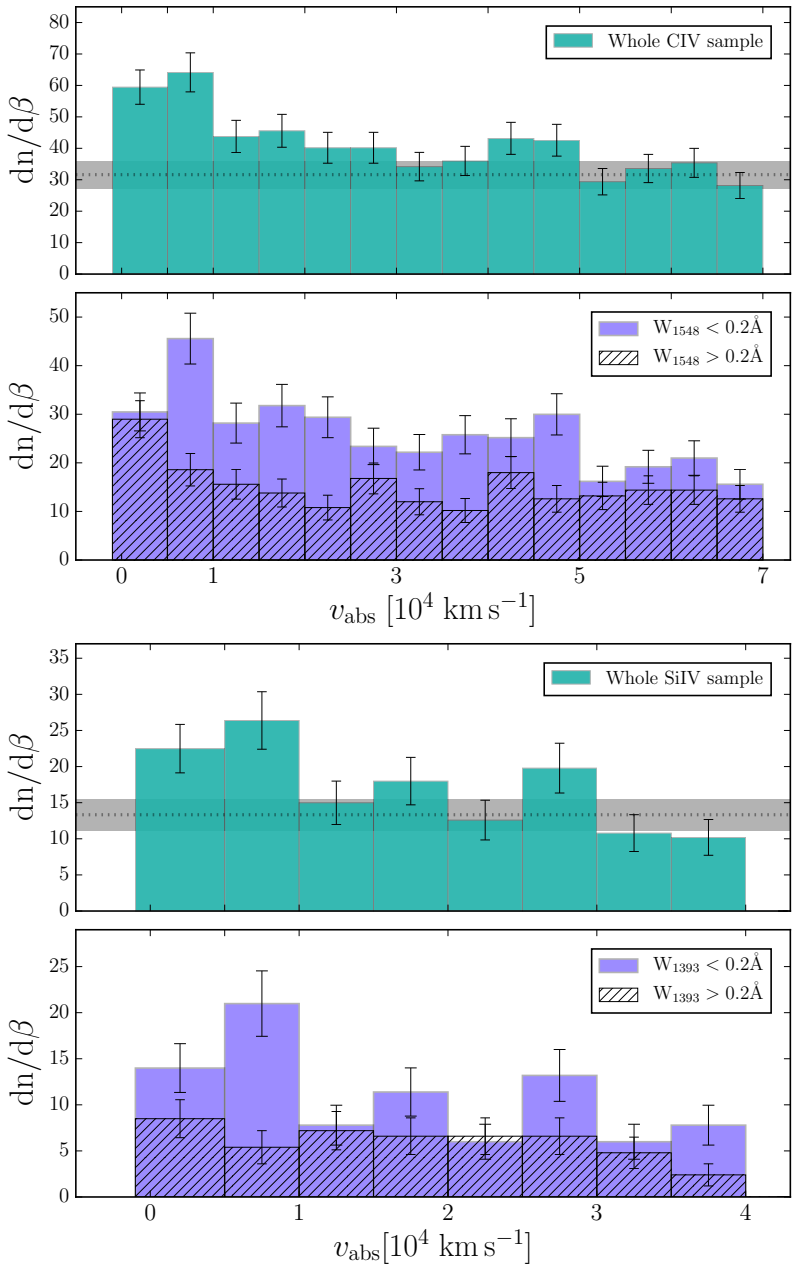

Figure 3.4: Velocity offset distribution of the number density of CIV (upper) and SiIV (lower) absorbers. Top panels: whole sample. Bottom panels: the color-shaded histogram represents the distribution of NALs with $W_0 < 0.2$ Å, the black hashed histogram represents the distribution of NALs with $W_0 > 0.2$ Å. The error bars represent the propagation of the Poissonian uncertainties. The horizontal dotted line represents the average number of systems measured in bins of 5000 km s^{-1} far from the z_{em}, and the shaded area around it is the 1σ error of this mean value. Contamination by the Ly-α forest prevented me from exploring the same velocity range for the two ions.

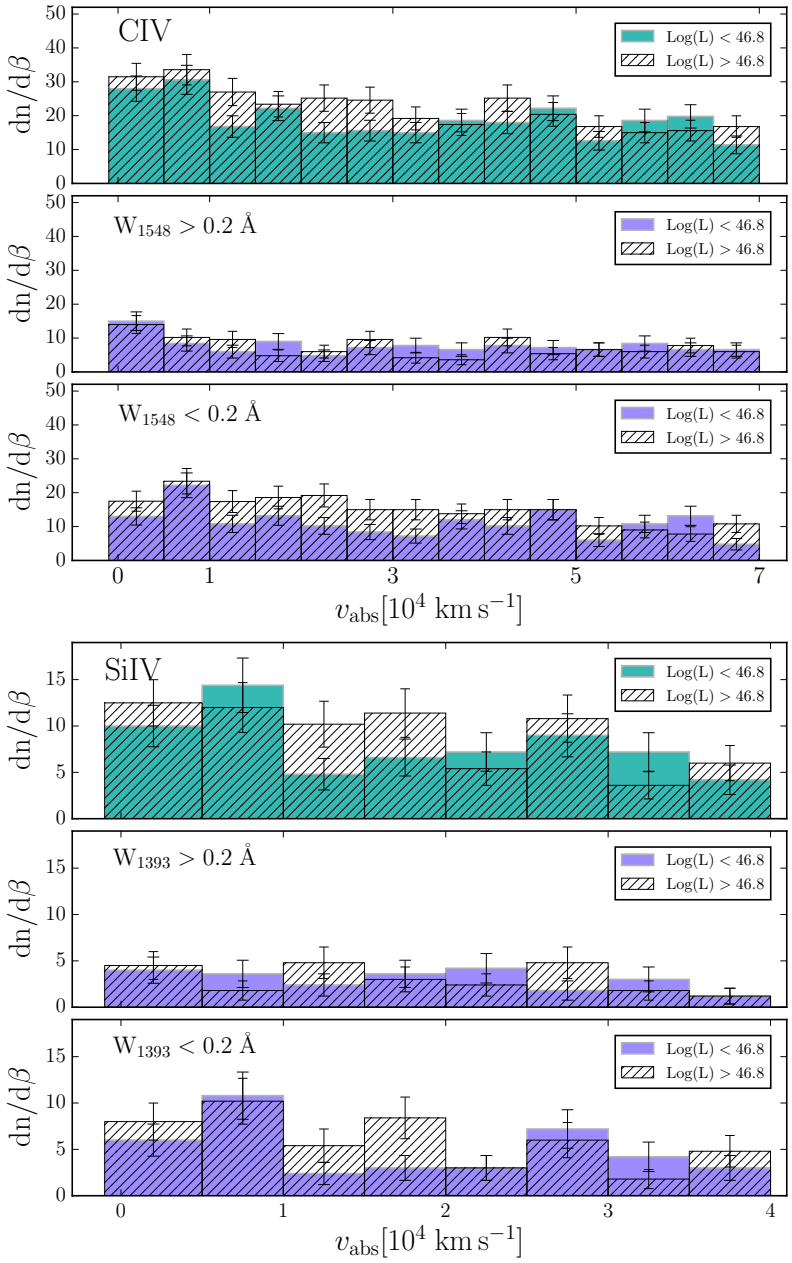

Figure 3.5: Velocity offset distribution of the number density of CIV (upper) and SiIV (lower) absorbers. The color-shaded histogram represents the distribution of NALs with $L_{bol} < 46.8$ erg s^{-1}, the black hashed histogram represents the distribution of NALs with $L_{bol} > 46.8$ erg s^{-1}. Top panels: whole sample. Middle panel: subsample of lines with $W_0 > 0.2$ Å. Bottom panels: subsample of lines with $W_0 < 0.2$ Å. The error bars represent the propagation of the Poissonian uncertainties.

is still significant ($\sim 6\,\sigma$). Most of the excess in the first bin can be explained by the subset of CIV absorptions with detected NV. Indeed, if I exclude those systems, I obtain a number density of 38, that is within $1.32\,\sigma$ of the average value. The equivalent values corresponding to weak ($W_0 < 0.2$ Å) and strong ($W_0 > 0.2$

Table 3.3: Occurrence of NALs in the CIV and SiIV velocity offset distributions.

	Random[a]	Excess[b]	Significance[c]
All CIV sample	32.2 ± 4.4	$59.5; 64.2$	$6.5\sigma; 7.6\sigma$
$W_{1548} > 0.2$ Å	13.2 ± 2.9	$29.0; 18.6$	$5.5\sigma; 1.9\sigma$
$W_{1548} < 0.2$ Å	17.5 ± 3.3	$30.5; 45.6$	$4.0\sigma; 8.6\sigma$
All SiIV sample	13.6 ± 2.8	$22.5; 26.4$	$3.1\sigma; 4.5\sigma$
$W_{1393} > 0.2$ Å	4.6 ± 1.7	$8.5; 5.4$	$2.3\sigma; 0.5\sigma$
$W_{1393} < 0.2$ Å	9.0 ± 2.3	$14.0; 21.0$	$2.1\sigma; 5.2\sigma$

[a] Average number density of NALs in bin of 5000 $\mathrm{km\,s^{-1}}$ away from the z_{em} ($v_{abs} > 5 \times 10^4$ $\mathrm{km\,s^{-1}}$, for CIV and $v_{abs} > 2 \times 10^4$ $\mathrm{km\,s^{-1}}$, for SiIV);
[b] number density of NALs in the first two bins: $-1000 < v_{abs} < 5000$ $\mathrm{km\,s^{-1}}$ and $5000 < v_{abs} < 10,000$ $\mathrm{km\,s^{-1}}$;
[c] significance of the excess over the random occurrence.

Å) lines and the propagation of counting statistics from the individual bins are reported in Table 3.3.

Hence, the excess is real over the random incidence for the whole sample of CIV NALs. When divided by equivalent width (see the bottom panel of Fig. 3.4) CIV absorbers show a significant excess over the random occurrence at $5000 < v_{abs} < 10,000$ $\mathrm{km\,s^{-1}}$ for both weak and strong lines. While, at $v_{abs} < 5000$ $\mathrm{km\,s^{-1}}$ the excess is more significant for the strong lines. I will come back to this point in section § 4.2.

The excess occurs also in the SiIV velocity offset distribution (see Fig. 3.4, lower panels). As was the case for CIV, the full SiIV sample shows an excess over a random incidence in the first two velocity bins ($< 10,000$ $\mathrm{km\,s^{-1}}$). I would like to highlight the different shape of the two distributions for the strong lines. The SiIV excess is less significant over the random incidence with respect to the CIV one. The possibility that these excesses are due to the environment surrounding the host galaxies of luminous quasars is discussed in the next chapter. All the computed numbers for the SiIV velocity offset distributions are reported in Table 3.3.

Next I investigate the possible dependence of the NAL velocity offset distributions on the quasar bolometric luminosity. The results are presented for CIV and SiIV in Fig. 3.5, upper and lower plots, respectively. To this aim the sample is split in two according to the quasar bolometric luminosity. In both diagrams the upper panel shows the velocity offset distribution for the whole sample of lines, and the middle and the bottom panels show the results for lines with $W_0 > 0.2$ Å and $W_0 < 0.2$ Å,

respectively. Color-shaded histograms represent the lines detected in quasars with luminosity $log\,(L_{bol}) < 46.8$ erg s^{-1}, while the black hashed histogram shows those in quasars with $log\,(L_{bol}) > 46.8$ erg s^{-1}.

In both of the upper panels, the more luminous objects exhibit a slightly larger fraction of absorbers. I explore the possibility that this trend is due to the different S/N between the quasar spectra. Although the S/N in my sample is quite homogeneous, the most luminous quasars have slightly larger S/N spectra, as shown in Fig 3.6. If the observed effect is due to S/N, I should not see the same behavior of the velocity offset distributions for the stronger lines, that are less affected by the different S/N. Indeed, I do not see any difference related with the bolometric luminosity for those lines (see middle panels of Fig. 3.5). The weaker lines show the same slight dependence from the bolometric luminosity I found in the whole sample (see lower panels of Fig. 3.5). Thus, there is no evidence of a correlation between the incidence of absorbers observed in the offset velocity distribution and the quasar bolometric luminosity for both CIV and SiIV. The difference in Fig. 3.5 can be ascribed to the slightly higher S/N of the spectra of the brighter objects. This effect with S/N was seen before for MgII absorbers (e.g., Lawther et al., 2012; Ménard et al., 2008).

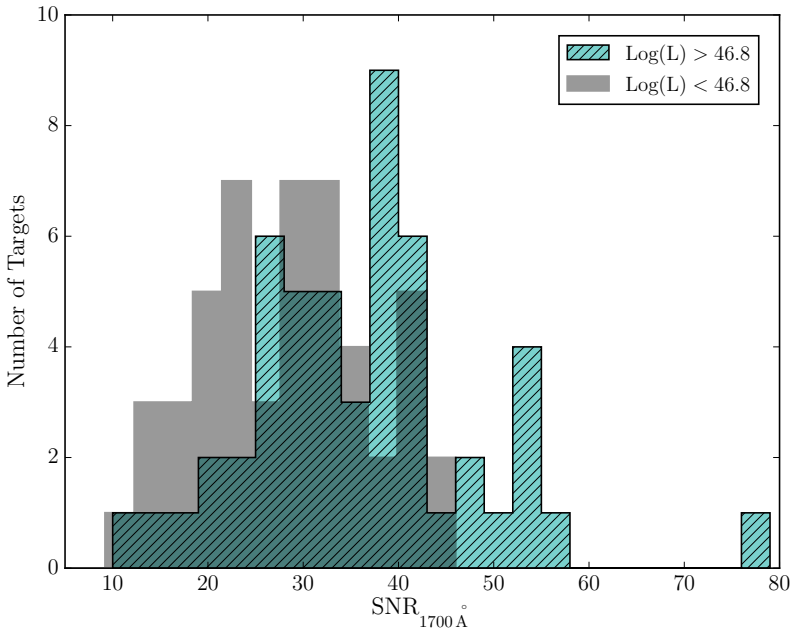

Figure 3.6: S/N (average pixel S/N near rest-frame wavelength 1700 Å) distribution of XQ-100 targets. The shaded histogram represents the quasars with $log(L_{bol}) > 46.8$, the diagonal filled histogram represents those with $log(L_{bol}) < 46.8$.

To summarize, I detect a $\sim 8\,\sigma$ excess of NALs within 10,000 km s^{-1} of the

z_{em} over the random occurrence of NALs. This excess is expected (Foltz et al., 1986; Ganguly et al., 2001; Vestergaard, 2003), but extends to somewhat larger velocities than the standard 5000 km s^{-1} velocity cut-off adopted to define associated system, in general agreement with the results of Weymann et al. (1979); Misawa et al. (2007); Tripp et al. (2008); Wild et al. (2008); Nestor et al. (2008). This commonly used cut-off is determined for relatively strong CIV NALs and if I limit my analysis to $W_{1548} > 0.2$ Å my results are consistent with those of previous works. The extended velocity range of associated NALs is seen especially for the weaker lines $W_{1548} < 0.2$ Å (but above my detection limit, 0.015 Å). Based on this excess frequency, I adopt 10,000 km s^{-1} as the nominal boundary between intervening and associated systems. Because this velocity range of associated absorbers is statistically motivated, additional associated NALs may be present at $v_{abs} > 10,000$ km s^{-1}, just as there may be some intervening NALs at $v_{abs} < 10,000$ km s^{-1}.

3.3.3 Absorber number density evolution

As a final test I want to assess whether the excess I find is due to the NAL redshift evolution. I estimate the number of absorbers in the considered range of velocity offset that are expected due to intervening structures at the same redshift. I calculate the number density evolution dn/dz splitting my sample into two: the associated CIV lines with $v_{abs} < 10,000$ km s^{-1} and the intervening ones with $v_{abs} > 10,000$ km s^{-1}.

The absorber number $n(z)$ is measured by counting the CIV absorption lines for a given equivalent width range in the considered redshift range for each line of sight. The line count n is then divided by the covered redshift interval Δz to obtain dn/dz. The result is presented in Fig. 3.7. We can see that the excess of the associated lines over the intervening ones is present in all covered redshift bins although its significance varies from bin to bin. This result supports the fact that the observed excess in the offset velocity distribution is not an effect of the NAL redshift evolution, but is due to quasar environment. This test is done only for CIV because contamination by the Ly-α forest prevented me from investigating the same wavelength coverage for other ions.

3.3.4 Covering Fraction of the studied ions

To better characterize the environment close to my quasar sample, I measure the covering fractions, f_C, of the studied ions as a function of the velocity offset from

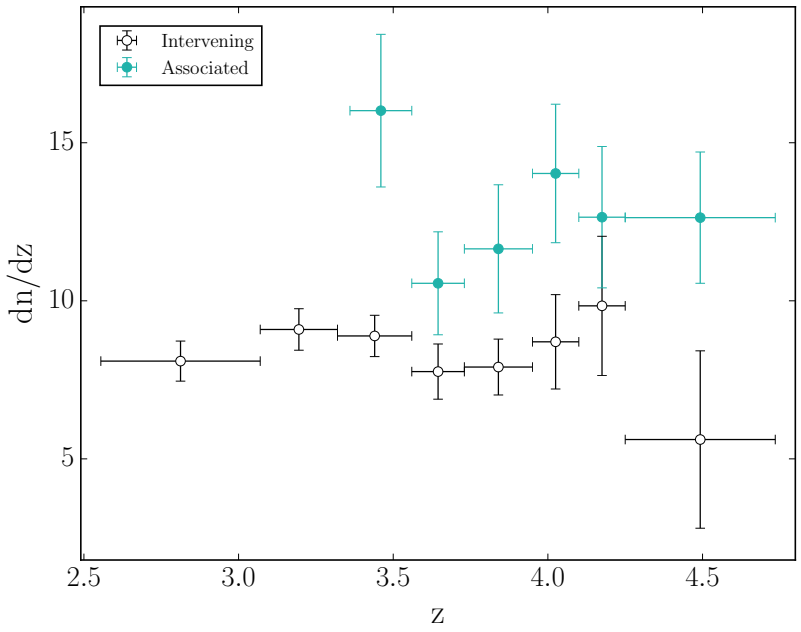

Figure 3.7: Absorber number density evolution dn/dz of the whole sample of CIV systems. Filled circles represent associated systems with $v_{abs} < 10,000$ km s^{-1} while open circles the intervening ones with $v_{abs} > 10,000$ km s^{-1}. The error bars represent the propagation of the Poissonian uncertainties.

z_{em}. These are defined as the ratio between the number of quasars exhibiting at least one absorber with $W_0 > 0.2$ Å within a given velocity separation of z_{em} and the total number of quasars. The error bars represent the propagation of the Poissonian uncertainties. The complete list of covering fraction measurements is reported in Tab. 3.4. I decide to consider lines with $W_0 > 0.2$ Å to better compare my results with previous works present in the literature (see section § 4.1), but measurements of the f_C based on the whole sample are also presented in Tab. 3.4.

Results are shown in Fig. 3.8 for CIV$_{1548}$ (upper) and SiIV$_{1393}$ (lower), compared with the random occurrence computed as the fraction of quasars showing at least one absorber with $W_0 > 0.2$ Å at large velocity separation from z_{em} ($v_{abs} > 5 \times 10^4$ km s^{-1}, for CIV and $v_{abs} > 2 \times 10^4$ km s^{-1}, for SiIV). The CIV covering fraction, f_C^{1548}, remains statistically significant over the random occurrence beyond $v_{abs} \approx 10,000$ km s^{-1}. Then, it shows a shallow declining incidence. This suggests that most of the excess of CIV gas at low velocities lies within the host halo. Interestingly, f_C^{1548} for $v_{abs} < 5000$ km s^{-1} and for $v_{abs} < 10,000$ km s^{-1} have the same value. Furthermore, I confirm that quasars showing an absorber with $5000 < v_{abs} < 10,000$ km s^{-1} always have an absorber with $v_{abs} < 5000$ km s^{-1}, but the opposite is not always true. This points out the presence of a complex velocity structure, increasing the probability of these absorbers to be part of outflows. I

Table 3.4: Covering fractions of CIV, SiIV, NV and CII and propagated counting errors from each quasar sightline.

Velocity [km s^{-1}]	f_C^{1548}	f_C^{1393}	f_C^{1238}	f_C^{1334}
		$W_0 > 0.2$Å		
v_{abs}<5000	0.43 ± 0.07	0.13 ± 0.04	0.22 ± 0.05	0.08 ± 0.03
5000<v_{abs}<10,000	0.27 ± 0.05	0.09 ± 0.03	-	0.02 ± 0.01
v_{abs}<10,000	0.43 ± 0.07	0.13 ± 0.04	-	0.10 ± 0.3
		Whole sample		
v_{abs}<5000	0.72 ± 0.09	0.32 ± 0.04	0.33 ± 0.06	0.15 ± 0.04
5000<v_{abs}<10,000	0.64 ± 0.08	0.39 ± 0.03	-	0.09 ± 0.03
v_{abs}<10,000	0.72 ± 0.08	0.32 ± 0.04	-	0.22 ± 0.05

note also that considering the whole sample (Tab. 3.4) almost 3/4 ($\sim$ 72 percent) of the quasars show CIV NALs within 10,000 km s^{-1}. This is comparable to the frequency ($\gtrsim$ 60 percent) observed by Vestergaard (2003) and shows how common this phenomenon is. Vestergaard (2003) also found that about 25 percent of the quasars have associated NALs with $W_{1548} > 0.5$ Å. To allow a more direct and quantitative comparison with this work, I can consider in my sample only the absorbers with $W_{1548} > 0.5$ Å and within $v_{abs} < 5000$ km s^{-1}. Indeed I do find exactly 25 percent. For SiIV, f_C^{1393} is marginally statistical significant over the random distribution only at $v_{abs} < 5000$ km s^{-1}. In fact, we have already seen in Fig. 3.4 that the SiIV excess is largely dominated by weak lines, with $W_{1393} < 0.2$ Å.

The covering fractions measured for NV$_{1238}$ (upper) and CII$_{1334}$ (lower) are presented in Fig. 3.9. The fraction f_C^{1238} (whole sample) is fairly high ~ 0.25 at $v_{abs} < 2500$ km s^{-1}, then it drops steeply to ~ 0.12 at $2500 < v_{abs} < 5000$ km s^{-1}. Since the velocity range in which I have been able to explore the presence of NV is relatively narrow because of the contamination by the Ly-α forest, I do not have a reference value to compare the f_C^{1238} with.

Fechner and Richter (2009) have carried out a survey of NV systems with a sample of 19 higher resolution spectra of quasars with $1.5 \lesssim z \lesssim 2.5$. They find that the fraction of intervening CIV systems showing NV absorption is ~ 11 percent, without any cut in equivalent width, while roughly 37 percent of associated CIV absorbers ($v_{abs} < 5000$ km s^{-1}) exhibit NV as well. They do not say how many quasars show at least one intervening NV thus, I could take their ~ 11 percent as an upper limit of the random occurrence and my detection frequency would remain statistically significant. The steep drop of the f_C^{1238}at $v_{abs} > 2500$ km s^{-1} close to values that are typical of intervening regions suggests that the NV gas with $v_{abs} < 2500$ km s^{-1} lies predominantly inside the host halo. In addition, I can

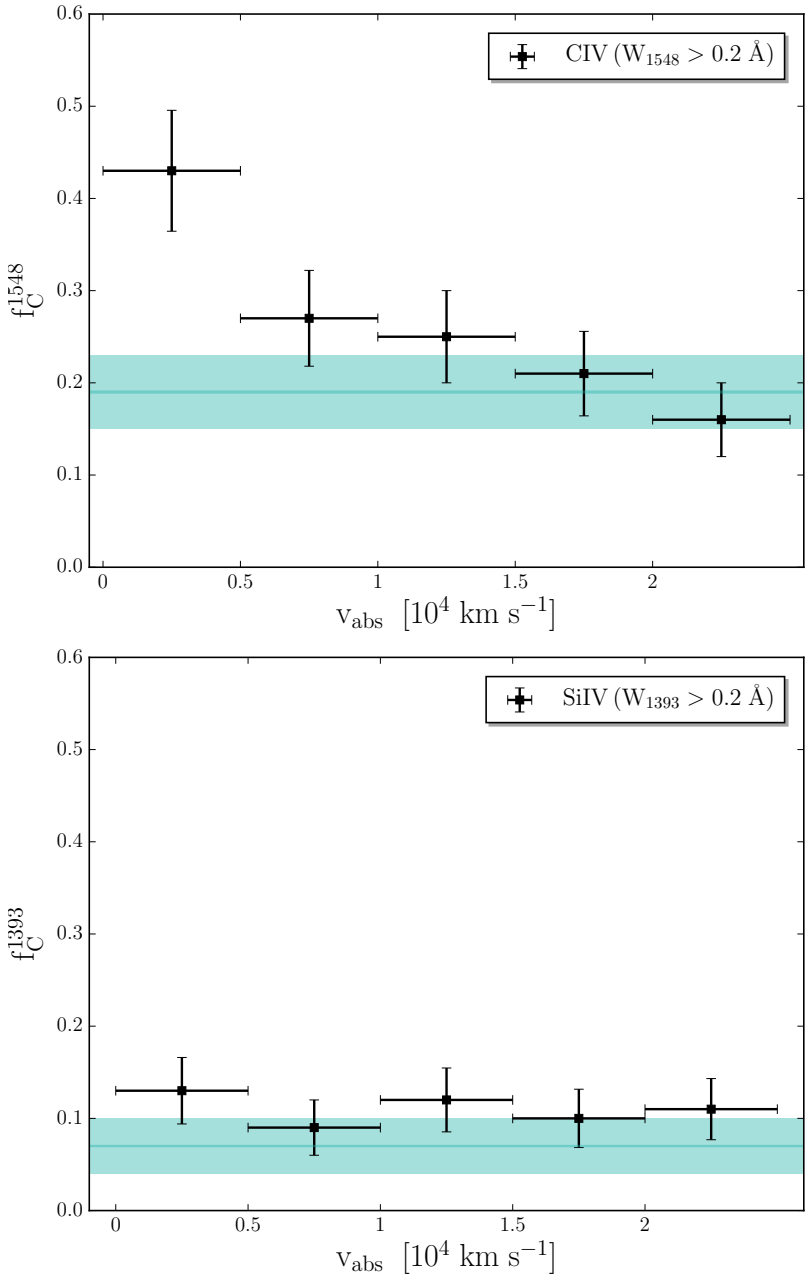

Figure 3.8: Covering fractions, f_C, for CIV_{1548} (upper) and $SiIV_{1393}$ (lower) estimated from the fraction of quasars exhibiting at least one absorber with $W_0 > 0.2$ Å, in bins of velocity offset from z_{em} (horizontal error bars). The horizontal solid line in both plots shows the mean covering fraction for $W_0 > 0.2$ Å lines measured for random 5000 km s^{-1} intervals far from the quasars, the shaded band represents the 1σ error.

directly compare their 11 percent to the fraction of CIV, with $v_{abs} < 5000$ km s^{-1}, exhibiting NV in my sample, that is ~ 35 percent. This is strong evidence that NV systems exhibit an excess above random occurrence. However, I have to take into account that the sample analyzed by Fechner and Richter (2009) is most likely

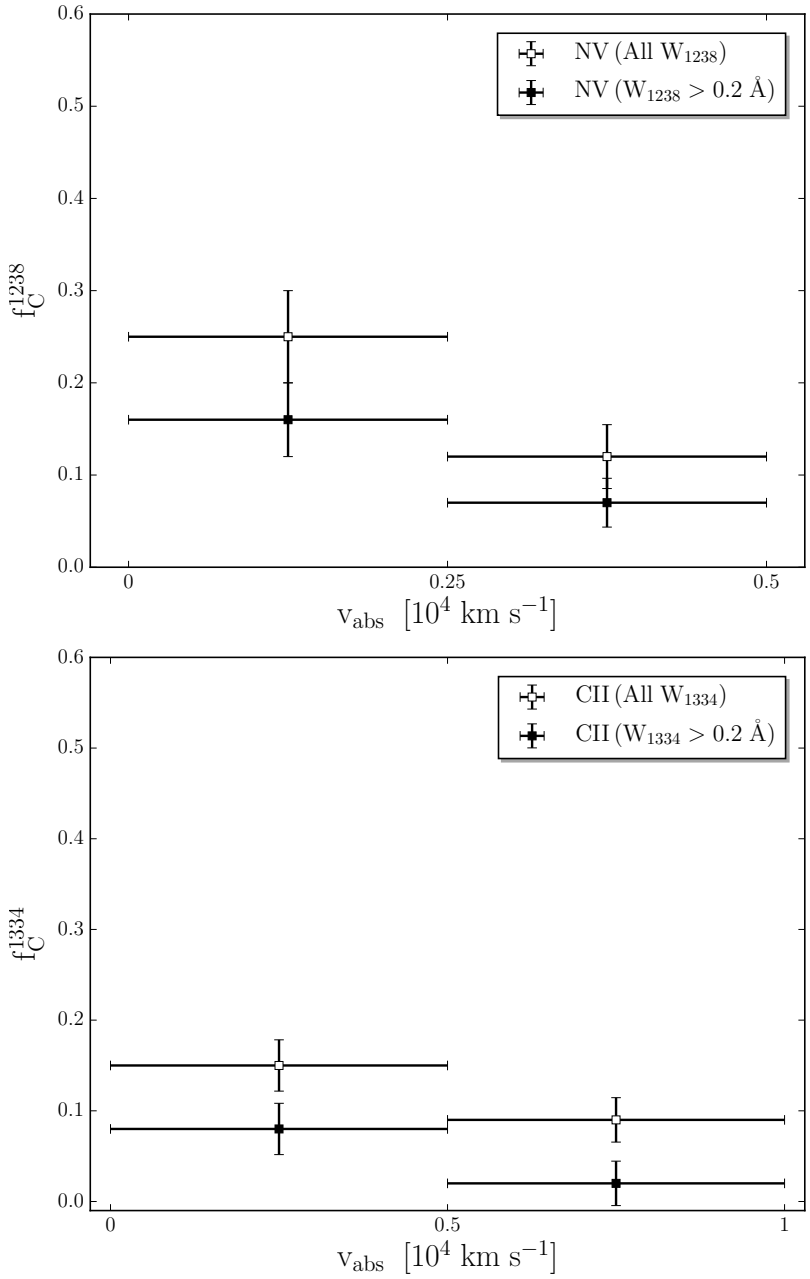

Figure 3.9: Covering fractions, f_C, for NV_{1238} (upper) and CII_{1334} (lower) estimated from the fraction of quasars exhibiting at least one absorber with $W_0 > 0.2$ Å (filled circles) or for the whole sample (open circles), in bins of velocity offset from z_{em}.

incomplete due to blending with the Ly-α forest. So, the actual rate of incidence might be higher, in particular for low column density features. I will discuss in section § 4.1 the possibility of different origins for intervening and associated NV systems, and the improvements that could be made to verify this hypothesis.

The CII covering fraction, f_C^{1334}, is smaller than that of NV. If I consider only the bin with $v_{abs} < 5000$ km s^{-1}, $f_C^{1238} = 0.33$ while $f_C^{1334} = 0.15$. Interestingly,

I notice that the CII detections with $W_{1334} > 0.2$ Å are all corresponding to damped Ly-*alpha* (DLA and sub-DLA) systems (Berg and et al., 2016; submitted). DLAs are defined to be systems where the hydrogen column density is larger than $N_{HI} > 2 \times 10^{20}$ cm^{-2}. I would like to emphasize that CII detections in my sample are probably not tracing gas sited in the host halo.

3.4 Ionization structure of the absorbers

Historically, it has been very difficult to separate intrinsic NALs from intervening ones without high-resolution spectra because of the similarities of their line profiles. Since one of my goals is to determine additional criteria that can be used to disentangle the two classes of absorbers, it is interesting to consider the relative number of NALs in different transitions and their velocity offset distributions. The ion that better traces the effects of the quasar ionization field will offer the best statistical means of identifying intrinsic systems.

The velocity offset distribution with respect to the quasar z_{em} of the ratios of NV and CIV (SiIV and CIV) equivalent width is shown in Fig. 3.10, upper (lower) panel. As already described in § 3.2.2, I have inspected all the spectra of my sample looking for NV and SiIV absorptions at the same CIV redshifts. NV is only measured out to 5500 km s^{-1} from z_{em}, hence the smaller velocity range of the diagram relative to previous ones. I search for a correlation between the offset velocity and the equivalent width of CIV and NV NALs. It is clear from Fig. 3.10 (upper) that CIV is equally distributed within the velocity range in which it has been possible to look for NV absorptions, even if the strongest systems preferentially reside at zero velocity shift. I divide the velocity range into two bins, the first one with $-1000 \leqslant v_{abs} \leqslant 2500$ km s^{-1} and the second one with $2500 \leqslant v_{abs} \leqslant 5500$ km s^{-1}. I find 72 CIV systems in the first bin and 68 in the second one. Most of the NV detections are located closer to the emission redshift: I identify 34 NV detections and 38 upper limits in the first bin ($-1000 < v_{abs} < 2500$ km s^{-1}) and 12 detections and 56 upper limits within the second bin ($2500 < v_{abs} < 5500$ km s^{-1}). In other words, looking at the CIV absorbers in the first bin I have a probability of 47 percent to find a NV at the same absorption redshift, while this probability decreases to 18 percent in the second bin. This trend can be explained if I consider the effect of the quasar ionizing radiation. Indeed, closer to the emission redshift the radiation field is more intense and it allows nitrogen to be highly ionized. As expected DLA systems (marked by open stars in the figure) do not have any detected associated NV absorption systems because of the self-shielding effects of HI, that prevents highly ionized atoms to be formed (but see Fox et al., 2009).

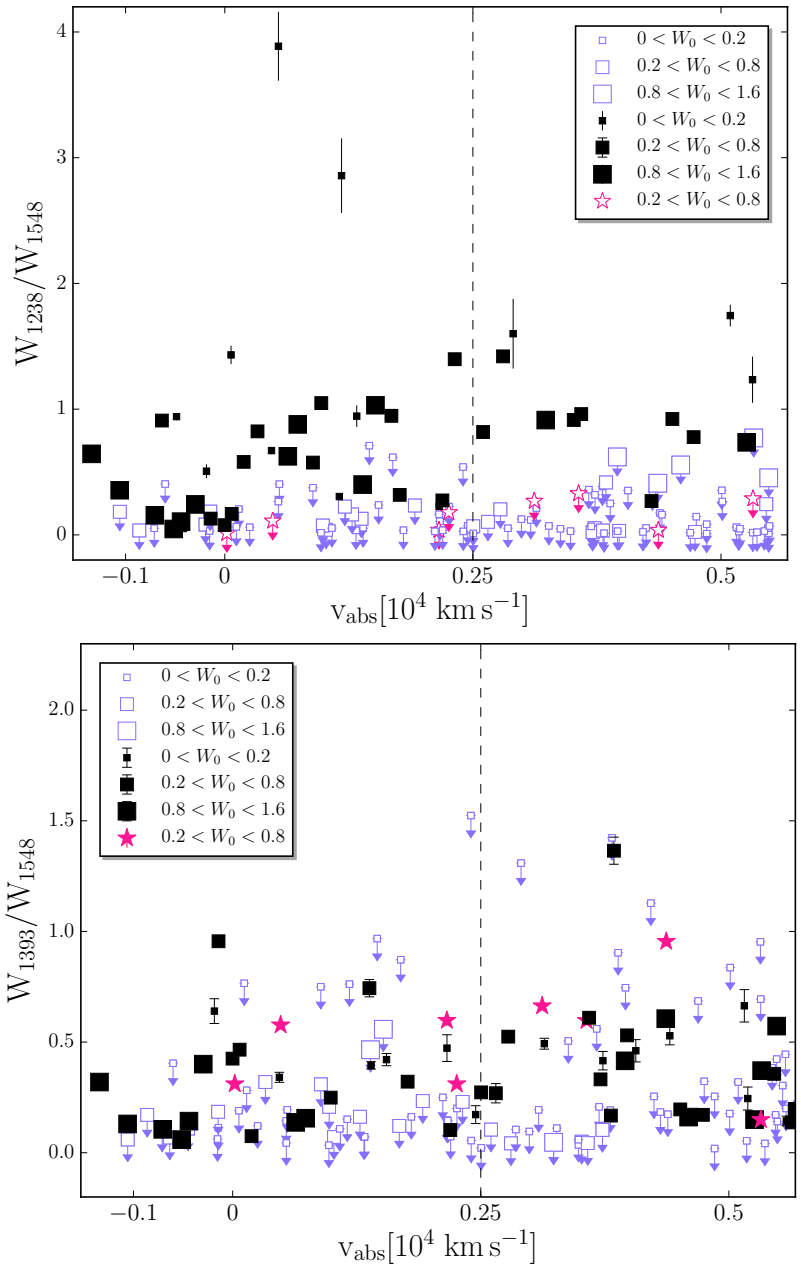

Figure 3.10: Velocity offset distribution with respect to the quasar z_{em} of the NV and CIV (upper), SiIV and CIV (lower) equivalent width ratio. The size of the symbol represents the corresponding W_{1548} Å strength, indicated by the legends. Detections (3σ) are the filled squares. The open squares show the rest-frame equivalent width 3σ upper limit values for the non-detections. The damped Ly-α (DLA) systems present in my sample are marked by open stars (filled stars) in the upper panel (lower panel) and they show NV upper limits (SiIV detections). The vertical dashed lines represent the separation of the velocity range in two bins.

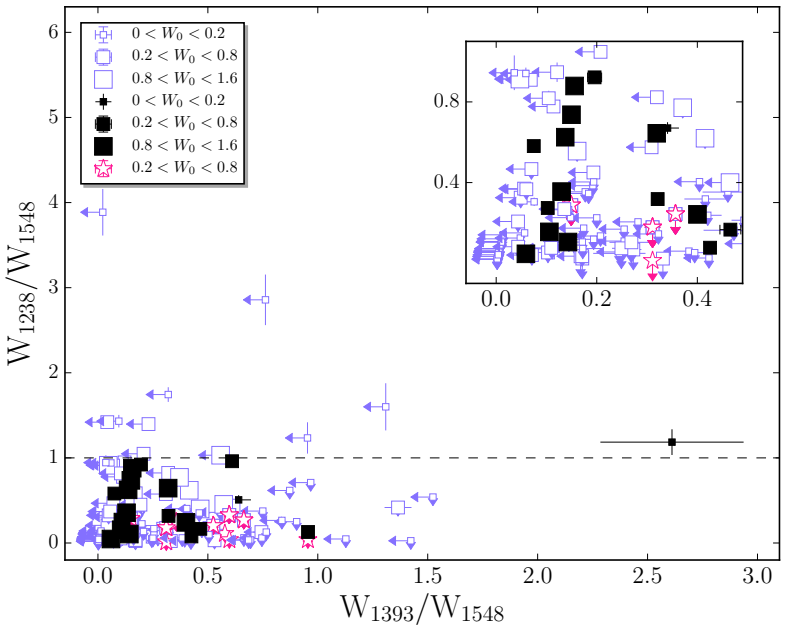

Figure 3.11: Equivalent width ratio between NV and CIV versus the one of SiIV and CIV. Same meaning of the symbols as in Fig. 3.10. The inset represents a zoom of the bottom left region of the diagram. The horizontal dashed line represents the equality of the NV and CIV equivalent widths.

I search also for a correlation between the offset velocity and the equivalent width ratio of CIV to SiIV NALs in the same velocity range. In Fig. 3.10 (lower), SiIV detections do not preferentially reside around z_{em}, nor do I find a clustering of the strongest systems close to z_{em}. I find 26 detections and 46 upper limits in the first bin ($-1000 < v_{abs} < 2500$ km s^{-1}); and 27 and 42, respectively, in the second one ($2500 < v_{abs} < 5500$ km s^{-1}). This corresponds to a probability of 36 percent to find a SiIV at the same redshift as CIV absorption in the first bin and a probability of 40 percent in the second one. Above unity, representing the equality of the equivalent widths ratio, I find only 2 SiIV detections. Indeed, there are not many systems with very strong SiIV absorption able to dominate over the CIV absorption. The DLA systems, indicated by the filled stars in the figure, exhibit SiIV detections and their values are distributed over the entire range of SiIV equivalent widths.

Bearing in mind the different behavior of NV and SiIV ionization paths, I match the results of the latter two figures. The result is shown in Fig. 3.11. Immediately, we can see that above the dashed horizontal line, representing the equality of the NV and CIV equivalent widths, there is only one system with a SiIV detection. When a strong NV is present, I find mainly upper limits for the SiIV. Conversely, the DLA systems show detections for the SiIV and only upper limits for the NV. I do not find a large number of systems showing both ions and most of them have

SiIV with $W_{1393} < 0.2$ Å (see Fig. 3.11). Interestingly many of them (9 out of 19) are at the same redshift as a strong CIV NAL, with $W_{1548} > 0.8$ Å. Once more, we can appreciate the effects of the quasar ionizing radiation. Since the NV and SiIV have very different ionization potentials, 97.9 and 33.5 eV respectively, it is easier to find NV absorbers with respect to SiIV where the radiation field is stronger and vice versa. Therefore, this result confirms that NV is a better tracer of the hard quasar spectra. For this reason, in the next chapter I will focus the attention on the NV NALs.

Chapter 4

4 The nature of NV absorbers at high redshift

Quasar outflows have been increasingly invoked from theoretical models of galaxy formation and evolution to regulate both the star formation in the host galaxies and the infall of matter towards the central SMBH (Granato et al., 2004; Di Matteo et al., 2005; Hopkins and Elvis, 2010). The SMBH at the center of galaxies can produce a terrific amount of energy ($\sim 10^{62}$ erg). Even if just a few percent of the quasar bolometric luminosity were released into the ISM of the host galaxy, it would represent significant feedback for the host galaxy evolution, (e.g. ~ 5 percent L_{bol}, Scannapieco and Oh, 2004; Di Matteo et al., 2005; Prochaska and Hennawi, 2009). This type of coupling via feedback could provide a natural explanation for the observed mass correlation between SMBHs and their host galaxy spheroids (e.g., King, 2003; McConnell and Ma, 2013).

A key piece of information to understand if outflow feedback can affect the host galaxy evolution, is the fraction of quasar driving outflows, as well as their energetics. The latter quantity can be inferred from the velocity, column density, and global covering factor of the outflowing gas. All these observable quantities are connected with the dynamical models of accretion disk winds. With the aim of studying quasar winds, we must carefully select absorption-line systems that truly sample outflowing gas. To this purpose, I have shown in the previous chapter that out of the ions studied in my work, NV is the ion that best traces the effects of the QSO ionization field, offering the cleanest approach to statistically identify intrinsic systems.

In this chapter I will investigate the statistical properties of the NV NAL subsample identified in the XQ-100 spectra (section § 4.1), then I will discuss the results of the study carried out on the XQ-100 sample in the context of relevant works (section § 4.2), finally I will test the robustness of the use of the NV NALs to select intrinsic systems (section § 4.3).

4.1 Statistics of NV systems

In the systematic search for highly ionized absorption species commonly used to identify outflows (e.g. CIV, SiIV, NV, OVI), the NV ion is detected in previous works with the lowest frequency. However, the fraction of these systems that are intrinsic is much larger than that of other excited-state species. Misawa et al. (2007) derived for the NV systems an intrinsic fraction of 75 percent, through partial coverage and line locking methods. Ganguly et al. (2013), using the same techniques, found an intrinsic fraction of 29-56 percent, and suggested to use NV in constructing large catalogs of intrinsic systems with lower resolution and/or lower S/N data. This is not surprising given the overabundance of nitrogen in AGN reported by some authors (e.g., Hamann and Ferland, 1999). Quasars are generally metal-rich (e.g., Dietrich et al., 2003) and about solar $[N/H]$ has been measured in associated systems (e.g., D'Odorico et al., 2004). There is also evidence for higher than solar metal abundances in AGN outflows from the analysis of NALs (Wu et al., 2010; Hamann et al., 2011), making NV easily detectable in proximate absorbers. These metallicities are very high and very rare for any intervening absorption system.

Strong NV absorptions are characteristic of many intrinsic NALs, that are known to be related to the AGN winds/host-galaxy because of velocities within $\sim$ 5000 km s^{-1} of the z_{em}, and evidence of partial coverage of the quasar continuum/broad emission line source (Hamann et al., 2000; Srianand et al., 2002; Wu et al., 2010). For example, Wu et al. (2010) addressed the origin of three 2.6<z<3.0 NV absorbers and pointed out how NV is a good estimator of the intrinsic nature of systems. They performed photoionization models to infer the physical conditions for these absorbers, and found metallicities greater than 10 times the solar value, and high ionization parameters ($log\, U \sim 0$). The unusual strength of these NV lines resulted from a combination of partial coverage, a high ionization state, and high metallicity.

On this basis, I compute the fraction of quasars in my sample hosting at least one intrinsic absorption system to be 33 percent exploiting the detection of NV corresponding to CIV absorptions. This value can be compared with the fraction of quasar showing at least one intrinsic NV absorber from previous studies (e.g., $\sim$ 19 percent, Misawa et al., 2007). I expect my estimate to be slightly higher than that derived through partial coverage or line-locking, because these selection criteria catch only $12 - 44$ percent of intrinsic systems (Ganguly et al., 2013). Indeed, intrinsic absorbers could be too far from the central engine to cause partial coverage, and may not be line locked.

I have shown in the previous chapter that NV is the ion that traces best (amongst

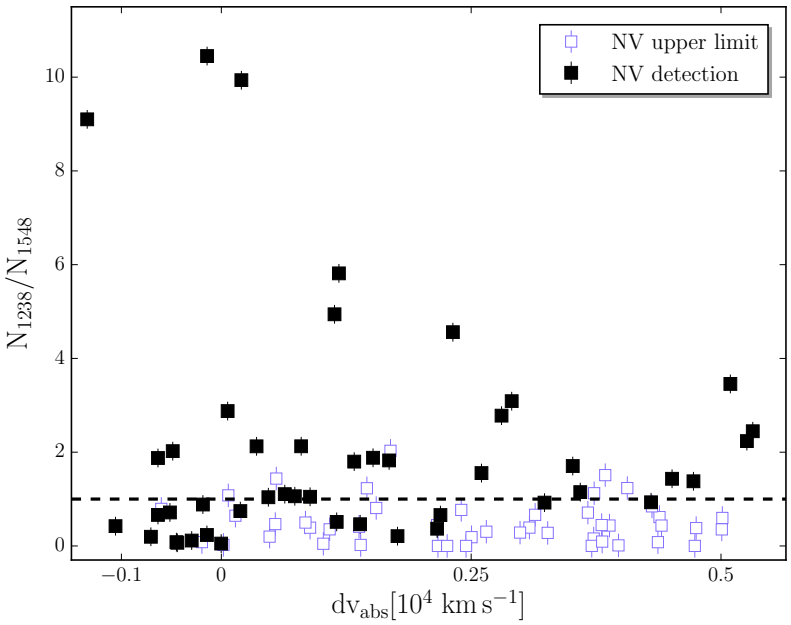

Figure 4.1: Velocity offset distribution of the NV vs CIV column density ratio. Detections (3σ) are marked by the filled squares. The open squares show the column density 3σ upper limit values for the non-detections. The dashed horizontal line represents the equality of the ratio.

those considered) the effects of the quasar ionization field, offering the best statistical tool to identify intrinsic systems. Furthermore, other studies present in the literature have argued that associated NV shows distinctive signatures of its intrinsic nature with respect to intervening systems. In particular, Fechner and Richter (2009) have constructed detailed photoionization models to study the physical conditions of the absorbers and to constrain the ionizing radiation field. This work has pointed out that intervening NV absorbers are not tracers of the spectral hardness of the ionizing radiation. These systems were found to be systematically weaker than both CIV and associated NV lines.

Motivated by these results, I explore in more detail the properties of my sample of NV absorbers. Fig. 4.1 represents the velocity offset distribution of the NV and CIV column density ratios of my sample. It is clear from Fig. 4.1 that most (~ 68 percent) of the detections have a column densities ratio larger than 1. This is consistent with the result by Fechner and Richter (2009): associated NV systems exhibit similar or even larger column density with respect to CIV. The fraction of quasars showing at least one NV absorption line with $N_{1238}/N_{1548} > 1$ is 26 percent.

Fig. 4.2 shows the distribution of the NV column densities of my sample (diagonal filled histogram), compared with the column density distributions by Fechner

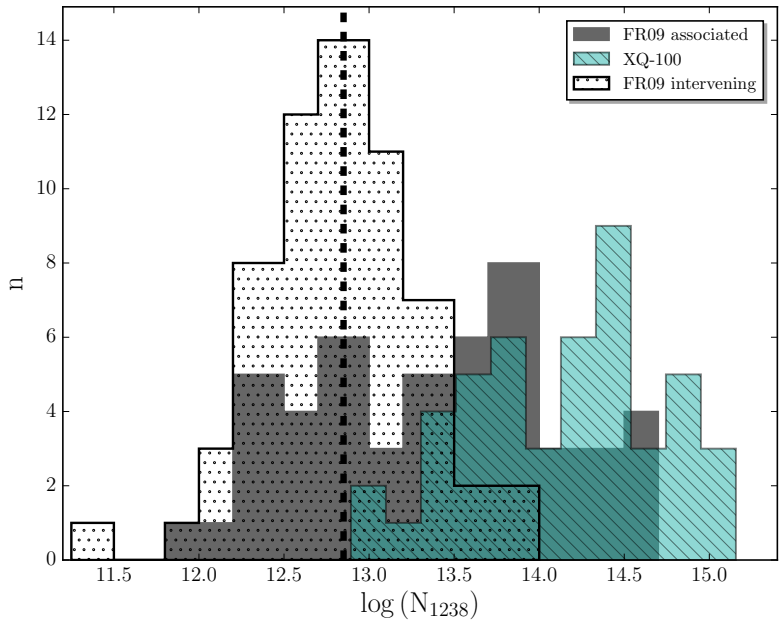

Figure 4.2: Distribution of the measured NV column densities of my sample (diagonal filled histogram). Also shown are the intervening (dotted histogram) and associated (dark shaded histogram) NV column density distributions from Fechner and Richter (2009; FR09). The dashed vertical line represents the detection limit of my sample, explaining the lack of low N_{1238} absorbers with respect to Fechner and Richter (2009) based on high resolution data.

and Richter (2009). It is clear from Fig. 4.2 that associated NV systems start dominating the distribution at values of the order of $log\, N_{1238} \sim 13.5$ and that no intervening NV system with $log\, N_{1238} > 14$ is detected. Looking at my sample, 85 percent of the NV absorbers have column densities larger than $log\, N_{1238} = 13.5$ and 55 percent have values larger than $log\, N_{1238} = 14$. The number of quasars showing at least one NV absorption line with $log\, N_{1238} > 13.5$ is 30 percent, which reduces to 19 percent if a threshold of $log\, N_{1238} > 14$ is considered.

Furthermore, Kuraszkiewicz and Green (2002) found that the NV/CIV ratio for the BEL gas correlates strongly with the NV/CIV ratio for the associated NAL systems, while the control sample of intervening NV absorbers in their analysis does not show this correlation. Their finding identifies an additional test for the intrinsic nature of NALs in any given object. I will explore this correlation for my sample in a forthcoming paper (Perrotta et al. in prep.).

4.2 Characterizing the quasar radiation field

I have shown in the previous chapter that I detect a statistically significant excess over the random occurrence of NALs up to 10,000 km s^{-1} from the systemic redshift. This excess does not show any dependence on the quasar bolometric luminosity.

Looking at the CIV and SiIV velocity offset distributions relative to the quasar z_{em}, we can appreciate the effect of the quasar radiation field influencing the gas along the propagation direction of the outflows. In particular, strong and weak lines in Fig. 3.4 (upper bottom panel) display a different behaviour in the velocity range $-1000 < v_{abs} < 5000$ km s^{-1}. Indeed, the excess is less significant for the weaker lines. A possible explanation could be that in the first bin I examine gas closer to the emission redshift and therefore more directly influenced by the quasar radiation. Closer to the quasar, the gas is more easily ionized and it is thus reasonable to expect that the occurrence of the weaker lines decreases there. Furthermore, in general I find a less significant SiIV excess with respect to CIV. This is probably due to the different ionization potentials needed to produce these ions: 33.5 and 47.9 eV, respectively. It is reasonable to expect that closer to the quasar, where the radiation field is more intense, a smaller fraction of Si is in the form of SiIV. I have shown in the previous section that intrinsic NV systems exhibit similar or even larger column density with respect to CIV. The strong NV could be explained by an ionization effect but could also trace higher metallicities and N/C abundances characteristic of quasar outflows and environment (e.g. Wu et al., 2010). The equivalent width of NV lines could also be boosted relative to other transitions with larger column densities as an effect of partial coverage. For what concerns the weaker lines, they are probably associated to galaxy halos in the quasar vicinity.

I compare my results on the quasar proximity environment along the line of sight with the results obtained in the transverse direction using quasar pairs at close angular separation on the sky (e.g., Prochaska et al., 2014, Prochaska et al. (2014) herafter). Recent studies (e.g., Hennawi et al., 2006; Prochaska et al., 2013; Farina et al., 2013) have revealed that quasar host galaxies exhibit strong absorption features due to cool gas (e.g. HI, MgII, CII) in the transverse direction. At impact parameters of $\sim$ 100 kpc, the incidence of optically thick gas is $>$ 50 percent and the gas is substantially enriched (Prochaska et al., 2013; Farina et al., 2014). This is in contrast with what I observe along the line of sight, suggesting a scenario where the ionizing emission of the quasar is anisotropic (as predicted in AGN unification models). I can exploit these studies to evaluate if the excess I find is statistically significant over the environmental absorption, comparing my results with those derived from gas not directly influenced by quasar outflows.

Prochaska et al. (2014) clearly demonstrate that the environment surrounding the host galaxies of luminous $z \sim 2$ quasars exhibit an excess of CIV absorption lines with $W_{1548} > 0.2$ Å to scales of 500 kpc from the quasar decreasing smoothly toward 1 Mpc. The authors quantify this excess by estimating the two-point-correlation function between CIV absorbers and quasars. The large clustering amplitude ($r_0 = 7.5^{+2.8}_{-1.4}\,h^{-1}$ Mpc) obtained from this analysis, implies that the CIV gas traces the same large-scale over densities as the halos hosting $z \sim 2$ quasars. This result has been interpreted as evidence that the CIV gas is physically related to the massive halos ($M > 10^{12}$ $M_\odot$) of galaxies that cluster with the quasar host. Clearly, I cannot directly compare my detection fraction (Fig. 3.8, left) with the one derived in the Prochaska et al. (2014) analysis (see their Fig. 5, right). In fact, the detected CIV velocity offset cannot be directly translated into a physical distance because the redshift includes also the information on the peculiar velocity of the absorber. If I did that, I would obtain a proper separation of the order of $\sim$ 10 Mpc, implying a lack of correlation between the absorber and the quasar host galaxy. Probably, all the gas studied by Prochaska et al. (2014) is contained in my first bin, within 5000 km s^{-1} of z_{em}. Indeed the average of their detection fraction (i.e. 0.51) is close to the value in my first bin (i.e. 0.43). In conclusion, I observe a comparable incidence of CIV absorptions along and across the line of sight, suggesting that this ion will not allow us to disentangle AGN outflow systems from environmental absorptions.

A completely different behavior is shown by NV NALs. In section § 3.3.4, I reported that, in my sample, NV exhibits an excess over random occurrence within 5000 km s^{-1} of z_{em}. Conversely, in the transverse direction only one NV detection has been detected in a sample of about 400 quasar pairs (Lau et al., 2015). This is further evidence that NV is the byproduct of the quasar ionizing radiation acting along the line of sight. I reported in sections § 3.3.2 and § 3.3.4 that the excess of CIV gas at low velocities lies within the host halo and that most of this excess can be explained by the subset of CIV absorptions with detected NV. I am not able to infer the physical separation of the absorbing gas from the quasar, but NV NALs likely originate at small distances from the central engine (Wu et al., 2010). This absorbing material might be part of outflows in the accretion disk wind itself and its density would be order of magnitude bigger than that of intervening systems. In a future work I will perform detailed photoionization models to infer the physical conditions of some detected NV NALs in my sample exploiting high-resolution spectra obtained with UVES/VLT.

In addition, in the transverse direction a huge amount of CII with $W_{1334} > 0.2$ Å extending to 200 kpc from the considered quasars was found by Prochaska

et al. (2014), (see their Fig. 5, left). The steep drop in covering fraction, f_C^{1334}, at distances larger than 200 kpc requires that this CII gas lies predominantly within the host halo. In contrast with this result, I have shown in section § 3.3.4, (Fig. 3.8, right), that the frequency with which CII is detected in the survey is very small. Moreover, if I consider only absorbers with $W_{1334} > 0.2$ Å, then I see that they are all associated with identified DLA (or sub-DLA) systems probably not related with the host halo. Hence, I verify the absence of cool gas (in particular CII) along the line of sight associated to the quasar host galaxy, in contrast with what is observed in the transverse direction.

Wild et al. (2008) used a cross-correlation analysis of quasar-absorber pairs to measure the strength of narrow absorber clustering around quasars. They claim that galaxies in the vicinity of the quasar may contribute as much as ~ 55 percent of the excess of the absorbers with $v_{abs} \lesssim 3000\,\mathrm{km\,s^{-1}}$. I will perform my own CIV clustering analysis to validate the observed excess in a forthcoming paper (Perrotta et al. in prep.).

4.3 Stack Analysis of NV in the Lyα forest

We have seen in the previous sections that, among the ions studied in this work, NV is the one that best traces the effects of the quasar ionization field, offering a great statistical tool for identifying intrinsic systems (Perrotta et al., 2016). We can use the detection of NV NAL to compute the fraction of quasar hosting intrinsic absorption systems. However, contamination by the Ly-α forest prevents me from exploring a large velocity range for NV (the maximum separation outside the Lyα forest is 5500 km s^{-1} of z_{em}).

As I mentioned in section § 2.2.1, quasars exhibits a much thicker forest of Lyα lines at high redshift. Thus, the complexity of the Lyα forest at $z_{em} = 3.5 - 4.5$, prevents me to search for individual NV lines in this spectral region. Fig. 4.3 shows the Lyα forest of a representative case of the whole XQ-100 sample.

To test the robustness of the use of NV as additional criterium to select intrinsic NALs, I will perform a stack analysis in the Lyα forest of the XQ-100 sample, to search for NV signal at larger velocity offsets. The stacked spectrum, by definition, yields the average observed flux, F_λ, of quasars at a given redshift. I will exploit the stochastic nature of the Lyα forest, to average together an ensemble of sight lines and investigate the presence of NV signal.

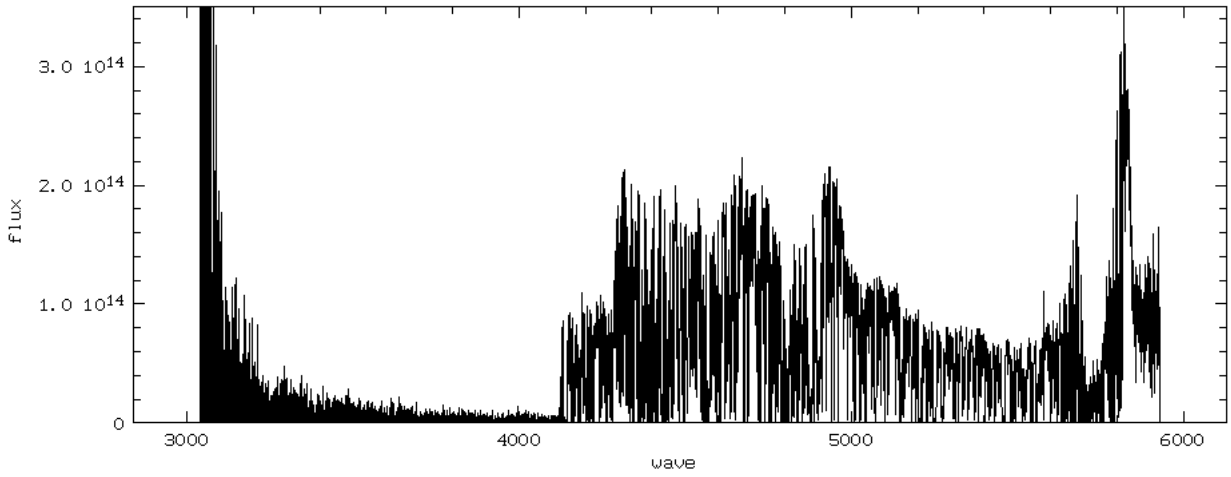

Figure 4.3: XQ-100 not normalized spectrum of quasar J1013+0650 at $z_{em} = 3.808$.

4.3.1 Average Spectrum Construction

The first step to produce the stacked spectrum is the continuum normalization of all the XQ-100 quasars spectra. The continuum placement in the Lyα forest is highly subjective due to the lack of clean quasar continuum (e.g. Kirkman et al., 2005), and is particularly difficult to identify around the Lyα absorption of DLAs. I use the continuum determination, in this wavelength region, made by the XQ-100 team. The estimate of the continuum level has been done by hand. The manually-placed continuum has been determined by selecting points along the quasar continuum free of absorption (by eye) as knots for a cubic spline. For all sightlines, the continuum placement has been visually inspected and adjusted such that the final fit resides within the variations of regions with clean continuum. The accuracy of the fits is as good or better than the S/N of these clean continuum regions (see Lopez et al., 2016 for a detailed description of the adopted procedure). The normalized version of the spectrum shown in Fig. 4.3 is presented in Fig. 4.4.

Then, for each sightline, I mask out the regions that have clear strong absorption features (i.e. Lyman break, DLAs and sub-DLAs). In particular, I take advantage of the DLA identification done by Sánchez-Ramírez et al. (2016). I define the extremes of the DLA absorption, at the wavelengths where the wings of the DLA match again the level of the continuum to within the values of the flux error array.

I follow the subsequent procedure for the construction of the average spectrum:

(1) For each of the 986 CIV doublets identified in the XQ-100 spectra (see section § 3.2.1), I calculate the barycenter position of the system weighting the wavelengths with the optical depth of the line profile.

(2) I use the CIV barycenter to select the region of the spectrum where the

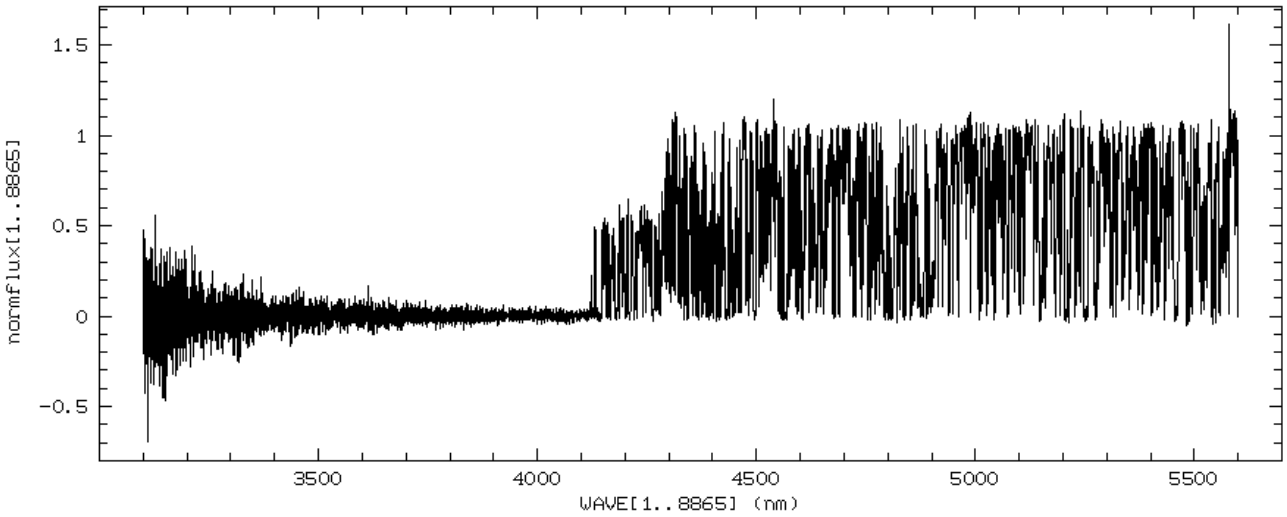

Figure 4.4: XQ-100 normalized spectrum of quasar J1013+0650 at $z_{em} = 3.808$.

corresponding NV doublet should be located. Specifically, I select a region of 1000 km s^{-1} around the expected position of the NV barycenter (for both the doublet components; i.e. NV λ1238 Å and NV λ1242 Å).

(3) Each selected region is shifted to the rest-frame.

(4) I generate a rest-frame wavelength array with fixed wavelength step $\Delta\lambda$. The step value is set to be large enough to include at least one entire pixel from the UV spectra. The visible arm of X-shooter has a mean resolution of 8800, while in the UV it goes down to 5100. Thus, a region with the same extent is sampled with a larger number of pixels in the visible than in the UV region of the spectrum.

(5) For each selected spectral region, I compute the contribution of each pixel to the cells of the final grid.

(6) All the flux values in each cell of the final grid are then averaged to produce the stacked spectrum.

My final sample consists of 836 NV selected regions whose barycenter is within $-1000 < v_{abs} < 73,000$ km s^{-1} of z_{em}. I exclude 150 regions because they completely or partially overlap with Lyman breaks or DLA and sub-DLA absorptions. The extension to -1000 km s^{-1} is justified and motivated by the need to take into account uncertainties in the quasar systemic redshift and to consider possible inflows (see section § 3.3.2).

I will also split the final sample according to the column density of the CIV absorptions, $N_{\rm CIV}$, in order to investigate the effects of this parameter to the final stacked spectrum. The column density distribution of the whole XQ-100 CIV NAL sample is presented in Fig. 4.5.

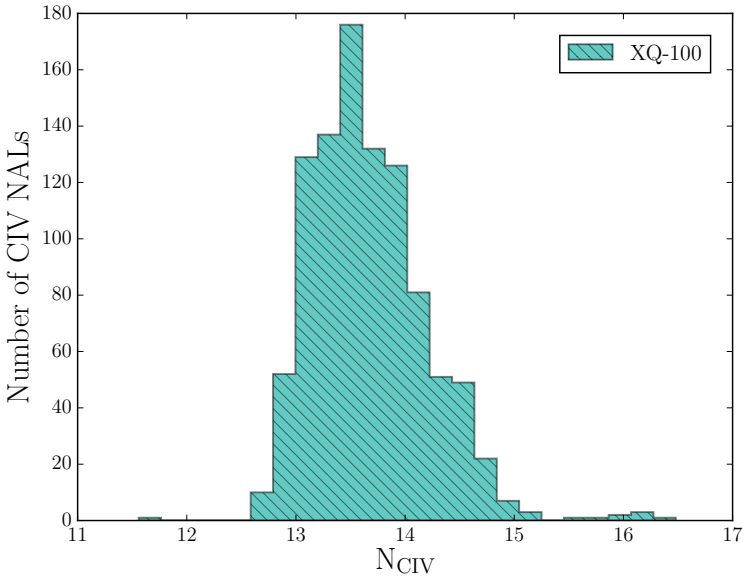

Figure 4.5: Column density distribution of the whole XQ-100 CIV NAL sample.

4.3.2 Preliminary Results

Below, I present very preliminary results from the stack analysis of NV absorbers in the Lyα forest of the XQ-100 sample.

Fig. 4.6 shows the stacked spectra for both the components of the NV doublet. We can see in the upper panel the result from stacking the whole sample. The average spectrum appears quite flat as expected in absence of a strong NV signal, due to the stochastic nature of the Lyα forest. Indeed, putting all together regions from multiple independent sightlines, the numerous HI absorptions that build the Lyα forest average each other and the resulting spectrum is flat. The middle panel of Fig. 4.6 shows the stacked spectrum for regions selected in the original spectra within any velocity separation of z_{em}, and with the column density of the corresponding CIV absorptions larger than 13.5. The profile of both the components of the NV doublets are quite flat also in this case. There is just a hint of coherent absorption of the two components. The regions that produce the stacked spectrum in the lower panel of Fig. 4.6 are chosen as in the middle panel but now, $N_{\rm CIV}$ is less than 13.5. The resulting spectrum is flat, as well.

The selection of the regions to be stacked will be the same in the next figures for what concerns the column density of the corresponding CIV absorptions, $N_{\rm CIV}$. Upper panels do not show any preferred column density; middle panels $N_{\rm CIV}$ larger than 13.5; lower panels $N_{\rm CIV}$ less than 13.5.

The regions to be stacked are chosen in Fig. 4.7 within a given velocity separation of z_{em} and as a function of the corresponding $N_{\rm CIV}$. In particular, the left panels

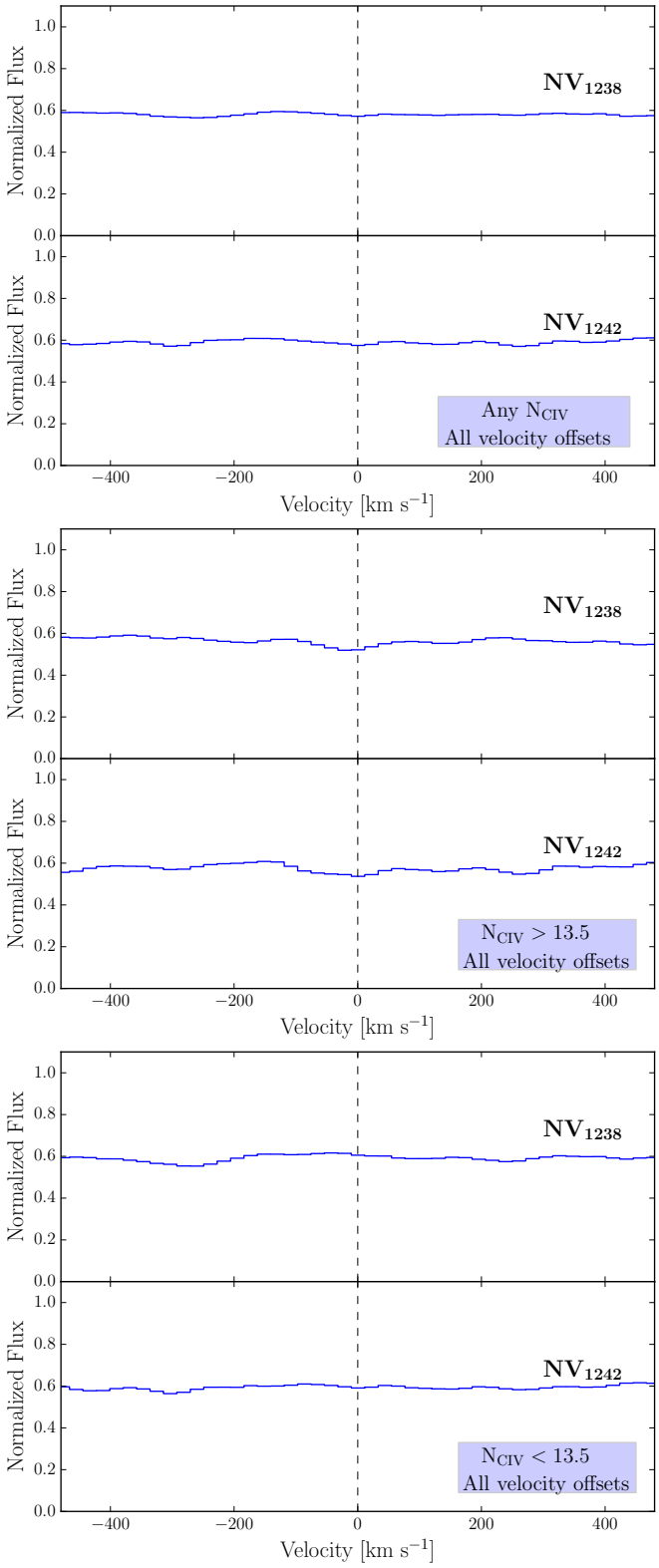

Figure 4.6: Average absorption line spectra for NV doublet, selected within any velocity separation of z_{em} as a function of the corresponding CIV column density, $N_{\rm CIV}$. Upper panel: all the column densities. Middle panel: $N_{\rm CIV}$ larger or equal to 13.5. Lower panel: $N_{\rm CIV}$ less than 13.5.

exhibit the stacked spectra of regions with $0 < v_{abs} < 5000$ km s^{-1}, while the right panels regions with $5000 < v_{abs} < 10,000$ km s^{-1}.

The absorbers with $-1000 < v_{abs} < 0$ km s^{-1} are added to the velocity bin

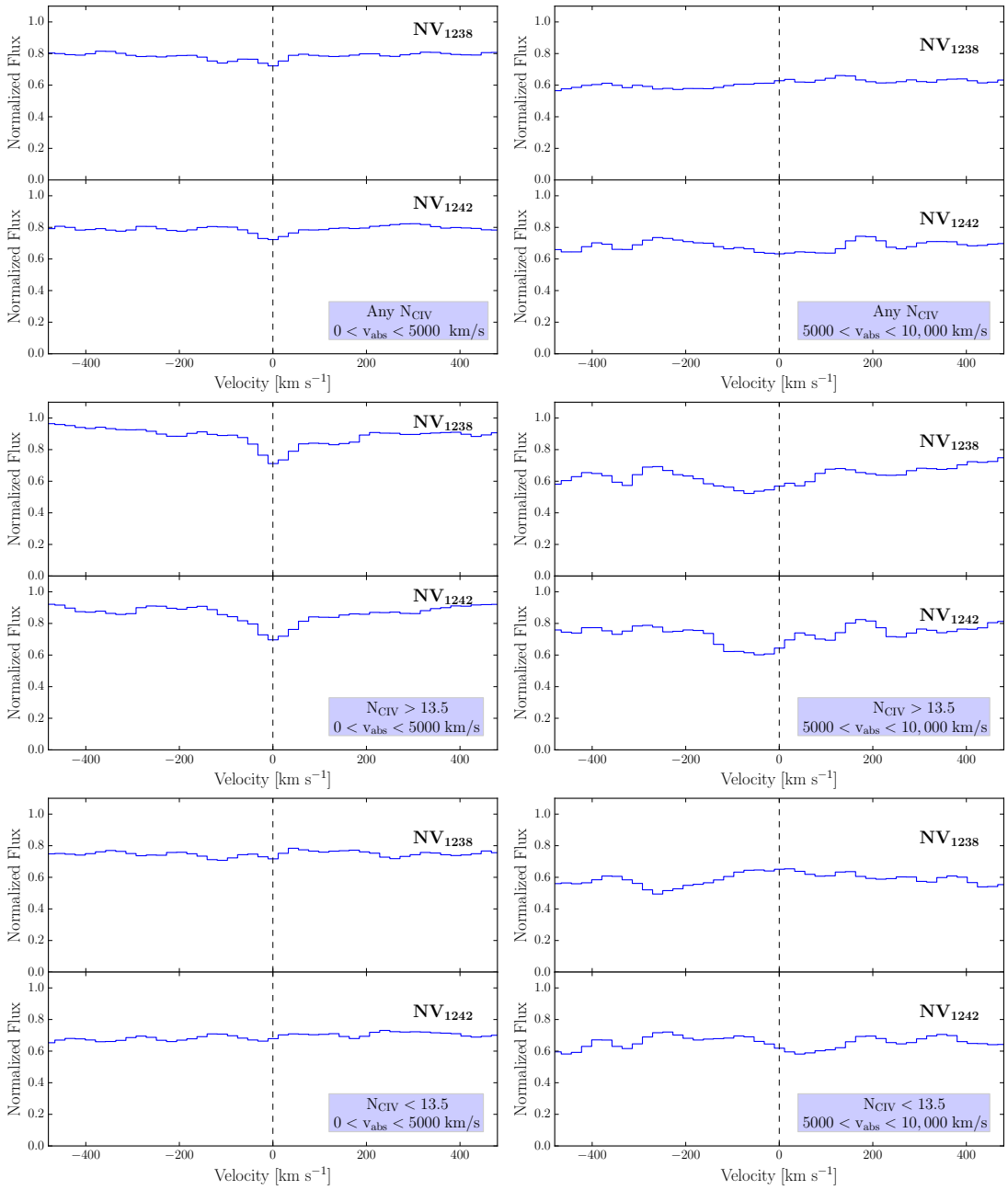

Figure 4.7: Average absorption line spectra for NV doublet, selected within a given velocity separation of z_{em} as a function of the corresponding CIV column density, $N_{\rm CIV}$. Left panels: NV doublets are selected with $0 < v_{abs} < 5000$ km s^{-1}. Right panels: NV doublets are selected with $5000 < v_{abs} < 10,000$ km s^{-1}. Upper panels: all the column densities; middle panels: $N_{\rm CIV}$ larger or equal to 13.5; lower panels: $N_{\rm CIV}$ less than 13.5.

$0 < v_{abs} < 5000$ km s^{-1}. Let's consider first the left part of the figure. The upper panel exhibits a slight coherent absorption in the profile of both the NV components. This feature is much more evident in the middle panel, once only the regions corresponding to the strongest CIV NALs ($N_{\rm CIV} > 13.5$) are selected to be stacked. The absorption disappears completely in the lower panel, where CIV absorptions with $N_{\rm CIV} < 13.5$ are considered to build the stacked spectrum.

The NV absorptions are outside the Lyα forest for approximately 5000 km s^{-1}, so these first plots have a quite regular behavior even if the number of lines stacked is a small fraction of the whole sample. The number of CIV NAL absorption doublets within a given velocity separation of z_{em}, as a function of the column density is reported in Tab. 4.1.

Table 4.1: Number of CIV NAL absorption doublets within a given velocity separation of z_{em}, as a function of their column density.

	Any $N_{\rm CIV}$	$N_{\rm CIV} \geq 13.5$	$N_{\rm CIV} < 13.5$
$0 < v^*_{abs} < 73,000$	836	364	472
$0 < v^*_{abs} < 5000$	126	44	82
$5000 < v^*_{abs} < 10,000$	75	31	44
$10,000 < v^*_{abs} < 15,000$	59	22	37
$15,000 < v^*_{abs} < 20,000$	59	19	40

* v_{abs} is measured in km s^{-1} (see Eq. 3.3).

Looking at the right part of Fig. 4.7, we can immediately see that all the three panels have a much more irregular behavior than the ones in Fig. 4.6. This is essentially due to a lower statistic. Moving further from the z_{em} the number of absorbers decreases until reaching a certain threshold (see section § 3.3.2). In the upper and lower panel of Fig. 4.7 there is not sign of any coherent absorption profile of the two NV doublet components. Possibly, in the middle panel we can see an hint of absorption, but not as clear as in the parallel panel on the left.

The stacked regions in Fig. 4.8 are selected with $10,000 < v_{abs} < 15,000$ km s^{-1} (left panels) and with with $15,000 < v_{abs} < 20,000$ km s^{-1} (right panels). Although the stacked spectra are not as regular as the ones in Fig. 4.6, we can clearly see that there is not imprint of any coherent absorption feature in the profile of the two NV doublet components. This is also true independently from the corresponding $N_{\rm CIV}$ considered to choose the regions that build these stacked spectra.

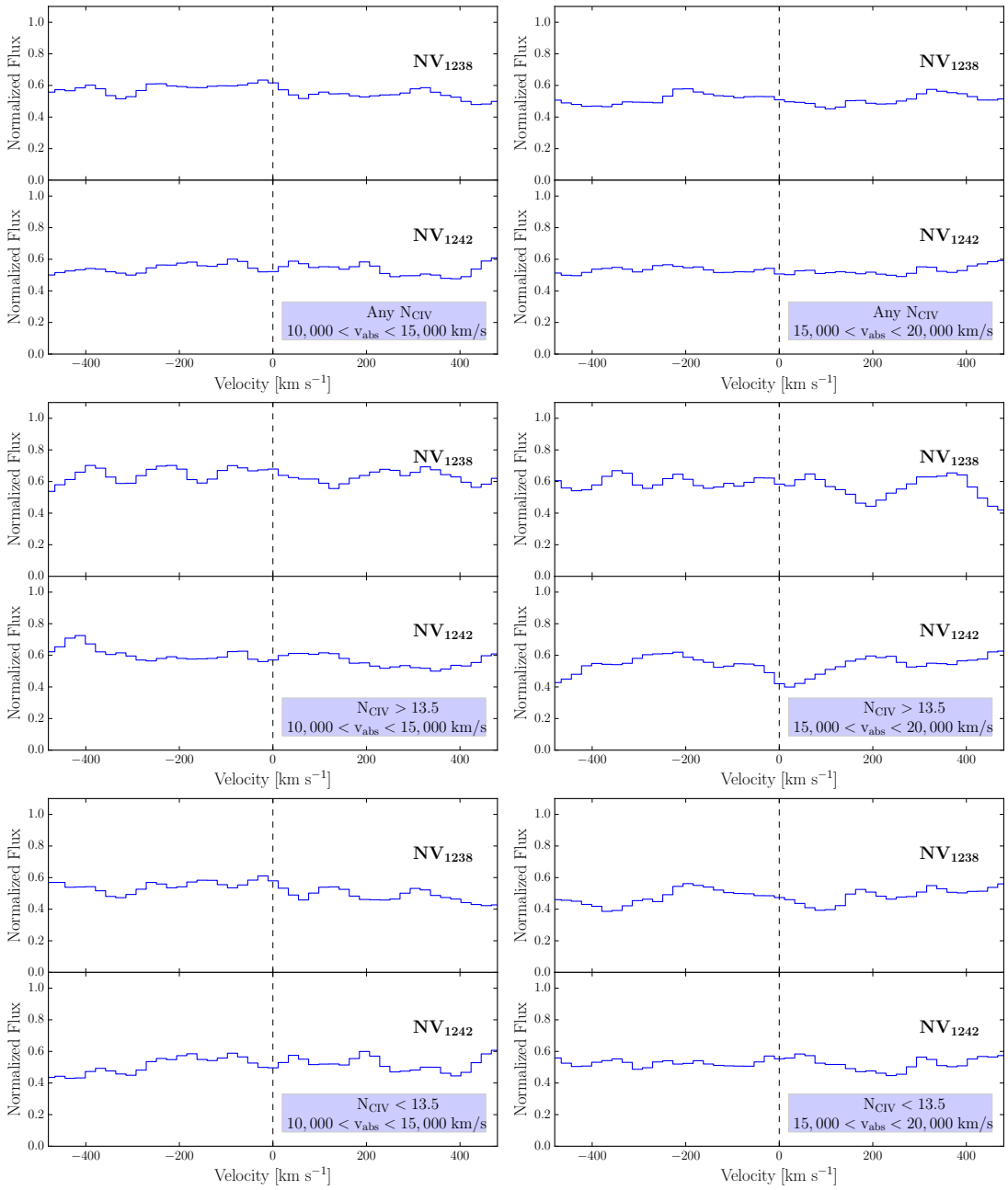

Figure 4.8: Average absorption line spectra for NV doublet, selected within a given velocity separation of z_{em} as a function of the corresponding CIV column density, $N_{\rm CIV}$. Left panels: NV doublets are selected with $10,000 < v_{abs} < 15,000$ km s^{-1}. Right panels: NV doublets are selected with $15,000 < v_{abs} < 20,000$ km s^{-1}. Upper panels: all the column densities; middle panels: $N_{\rm CIV}$ larger or equal to 13.5; lower panels: $N_{\rm CIV}$ less than 13.5.

To increase the statistic of the absorption lines stacked in a single bin of velocity, I group together the regions presented in Fig. 4.7 and in Fig. 4.8.

Fig. 4.9 shows the stacked spectrum for NV regions selected in the original spectra

with $0 < v_{abs} < 10,000\ \mathrm{km\,s^{-1}}$ (left panels) and with $10,000 < v_{abs} < 20,000\ \mathrm{km\,s^{-1}}$ (right panel), always as a function of N_{CIV}.

A clear signature imprinted on the stacked spectrum of both the two NV doublet

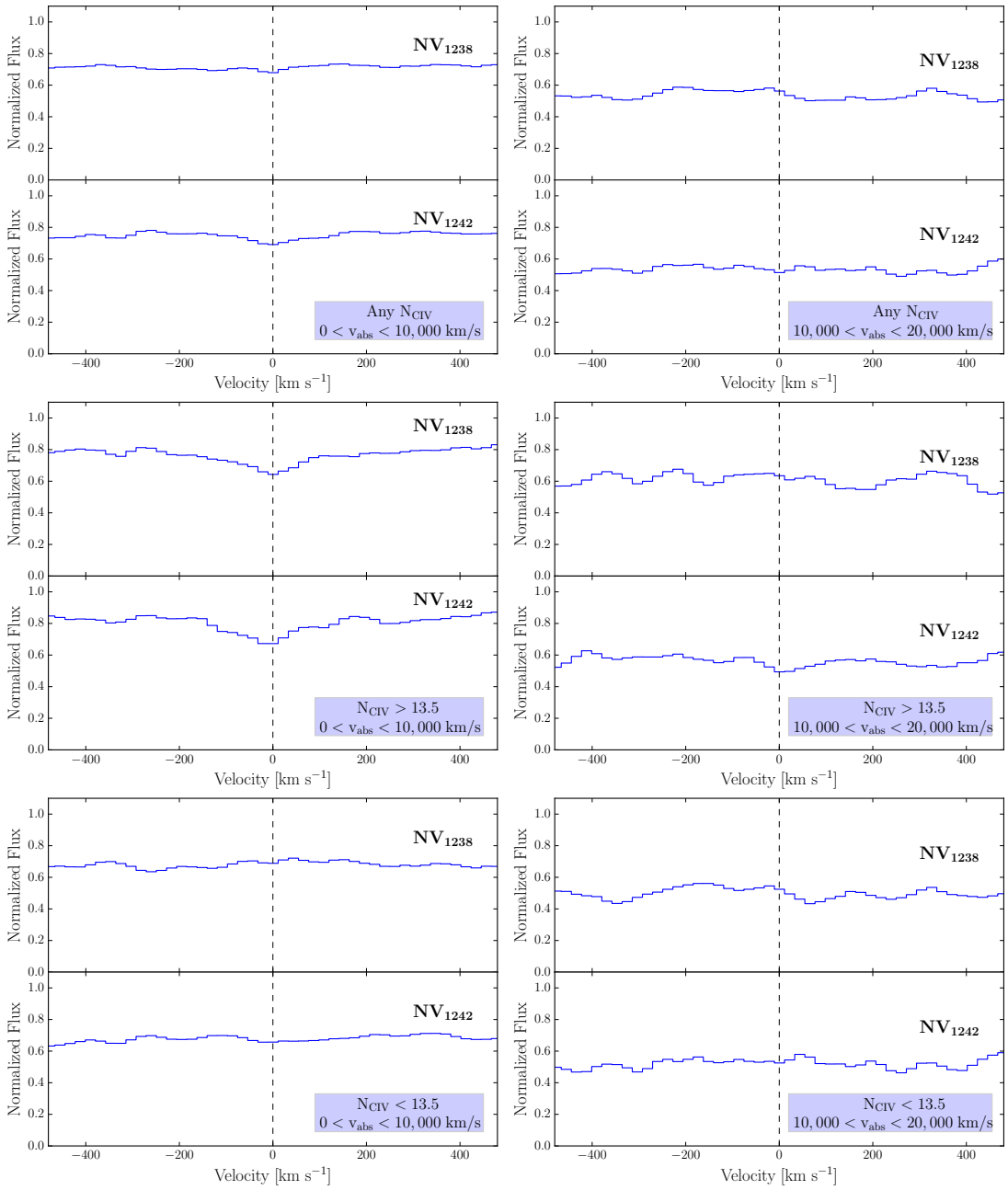

Figure 4.9: Average absorption line spectra for NV doublet, selected within a given velocity separation of z_{em} as a function of the corresponding CIV column density, N_{CIV}. Left panels: NV doublets are selected with $0 < v_{abs} < 10,000\ \mathrm{km\,s^{-1}}$. Right panels: NV doublets are selected with $10,000 < v_{abs} < 20,000\ \mathrm{km\,s^{-1}}$. Upper panels: all the column densities; middle panels: N_{CIV} larger or equal to 13.5; lower panels: N_{CIV} less than 13.5.

components is visible within 10,000 km s^{-1} of the z_{em} and only when $N_{\rm CIV}$ larger or equal to 13.5 are considered (left middle panel). Moving further from the z_{em}, it is evident that there is not any clear absorption feature in the NV stacked spectra independently from the $N_{\rm CIV}$ considered (right side panels of Fig. 4.9).

As mentioned at the beginning of the current section, all the results presented are very preliminary. Several checks of the followed procedure have been done. Uncertainties on the observed stack will be estimated through the bootstrap resampling technique. In addition, I will build a control sample to validate the robustness of the obtained results.

The control sample will be constructed as follows. For each NV region to be stacked in my sample:

(1) I choose a region of the same extent (1000 km s^{-1}) in the spectrum of a quasar of the XQ-100 survey with a S/N as similar as possible to the original one.

(2) The new region has to be at the same redshift of the one in the principal sample.

(3) The region around (1000 km s^{-1}) the expected position, in the new spectrum, of the corresponding CIV doublet has to be free from CIV absorptions.

(4) The barycenter of the new region has to be almost at the same velocity separation, from its own z_{em}, of the original one ($\pm$500 km s^{-1}). In this way, I am sure that I am investigating areas with a similar influence of the quasar.

Although the S/N in XQ-100 is quite homogeneous, the most luminous quasars have slightly larger S/N spectra (see Fig. 3.6). To be sure that the S/N has not effects in building the control sample, I will create a second one with another procedure. Per each NV region to be stacked in my sample:

(1) I choose two regions of 1000 km s^{-1} in the same spectrum, on the left and right side of the original one.

(2) The regions around (1000 km s^{-1}) the expected positions of the corresponding CIV doublets have to be free from CIV absorptions.

I expect that the stacked spectra from the control samples will not show trace of any coherent absorption in both the line profile of the two NV doublet components, independently from the velocity separation from the z_{em} and the $N_{\rm CIV}$ considered. This result would confirm that the NV is an excellent tracer of the intrinsic systems, and it can be used to construct large catalogs of intrinsic NALs also when high resolution and/or high S/N data are not available, in agreement with what suggested by Ganguly et al. (2013).

Chapter 5

5 Summary and Future Perspectives

A key problem in galaxy formation and evolution is understanding how active galactic nuclei (AGN) interact with their host galaxies.

In the last decade, the potential impact of galaxy-scale outflows driven by quasars on their environment has become widely recognized. (e.g., Blandford and Begelman, 2004; Scannapieco and Oh, 2004; Vernaleo and Reynolds, 2006; Kormendy and Ho, 2013). These outflows provide a mechanism that can possibly regulate and quench star formation activity in the host galaxy by blowing away the gas that feeds star formation and black hole growth.

Theoretical studies and simulations show that this so-called AGN *feedback* can provide an explanation for a variety of observations, e.g., the chemical enrichment of the intergalactic medium (IGM), the self-regulation of the growth of the supermassive black hole (SMBH) and of the galactic bulge, the steep slope of the high end of the stellar mass function, the existence of the red sequence of massive passive galaxies (e.g., Silk and Rees, 1998; Granato et al., 2004; Di Matteo et al., 2005; Elvis, 2006; Hopkins and Elvis, 2010).

Observationally, quasar outflows are detected as absorption troughs in quasar spectra that are blueshifted with respect to the systemic redshift of their emission-line counterparts. The absorption features are mainly associated with UV resonance lines of various ionic species (e.g., Mg II $\lambda\lambda$ 2796.35, 2803.53; C IV $\lambda\lambda$ 1548.20, 1550.77; SiIV $\lambda\lambda$ 1393.75, 1402.77; and NV $\lambda\lambda$ 1238.82, 1242.80). Narrow absorption lines (NALs) with velocity widths less than 500 km s^{-1}, broad absorption lines (BALs), with velocity widths greater than a few thousand km s^{-1} and mini-BALs, defined as intermediate between NALs and BALs, are examples of these potential outflow signatures.

A major challenge is to understand how NALs, BALs, and mini-BALs fit together into an single paradigm of quasar outflows.

Quantifying the impact of quasar outflows on the surrounding host galaxy, requires estimating their kinetic luminosity, mass-flow rate as well as their frequency of oc-

currence. With the aim to constrain the frequency with which outflows are observed, we must carefully select absorption-line systems that truly sample outflowing gas.

In this thesis I have addressed this problem exploiting the spectra of 100 quasars at emission redshift $z_{em} = 3.5 - 4.5$ to construct a large, relatively unbiased, sample of NAL systems and statistically study their physical properties. The observations have been carried out with VLT/X-shooter in the context of the XQ-100 Legacy Survey (Lopez et al., 2016). The combination of high S/N, large wavelength coverage and intermediate resolution makes XQ-100 a unique dataset to study NALs of high-z quasars in a single, homogeneous and statistically significant sample. Inspecting the whole dataset I have identified almost one thousand CIV systems, covering the redshift range $2.55 < z < 4.73$. Furthermore, the quality and wavelength extent of these spectra allow me to look for other common ions (NV, SiIV and CII) at the same redshifts of the detected CIV absorbers. Contamination by the Ly-α forest prevents me from exploring the same velocity range for all the ions. In particular, these data allow me to look for NV only within 5500 km s^{-1} of z_{em}. The final sample contains 986 CIV, 236 SiIV, 46 NV and 28 CII$_{1334}$ NAL detections. My primary results are as follows.

(1) The CIV sample exhibits a statistically significant excess ($\sim 8\sigma$) within 10,000 km s^{-1} of z_{em} with respect to the random occurrence of NALs, which is particularly evident for lines with $W_0 < 0.2$ Å. The excess is expected, but extends to larger velocities than the standard 5000 km s^{-1} velocity cut-off usually adopted to identify associated system. The observed excess in the offset velocity distribution is not an effect of the NAL redshift evolution, but is likely due to quasar environment. This excess is detected with a larger significance with respect to previous results and it does not show a significant dependence from the quasar bolometric luminosity. Therefore, I suggest to modify the traditional definition of associated systems when also weak absorbers ($W_0 < 0.2$ Å) are considered, extending to 10,000 km s^{-1} the velocity cut-off mostly adopted in the literature.

(2) The CIV covering fraction, defined as the ratio between the number of quasars exhibiting at least one absorber with $W_0 > 0.2$ Å and the total number of quasars within a given velocity offset of z_{em}, has the same value for $v_{abs} < 5000$ km s^{-1} and $v_{abs} < 10,000$ km s^{-1} of z_{em}. Furthermore, I confirm that each quasar showing an absorber with $5000\ km\ s^{-1} < v_{abs} < 10,000$ km s^{-1} has always at least an absorber with $v_{abs} < 5000$ km s^{-1}, while the opposite is not always true. This indicates the presence of a complex velocity structure, increasing the probability that these absorbers are part of outflows.

(3) Out of the ions studied in this work, NV is the ion that best traces the

effects of the quasar ionization field, offering an excellent statistical tool for identifying intrinsic systems. Based thereon, I compute the fraction of quasar hosting at least one intrinsic absorption system using the detection of NV corresponding to CIV absorptions in our sample to be 33 percent. This fraction is consistent with previous determinations based on other techniques (e.g., Misawa et al., 2007; Ganguly et al., 2013).

(4) Most of the NV lines in my sample have properties compatible with those of the intrinsic ones (see section § 4.1): 85 percent of the NV absorbers have column densities larger than $log\, N_{1238} > 13.5$ and 55 percent have values larger than $log\, N_{1238} > 14$. In addition, 68 percent of the NV systems have column densities larger than the associated CIV. If I consider the subsample of NV with $N_{1238}/N_{1548} > 1$ the fraction of quasars with at least one intrinsic absorption-line becomes 26 percent. Alternatively, if I consider only systems with $log\, N_{1238} > 13.5$ and $log\, N_{1238} > 14$ I get values of the order of 30 and 19 percent, respectively.

(5) Considering the radio properties of my sample the results of this work are in general agreement with those by Vestergaard (2003), although the latter sample has approximately an equal number of RLQs and RQQs, while our sample is almost entirely composed of RQQs. Taking into account the Vestergaard (2003) findings, I predict the number of CIV NAL with $W_{1548} > 1.5$ Å to be 2. I do find exactly 2 absorbers. The number of quasars showing CIV NALs in this work ($\sim$ 72 percent) is comparable to the frequency ($>$ 60 percent) observed by Vestergaard (2003). Finally, considering only NALs with $W_{1548} > 0.5$ Å we find exactly the same percentage (25 percent) of quasars with at least one associated CIV absorber within $v_{abs} < 5000$ km s^{-1} of z_{em} as does Vestergaard (2003).

(6) I verify the absence of cool gas (in particular CII) and the presence of highly ionized gas (traced by NV) along the line of sight associated to the quasar host galaxy, in contrast with what is observed in the transverse direction (see Prochaska et al., 2014 and section § 4.2 of this current work). This result suggest a scenario where the ionizing emission of the quasar is anisotropic (as predicted by AGN unification models).

The results of the analysis carried out on the XQ-100 sample (Perrotta et al., 2016) show strong evidence that NV is the byproduct of the quasar ionizing radiation acting along the line of sight. Therefore, it seems reasonable to use the presence of NV related to CIV absorbers to select the best outflow/intrinsic candidate NALs. This is extremely helpful when high resolution and/or high S/N data are not available. These results, therefore, inspired several lines of future inquiry.

First of all, I started verifying the robustness of this criterium to identify intrinsic systems. To do that, I performed a stack analysis of NV absorbers in the Lyα forest, selected thanks to the large sample of CIV NALs identified investigating the XQ-100 spectra. This technique allows me to look for NV signal at large velocity separation from the z_{em}. Preliminary results of the stack analysis are available and they seem to verify the absence of NV signal far from the sphere of influence of the quasar radiation field. This result confirms the goodness of using the detection of NV as an additional criterium to select intrinsic systems. Further investigations are needed to validate my results. First of all, I will build a control sample to verify the reliability and the significance of the NV signal I found in the real sample.

5.1 Future Work

The XQ-100 Legacy Survey is a unique dataset to study NALs in the spectra of quasars at high redshift. From the analysis of these spectra I identified a large sample of NAL absorptions. Then, I took advantage of this catalogue of lines to carefully select targets with the best outflow candidate NALs and start an observational program to study their metallicity.

Measurements based on BELs show that near-quasar environments tend to be metal rich, from solar to a few times solar (Dietrich et al., 2003; Nagao et al., 2006). Interestingly, these studies reveal a lack of metallicity evolution with redshift (Pentericci et al., 2002; Juarez et al., 2009) out to $z \sim 6.4$ (Maiolino, 2009).

Investigations of AALs in low-redshift samples have found solar or super-solar metallicities as well (Hamann and Ferland, 1999; Ganguly et al., 2003; Gabel et al., 2006). In particular, D'Odorico et al. (2004) determined C, N and α-element relative abundances in the gas traced by six AALs at an average redshift $< z > \sim 2.4$. They found that five systems have a metallicity (measured by C/H) consistent or above the solar value. A possible correlation of [N/C] and anticorrelation of [Si/C] with [C/H] was also detected with supersolar values of [Si/C]. This suggests a rapid enrichment caused by a short star formation burst, of duration ~ 1 Gyr. The observational results were successfully compared with the predictions based on a model for the co-evolution of quasar and host galaxy systems run in a cosmological context (Romano et al., 2002; Granato et al., 2004). A fundamental prediction of those semi-analytical models, supported by BELs observations, is that chemical abundances in AGN galaxies remain essentially the same at larger redshift. In Fig. 5.1, I show the predicted [Si/C] – [C/H] and [N/C] – [C/H] abundance distributions for a sample of galaxies hosting an active quasar in the redshift range

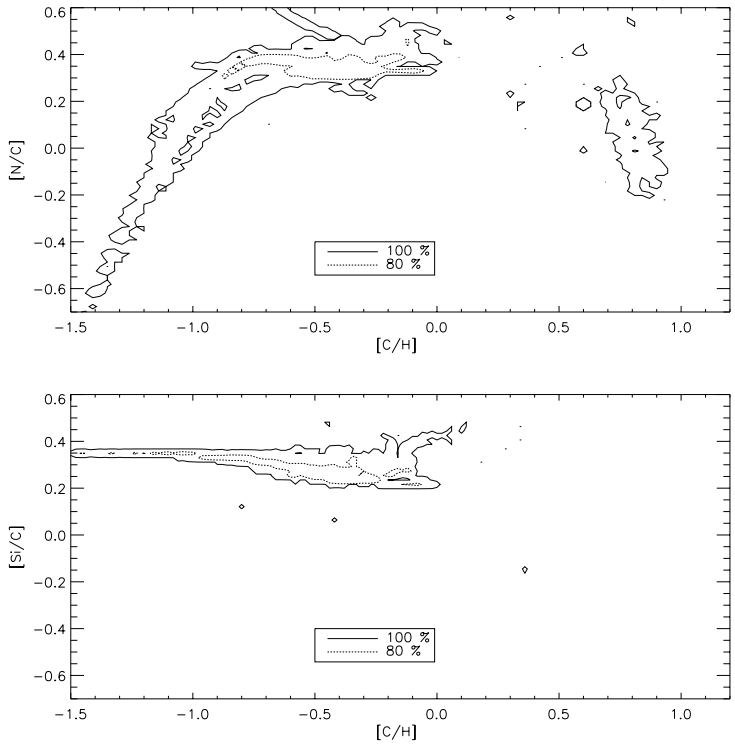

Figure 5.1: Predicted [N/C] − [C/H] and [Si/C] − [C/H] abundance distributions, computed as follows: from the catalogue of Calura and Menci (2009), I have selected all the galaxies hosting an active quasar in the redshift range $> z > 3.5$, and for these systems I have computed the evolution of their chemical abundance pattern starting from their star formation histories, as described in Romano and Starkenburg (2013). In each panel, the solid and dotted contour lines represent the regions where 100% and 80% of our predictions lie, respectively.

$4.5 > z > 3.5$ selected from the catalogue of Calura and Menci (2009), for which Calura and Romano have computed the evolution of their chemical abundance pattern starting from their star formation histories, as described in Romano and Starkenburg (2013).

Observationally the existing sample of high redshift AALs is very small. Only one line of sight with five AALs at $z \sim 4$ has been analyzed (Savaglio et al., 1997), suggesting average abundances of [C/H] ~ -0.5. This value is about one order of magnitude higher than that found in intervening systems at about the same redshift, although slightly lower than what found for the bulk of the sample at $z \sim 2 - 2.5$. Thus, in order to draw statistically significant conclusions it is crucial to enlarge the sample of high redshift AALs. The need of increasing the sample of AALs at $z \sim 4$ is also driven by the wide range of properties and physical origins of those systems shown by previous works.

To carry out a comprehensive study of quasar AALs, I needed higher resolution data. Therefore, with the main aim of investigating the redshift evolution of chemical abundances in quasar host galaxies, I proposed and obtained high resolution, high signal-to-noise ratio UVES spectra of 2 quasars at $z_{em} \sim 3.5-4$. Two more objects are already available in the UVES archive, and the presence of AALs in these two quasars has been pointed out by my analysis of the XQ-100 spectra.

I have had the unique opportunity to carefully select my AAL targets at $z \sim 3.5-4$ from the XQ-100 survey. I selected the best lines of sight based on the following criteria:

(1) They have AALs that are clear candidates to be outflow/intrinsic in nature, according to the characteristics listed in section § 2.2.2, but especially the presence of NV NAL absorption. Indeed, I have identified NV as the ion that best traces the effects of the quasar ionization field, offering the cleanest approach to statistically identify intrinsic systems (Perrotta et al., 2016).

(2) The AALs show at least two ionization stages of the same element: e.g. CIV and CIII and/or NV and NIII, this characteristic is fundamental to constrain the Cloudy (Ferland et al., 2013) photoionization models and get reliable results for the metallicity and the element relative abundances.

(3) The HI content of the AALs can be reliably measured from the Lyman-α line plus at least another line of the Lyman series.

The results of this pilot analysis, based on 4 targets, will be helpful to obtain additional observing time in the next periods.

High resolution UVES spectra are fundamental for this kind of study because I will better resolve the narrow metal absorption lines. This is essential to derive accurate column densities of the observed ionic species and therefore to constrain the photoionization models; to be more sensitive to weak lines (e.g., CII* 1335); to confirm the hints of partial coverage which represents an essential clue to the intrinsic nature of AALs; to dig into the Lyα forest and deblend metal lines in that region.

Moreover, I will compare the UVES spectra to the existing XQ-100 data, looking for time-variable line strengths as a test to identify intrinsic systems.

The column densities derived by fitting the detected transitions with Voigt profiles will be compared with the predictions of state-of-the-art semi-analytical models (e.g., Fig. 5.1) and with metallicities derived from BELs. This sample, in addition to the ones at lower redshift, will allow to better characterize the physical conditions in the quasar environment and put stronger constraints to the model predictions. Indeed,

the results of this project, will improve our understanding of the evolutionary status of the host galaxies (the extent of prior star formation) during the stage when a central quasar is active and possibly participating in a blowout.

A

Appendix A

XQ-100 NAL Catalogue

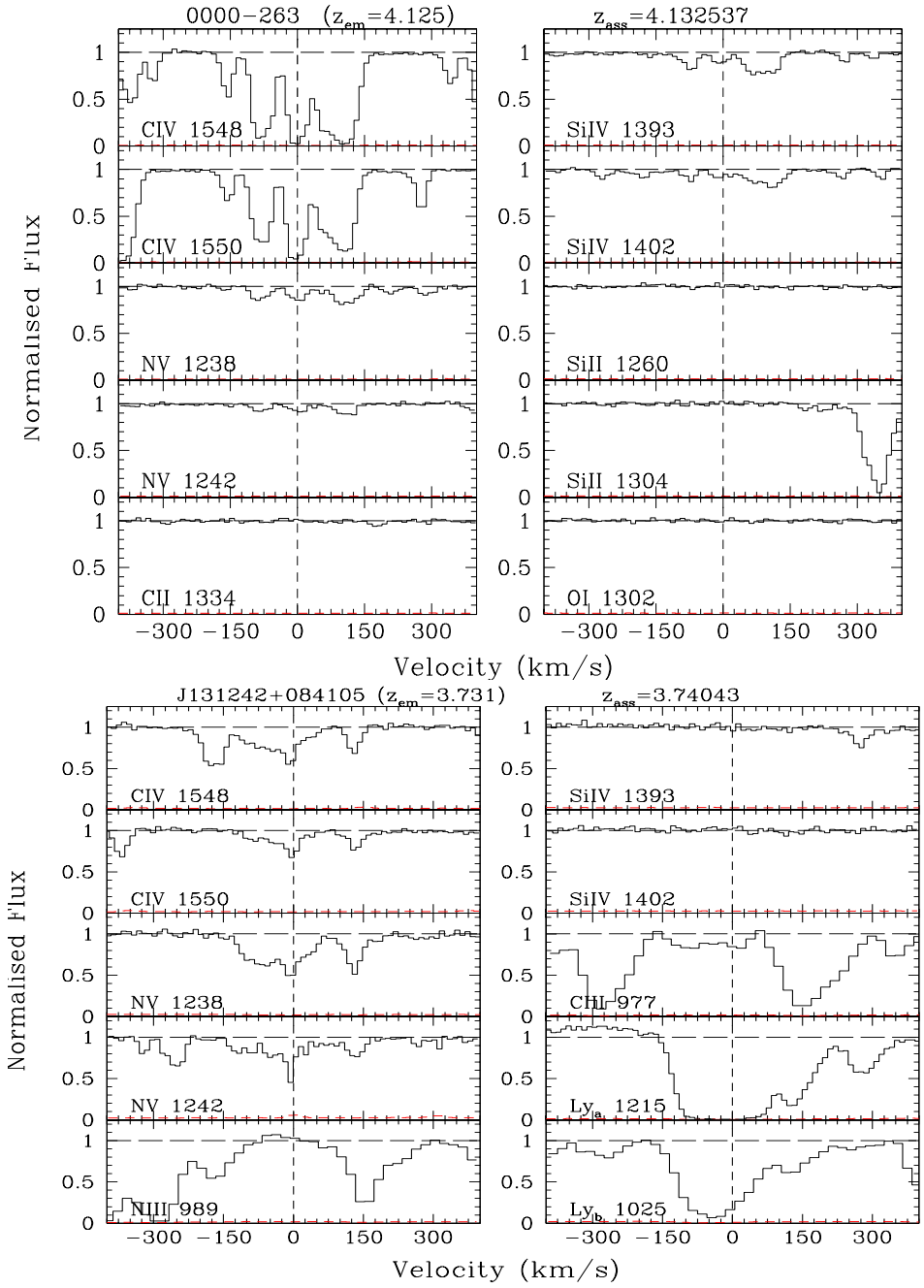

Figure A.1: Some examples of the identified absorbers.

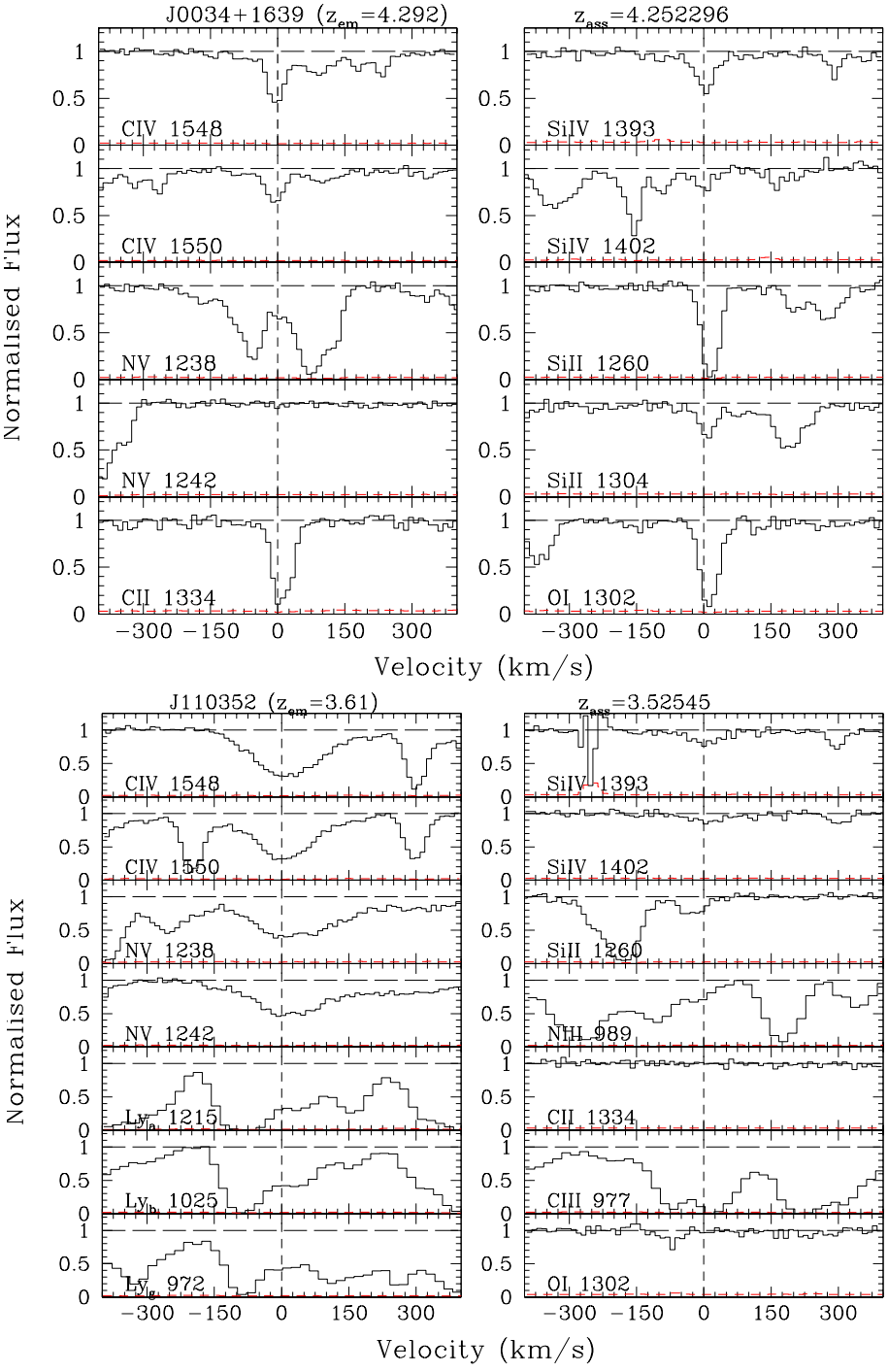

Figure A.2: Some examples of the identified absorbers.

Table A.1: XQ-100 Narrow Absorption Line catalogue.

Quasar	z_{em}	L_{bol}	σL_{bol}	Radio type	z_{abs}	N CIV	σ N CIV	W CIV	σ W CIV	N SiIV	σ N SiIV	W SiIV	σ W SiIV	N NV	σ N NV	W NV	σW NV	N CII	σ N CII	W CII	σW CII
(1)	(2)	(3)	(4)	(5)	(6)	(7)	(8)	(9)	(10)	(11)	(12)	(13)	(14)	(15)	(16)	(17)	(18)	(19)	(20)	(21)	(22)
J1013+0650	3.808	46.100	0.014	RL	2.911	13.92	0.04	0.278	0.007	0.00	0.00	0.000	0.000	0.00	0.00	0.000	0.000	0.00	0.00	0.000	0.000
J1013+0650	3.808	46.100	0.014	RL	2.944	13.39	0.05	0.091	0.006	0.00	0.00	0.000	0.000	0.00	0.00	0.000	0.000	0.00	0.00	0.000	0.000
J1013+0650	3.808	46.100	0.014	RL	3.081	13.48	0.05	0.098	0.005	0.00	0.00	0.000	0.000	0.00	0.00	0.000	0.000	0.00	0.00	0.000	0.000
J1013+0650	3.808	46.100	0.014	RL	3.236	14.14	0.06	0.428	0.005	13.56	0.04	0.266	0.005	0.00	0.00	0.000	0.000	0.00	0.00	0.000	0.000
J1013+0650	3.808	46.100	0.014	RL	3.283	13.95	0.04	0.318	0.006	12.69	0.03	0.046	0.005	0.00	0.00	0.000	0.000	0.00	0.00	0.000	0.000
J1013+0650	3.808	46.100	0.014	RL	3.489	13.71	0.06	0.172	0.007	13.51	0.06	0.233	0.006	0.00	0.00	0.000	0.000	0.00	0.00	0.000	0.000
J1013+0650	3.808	46.100	0.014	RL	3.322	14.57	0.06	0.567	0.004	0.00	0.00	0.686	0.008	0.00	0.00	0.000	0.000	0.00	0.00	0.000	0.000
J1013+0650	3.808	46.100	0.014	RL	3.685	13.93	0.07	0.250	0.005	13.11	0.04	0.105	0.006	0.00	0.00	0.000	0.000	0.00	0.00	0.000	0.000
J1013+0650	3.808	46.100	0.014	RL	3.727	13.68	0.04	0.172	0.008	0.00	0.00	0.000	0.000	14.22	0.04	0.300	0.005	0.00	0.00	0.000	0.000
J1018+0548	3.515	46.686	0.013	not	2.718	14.10	0.03	0.277	0.006	0.00	0.00	0.000	0.000	0.00	0.00	0.000	0.000	0.00	0.00	0.000	0.000
J1018+0548	3.515	46.686	0.013	not	2.778	13.44	0.04	0.099	0.005	0.00	0.00	0.000	0.000	0.00	0.00	0.000	0.000	0.00	0.00	0.000	0.000
J1018+0548	3.515	46.686	0.013	not	2.831	13.81	0.07	0.225	0.008	0.00	0.00	0.000	0.000	0.00	0.00	0.000	0.000	0.00	0.00	0.000	0.000
J1018+0548	3.515	46.686	0.013	not	3.005	13.49	0.05	0.117	0.005	0.00	0.00	0.000	0.000	0.00	0.00	0.000	0.000	0.00	0.00	0.000	0.000
J1018+0548	3.515	46.686	0.013	not	3.147	13.44	0.07	0.093	0.004	12.47	0.05	0.029	0.004	0.00	0.00	0.000	0.000	0.00	0.00	0.000	0.000
J1018+0548	3.515	46.686	0.013	not	3.225	13.15	0.08	0.041	0.005	0.00	0.00	0.000	0.000	0.00	0.00	0.000	0.000	0.00	0.00	0.000	0.000
J1018+0548	3.515	46.686	0.013	not	3.230	13.09	0.04	0.047	0.004	0.00	0.00	0.000	0.000	0.00	0.00	0.000	0.000	0.00	0.00	0.000	0.000
J1018+0548	3.515	46.686	0.013	not	3.274	13.47	0.11	0.110	0.006	0.00	0.00	0.000	0.000	0.00	0.00	0.000	0.000	0.00	0.00	0.000	0.000
J1018+0548	3.515	46.686	0.013	not	3.344	13.47	0.05	0.109	0.006	0.00	0.00	0.000	0.000	0.00	0.00	0.000	0.000	0.00	0.00	0.000	0.000
J1018+0548	3.515	46.686	0.013	not	3.386	13.98	0.06	0.329	0.005	13.52	0.04	0.253	0.009	0.00	0.00	0.000	0.000	14.00	0.06	0.160	0.005
J1018+0548	3.515	46.686	0.013	not	3.396	13.60	0.07	0.137	0.005	12.61	0.05	0.033	0.004	0.00	0.00	0.000	0.000	0.00	0.00	0.000	0.000
J1018+0548	3.515	46.686	0.013	not	3.416	13.46	0.04	0.107	0.006	0.00	0.00	0.000	0.000	0.00	0.00	0.000	0.000	13.22	0.05	0.031	0.004
J1018+0548	3.515	46.686	0.013	not	3.490	13.94	0.04	0.322	0.007	0.00	0.00	0.000	0.000	14.21	0.05	0.305	0.014	0.00	0.00	0.000	0.000
J1018+0548	3.515	46.686	0.013	not	3.508	13.85	0.07	0.179	0.002	12.89	0.06	0.061	0.004	13.87	0.04	0.120	0.005	0.00	0.00	0.000	0.000
J1018+0548	3.515	46.686	0.013	not	3.523	14.87	0.06	0.812	0.004	12.75	0.04	0.048	0.004	14.72	0.03	0.377	0.006	0.00	0.00	0.000	0.000
J1018+0548	3.515	46.686	0.013	not	3.518	13.35	0.03	0.075	0.002	0.00	0.00	0.000	0.000	13.29	0.06	0.038	0.004	0.00	0.00	0.000	0.000
J1020+0922	3.640	46.699	0.019	RQ	2.749	13.22	0.05	0.064	0.008	0.00	0.00	0.000	0.000	0.00	0.00	0.000	0.000	0.00	0.00	0.000	0.000
J1020+0922	3.640	46.699	0.019	RQ	2.779	14.15	0.04	0.295	0.008	0.00	0.00	0.000	0.000	0.00	0.00	0.000	0.000	0.00	0.00	0.000	0.000
J1020+0922	3.640	46.699	0.019	RQ	2.874	13.80	0.03	0.202	0.010	0.00	0.00	0.000	0.000	0.00	0.00	0.000	0.000	0.00	0.00	0.000	0.000
J1020+0922	3.640	46.699	0.019	RQ	2.997	13.65	0.03	0.159	0.010	0.00	0.00	0.000	0.000	0.00	0.00	0.000	0.000	0.00	0.00	0.000	0.000
J1020+0922	3.640	46.699	0.019	RQ	3.110	13.43	0.03	0.100	0.007	0.00	0.00	0.000	0.000	0.00	0.00	0.000	0.000	0.00	0.00	0.000	0.000
J1020+0922	3.640	46.699	0.019	RQ	3.316	13.34	0.04	0.076	0.006	0.00	0.00	0.000	0.000	0.00	0.00	0.000	0.000	0.00	0.00	0.000	0.000
J1020+0922	3.640	46.699	0.019	RQ	3.366	13.23	0.05	0.057	0.006	0.00	0.00	0.000	0.000	0.00	0.00	0.000	0.000	0.00	0.00	0.000	0.000
J1020+0922	3.640	46.699	0.019	RQ	3.376	13.46	0.04	0.104	0.008	0.00	0.00	0.000	0.000	0.00	0.00	0.000	0.000	0.00	0.00	0.000	0.000
J1020+0922	3.640	46.699	0.019	RQ	3.405	13.32	0.05	0.074	0.007	0.00	0.00	0.000	0.000	0.00	0.00	0.000	0.000	0.00	0.00	0.000	0.000
J1020+0922	3.640	46.699	0.019	RQ	3.479	14.25	0.06	0.570	0.012	13.33	0.05	0.169	0.010	0.00	0.00	0.000	0.000	13.62	0.04	0.073	0.007
J1020+0922	3.640	46.699	0.019	RQ	3.588	13.72	0.05	0.097	0.007	0.00	0.00	0.000	0.000	0.00	0.00	0.000	0.000	0.00	0.00	0.000	0.000

Note: 1) Name of the targets; 2) Emission redshift of the targets; 3) Log bolometric luminosity of the targets; 4) Log bolometric luminosity error; 5) Radio type; 6) Redshift of the NAL absorbers; 7) Log CIV 1548 column density; 8) Log CIV 1548 column density error; 8) CIV 1548 rest-frame equivalent width Å; 10) CIV 1548 rest-frame equivalent width error Å, computed integrating the error-spectrum over the interval defining the line; 11) Log SiIV 1393 column density; 12) Log SiIV 1393 column density error; 13) SiIV 1393 rest-frame equivalent width Å; 14) SiIV 1393 rest-frame equivalent width error Å; 15) Log NV 1238 column density; 16) Log NV 1238 column density error; 17) NV 1238 rest-frame equivalent width Å; 18) NV 1238 rest-frame equivalent width error Å; 19) Log CII 1334 column density; 20) Log CII 1334 column density error; 21) CII 1334 rest-frame equivalent width Å; 22) CII 1334 rest-frame equivalent width error Å.

Tab. A.1 — Continued.

Quasar	z_{em}	L_{bol}	σL_{bol}	Radio type	z_{abs}	N CIV	σ N CIV	W CIV	σ W CIV	N SiIV	σ N SiIV	W SiIV	σ W SiIV	N NV	σ N NV	W NV	σW NV	N CII	σ N CII	W CII	σW CII
(1)	(2)	(3)	(4)	(5)	(6)	(7)	(8)	(9)	(10)	(11)	(12)	(13)	(14)	(15)	(16)	(17)	(18)	(19)	(20)	(21)	(22)
J1024+1819	3.524	46.824	0.015	RQ	2.843	13.55	0.03	0.100	0.009	0.00	0.00	0.000	0.000	0.00	0.00	0.000	0.000	0.00	0.00	0.000	0.000
J1024+1819	3.524	46.824	0.015	RQ	3.159	13.90	0.06	0.248	0.009	13.33	0.04	0.154	0.010	0.00	0.00	0.000	0.000	0.00	0.00	0.000	0.000
J1024+1819	3.524	46.824	0.015	RQ	3.183	13.79	0.06	0.184	0.007	0.00	0.00	0.000	0.000	0.00	0.00	0.000	0.000	0.00	0.00	0.000	0.000
J1024+1819	3.524	46.824	0.015	RQ	3.189	14.12	0.05	0.367	0.008	13.47	0.05	0.229	0.010	0.00	0.00	0.000	0.000	0.00	0.00	0.000	0.000
J1024+1819	3.524	46.824	0.015	RQ	3.358	13.69	0.04	0.140	0.008	0.00	0.00	0.000	0.000	0.00	0.00	0.000	0.000	0.00	0.00	0.000	0.000
J1024+1819	3.524	46.824	0.015	RQ	3.497	13.34	0.07	0.074	0.004	0.00	0.00	0.000	0.000	0.00	0.00	0.000	0.000	0.00	0.00	0.000	0.000
J1024+1819	3.524	46.824	0.015	RQ	3.404	13.33	0.12	0.066	0.004	12.68	0.06	0.038	0.006	0.00	0.00	0.000	0.000	13.72	0.05	0.079	0.006
J1032+0927	3.985	46.900	0.014	RQ	2.968	13.45	0.09	0.109	0.007	0.00	0.00	0.000	0.000	0.00	0.00	0.000	0.000	0.00	0.00	0.000	0.000
J1032+0927	3.985	46.900	0.014	RQ	3.077	13.70	0.07	0.170	0.007	0.00	0.00	0.000	0.000	0.00	0.00	0.000	0.000	0.00	0.00	0.000	0.000
J1032+0927	3.985	46.900	0.014	RQ	3.272	13.65	0.04	0.163	0.008	0.00	0.00	0.000	0.000	0.00	0.00	0.000	0.000	0.00	0.00	0.000	0.000
J1032+0927	3.985	46.900	0.014	RQ	3.325	13.30	0.07	0.075	0.006	0.00	0.00	0.000	0.000	0.00	0.00	0.000	0.000	0.00	0.00	0.000	0.000
J1032+0927	3.985	46.900	0.014	RQ	3.354	13.51	0.06	0.120	0.007	0.00	0.00	0.000	0.000	0.00	0.00	0.000	0.000	0.00	0.00	0.000	0.000
J1032+0927	3.985	46.900	0.014	RQ	3.804	13.75	0.05	0.102	0.006	13.05	0.05	0.092	0.007	0.00	0.00	0.000	0.000	0.00	0.00	0.000	0.000
J1032+0927	3.985	46.900	0.014	RQ	3.812	14.70	0.05	0.772	0.010	0.00	0.00	0.000	0.000	0.00	0.00	0.000	0.000	0.00	0.00	0.000	0.000
J1032+0927	3.985	46.900	0.014	RQ	3.879	13.93	0.04	0.315	0.009	12.84	0.03	0.058	0.006	0.00	0.00	0.000	0.000	0.00	0.00	0.000	0.000
J1036-0343	4.531	46.893	0.011	RQ	3.705	13.48	0.04	0.145	0.003	0.00	0.00	0.000	0.000	0.00	0.00	0.000	0.000	0.00	0.00	0.000	0.000
J1036-0343	4.531	46.893	0.011	RQ	3.670	13.95	0.05	0.377	0.006	0.00	0.00	0.000	0.000	0.00	0.00	0.000	0.000	0.00	0.00	0.000	0.000
J1036-0343	4.531	46.893	0.011	RQ	4.444	13.22	0.05	0.062	0.003	0.00	0.00	0.000	0.000	0.00	0.00	0.000	0.000	0.00	0.00	0.000	0.000
J1036-0343	4.531	46.893	0.011	RQ	4.174	13.52	0.06	0.122	0.006	13.00	0.05	0.082	0.004	0.00	0.00	0.000	0.000	0.00	0.00	0.000	0.000
J1036-0343	4.531	46.893	0.011	RQ	4.021	12.94	0.07	0.035	0.003	0.00	0.00	0.000	0.000	0.00	0.00	0.000	0.000	0.00	0.00	0.000	0.000
J1036-0343	4.531	46.893	0.011	RQ	3.509	13.41	0.03	0.093	0.004	0.00	0.00	0.000	0.000	0.00	0.00	0.000	0.000	0.00	0.00	0.000	0.000
J1036-0343	4.531	46.893	0.011	RQ	4.153	13.38	0.06	0.088	0.003	0.00	0.00	0.000	0.000	0.00	0.00	0.000	0.000	0.00	0.00	0.000	0.000
J1036-0343	4.531	46.893	0.011	RQ	4.234	13.25	0.05	0.066	0.004	13.26	0.04	0.128	0.003	0.00	0.00	0.000	0.000	0.00	0.00	0.000	0.000
J1034+1102	4.269	46.693	0.015	RQ	4.152	14.08	0.04	0.390	0.006	0.00	0.00	0.000	0.000	0.00	0.00	0.000	0.000	0.00	0.00	0.000	0.000
J1034+1102	4.269	46.693	0.015	RQ	3.313	13.08	0.05	0.045	0.004	0.00	0.00	0.000	0.000	0.00	0.00	0.000	0.000	0.00	0.00	0.000	0.000
J1034+1102	4.269	46.693	0.015	RQ	4.278	13.57	0.06	0.118	0.003	0.00	0.00	0.000	0.000	13.87	0.05	0.111	0.004	0.00	0.00	0.000	0.000
J1034+1102	4.269	46.693	0.015	RQ	3.463	13.19	0.04	0.051	0.003	0.00	0.00	0.000	0.000	0.00	0.00	0.000	0.000	0.00	0.00	0.000	0.000
J1034+1102	4.269	46.693	0.015	RQ	3.261	13.55	0.06	0.138	0.006	0.00	0.00	0.000	0.000	0.00	0.00	0.000	0.000	0.00	0.00	0.000	0.000
J1034+1102	4.269	46.693	0.015	RQ	3.376	13.34	0.06	0.083	0.005	0.00	0.00	0.000	0.000	0.00	0.00	0.000	0.000	0.00	0.00	0.000	0.000
J1034+1102	4.269	46.693	0.015	RQ	3.730	13.42	0.07	0.095	0.004	0.00	0.00	0.000	0.000	0.00	0.00	0.000	0.000	0.00	0.00	0.000	0.000
J1037+0704	4.127	46.948	0.009	RQ	3.137	13.94	0.04	0.290	0.005	0.00	0.00	0.000	0.000	0.00	0.00	0.000	0.000	0.00	0.00	0.000	0.000
J1037+0704	4.127	46.948	0.009	RQ	3.282	13.68	0.07	0.170	0.005	0.00	0.00	0.000	0.000	0.00	0.00	0.000	0.000	0.00	0.00	0.000	0.000
J1037+0704	4.127	46.948	0.009	RQ	3.338	13.55	0.06	0.131	0.005	0.00	0.00	0.000	0.000	0.00	0.00	0.000	0.000	0.00	0.00	0.000	0.000
J1037+0704	4.127	46.948	0.009	RQ	3.515	13.07	0.04	0.045	0.004	0.00	0.00	0.000	0.000	0.00	0.00	0.000	0.000	0.00	0.00	0.000	0.000
J1037+0704	4.127	46.948	0.009	RQ	3.529	14.44	0.04	0.618	0.005	13.77	0.05	0.392	0.005	0.00	0.00	0.000	0.000	0.00	0.00	0.000	0.000
J1037+0704	4.127	46.948	0.009	RQ	3.617	12.95	0.06	0.034	0.003	0.00	0.00	0.000	0.000	0.00	0.00	0.000	0.000	0.00	0.00	0.000	0.000
J1037+0704	4.127	46.948	0.009	RQ	3.799	13.18	0.07	0.059	0.004	0.00	0.00	0.000	0.000	0.00	0.00	0.000	0.000	0.00	0.00	0.000	0.000
J1037+0704	4.127	46.948	0.009	RQ	3.848	13.28	0.07	0.074	0.004	0.00	0.00	0.000	0.000	0.00	0.00	0.000	0.000	0.00	0.00	0.000	0.000
J1037+0704	4.127	46.948	0.009	RQ	3.893	14.45	0.05	0.835	0.007	14.04	0.03	0.726	0.006	0.00	0.00	0.000	0.000	14.22	0.05	0.299	0.006
J1037+0704	4.127	46.948	0.009	RQ	4.012	13.90	0.06	0.271	0.005	12.93	0.06	0.108	0.003	0.00	0.00	0.000	0.000	0.00	0.00	0.000	0.000
J1037+0704	4.127	46.948	0.009	RQ	4.084	13.89	0.04	0.264	0.005	13.22	0.04	0.072	0.004	0.00	0.00	0.000	0.000	0.00	0.00	0.000	0.000

Tab. A.1 — Continued.

Quasar	z_{em}	L_{bol}	σL_{bol}	Radio type	z_{abs}	N CIV	σ N CIV	W CIV	σ W CIV	N SiIV	σ N SiIV	W SiIV	σ W SiIV	N NV	σ N NV	W NV	σW NV	N CII	σ N CII	W CII	σW CII
(1)	(2)	(3)	(4)	(5)	(6)	(7)	(8)	(9)	(10)	(11)	(12)	(13)	(14)	(15)	(16)	(17)	(18)	(19)	(20)	(21)	(22)
J1037+0704	4.127	46.948	0.009	RQ	4.112	13.80	0.03	0.233	0.006	0.00	0.00	0.000	0.000	13.82	0.05	0.134	0.007	0.00	0.00	0.000	0.000
J1037+2135	3.626	47.020	0.009	RQ	3.559	13.07	0.06	0.045	0.004	0.00	0.00	0.000	0.000	0.00	0.00	0.000	0.000	0.00	0.00	0.000	0.000
J1037+2135	3.626	47.020	0.009	RQ	3.542	13.83	0.05	0.244	0.006	13.35	0.04	0.174	0.005	0.00	0.00	0.000	0.000	0.00	0.00	0.000	0.000
J1037+2135	3.626	47.020	0.009	RQ	2.815	13.25	0.06	0.069	0.004	0.00	0.00	0.000	0.000	0.00	0.00	0.000	0.000	0.00	0.00	0.000	0.000
J1037+2135	3.626	47.020	0.009	RQ	2.935	13.39	0.07	0.089	0.005	0.00	0.00	0.000	0.000	0.00	0.00	0.000	0.000	0.00	0.00	0.000	0.000
J1037+2135	3.626	47.020	0.009	RQ	3.050	13.55	0.07	0.125	0.004	0.00	0.00	0.000	0.000	0.00	0.00	0.000	0.000	0.00	0.00	0.000	0.000
J1037+2135	3.626	47.020	0.009	RQ	3.070	13.53	0.04	0.116	0.010	0.00	0.00	0.000	0.000	0.00	0.00	0.000	0.000	0.00	0.00	0.000	0.000
J1037+2135	3.626	47.020	0.009	RQ	3.209	13.59	0.07	0.141	0.004	12.31	0.04	0.017	0.003	0.00	0.00	0.000	0.000	0.00	0.00	0.000	0.000
J1037+2135	3.626	47.020	0.009	RQ	3.265	13.35	0.08	0.087	0.005	0.00	0.00	0.000	0.000	0.00	0.00	0.000	0.000	0.00	0.00	0.000	0.000
J1037+2135	3.626	47.020	0.009	RQ	3.320	13.27	0.06	0.073	0.005	0.00	0.00	0.000	0.000	0.00	0.00	0.000	0.000	0.00	0.00	0.000	0.000
J1042+1957	3.630	46.700	0.013	RQ	3.514	13.05	0.04	0.045	0.003	12.48	0.05	0.024	0.004	0.00	0.00	0.000	0.000	0.00	0.00	0.000	0.000
J1042+1957	3.630	46.700	0.013	RQ	3.269	14.03	0.07	0.361	0.008	13.02	0.06	0.080	0.005	0.00	0.00	0.000	0.000	0.00	0.00	0.000	0.000
J1042+1957	3.630	46.700	0.013	RQ	3.229	13.87	0.06	0.235	0.006	12.90	0.04	0.064	0.006	0.00	0.00	0.000	0.000	0.00	0.00	0.000	0.000
J1042+1957	3.630	46.700	0.013	RQ	3.596	14.62	0.07	0.624	0.006	12.89	0.05	0.064	0.005	14.44	0.05	0.423	0.005	0.00	0.00	0.000	0.000
J1042+1957	3.630	46.700	0.013	RQ	3.590	13.76	0.04	0.209	0.006	0.00	0.00	0.000	0.000	13.95	0.04	0.171	0.006	0.00	0.00	0.000	0.000
J1042+1957	3.630	46.700	0.013	RQ	2.751	14.14	0.06	0.358	0.006	0.00	0.00	0.000	0.000	0.00	0.00	0.000	0.000	0.00	0.00	0.000	0.000
J1042+1957	3.630	46.700	0.013	RQ	2.819	13.45	0.07	0.101	0.007	0.00	0.00	0.000	0.000	0.00	0.00	0.000	0.000	0.00	0.00	0.000	0.000
J1042+1957	3.630	46.700	0.013	RQ	2.842	13.97	0.07	0.176	0.006	0.00	0.00	0.000	0.000	0.00	0.00	0.000	0.000	0.00	0.00	0.000	0.000
J1042+1957	3.630	46.700	0.013	RQ	2.950	13.60	0.12	0.132	0.007	0.00	0.00	0.000	0.000	0.00	0.00	0.000	0.000	0.00	0.00	0.000	0.000
J1042+1957	3.630	46.700	0.013	RQ	2.973	13.43	0.11	0.100	0.007	0.00	0.00	0.000	0.000	0.00	0.00	0.000	0.000	0.00	0.00	0.000	0.000
J1042+1957	3.630	46.700	0.013	RQ	2.990	13.53	0.10	0.122	0.007	0.00	0.00	0.000	0.000	0.00	0.00	0.000	0.000	0.00	0.00	0.000	0.000
J1042+1957	3.630	46.700	0.013	RQ	3.099	13.19	0.04	0.058	0.004	0.00	0.00	0.000	0.000	0.00	0.00	0.000	0.000	0.00	0.00	0.000	0.000
J1042+1957	3.630	46.700	0.013	RQ	3.134	13.50	0.12	0.112	0.005	0.00	0.00	0.000	0.000	0.00	0.00	0.000	0.000	0.00	0.00	0.000	0.000
J1042+1957	3.630	46.700	0.013	RQ	3.225	14.13	0.05	0.405	0.008	12.92	0.06	0.065	0.005	0.00	0.00	0.000	0.000	0.00	0.00	0.000	0.000
J1054+0215	3.971	46.335	0.027	RQ	2.927	13.88	0.06	0.249	0.005	0.00	0.00	0.000	0.000	0.00	0.00	0.000	0.000	0.00	0.00	0.000	0.000
J1054+0215	3.971	46.335	0.027	RQ	2.991	14.32	0.07	0.600	0.012	0.00	0.00	0.000	0.000	0.00	0.00	0.000	0.000	0.00	0.00	0.000	0.000
J1054+0215	3.971	46.335	0.027	RQ	3.263	13.48	0.16	0.114	0.013	0.00	0.00	0.000	0.000	0.00	0.00	0.000	0.000	0.00	0.00	0.000	0.000
J1054+0215	3.971	46.335	0.027	RQ	3.314	13.61	0.05	0.130	0.010	0.00	0.00	0.000	0.000	0.00	0.00	0.000	0.000	0.00	0.00	0.000	0.000
J1054+0215	3.971	46.335	0.027	RQ	3.402	13.99	0.06	0.320	0.010	13.30	0.08	0.161	0.010	0.00	0.00	0.000	0.000	0.00	0.00	0.000	0.000
J1054+0215	3.971	46.335	0.027	RQ	3.721	13.87	0.07	0.241	0.009	0.00	0.00	0.000	0.000	0.00	0.00	0.000	0.000	0.00	0.00	0.000	0.000
J1054+0215	3.971	46.335	0.027	RQ	3.744	13.00	0.07	0.038	0.008	0.00	0.00	0.000	0.000	0.00	0.00	0.000	0.000	0.00	0.00	0.000	0.000
J1054+0215	3.971	46.335	0.027	RQ	3.978	14.53	0.03	0.722	0.006	0.00	0.00	0.000	0.000	13.43	0.06	0.055	0.006	0.00	0.00	0.000	0.000
J1054+0215	3.971	46.335	0.027	RQ	3.836	13.47	0.06	0.098	0.008	12.40	0.05	0.026	0.009	0.00	0.00	0.000	0.000	0.00	0.00	0.000	0.000
J1057+1910	4.128	46.598	0.021	RQ	3.456	13.78	0.05	0.163	0.011	0.00	0.00	0.000	0.000	0.00	0.00	0.000	0.000	0.00	0.00	0.000	0.000
J1057+1910	4.128	46.598	0.021	RQ	3.661	13.76	0.06	0.165	0.009	0.00	0.00	0.000	0.000	0.00	0.00	0.000	0.000	0.00	0.00	0.000	0.000
J1057+1910	4.128	46.598	0.021	RQ	3.465	13.55	0.03	0.123	0.011	0.00	0.00	0.000	0.000	0.00	0.00	0.000	0.000	0.00	0.00	0.000	0.000
J1057+1910	4.128	46.598	0.021	RQ	3.151	13.74	0.06	0.181	0.009	0.00	0.00	0.000	0.000	0.00	0.00	0.000	0.000	0.00	0.00	0.000	0.000
J1057+1910	4.128	46.598	0.021	RQ	3.196	14.19	0.05	0.496	0.012	0.00	0.00	0.000	0.000	0.00	0.00	0.000	0.000	0.00	0.00	0.000	0.000
J1057+1910	4.128	46.598	0.021	RQ	4.008	0.00	0.00	1.115	0.017	14.00	0.08	0.599	0.013	13.65	0.05	0.088	0.005	13.57	0.06	0.068	0.006
J1057+1910	4.128	46.598	0.021	RQ	4.062	13.13	0.05	0.052	0.006	0.00	0.00	0.000	0.000	0.00	0.00	0.000	0.000	0.00	0.00	0.000	0.000
J1057+1910	4.128	46.598	0.021	RQ	4.079	13.16	0.03	0.055	0.009	0.00	0.00	0.000	0.000	0.00	0.00	0.000	0.000	0.00	0.00	0.000	0.000

Tab. A.1 — Continued.

Quasar	z_{em}	L_{bol}	σL_{bol}	Radio type	z_{abs}	N CIV	σ N CIV	W CIV	σ W CIV	N SiIV	σ N SiIV	W SiIV	σ W SiIV	N NV	σ N NV	W NV	σW NV	N CII	σ N CII	W CII	σW CII
(1)	(2)	(3)	(4)	(5)	(6)	(7)	(8)	(9)	(10)	(11)	(12)	(13)	(14)	(15)	(16)	(17)	(18)	(19)	(20)	(21)	(22)
J1057+1910	4.128	46.598	0.021	RQ	3.372	14.42	0.06	0.734	0.014	0.00	0.00	0.000	0.000	0.00	0.00	0.000	0.000	0.00	0.00	0.000	0.000
J1057+1910	4.128	46.598	0.021	RQ	3.798	14.40	0.05	0.575	0.012	13.37	0.06	0.177	0.010	0.00	0.00	0.000	0.000	0.00	0.00	0.000	0.000
J1057+1910	4.128	46.598	0.021	RQ	3.745	13.76	0.03	0.198	0.011	13.43	0.06	0.197	0.011	0.00	0.00	0.000	0.000	0.00	0.00	0.000	0.000
J1058+1245	4.341	46.725	0.018	RQ	3.430	14.43	0.06	0.372	0.007	0.00	0.00	0.000	0.000	0.00	0.00	0.000	0.000	0.00	0.00	0.000	0.000
J1058+1245	4.341	46.725	0.018	RQ	4.230	13.73	0.05	0.261	0.006	0.00	0.00	0.000	0.000	0.00	0.00	0.000	0.000	0.00	0.00	0.000	0.000
J1058+1245	4.341	46.725	0.018	RQ	4.236	13.15	0.06	0.054	0.005	0.00	0.00	0.000	0.000	0.00	0.00	0.000	0.000	0.00	0.00	0.000	0.000
J1058+1245	4.341	46.725	0.018	RQ	3.335	13.87	0.03	0.264	0.009	0.00	0.00	0.000	0.000	0.00	0.00	0.000	0.000	0.00	0.00	0.000	0.000
J1058+1245	4.341	46.725	0.018	RQ	3.602	13.91	0.06	0.299	0.011	0.00	0.00	0.000	0.000	0.00	0.00	0.000	0.000	0.00	0.00	0.000	0.000
J1058+1245	4.341	46.725	0.018	RQ	3.365	13.68	0.04	0.169	0.007	0.00	0.00	0.000	0.000	0.00	0.00	0.000	0.000	0.00	0.00	0.000	0.000
J1058+1245	4.341	46.725	0.018	RQ	3.429	14.44	0.05	0.376	0.007	0.00	0.00	0.000	0.000	0.00	0.00	0.000	0.000	0.00	0.00	0.000	0.000
J1058+1245	4.341	46.725	0.018	RQ	3.583	13.80	0.06	0.210	0.007	0.00	0.00	0.000	0.000	0.00	0.00	0.000	0.000	0.00	0.00	0.000	0.000
J1058+1245	4.341	46.725	0.018	RQ	4.316	0.00	0.00	0.930	0.004	0.00	0.00	0.000	0.000	14.34	0.07	0.000	0.000	0.00	0.00	0.000	0.000
J1103+1004	3.607	46.695	0.012	RQ	3.456	13.79	0.03	0.147	0.005	0.00	0.00	0.000	0.000	0.00	0.00	0.000	0.000	0.00	0.00	0.000	0.000
J1103+1004	3.607	46.695	0.012	RQ	3.387	13.85	0.05	0.252	0.009	0.00	0.00	0.000	0.000	0.00	0.00	0.000	0.000	0.00	0.00	0.000	0.000
J1103+1004	3.607	46.695	0.012	RQ	3.243	13.73	0.06	0.187	0.005	13.13	0.02	0.117	0.010	0.00	0.00	0.000	0.000	0.00	0.00	0.000	0.000
J1103+1004	3.607	46.695	0.012	RQ	3.131	14.60	0.07	0.811	0.008	13.35	0.01	0.175	0.009	0.00	0.00	0.000	0.000	0.00	0.00	0.000	0.000
J1103+1004	3.607	46.695	0.012	RQ	3.017	14.52	0.08	0.387	0.005	0.00	0.00	0.000	0.000	0.00	0.00	0.000	0.000	0.00	0.00	0.000	0.000
J1103+1004	3.607	46.695	0.012	RQ	2.761	13.41	0.10	0.095	0.007	0.00	0.00	0.000	0.000	0.00	0.00	0.000	0.000	0.00	0.00	0.000	0.000
J1103+1004	3.607	46.695	0.012	RQ	3.602	14.48	0.07	0.639	0.003	0.00	0.00	0.000	0.000	14.68	0.05	0.526	0.006	0.00	0.00	0.000	0.000
J1103+1004	3.607	46.695	0.012	RQ	3.547	13.21	0.08	0.059	0.004	0.00	0.00	0.000	0.000	0.00	0.00	0.000	0.000	0.00	0.00	0.000	0.000
J1103+1004	3.607	46.695	0.012	RQ	3.558	14.78	0.06	0.933	0.007	0.00	0.00	0.000	0.000	14.75	0.03	0.852	0.007	0.00	0.00	0.000	0.000
J1103+1004	3.607	46.695	0.012	RQ	3.507	14.10	0.06	0.445	0.008	0.00	0.00	0.000	0.000	0.00	0.00	0.000	0.000	0.00	0.00	0.000	0.000
J1103+1004	3.607	46.695	0.012	RQ	3.527	14.60	0.06	0.982	0.005	13.03	0.05	0.147	0.006	14.95	0.07	0.723	0.008	0.00	0.00	0.000	0.000
J1103+1004	3.607	46.695	0.012	RQ	2.833	13.18	0.03	0.059	0.006	0.00	0.00	0.000	0.000	0.00	0.00	0.000	0.000	0.00	0.00	0.000	0.000
J1110+0244	4.146	47.098	0.011	RQ	3.691	13.72	0.04	0.094	0.005	0.00	0.00	0.000	0.000	0.00	0.00	0.000	0.000	0.00	0.00	0.000	0.000
J1110+0244	4.146	47.098	0.011	RQ	3.442	13.90	0.04	0.161	0.004	0.00	0.00	0.000	0.000	0.00	0.00	0.000	0.000	0.00	0.00	0.000	0.000
J1110+0244	4.146	47.098	0.011	RQ	3.477	13.86	0.07	0.298	0.008	0.00	0.00	0.000	0.000	0.00	0.00	0.000	0.000	0.00	0.00	0.000	0.000
J1110+0244	4.146	47.098	0.011	RQ	4.129	14.07	0.07	0.394	0.005	0.00	0.00	0.000	0.000	0.00	0.00	0.000	0.000	0.00	0.00	0.000	0.000
J1110+0244	4.146	47.098	0.011	RQ	4.109	13.50	0.04	0.115	0.005	0.00	0.00	0.000	0.000	13.07	0.05	0.026	0.003	0.00	0.00	0.000	0.000
J1110+0244	4.146	47.098	0.011	RQ	3.269	14.42	0.05	0.549	0.007	0.00	0.00	0.000	0.000	0.00	0.00	0.000	0.000	0.00	0.00	0.000	0.000
J1110+0244	4.146	47.098	0.011	RQ	3.400	13.53	0.04	0.128	0.007	0.00	0.00	0.000	0.000	0.00	0.00	0.000	0.000	0.00	0.00	0.000	0.000
J1110+0244	4.146	47.098	0.011	RQ	3.736	13.06	0.03	0.044	0.004	0.00	0.00	0.000	0.000	0.00	0.00	0.000	0.000	0.00	0.00	0.000	0.000
J1110+0244	4.146	47.098	0.011	RQ	3.112	13.43	0.05	0.093	0.004	0.00	0.00	0.000	0.000	0.00	0.00	0.000	0.000	0.00	0.00	0.000	0.000
J1110+0244	4.146	47.098	0.011	RQ	3.065	13.68	0.05	0.171	0.004	0.00	0.00	0.000	0.000	0.00	0.00	0.000	0.000	0.00	0.00	0.000	0.000
J1110+0244	4.146	47.098	0.011	RQ	3.826	13.13	0.07	0.052	0.004	0.00	0.00	0.000	0.000	0.00	0.00	0.000	0.000	0.00	0.00	0.000	0.000
J1110+0244	4.146	47.098	0.011	RQ	3.224	13.79	0.06	0.216	0.007	0.00	0.00	0.000	0.000	0.00	0.00	0.000	0.000	0.00	0.00	0.000	0.000
J1110+0244	4.146	47.098	0.011	RQ	3.766	13.15	0.03	0.056	0.004	0.00	0.00	0.000	0.000	0.00	0.00	0.000	0.000	0.00	0.00	0.000	0.000
J1108+1209	3.678	46.285	0.014	RQ	3.486	14.24	0.05	0.301	0.006	0.00	0.00	0.000	0.000	0.00	0.00	0.000	0.000	0.00	0.00	0.000	0.000
J1108+1209	3.678	46.285	0.014	RQ	3.545	14.07	0.06	0.371	0.006	13.70	0.04	0.323	0.007	0.00	0.00	0.000	0.000	0.00	0.00	0.838	0.005
J1108+1209	3.678	46.285	0.014	RQ	3.528	13.70	0.04	0.167	0.006	12.42	0.05	0.023	0.004	0.00	0.00	0.000	0.000	0.00	0.00	0.000	0.000
J1108+1209	3.678	46.285	0.014	RQ	3.425	13.58	0.03	0.130	0.006	0.00	0.00	0.000	0.000	0.00	0.00	0.000	0.000	0.00	0.00	0.000	0.000

Tab. A.1 — Continued.

Quasar	z_{em}	L_{bol}	σL_{bol}	Radio type	z_{abs}	N CIV	σ N CIV	W CIV	σ W CIV	N SiIV	σ N SiIV	W SiIV	σ W SiIV	N NV	σ N NV	W NV	σW NV	N CII	σ N CII	W CII	σW CII
(1)	(2)	(3)	(4)	(5)	(6)	(7)	(8)	(9)	(10)	(11)	(12)	(13)	(14)	(15)	(16)	(17)	(18)	(19)	(20)	(21)	(22)
J1108+1209	3.678	46.285	0.014	RQ	3.616	13.95	0.06	0.313	0.005	13.35	0.06	0.166	0.005	0.00	0.00	0.000	0.000	13.72	0.05	0.100	0.006
J1108+1209	3.678	46.285	0.014	RQ	3.585	13.02	0.06	0.040	0.003	0.00	0.00	0.000	0.000	0.00	0.00	0.000	0.000	0.00	0.00	0.000	0.000
J1108+1209	3.678	46.285	0.014	RQ	3.590	13.54	0.03	0.129	0.005	0.00	0.00	0.000	0.000	0.00	0.00	0.000	0.000	0.00	0.00	0.000	0.000
J1108+1209	3.678	46.285	0.014	RQ	2.736	14.57	0.04	0.799	0.005	0.00	0.00	0.000	0.000	0.00	0.00	0.000	0.000	0.00	0.00	0.000	0.000
J1108+1209	3.678	46.285	0.014	RQ	2.755	13.50	0.05	0.117	0.006	0.00	0.00	0.000	0.000	0.00	0.00	0.000	0.000	0.00	0.00	0.000	0.000
J1108+1209	3.678	46.285	0.014	RQ	2.870	13.24	0.06	0.067	0.007	0.00	0.00	0.000	0.000	0.00	0.00	0.000	0.000	0.00	0.00	0.000	0.000
J1108+1209	3.678	46.285	0.014	RQ	3.038	14.15	0.07	0.462	0.009	0.00	0.00	0.000	0.000	0.00	0.00	0.000	0.000	0.00	0.00	0.000	0.000
J1108+1209	3.678	46.285	0.014	RQ	3.064	14.23	0.07	0.515	0.008	0.00	0.00	0.000	0.000	0.00	0.00	0.000	0.000	0.00	0.00	0.000	0.000
J1108+1209	3.678	46.285	0.014	RQ	3.396	14.16	0.07	0.258	0.007	13.74	0.04	0.198	0.006	0.00	0.00	0.000	0.000	0.00	0.00	0.000	0.000
J1108+1209	3.678	46.285	0.014	RQ	3.109	13.22	0.05	0.063	0.005	0.00	0.00	0.000	0.000	0.00	0.00	0.000	0.000	0.00	0.00	0.000	0.000
J1108+1209	3.678	46.285	0.014	RQ	3.125	13.13	0.04	0.053	0.005	0.00	0.00	0.000	0.000	0.00	0.00	0.000	0.000	0.00	0.00	0.000	0.000
J1117+1311	3.622	46.675	0.012	RL	2.822	15.72	0.04	0.078	0.006	0.00	0.00	0.000	0.000	0.00	0.00	0.000	0.000	0.00	0.00	0.000	0.000
J1117+1311	3.622	46.675	0.012	RL	2.998	15.62	0.03	0.039	0.005	0.00	0.00	0.000	0.000	0.00	0.00	0.000	0.000	0.00	0.00	0.000	0.000
J1117+1311	3.622	46.675	0.012	RL	3.024	16.07	0.06	0.386	0.007	0.00	0.00	0.000	0.000	0.00	0.00	0.000	0.000	0.00	0.00	0.000	0.000
J1117+1311	3.622	46.675	0.012	RL	3.056	16.17	0.04	0.121	0.008	0.00	0.00	0.000	0.000	0.00	0.00	0.000	0.000	0.00	0.00	0.000	0.000
J1117+1311	3.622	46.675	0.012	RL	3.275	16.14	0.06	0.660	0.006	0.00	0.00	0.870	0.010	0.00	0.00	0.000	0.000	0.00	0.00	0.000	0.000
J1117+1311	3.622	46.675	0.012	RL	3.287	15.98	0.05	0.134	0.006	0.00	0.00	0.000	0.000	0.00	0.00	0.000	0.000	0.00	0.00	0.000	0.000
J1117+1311	3.622	46.675	0.012	RL	3.434	16.48	0.06	0.583	0.008	0.00	0.00	1.686	0.013	0.00	0.00	0.000	0.000	0.00	0.00	0.000	0.000
J1117+1311	3.622	46.675	0.012	RL	3.485	16.04	0.04	0.150	0.006	0.00	0.00	0.000	0.000	0.00	0.00	0.000	0.000	0.00	0.00	0.000	0.000
J1126-0126	3.634	46.481	0.018	RQ	3.451	13.58	0.07	0.105	0.008	0.00	0.00	0.000	0.000	0.00	0.00	0.000	0.000	0.00	0.00	0.000	0.000
J1126-0126	3.634	46.481	0.018	RQ	2.753	13.08	0.07	0.050	0.005	0.00	0.00	0.000	0.000	0.00	0.00	0.000	0.000	0.00	0.00	0.000	0.000
J1126-0126	3.634	46.481	0.018	RQ	2.805	13.36	0.04	0.083	0.015	0.00	0.00	0.000	0.000	0.00	0.00	0.000	0.000	0.00	0.00	0.000	0.000
J1126-0126	3.634	46.481	0.018	RQ	2.837	14.70	0.06	1.025	0.016	0.00	0.00	0.000	0.000	0.00	0.00	0.000	0.000	0.00	0.00	0.000	0.000
J1126-0126	3.634	46.481	0.018	RQ	3.258	14.08	0.06	0.372	0.011	0.00	0.00	0.000	0.000	0.00	0.00	0.000	0.000	0.00	0.00	0.000	0.000
J1126-0126	3.634	46.481	0.018	RQ	3.597	13.23	0.07	0.063	0.003	0.00	0.00	0.000	0.000	0.00	0.00	0.000	0.000	0.00	0.00	0.000	0.000
J1126-0126	3.634	46.481	0.018	RQ	2.687	13.06	0.03	0.043	0.004	0.00	0.00	0.000	0.000	0.00	0.00	0.000	0.000	0.00	0.00	0.000	0.000
J1126-0124	3.765	46.294	0.024	RQ	2.804	13.58	0.05	0.127	0.006	0.00	0.00	0.000	0.000	0.00	0.00	0.000	0.000	0.00	0.00	0.000	0.000
J1126-0124	3.765	46.294	0.024	RQ	3.021	14.14	0.10	0.421	0.014	0.00	0.00	0.000	0.000	0.00	0.00	0.000	0.000	0.00	0.00	0.000	0.000
J1126-0124	3.765	46.294	0.024	RQ	3.094	13.32	0.08	0.079	0.007	0.00	0.00	0.000	0.000	0.00	0.00	0.000	0.000	0.00	0.00	0.000	0.000
J1126-0124	3.765	46.294	0.024	RQ	3.223	13.27	0.05	0.067	0.006	0.00	0.00	0.000	0.000	0.00	0.00	0.000	0.000	0.00	0.00	0.000	0.000
J1126-0124	3.765	46.294	0.024	RQ	3.472	13.90	0.03	0.276	0.009	0.00	0.00	0.000	0.000	0.00	0.00	0.000	0.000	0.00	0.00	0.000	0.000
J1126-0124	3.765	46.294	0.024	RQ	3.496	13.83	0.05	0.231	0.012	12.53	0.05	0.031	0.010	0.00	0.00	0.000	0.000	0.00	0.00	0.000	0.000
J1126-0124	3.765	46.294	0.024	RQ	3.545	13.83	0.03	0.225	0.012	0.00	0.00	0.000	0.000	0.00	0.00	0.000	0.000	0.00	0.00	0.000	0.000
J1126-0124	3.765	46.294	0.024	RQ	3.686	13.42	0.05	0.096	0.009	0.00	0.00	0.000	0.000	0.00	0.00	0.000	0.000	0.00	0.00	0.000	0.000
J1126-0124	3.765	46.294	0.024	RQ	3.705	13.45	0.06	0.104	0.009	0.00	0.00	0.000	0.000	0.00	0.00	0.000	0.000	0.00	0.00	0.000	0.000
J1135+0842	3.834	47.062	0.009	RQ	3.734	14.35	0.03	0.709	0.006	12.60	0.04	0.035	0.004	0.00	0.00	0.000	0.000	0.00	0.00	0.000	0.000
J1135+0842	3.834	47.062	0.009	RQ	3.698	14.36	0.06	0.788	0.009	13.16	0.05	0.121	0.005	0.00	0.00	0.000	0.000	0.00	0.00	0.000	0.000
J1135+0842	3.834	47.062	0.009	RQ	3.820	13.12	0.06	0.048	0.003	0.00	0.00	0.000	0.000	0.00	0.00	0.000	0.000	0.00	0.00	0.000	0.000
J1135+0842	3.834	47.062	0.009	RQ	3.807	13.07	0.03	0.047	0.003	0.00	0.00	0.000	0.000	0.00	0.00	0.000	0.000	0.00	0.00	0.000	0.000
J1135+0842	3.834	47.062	0.009	RQ	2.806	13.78	0.03	0.203	0.005	0.00	0.00	0.000	0.000	0.00	0.00	0.000	0.000	0.00	0.00	0.000	0.000
J1135+0842	3.834	47.062	0.009	RQ	2.985	13.44	0.03	0.104	0.005	0.00	0.00	0.000	0.000	0.00	0.00	0.000	0.000	0.00	0.00	0.000	0.000

Tab. A.1 — Continued.

Quasar	z_{em}	L_{bol}	σL_{bol}	Radio type	z_{abs}	N CIV	σ N CIV	W CIV	σ W CIV	N SiIV	σ N SiIV	W SiIV	σ W SiIV	N NV	σ N NV	W NV	σW NV	N CII	σ N CII	W CII	σW CII
(1)	(2)	(3)	(4)	(5)	(6)	(7)	(8)	(9)	(10)	(11)	(12)	(13)	(14)	(15)	(16)	(17)	(18)	(19)	(20)	(21)	(22)
J1135+0842	3.834	47.062	0.009	RQ	3.163	13.72	0.04	0.166	0.004	0.00	0.00	0.000	0.000	0.00	0.00	0.000	0.000	0.00	0.00	0.000	0.000
J1135+0842	3.834	47.062	0.009	RQ	3.009	13.01	0.03	0.040	0.003	0.00	0.00	0.000	0.000	0.00	0.00	0.000	0.000	0.00	0.00	0.000	0.000
J1135+0842	3.834	47.062	0.009	RQ	3.180	13.36	0.03	0.090	0.004	0.00	0.00	0.000	0.000	0.00	0.00	0.000	0.000	0.00	0.00	0.000	0.000
J1135+0842	3.834	47.062	0.009	RQ	3.203	13.35	0.03	0.086	0.005	0.00	0.00	0.000	0.000	0.00	0.00	0.000	0.000	0.00	0.00	0.000	0.000
J1135+0842	3.834	47.062	0.009	RQ	3.395	13.43	0.04	0.098	0.003	12.24	0.06	0.016	0.003	0.00	0.00	0.000	0.000	0.00	0.00	0.000	0.000
J1135+0842	3.834	47.062	0.009	RQ	3.426	12.90	0.03	0.030	0.003	0.00	0.00	0.000	0.000	0.00	0.00	0.000	0.000	0.00	0.00	0.000	0.000
J1135+0842	3.834	47.062	0.009	RQ	3.624	13.07	0.03	0.033	0.003	0.00	0.00	0.000	0.000	0.00	0.00	0.000	0.000	0.00	0.00	0.000	0.000
J1201+1206	3.522	47.329	0.008	RQ	3.439	13.47	0.05	0.018	0.003	0.00	0.00	0.000	0.000	0.00	0.00	0.000	0.000	0.00	0.00	0.000	0.000
J1201+1206	3.522	47.329	0.008	RQ	3.226	13.41	0.04	0.093	0.004	0.00	0.00	0.000	0.000	0.00	0.00	0.000	0.000	0.00	0.00	0.000	0.000
J1201+1206	3.522	47.329	0.008	RQ	3.262	13.69	0.03	0.167	0.004	0.00	0.00	0.000	0.000	0.00	0.00	0.000	0.000	0.00	0.00	0.000	0.000
J1201+1206	3.522	47.329	0.008	RQ	3.379	12.87	0.05	0.029	0.003	0.00	0.00	0.000	0.000	0.00	0.00	0.000	0.000	0.00	0.00	0.000	0.000
J1201+1206	3.522	47.329	0.008	RQ	3.405	13.46	0.04	0.108	0.004	0.00	0.00	0.000	0.000	0.00	0.00	0.000	0.000	0.00	0.00	0.000	0.000
J1201+1206	3.522	47.329	0.008	RQ	3.427	13.06	0.06	0.043	0.003	0.00	0.00	0.000	0.000	0.00	0.00	0.000	0.000	0.00	0.00	0.000	0.000
J1201+1206	3.522	47.329	0.008	RQ	3.526	15.05	0.07	0.912	0.003	13.91	0.04	0.365	0.003	14.11	0.05	0.221	0.003	13.64	0.05	0.042	0.004
J1201+1206	3.522	47.329	0.008	RQ	3.204	12.64	0.06	0.018	0.003	0.00	0.00	0.000	0.000	0.00	0.00	0.000	0.000	0.00	0.00	0.000	0.000
J1202-0054	3.592	46.307	0.022	RQ	3.427	13.10	0.04	0.092	0.010	0.00	0.00	0.000	0.000	0.00	0.00	0.000	0.000	0.00	0.00	0.000	0.000
J1202-0054	3.592	46.307	0.022	RQ	2.687	13.61	0.04	0.157	0.005	0.00	0.00	0.000	0.000	0.00	0.00	0.000	0.000	0.00	0.00	0.000	0.000
J1202-0054	3.592	46.307	0.022	RQ	2.770	14.26	0.03	0.465	0.011	0.00	0.00	0.000	0.000	0.00	0.00	0.000	0.000	0.00	0.00	0.000	0.000
J1202-0054	3.592	46.307	0.022	RQ	2.834	13.57	0.04	0.134	0.013	0.00	0.00	0.000	0.000	0.00	0.00	0.000	0.000	0.00	0.00	0.000	0.000
J1202-0054	3.592	46.307	0.022	RQ	2.981	13.98	0.06	0.214	0.009	0.00	0.00	0.000	0.000	0.00	0.00	0.000	0.000	0.00	0.00	0.000	0.000
J1202-0054	3.592	46.307	0.022	RQ	3.509	12.80	0.04	0.026	0.006	0.00	0.00	0.000	0.000	0.00	0.00	0.000	0.000	0.00	0.00	0.000	0.000
J1202-0054	3.592	46.307	0.022	RQ	3.298	14.02	0.06	0.324	0.011	0.00	0.00	0.000	0.000	0.00	0.00	0.000	0.000	0.00	0.00	0.000	0.000
J1202-0054	3.592	46.307	0.022	RQ	2.661	13.88	0.06	0.260	0.007	0.00	0.00	0.000	0.000	0.00	0.00	0.000	0.000	0.00	0.00	0.000	0.000
J1248+1304	3.721	46.832	0.010	RQ	3.444	13.63	0.07	0.090	0.004	0.00	0.00	0.000	0.000	0.00	0.00	0.000	0.000	0.00	0.00	0.000	0.000
J1248+1304	3.721	46.832	0.010	RQ	3.003	13.24	0.05	0.065	0.004	0.00	0.00	0.000	0.000	0.00	0.00	0.000	0.000	0.00	0.00	0.000	0.000
J1248+1304	3.721	46.832	0.010	RQ	3.225	13.40	0.03	0.093	0.004	0.00	0.00	0.000	0.000	0.00	0.00	0.000	0.000	0.00	0.00	0.000	0.000
J1248+1304	3.721	46.832	0.010	RQ	3.329	12.80	0.05	0.025	0.004	0.00	0.00	0.000	0.000	0.00	0.00	0.000	0.000	0.00	0.00	0.000	0.000
J1248+1304	3.721	46.832	0.010	RQ	3.338	13.16	0.06	0.056	0.005	0.00	0.00	0.000	0.000	0.00	0.00	0.000	0.000	0.00	0.00	0.000	0.000
J1248+1304	3.721	46.832	0.010	RQ	3.406	13.96	0.04	0.280	0.005	13.89	0.05	0.267	0.006	0.00	0.00	0.000	0.000	0.00	0.00	0.000	0.000
J1248+1304	3.721	46.832	0.010	RQ	3.519	13.03	0.06	0.041	0.004	0.00	0.00	0.000	0.000	0.00	0.00	0.000	0.000	0.00	0.00	0.000	0.000
J1248+1304	3.721	46.832	0.010	RQ	3.558	14.14	0.04	0.419	0.005	13.69	0.06	0.310	0.007	0.00	0.00	0.000	0.000	0.00	0.00	0.000	0.000
J1248+1304	3.721	46.832	0.010	RQ	3.283	13.15	0.02	0.054	0.004	0.00	0.00	0.000	0.000	0.00	0.00	0.000	0.000	0.00	0.00	0.000	0.000
J1249-0159	3.629	46.831	0.015	RQ	3.456	13.76	0.06	0.130	0.005	0.00	0.00	0.000	0.000	0.00	0.00	0.000	0.000	0.00	0.00	0.000	0.000
J1249-0159	3.629	46.831	0.015	RQ	3.102	14.15	0.07	0.403	0.008	13.97	0.04	0.506	0.005	0.00	0.00	0.000	0.000	0.00	0.00	0.000	0.000
J1249-0159	3.629	46.831	0.015	RQ	3.572	13.85	0.05	0.135	0.007	0.00	0.00	0.000	0.000	0.00	0.00	0.000	0.000	0.00	0.00	0.000	0.000
J1249-0159	3.629	46.831	0.015	RQ	3.564	13.45	0.04	0.110	0.008	0.00	0.00	0.000	0.000	0.00	0.00	0.000	0.000	0.00	0.00	0.000	0.000
J1304+0239	3.648	46.940	0.010	RQ	2.733	12.99	0.05	0.037	0.004	0.00	0.00	0.000	0.000	0.00	0.00	0.000	0.000	0.00	0.00	0.000	0.000
J1304+0239	3.648	46.940	0.010	RQ	2.883	13.99	0.06	0.305	0.008	0.00	0.00	0.000	0.000	0.00	0.00	0.000	0.000	0.00	0.00	0.000	0.000
J1304+0239	3.648	46.940	0.010	RQ	2.904	13.76	0.04	0.110	0.006	0.00	0.00	0.000	0.000	0.00	0.00	0.000	0.000	0.00	0.00	0.000	0.000
J1304+0239	3.648	46.940	0.010	RQ	3.211	15.13	0.06	3.007	0.005	14.06	0.06	0.669	0.007	0.00	0.00	0.000	0.000	0.00	0.00	0.000	0.000
J1304+0239	3.648	46.940	0.010	RQ	3.206	14.70	0.07	0.430	0.004	14.16	0.05	0.794	0.007	0.00	0.00	0.000	0.000	0.00	0.00	0.000	0.000

Tab. A.1 — Continued.

Quasar	z_{em}	L_{bol}	σL_{bol}	Radio type	z_{abs}	N CIV	σ N CIV	W CIV	σ W CIV	N SiIV	σ N SiIV	W SiIV	σ W SiIV	N NV	σ N NV	W NV	σW NV	N CII	σ N CII	W CII	σW CII
(1)	(2)	(3)	(4)	(5)	(6)	(7)	(8)	(9)	(10)	(11)	(12)	(13)	(14)	(15)	(16)	(17)	(18)	(19)	(20)	(21)	(22)
J1304+0239	3.648	46.940	0.010	RQ	3.240	14.17	0.05	0.459	0.008	0.00	0.00	0.000	0.000	0.00	0.00	0.000	0.000	0.00	0.00	0.000	0.000
J1304+0239	3.648	46.940	0.010	RQ	3.295	13.01	0.03	0.041	0.005	0.00	0.00	0.000	0.000	0.00	0.00	0.000	0.000	0.00	0.00	0.000	0.000
J1304+0239	3.648	46.940	0.010	RQ	3.343	13.63	0.03	0.153	0.006	0.00	0.00	0.000	0.000	0.00	0.00	0.000	0.000	0.00	0.00	0.000	0.000
J1304+0239	3.648	46.940	0.010	RQ	3.582	13.86	0.06	0.185	0.004	0.00	0.00	0.000	0.000	0.00	0.00	0.000	0.000	0.00	0.00	0.000	0.000
J1304+0239	3.648	46.940	0.010	RQ	3.639	13.51	0.04	0.129	0.004	0.00	0.00	0.000	0.000	0.00	0.00	0.000	0.000	0.00	0.00	0.000	0.000
J1312+0841	3.731	46.764	0.012	RL	3.457	13.74	0.05	0.132	0.006	0.00	0.00	0.000	0.000	0.00	0.00	0.000	0.000	0.00	0.00	0.000	0.000
J1312+0841	3.731	46.764	0.012	RL	3.440	13.77	0.03	0.079	0.004	0.00	0.00	0.000	0.000	0.00	0.00	0.000	0.000	0.00	0.00	0.000	0.000
J1312+0841	3.731	46.764	0.012	RL	3.020	13.97	0.07	0.166	0.007	0.00	0.00	0.000	0.000	0.00	0.00	0.000	0.000	0.00	0.00	0.000	0.000
J1312+0841	3.731	46.764	0.012	RL	3.013	13.13	0.04	0.054	0.005	0.00	0.00	0.000	0.000	0.00	0.00	0.000	0.000	0.00	0.00	0.000	0.000
J1312+0841	3.731	46.764	0.012	RL	3.081	14.17	0.04	0.392	0.006	0.00	0.00	0.000	0.000	0.00	0.00	0.000	0.000	0.00	0.00	0.000	0.000
J1312+0841	3.731	46.764	0.012	RL	3.223	13.35	0.05	0.078	0.005	0.00	0.00	0.000	0.000	0.00	0.00	0.000	0.000	0.00	0.00	0.000	0.000
J1312+0841	3.731	46.764	0.012	RL	3.550	13.56	0.06	0.133	0.006	0.00	0.00	0.000	0.000	0.00	0.00	0.000	0.000	0.00	0.00	0.000	0.000
J1312+0841	3.731	46.764	0.012	RL	3.613	13.50	0.04	0.117	0.005	12.76	0.05	0.048	0.005	0.00	0.00	0.000	0.000	0.00	0.00	0.000	0.000
J1312+0841	3.731	46.764	0.012	RL	3.644	13.15	0.06	0.056	0.004	0.00	0.00	0.000	0.000	0.00	0.00	0.000	0.000	0.00	0.00	0.000	0.000
J1312+0841	3.731	46.764	0.012	RL	3.730	12.83	0.06	0.204	0.003	13.09	0.04	0.095	0.004	14.30	0.05	0.251	0.005	0.00	0.00	0.000	0.000
J1312+0841	3.731	46.764	0.012	RL	3.741	13.89	0.03	0.276	0.004	0.00	0.00	0.000	0.000	14.29	0.06	0.343	0.007	0.00	0.00	0.000	0.000
J1312+0841	3.731	46.764	0.012	RL	3.311	12.98	0.04	0.037	0.005	12.73	0.04	0.043	0.006	0.00	0.00	0.000	0.000	0.00	0.00	0.000	0.000
J1312+0841	3.731	46.764	0.012	RL	3.274	13.32	0.04	0.077	0.005	0.00	0.00	0.000	0.000	0.00	0.00	0.000	0.000	0.00	0.00	0.000	0.000
J1320-0523	3.717	47.059	0.010	RQ	2.832	13.84	0.04	0.216	0.004	0.00	0.00	0.000	0.000	0.00	0.00	0.000	0.000	0.00	0.00	0.000	0.000
J1320-0523	3.717	47.059	0.010	RQ	2.836	13.67	0.03	0.160	0.005	0.00	0.00	0.000	0.000	0.00	0.00	0.000	0.000	0.00	0.00	0.000	0.000
J1320-0523	3.717	47.059	0.010	RQ	2.934	13.27	0.05	0.071	0.006	0.00	0.00	0.000	0.000	0.00	0.00	0.000	0.000	0.00	0.00	0.000	0.000
J1320-0523	3.717	47.059	0.010	RQ	3.057	13.56	0.03	0.139	0.007	0.00	0.00	0.000	0.000	0.00	0.00	0.000	0.000	0.00	0.00	0.000	0.000
J1320-0523	3.717	47.059	0.010	RQ	3.081	13.48	0.06	0.114	0.005	0.00	0.00	0.000	0.000	0.00	0.00	0.000	0.000	0.00	0.00	0.000	0.000
J1320-0523	3.717	47.059	0.010	RQ	3.092	13.07	0.05	0.045	0.004	0.00	0.00	0.000	0.000	0.00	0.00	0.000	0.000	0.00	0.00	0.000	0.000
J1320-0523	3.717	47.059	0.010	RQ	3.278	12.95	0.04	0.038	0.003	0.00	0.00	0.000	0.000	0.00	0.00	0.000	0.000	0.00	0.00	0.000	0.000
J1320-0523	3.717	47.059	0.010	RQ	3.288	14.19	0.04	0.436	0.005	13.42	0.05	0.188	0.006	0.00	0.00	0.000	0.000	0.00	0.00	0.000	0.000
J1320-0523	3.717	47.059	0.010	RQ	3.302	13.31	0.03	0.077	0.004	0.00	0.00	0.000	0.000	0.00	0.00	0.000	0.000	0.00	0.00	0.000	0.000
J1320-0523	3.717	47.059	0.010	RQ	3.360	13.10	0.04	0.050	0.005	0.00	0.00	0.000	0.000	0.00	0.00	0.000	0.000	0.00	0.00	0.000	0.000
J1320-0523	3.717	47.059	0.010	RQ	3.372	12.90	0.05	0.032	0.003	0.00	0.00	0.000	0.000	0.00	0.00	0.000	0.000	0.00	0.00	0.000	0.000
J1320-0523	3.717	47.059	0.010	RQ	3.377	13.17	0.06	0.053	0.003	0.00	0.00	0.000	0.000	0.00	0.00	0.000	0.000	0.00	0.00	0.000	0.000
J1323+1405	4.054	46.432	0.018	RQ	3.460	13.15	0.03	0.033	0.006	0.00	0.00	0.000	0.000	0.00	0.00	0.000	0.000	0.00	0.00	0.000	0.000
J1323+1405	4.054	46.432	0.018	RQ	3.449	13.34	0.05	0.107	0.008	0.00	0.00	0.000	0.000	0.00	0.00	0.000	0.000	0.00	0.00	0.000	0.000
J1323+1405	4.054	46.432	0.018	RQ	4.032	13.99	0.06	0.325	0.004	0.00	0.00	0.000	0.000	0.00	0.00	0.000	0.000	0.00	0.00	0.000	0.000
J1323+1405	4.054	46.432	0.018	RQ	3.294	13.31	0.03	0.080	0.006	0.00	0.00	0.000	0.000	0.00	0.00	0.000	0.000	0.00	0.00	0.000	0.000
J1330-2522	3.948	46.890	0.011	not	3.474	13.61	0.05	0.175	0.005	0.00	0.00	0.000	0.000	0.00	0.00	0.000	0.000	0.00	0.00	0.000	0.000
J1330-2522	3.948	46.890	0.011	not	3.389	13.75	0.06	0.190	0.005	12.66	0.05	0.039	0.004	0.00	0.00	0.000	0.000	0.00	0.00	0.000	0.000
J1330-2522	3.948	46.890	0.011	not	3.299	13.31	0.04	0.076	0.004	0.00	0.00	0.000	0.000	0.00	0.00	0.000	0.000	0.00	0.00	0.000	0.000
J1330-2522	3.948	46.890	0.011	not	3.082	14.44	0.06	0.723	0.006	0.00	0.00	0.000	0.000	0.00	0.00	0.000	0.000	0.00	0.00	0.000	0.000
J1330-2522	3.948	46.890	0.011	not	3.411	13.15	0.07	0.053	0.004	0.00	0.00	0.000	0.000	0.00	0.00	0.000	0.000	0.00	0.00	0.000	0.000
J1330-2522	3.948	46.890	0.011	not	3.649	13.26	0.05	0.068	0.004	12.43	0.04	0.024	0.003	0.00	0.00	0.000	0.000	0.00	0.00	0.000	0.000
J1330-2522	3.948	46.890	0.011	not	3.678	12.93	0.03	0.031	0.004	0.00	0.00	0.000	0.000	0.00	0.00	0.000	0.000	0.00	0.00	0.000	0.000

Tab. A.1 — Continued.

Quasar	z_{em}	L_{bol}	σL_{bol}	Radio type	z_{abs}	N CIV	σ N CIV	W CIV	σ W CIV	N SiIV	σ N SiIV	W SiIV	σ W SiIV	N NV	σ N NV	W NV	σW NV	N CII	σ N CII	W CII	σW CII
(1)	(2)	(3)	(4)	(5)	(6)	(7)	(8)	(9)	(10)	(11)	(12)	(13)	(14)	(15)	(16)	(17)	(18)	(19)	(20)	(21)	(22)
J1330-2522	3.948	46.890	0.011	not	3.709	14.09	0.03	0.401	0.007	13.29	0.05	0.140	0.004	0.00	0.00	0.000	0.000	0.00	0.00	0.000	0.000
J1330-2522	3.948	46.890	0.011	not	3.720	13.35	0.06	0.081	0.003	0.00	0.00	0.000	0.000	0.00	0.00	0.000	0.000	0.00	0.00	0.000	0.000
J1330-2522	3.948	46.890	0.011	not	3.794	13.29	0.04	0.072	0.004	0.00	0.00	0.000	0.000	0.00	0.00	0.000	0.000	0.00	0.00	0.000	0.000
J1330-2522	3.948	46.890	0.011	not	3.851	13.09	0.05	0.047	0.003	0.00	0.00	0.000	0.000	0.00	0.00	0.000	0.000	0.00	0.00	0.000	0.000
J1330-2522	3.948	46.890	0.011	not	3.890	14.46	0.03	0.721	0.006	0.00	0.00	0.000	0.000	14.69	0.06	0.659	0.004	0.00	0.00	0.000	0.000
J1330-2522	3.948	46.890	0.011	not	3.859	13.46	0.07	0.105	0.004	0.00	0.00	0.000	0.000	0.00	0.00	0.000	0.000	0.00	0.00	0.000	0.000
J1330-2522	3.948	46.890	0.011	not	3.769	14.14	0.09	0.382	0.004	13.31	0.06	0.155	0.004	0.00	0.00	0.000	0.000	0.00	0.00	0.000	0.000
J1330-2522	3.948	46.890	0.011	not	3.948	14.66	0.08	0.649	0.005	13.74	0.05	0.276	0.005	13.37	0.05	0.050	0.005	0.00	0.00	0.000	0.000
J1332+0052	3.508	46.660	0.008	RQ	2.712	0.00	0.00	0.812	0.007	0.00	0.00	0.000	0.000	0.00	0.00	0.000	0.000	0.00	0.00	0.000	0.000
J1332+0052	3.508	46.660	0.008	RQ	2.748	13.20	0.05	0.057	0.007	0.00	0.00	0.000	0.000	0.00	0.00	0.000	0.000	0.00	0.00	0.000	0.000
J1332+0052	3.508	46.660	0.008	RQ	2.775	13.84	0.04	0.237	0.009	0.00	0.00	0.000	0.000	0.00	0.00	0.000	0.000	0.00	0.00	0.000	0.000
J1332+0052	3.508	46.660	0.008	RQ	2.913	12.90	0.05	0.030	0.006	0.00	0.00	0.000	0.000	0.00	0.00	0.000	0.000	0.00	0.00	0.000	0.000
J1332+0052	3.508	46.660	0.008	RQ	3.015	14.10	0.03	0.414	0.011	13.14	0.05	0.113	0.006	0.00	0.00	0.000	0.000	0.00	0.00	0.000	0.000
J1332+0052	3.508	46.660	0.008	RQ	3.084	0.00	0.00	0.801	0.006	13.99	0.06	0.482	0.007	0.00	0.00	0.000	0.000	0.00	0.00	0.000	0.000
J1332+0052	3.508	46.660	0.008	RQ	3.116	14.11	0.06	0.324	0.007	13.26	0.04	0.130	0.007	0.00	0.00	0.000	0.000	0.00	0.00	0.000	0.000
J1332+0052	3.508	46.660	0.008	RQ	3.142	13.20	0.06	0.060	0.005	0.00	0.00	0.000	0.000	0.00	0.00	0.000	0.000	0.00	0.00	0.000	0.000
J1332+0052	3.508	46.660	0.008	RQ	3.421	13.45	0.04	0.102	0.005	13.13	0.05	0.102	0.006	0.00	0.00	0.000	0.000	13.68	0.04	0.082	0.005
J1332+0052	3.508	46.660	0.008	RQ	3.476	13.26	0.07	0.083	0.004	0.00	0.00	0.000	0.000	0.00	0.00	0.000	0.000	0.00	0.00	0.000	0.000
J1352+1303	3.706	47.630	0.009	RQ	3.007	14.23	0.05	0.518	0.009	0.00	0.00	0.000	0.000	0.00	0.00	0.000	0.000	0.00	0.00	0.000	0.000
J1352+1303	3.706	47.630	0.009	RQ	3.129	14.36	0.07	0.365	0.007	0.00	0.00	0.000	0.000	0.00	0.00	0.000	0.000	0.00	0.00	0.000	0.000
J1352+1303	3.706	47.630	0.009	RQ	3.166	13.05	0.04	0.043	0.005	0.00	0.00	0.000	0.000	0.00	0.00	0.000	0.000	0.00	0.00	0.000	0.000
J1352+1303	3.706	47.630	0.009	RQ	3.280	13.25	0.06	0.070	0.005	0.00	0.00	0.000	0.000	0.00	0.00	0.000	0.000	0.00	0.00	0.000	0.000
J1352+1303	3.706	47.630	0.009	RQ	3.291	14.27	0.06	0.397	0.007	0.00	0.00	0.000	0.000	0.00	0.00	0.000	0.000	0.00	0.00	0.000	0.000
J1352+1303	3.706	47.630	0.009	RQ	3.362	13.01	0.05	0.022	0.004	0.00	0.00	0.000	0.000	0.00	0.00	0.000	0.000	0.00	0.00	0.000	0.000
J1352+1303	3.706	47.630	0.009	RQ	3.507	13.90	0.07	0.257	0.006	13.12	0.04	0.103	0.006	0.00	0.00	0.000	0.000	0.00	0.00	0.000	0.000
J1352+1303	3.706	47.630	0.009	RQ	3.576	13.54	0.04	0.127	0.005	0.00	0.00	0.000	0.000	0.00	0.00	0.000	0.000	0.00	0.00	0.000	0.000
J1352+1303	3.706	47.630	0.009	RQ	3.586	13.41	0.06	0.096	0.005	0.00	0.00	0.000	0.000	0.00	0.00	0.000	0.000	0.00	0.00	0.000	0.000
J1336+0243	3.801	46.664	0.014	RQ	3.639	13.84	0.04	0.232	0.006	12.91	0.05	0.071	0.006	0.00	0.00	0.000	0.000	0.00	0.00	0.000	0.000
J1336+0243	3.801	46.664	0.014	RQ	2.819	13.32	0.06	0.076	0.004	0.00	0.00	0.000	0.000	0.00	0.00	0.000	0.000	0.00	0.00	0.000	0.000
J1336+0243	3.801	46.664	0.014	RQ	3.110	13.29	0.07	0.073	0.005	0.00	0.00	0.000	0.000	0.00	0.00	0.000	0.000	0.00	0.00	0.000	0.000
J1336+0243	3.801	46.664	0.014	RQ	3.385	12.96	0.04	0.037	0.005	0.00	0.00	0.000	0.000	0.00	0.00	0.000	0.000	0.00	0.00	0.000	0.000
J1336+0243	3.801	46.664	0.014	RQ	3.405	13.70	0.05	0.183	0.008	0.00	0.00	0.000	0.000	0.00	0.00	0.000	0.000	0.00	0.00	0.000	0.000
J1336+0243	3.801	46.664	0.014	RQ	3.424	13.75	0.04	0.190	0.007	12.39	0.10	0.044	0.006	0.00	0.00	0.000	0.000	0.00	0.00	0.000	0.000
J1336+0243	3.801	46.664	0.014	RQ	3.531	13.82	0.03	0.230	0.009	0.00	0.00	0.000	0.000	0.00	0.00	0.000	0.000	0.00	0.00	0.000	0.000
J1336+0243	3.801	46.664	0.014	RQ	3.553	13.00	0.06	0.039	0.004	0.00	0.00	0.000	0.000	0.00	0.00	0.000	0.000	0.00	0.00	0.000	0.000
J1336+0243	3.801	46.664	0.014	RQ	3.762	13.61	0.07	0.151	0.006	12.42	0.05	0.026	0.006	0.00	0.00	0.000	0.000	0.00	0.00	0.000	0.000
J1336+0243	3.801	46.664	0.014	RQ	3.780	13.26	0.04	0.071	0.004	0.00	0.00	0.000	0.000	0.00	0.00	0.000	0.000	0.00	0.00	0.000	0.000
J1336+0243	3.801	46.664	0.014	RQ	2.897	13.09	0.05	0.046	0.005	0.00	0.00	0.000	0.000	0.00	0.00	0.000	0.000	0.00	0.00	0.000	0.000
J1401+0244	4.4136	48.616	0.009	RQ	4.288	13.34	0.05	0.082	0.003	13.02	0.04	0.086	0.005	0.00	0.00	0.000	0.000	0.00	0.00	0.000	0.000
J1401+0244	4.4136	48.616	0.009	RQ	3.315	13.17	0.06	0.058	0.004	0.00	0.00	0.000	0.000	0.00	0.00	0.000	0.000	0.00	0.00	0.000	0.000
J1401+0244	4.4136	48.616	0.009	RQ	3.604	13.11	0.04	0.050	0.004	0.00	0.00	0.000	0.000	0.00	0.00	0.000	0.000	0.00	0.00	0.000	0.000

Tab. A.1 — Continued.

Quasar	z_{em}	L_{bol}	σL_{bol}	Radio type	z_{abs}	N CIV	σ N CIV	W CIV	σ W CIV	N SiIV	σ N SiIV	W SiIV	σ W SiIV	N NV	σ N NV	W NV	σW NV	N CII	σ N CII	W CII	σW CII
(1)	(2)	(3)	(4)	(5)	(6)	(7)	(8)	(9)	(10)	(11)	(12)	(13)	(14)	(15)	(16)	(17)	(18)	(19)	(20)	(21)	(22)
J1401+0244	4.4136	48.616	0.009	RQ	3.804	13.34	0.03	0.078	0.004	12.85	0.05	0.055	0.002	0.00	0.00	0.000	0.000	0.00	0.00	0.000	0.000
J1401+0244	4.4136	48.616	0.009	RQ	3.856	14.17	0.05	0.450	0.005	13.21	0.05	0.136	0.005	0.00	0.00	0.000	0.000	0.00	0.00	0.000	0.000
J1401+0244	4.4136	48.616	0.009	RQ	4.082	13.36	0.06	0.086	0.004	0.00	0.00	0.000	0.000	0.00	0.00	0.000	0.000	0.00	0.00	0.000	0.000
J1401+0244	4.4136	48.616	0.009	RQ	4.074	13.16	0.06	0.053	0.006	12.41	0.03	0.023	0.002	0.00	0.00	0.000	0.000	0.00	0.00	0.000	0.000
J1401+0244	4.4136	48.616	0.009	RQ	4.186	13.39	0.04	0.096	0.007	0.00	0.00	0.000	0.000	0.00	0.00	0.000	0.000	0.00	0.00	0.000	0.000
J1401+0244	4.4136	48.616	0.009	RQ	4.393	13.64	0.06	0.151	0.003	0.00	0.00	0.000	0.000	13.35	0.04	0.046	0.003	0.00	0.00	0.000	0.000
J1401+0244	4.4136	48.616	0.009	RQ	4.410	14.91	0.07	0.642	0.003	12.75	0.05	0.048	0.003	14.91	0.06	0.373	0.003	0.00	0.00	0.000	0.000
J1401+0244	4.4136	48.616	0.009	RQ	4.426	14.85	0.05	1.324	0.003	13.25	0.04	0.140	0.004	14.14	0.05	0.206	0.003	0.00	0.00	0.000	0.000
J1401+0244	4.4136	48.616	0.009	RQ	3.991	12.95	0.03	0.038	0.004	12.11	0.03	0.014	0.003	0.00	0.00	0.000	0.000	0.00	0.00	0.000	0.000
J1421-0643	3.688	46.874	0.011	RL	3.445	14.33	0.04	0.331	0.004	13.31	0.05	0.158	0.005	0.00	0.00	0.000	0.000	0.00	0.00	0.000	0.000
J1421-0643	3.688	46.874	0.011	RL	3.028	13.41	0.03	0.093	0.006	0.00	0.00	0.000	0.000	0.00	0.00	0.000	0.000	0.00	0.00	0.000	0.000
J1421-0643	3.688	46.874	0.011	RL	3.511	12.83	0.05	0.027	0.004	0.00	0.00	0.000	0.000	0.00	0.00	0.000	0.000	0.00	0.00	0.000	0.000
J1421-0643	3.688	46.874	0.011	RL	3.590	13.79	0.06	0.204	0.005	12.11	0.06	0.015	0.004	0.00	0.00	0.000	0.000	0.00	0.00	0.000	0.000
J1421-0643	3.688	46.874	0.011	RL	3.413	13.45	0.03	0.099	0.005	0.00	0.00	0.000	0.000	0.00	0.00	0.000	0.000	0.00	0.00	0.000	0.000
J1416+1811	3.593	46.481	0.023	RQ	2.650	14.00	0.05	0.325	0.007	0.00	0.00	0.000	0.000	0.00	0.00	0.000	0.000	0.00	0.00	0.000	0.000
J1416+1811	3.593	46.481	0.023	RQ	2.663	13.87	0.03	0.252	0.009	0.00	0.00	0.000	0.000	0.00	0.00	0.000	0.000	0.00	0.00	0.000	0.000
J1416+1811	3.593	46.481	0.023	RQ	3.265	14.02	0.04	0.335	0.012	13.54	0.05	0.269	0.018	0.00	0.00	0.000	0.000	0.00	0.00	0.000	0.000
J1416+1811	3.593	46.481	0.023	RQ	2.883	13.90	0.06	0.141	0.013	0.00	0.00	0.000	0.000	0.00	0.00	0.000	0.000	0.00	0.00	0.000	0.000
J1416+1811	3.593	46.481	0.023	RQ	3.321	13.59	0.03	0.126	0.009	0.00	0.00	0.000	0.000	0.00	0.00	0.000	0.000	0.00	0.00	0.000	0.000
J1416+1811	3.593	46.481	0.023	RQ	3.393	13.95	0.06	0.274	0.012	0.00	0.00	0.000	0.000	0.00	0.00	0.000	0.000	0.00	0.00	0.000	0.000
J1416+1811	3.593	46.481	0.023	RQ	3.529	13.08	0.04	0.047	0.005	0.00	0.00	0.000	0.000	0.00	0.00	0.000	0.000	0.00	0.00	0.000	0.000
J1416+1811	3.593	46.481	0.023	RQ	3.512	13.23	0.06	0.064	0.007	0.00	0.00	0.000	0.000	13.62	0.04	0.079	0.008	0.00	0.00	0.000	0.000
J1442+0920	3.532	47.080	0.011	RQ	2.646	13.79	0.04	0.232	0.008	0.00	0.00	0.000	0.000	0.00	0.00	0.000	0.000	0.00	0.00	0.000	0.000
J1442+0920	3.532	47.080	0.011	RQ	2.743	13.55	0.05	0.132	0.006	0.00	0.00	0.000	0.000	0.00	0.00	0.000	0.000	0.00	0.00	0.000	0.000
J1442+0920	3.532	47.080	0.011	RQ	2.775	13.23	0.04	0.062	0.004	0.00	0.00	0.000	0.000	0.00	0.00	0.000	0.000	0.00	0.00	0.000	0.000
J1442+0920	3.532	47.080	0.011	RQ	2.890	13.02	0.06	0.041	0.005	0.00	0.00	0.000	0.000	0.00	0.00	0.000	0.000	0.00	0.00	0.000	0.000
J1442+0920	3.532	47.080	0.011	RQ	2.899	13.09	0.05	0.048	0.005	0.00	0.00	0.000	0.000	0.00	0.00	0.000	0.000	0.00	0.00	0.000	0.000
J1442+0920	3.532	47.080	0.011	RQ	3.013	13.49	0.04	0.114	0.006	0.00	0.00	0.000	0.000	0.00	0.00	0.000	0.000	0.00	0.00	0.000	0.000
J1442+0920	3.532	47.080	0.011	RQ	3.025	13.19	0.03	0.060	0.005	0.00	0.00	0.000	0.000	0.00	0.00	0.000	0.000	0.00	0.00	0.000	0.000
J1442+0920	3.532	47.080	0.011	RQ	3.038	13.37	0.05	0.086	0.004	0.00	0.00	0.000	0.000	0.00	0.00	0.000	0.000	0.00	0.00	0.000	0.000
J1442+0920	3.532	47.080	0.011	RQ	3.046	12.93	0.10	0.033	0.004	0.00	0.00	0.000	0.000	0.00	0.00	0.000	0.000	0.00	0.00	0.000	0.000
J1442+0920	3.532	47.080	0.011	RQ	3.090	12.85	0.09	0.015	0.003	0.00	0.00	0.000	0.000	0.00	0.00	0.000	0.000	0.00	0.00	0.000	0.000
J1442+0920	3.532	47.080	0.011	RQ	3.096	14.06	0.08	0.199	0.006	12.64	0.05	0.037	0.004	0.00	0.00	0.000	0.000	0.00	0.00	0.000	0.000
J1442+0920	3.532	47.080	0.011	RQ	3.156	13.11	0.05	0.048	0.004	0.00	0.00	0.000	0.000	0.00	0.00	0.000	0.000	0.00	0.00	0.000	0.000
J1442+0920	3.532	47.080	0.011	RQ	3.195	12.82	0.06	0.027	0.005	0.00	0.00	0.000	0.000	0.00	0.00	0.000	0.000	0.00	0.00	0.000	0.000
J1442+0920	3.532	47.080	0.011	RQ	3.207	13.81	0.07	0.215	0.006	13.14	0.06	0.110	0.006	0.00	0.00	0.000	0.000	0.00	0.00	0.000	0.000
J1442+0920	3.532	47.080	0.011	RQ	3.266	13.54	0.07	0.117	0.005	12.39	0.05	0.021	0.004	0.00	0.00	0.000	0.000	0.00	0.00	0.000	0.000
J1442+0920	3.532	47.080	0.011	RQ	3.291	13.14	0.04	0.054	0.004	0.00	0.00	0.000	0.000	0.00	0.00	0.000	0.000	0.00	0.00	0.000	0.000
J1442+0920	3.532	47.080	0.011	RQ	3.498	13.63	0.06	0.160	0.005	0.00	0.00	0.000	0.000	0.00	0.00	0.000	0.000	0.00	0.00	0.000	0.000
J1445+0958	3.562	47.076	0.010	RL	2.598	13.20	0.05	0.081	0.007	0.00	0.00	0.000	0.000	0.00	0.00	0.000	0.000	0.00	0.00	0.000	0.000
J1445+0958	3.562	47.076	0.010	RL	2.633	0.00	0.00	0.250	0.006	0.00	0.00	0.000	0.000	0.00	0.00	0.000	0.000	0.00	0.00	0.000	0.000

Tab. A.1 — Continued.

Quasar	z_{em}	L_{bol}	σL_{bol}	Radio type	z_{abs}	N CIV	σ N CIV	W CIV	σ W CIV	N SiIV	σ N SiIV	W SiIV	σ W SiIV	N NV	σ N NV	W NV	σW NV	N CII	σ N CII	W CII	σW CII
(1)	(2)	(3)	(4)	(5)	(6)	(7)	(8)	(9)	(10)	(11)	(12)	(13)	(14)	(15)	(16)	(17)	(18)	(19)	(20)	(21)	(22)
J1445+0958	3.562	47.076	0.010	RL	2.942	13.08	0.05	0.047	0.004	0.00	0.00	0.000	0.000	0.00	0.00	0.000	0.000	0.00	0.00	0.000	0.000
J1445+0958	3.562	47.076	0.010	RL	2.992	13.10	0.05	0.049	0.005	0.00	0.00	0.000	0.000	0.00	0.00	0.000	0.000	0.00	0.00	0.000	0.000
J1445+0958	3.562	47.076	0.010	RL	3.047	13.63	0.04	0.148	0.006	0.00	0.00	0.000	0.000	0.00	0.00	0.000	0.000	0.00	0.00	0.000	0.000
J1445+0958	3.562	47.076	0.010	RL	3.104	13.09	0.06	0.049	0.004	0.00	0.00	0.000	0.000	0.00	0.00	0.000	0.000	0.00	0.00	0.000	0.000
J1445+0958	3.562	47.076	0.010	RL	3.352	13.05	0.04	0.043	0.004	0.00	0.00	0.000	0.000	0.00	0.00	0.000	0.000	0.00	0.00	0.000	0.000
J1503+0419	3.692	46.685	0.017	RL	2.768	13.56	0.05	0.129	0.007	0.00	0.00	0.000	0.000	0.00	0.00	0.000	0.000	0.00	0.00	0.000	0.000
J1503+0419	3.692	46.685	0.017	RL	2.773	13.23	0.04	0.064	0.005	0.00	0.00	0.000	0.000	0.00	0.00	0.000	0.000	0.00	0.00	0.000	0.000
J1503+0419	3.692	46.685	0.017	RL	2.812	13.09	0.03	0.046	0.006	0.00	0.00	0.000	0.000	0.00	0.00	0.000	0.000	0.00	0.00	0.000	0.000
J1503+0419	3.692	46.685	0.017	RL	2.791	13.13	0.05	0.053	0.006	0.00	0.00	0.000	0.000	0.00	0.00	0.000	0.000	0.00	0.00	0.000	0.000
J1503+0419	3.692	46.685	0.017	RL	2.992	14.36	0.04	0.453	0.009	0.00	0.00	0.000	0.000	0.00	0.00	0.000	0.000	0.00	0.00	0.000	0.000
J1503+0419	3.692	46.685	0.017	RL	3.095	13.69	0.05	0.185	0.012	0.00	0.00	0.000	0.000	0.00	0.00	0.000	0.000	0.00	0.00	0.000	0.000
J1503+0419	3.692	46.685	0.017	RL	3.112	13.05	0.06	0.042	0.005	0.00	0.00	0.000	0.000	0.00	0.00	0.000	0.000	0.00	0.00	0.000	0.000
J1503+0419	3.692	46.685	0.017	RL	3.147	13.76	0.03	0.201	0.009	13.19	0.04	0.121	0.006	0.00	0.00	0.000	0.000	0.00	0.00	0.000	0.000
J1503+0419	3.692	46.685	0.017	RL	3.228	14.62	0.05	0.775	0.007	14.06	0.05	0.590	0.010	0.00	0.00	0.000	0.000	0.00	0.00	0.000	0.000
J1503+0419	3.692	46.685	0.017	RL	3.596	13.15	0.06	0.054	0.006	13.25	0.05	0.141	0.008	13.50	0.05	0.064	0.004	0.00	0.00	0.000	0.000
J1503+0419	3.692	46.685	0.017	RL	3.377	12.85	0.04	0.030	0.005	0.00	0.00	0.000	0.000	0.00	0.00	0.000	0.000	0.00	0.00	0.000	0.000
J1517+0511	3.555	46.763	0.011	RQ	3.457	13.90	0.05	0.186	0.005	12.46	0.05	0.024	0.004	0.00	0.00	0.000	0.000	0.00	0.00	0.000	0.000
J1517+0511	3.555	46.763	0.011	RQ	3.037	13.73	0.05	0.196	0.008	0.00	0.00	0.000	0.000	0.00	0.00	0.000	0.000	0.00	0.00	0.000	0.000
J1517+0511	3.555	46.763	0.011	RQ	3.136	13.80	0.04	0.232	0.008	0.00	0.00	0.000	0.000	0.00	0.00	0.000	0.000	0.00	0.00	0.000	0.000
J1517+0511	3.555	46.763	0.011	RQ	3.158	13.52	0.06	0.125	0.006	0.00	0.00	0.000	0.000	0.00	0.00	0.000	0.000	0.00	0.00	0.000	0.000
J1517+0511	3.555	46.763	0.011	RQ	3.283	13.52	0.06	0.122	0.006	12.91	0.04	0.070	0.006	0.00	0.00	0.000	0.000	0.00	0.00	0.000	0.000
J1517+0511	3.555	46.763	0.011	RQ	3.266	14.07	0.07	0.406	0.008	13.62	0.06	0.303	0.009	0.00	0.00	0.000	0.000	0.00	0.00	0.000	0.000
J1517+0511	3.555	46.763	0.011	RQ	3.532	13.67	0.04	0.164	0.005	12.92	0.05	0.069	0.004	0.00	0.00	0.000	0.000	0.00	0.00	0.000	0.000
J1517+0511	3.555	46.763	0.011	RQ	3.398	13.67	0.03	0.175	0.007	0.00	0.00	0.000	0.000	0.00	0.00	0.000	0.000	0.00	0.00	0.000	0.000
J1517+0511	3.555	46.763	0.011	RQ	2.688	13.74	0.05	0.174	0.005	0.00	0.00	0.000	0.000	0.00	0.00	0.000	0.000	0.00	0.00	0.000	0.000
J1517+0511	3.555	46.763	0.011	RQ	3.428	13.84	0.06	0.224	0.005	0.00	0.00	0.000	0.000	0.00	0.00	0.000	0.000	0.00	0.00	0.000	0.000
J1524+2123	3.600	46.828	0.014	RQ	3.464	13.87	0.07	0.184	0.006	13.02	0.06	0.086	0.007	0.00	0.00	0.000	0.000	0.00	0.00	0.000	0.000
J1524+2123	3.600	46.828	0.014	RQ	2.732	13.44	0.04	0.100	0.007	0.00	0.00	0.000	0.000	0.00	0.00	0.000	0.000	0.00	0.00	0.000	0.000
J1524+2123	3.600	46.828	0.014	RQ	2.885	13.40	0.05	0.088	0.005	0.00	0.00	0.000	0.000	0.00	0.00	0.000	0.000	0.00	0.00	0.000	0.000
J1524+2123	3.600	46.828	0.014	RQ	2.880	13.22	0.05	0.062	0.006	0.00	0.00	0.000	0.000	0.00	0.00	0.000	0.000	0.00	0.00	0.000	0.000
J1524+2123	3.600	46.828	0.014	RQ	2.910	13.21	0.03	0.061	0.007	0.00	0.00	0.000	0.000	0.00	0.00	0.000	0.000	0.00	0.00	0.000	0.000
J1524+2123	3.600	46.828	0.014	RQ	2.926	13.88	0.05	0.270	0.009	0.00	0.00	0.000	0.000	0.00	0.00	0.000	0.000	0.00	0.00	0.000	0.000
J1524+2123	3.600	46.828	0.014	RQ	2.941	13.17	0.03	0.056	0.005	0.00	0.00	0.000	0.000	0.00	0.00	0.000	0.000	0.00	0.00	0.000	0.000
J1524+2123	3.600	46.828	0.014	RQ	2.974	13.84	0.04	0.230	0.007	0.00	0.00	0.000	0.000	0.00	0.00	0.000	0.000	0.00	0.00	0.000	0.000
J1524+2123	3.600	46.828	0.014	RQ	3.258	13.36	0.05	0.085	0.006	0.00	0.00	0.000	0.000	0.00	0.00	0.000	0.000	0.00	0.00	0.000	0.000
J1524+2123	3.600	46.828	0.014	RQ	3.292	13.21	0.06	0.060	0.005	0.00	0.00	0.000	0.000	0.00	0.00	0.000	0.000	0.00	0.00	0.000	0.000
J1524+2123	3.600	46.828	0.014	RQ	3.553	13.69	0.07	0.160	0.006	0.00	0.00	0.000	0.000	0.00	0.00	0.000	0.000	0.00	0.00	0.000	0.000
J1524+2123	3.600	46.828	0.014	RQ	3.408	13.33	0.05	0.080	0.006	0.00	0.00	0.000	0.000	0.00	0.00	0.000	0.000	0.00	0.00	0.000	0.000
J1524+2123	3.600	46.828	0.014	RQ	2.634	13.93	0.04	0.298	0.007	0.00	0.00	0.000	0.000	0.00	0.00	0.000	0.000	0.00	0.00	0.000	0.000
J1542+0955	3.986	46.825	0.013	RQ	3.282	13.90	0.05	0.134	0.004	0.00	0.00	0.000	0.000	0.00	0.00	0.000	0.000	0.00	0.00	0.000	0.000
J1542+0955	3.986	46.825	0.013	RQ	3.332	14.42	0.06	0.644	0.003	0.00	0.00	0.000	0.000	0.00	0.00	0.000	0.000	0.00	0.00	0.000	0.000

Tab. A.1 — Continued.

Quasar	z_{em}	L_{bol}	σL_{bol}	Radio type	z_{abs}	N CIV	σ N CIV	W CIV	σ W CIV	N SiIV	σ N SiIV	W SiIV	σ W SiIV	N NV	σ N NV	W NV	σW NV	N CII	σ N CII	W CII	σW CII
(1)	(2)	(3)	(4)	(5)	(6)	(7)	(8)	(9)	(10)	(11)	(12)	(13)	(14)	(15)	(16)	(17)	(18)	(19)	(20)	(21)	(22)
J1542+0955	3.986	46.825	0.013	RQ	3.399	13.31	0.04	0.040	0.002	0.00	0.00	0.000	0.000	0.00	0.00	0.000	0.000	0.00	0.00	0.000	0.000
J1542+0955	3.986	46.825	0.013	RQ	3.472	14.08	0.06	0.392	0.004	0.00	0.00	0.000	0.000	0.00	0.00	0.000	0.000	0.00	0.00	0.000	0.000
J1542+0955	3.986	46.825	0.013	RQ	3.554	13.36	0.03	0.083	0.002	0.00	0.00	0.000	0.000	0.00	0.00	0.000	0.000	0.00	0.00	0.000	0.000
J1542+0955	3.986	46.825	0.013	RQ	3.607	13.09	0.05	0.046	0.004	0.00	0.00	0.000	0.000	0.00	0.00	0.000	0.000	0.00	0.00	0.000	0.000
J1542+0955	3.986	46.825	0.013	RQ	3.613	13.91	0.04	0.269	0.003	0.00	0.00	0.000	0.000	0.00	0.00	0.000	0.000	0.00	0.00	0.000	0.000
J1552+1005	3.722	46.821	0.010	RQ	3.077	14.14	0.05	0.400	0.008	0.00	0.00	0.000	0.000	0.00	0.00	0.000	0.000	0.00	0.00	0.000	0.000
J1552+1005	3.722	46.821	0.010	RQ	3.113	14.47	0.03	0.574	0.007	0.00	0.00	0.000	0.000	0.00	0.00	0.000	0.000	0.00	0.00	0.000	0.000
J1552+1005	3.722	46.821	0.010	RQ	3.147	13.81	0.05	0.205	0.005	0.00	0.00	0.000	0.000	0.00	0.00	0.000	0.000	0.00	0.00	0.000	0.000
J1552+1005	3.722	46.821	0.010	RQ	3.442	14.46	0.05	0.426	0.007	13.54	0.06	0.237	0.006	0.00	0.00	0.000	0.000	0.00	0.00	0.000	0.000
J1552+1005	3.722	46.821	0.010	RQ	3.489	13.04	0.06	0.020	0.003	0.00	0.00	0.000	0.000	0.00	0.00	0.000	0.000	0.00	0.00	0.000	0.000
J1552+1005	3.722	46.821	0.010	RQ	3.576	12.80	0.06	0.020	0.003	0.00	0.00	0.000	0.000	0.00	0.00	0.000	0.000	0.00	0.00	0.000	0.000
J1552+1005	3.722	46.821	0.010	RQ	3.589	13.87	0.04	0.240	0.005	0.00	0.00	0.000	0.000	0.00	0.00	0.000	0.000	0.00	0.00	0.000	0.000
J1552+1005	3.722	46.821	0.010	RQ	3.601	13.29	0.06	0.398	0.005	12.91	0.05	0.064	0.003	0.00	0.00	0.000	0.000	0.00	0.00	0.446	0.004
J1552+1005	3.722	46.821	0.010	RQ	3.666	13.84	0.04	0.207	0.005	0.00	0.00	0.000	0.000	0.00	0.00	0.000	0.000	0.00	0.00	0.858	0.007
J1552+1005	3.722	46.821	0.010	RQ	3.731	13.24	0.04	0.047	0.004	0.00	0.00	0.000	0.000	0.00	0.00	0.000	0.000	0.00	0.00	0.000	0.000
J1552+1005	3.720	46.821	0.010	RQ	3.678	14.01	0.06	0.212	0.005	0.00	0.00	0.000	0.000	14.37	0.04	0.301	0.004	0.00	0.00	0.000	0.000
J1621-0042	3.711	47.001	0.011	not	2.874	13.02	0.05	0.042	0.004	0.00	0.00	0.000	0.000	0.00	0.00	0.000	0.000	0.00	0.00	0.000	0.000
J1621-0042	3.711	47.001	0.011	not	2.890	14.04	0.04	0.372	0.008	0.00	0.00	0.000	0.000	0.00	0.00	0.000	0.000	0.00	0.00	0.000	0.000
J1621-0042	3.711	47.001	0.011	not	2.920	13.20	0.05	0.057	0.004	0.00	0.00	0.000	0.000	0.00	0.00	0.000	0.000	0.00	0.00	0.000	0.000
J1621-0042	3.711	47.001	0.011	not	2.972	13.10	0.06	0.047	0.003	0.00	0.00	0.000	0.000	0.00	0.00	0.000	0.000	0.00	0.00	0.000	0.000
J1621-0042	3.711	47.001	0.011	not	3.021	12.78	0.07	0.024	0.004	0.00	0.00	0.000	0.000	0.00	0.00	0.000	0.000	0.00	0.00	0.000	0.000
J1621-0042	3.711	47.001	0.011	not	3.061	13.34	0.06	0.083	0.005	0.00	0.00	0.000	0.000	0.00	0.00	0.000	0.000	0.00	0.00	0.000	0.000
J1621-0042	3.711	47.001	0.011	not	3.066	13.69	0.05	0.160	0.004	0.00	0.00	0.000	0.000	0.00	0.00	0.000	0.000	0.00	0.00	0.000	0.000
J1621-0042	3.711	47.001	0.011	not	3.108	14.66	0.06	0.986	0.007	0.00	0.00	0.000	0.000	0.00	0.00	0.000	0.000	0.00	0.00	0.000	0.000
J1621-0042	3.711	47.001	0.011	not	3.201	13.14	0.04	0.055	0.004	0.00	0.00	0.000	0.000	0.00	0.00	0.000	0.000	0.00	0.00	0.000	0.000
J1621-0042	3.711	47.001	0.011	not	3.488	13.31	0.05	0.077	0.004	0.00	0.00	0.000	0.000	0.00	0.00	0.000	0.000	0.00	0.00	0.000	0.000
J1633+1411	4.365	46.827	0.011	RQ	3.347	13.54	0.05	0.126	0.006	0.00	0.00	0.000	0.000	0.00	0.00	0.000	0.000	0.00	0.00	0.000	0.000
J1633+1411	4.365	46.827	0.011	RQ	3.505	14.55	0.06	0.615	0.007	0.00	0.00	0.000	0.000	0.00	0.00	0.000	0.000	0.00	0.00	0.000	0.000
J1633+1411	4.365	46.827	0.011	RQ	3.582	13.67	0.05	0.167	0.006	0.00	0.00	0.000	0.000	0.00	0.00	0.000	0.000	0.00	0.00	0.000	0.000
J1633+1411	4.365	46.827	0.011	RQ	4.031	13.39	0.04	0.091	0.005	0.00	0.00	0.000	0.000	0.00	0.00	0.000	0.000	0.00	0.00	0.000	0.000
J1633+1411	4.365	46.827	0.011	RQ	4.125	13.54	0.04	0.138	0.005	0.00	0.00	0.000	0.000	0.00	0.00	0.000	0.000	0.00	0.00	0.000	0.000
J1633+1411	4.365	46.827	0.011	RQ	4.210	13.34	0.06	0.078	0.005	0.00	0.00	0.000	0.000	0.00	0.00	0.000	0.000	0.00	0.00	0.000	0.000
J1633+1411	4.365	46.827	0.011	RQ	4.227	13.78	0.04	0.236	0.005	0.00	0.00	0.000	0.000	0.00	0.00	0.000	0.000	0.00	0.00	0.000	0.000
J1633+1411	4.365	46.827	0.011	RQ	4.251	13.73	0.03	0.181	0.004	0.00	0.00	0.000	0.000	0.00	0.00	0.000	0.000	0.00	0.00	0.000	0.000
J1633+1411	4.365	46.827	0.011	RQ	4.258	14.01	0.05	0.272	0.006	13.51	0.05	0.246	0.009	0.00	0.00	0.000	0.000	13.41	0.06	0.046	0.004
J1633+1411	4.365	46.827	0.011	RQ	4.368	13.52	0.05	0.113	0.003	0.00	0.00	0.000	0.000	12.89	0.06	0.036	0.003	0.00	0.00	0.000	0.000
J1633+1411	4.365	46.827	0.011	RQ	4.309	13.61	0.06	0.136	0.003	12.92	0.03	0.067	0.003	0.00	0.00	0.000	0.000	0.00	0.00	0.000	0.000
J1633+1411	4.365	46.827	0.011	RQ	4.285	14.24	0.07	0.511	0.007	13.07	0.04	0.100	0.007	14.40	0.04	0.471	0.005	0.00	0.00	0.000	0.000
J1658-0739	3.749	46.649	0.014	not	3.546	14.81	0.06	1.066	0.010	13.96	0.04	0.570	0.011	0.00	0.00	0.000	0.000	0.00	0.00	0.000	0.000
J1658-0739	3.749	46.649	0.014	not	3.240	13.67	0.04	0.171	0.009	0.00	0.00	0.000	0.000	0.00	0.00	0.000	0.000	0.00	0.00	0.000	0.000
J1658-0739	3.749	46.649	0.014	not	3.689	13.77	0.05	0.211	0.006	13.57	0.05	0.288	0.010	0.00	0.00	0.000	0.000	13.49	0.04	0.060	0.006

Tab. A.1 — Continued.

Quasar	z_{em}	L_{bol}	σL_{bol}	Radio type	z_{abs}	N CIV	σ N CIV	W CIV	σ W CIV	N SiIV	σ N SiIV	W SiIV	σ W SiIV	N NV	σ N NV	W NV	σW NV	N CII	σ N CII	W CII	σW CII
(1)	(2)	(3)	(4)	(5)	(6)	(7)	(8)	(9)	(10)	(11)	(12)	(13)	(14)	(15)	(16)	(17)	(18)	(19)	(20)	(21)	(22)
J1658-0739	3.749	46.649	0.014	not	3.393	13.67	0.06	0.167	0.008	0.00	0.00	0.000	0.000	0.00	0.00	0.000	0.000	0.00	0.00	0.000	0.000
J1658-0739	3.749	46.649	0.014	not	2.795	14.11	0.04	0.431	0.011	0.00	0.00	0.000	0.000	0.00	0.00	0.000	0.000	0.00	0.00	0.000	0.000
J1658-0739	3.749	46.649	0.014	not	3.041	13.49	0.03	0.118	0.009	0.00	0.00	0.000	0.000	0.00	0.00	0.000	0.000	0.00	0.00	0.000	0.000
J1658-0739	3.749	46.649	0.014	not	3.056	13.94	0.06	0.265	0.008	0.00	0.00	0.000	0.000	0.00	0.00	0.000	0.000	0.00	0.00	0.000	0.000
J1658-0739	3.749	46.649	0.014	not	3.276	13.59	0.05	0.143	0.007	13.07	0.06	0.098	0.009	0.00	0.00	0.000	0.000	0.00	0.00	0.000	0.000
J1658-0739	3.749	46.649	0.014	not	3.532	13.26	0.03	0.067	0.007	0.00	0.00	0.000	0.000	0.00	0.00	0.000	0.000	0.00	0.00	0.000	0.000
J1723+2243	4.531	46.844	0.015	not	3.699	14.82	0.05	1.016	0.010	0.00	0.00	0.000	0.000	0.00	0.00	0.000	0.000	0.00	0.00	0.000	0.000
J1723+2243	4.531	46.844	0.015	not	3.677	13.69	0.04	0.175	0.005	0.00	0.00	0.000	0.000	0.00	0.00	0.000	0.000	0.00	0.00	0.000	0.000
J1723+2243	4.531	46.844	0.015	not	3.604	12.85	0.06	0.030	0.003	0.00	0.00	0.000	0.000	0.00	0.00	0.000	0.000	0.00	0.00	0.000	0.000
J1723+2243	4.531	46.844	0.015	not	3.563	12.91	0.07	0.054	0.004	0.00	0.00	0.000	0.000	0.00	0.00	0.000	0.000	0.00	0.00	0.000	0.000
J1723+2243	4.531	46.844	0.015	not	3.789	12.69	0.07	0.015	0.002	0.00	0.00	0.000	0.000	0.00	0.00	0.000	0.000	0.00	0.00	0.000	0.000
J1723+2243	4.531	46.844	0.015	not	3.822	13.27	0.05	0.053	0.004	0.00	0.00	0.000	0.000	0.00	0.00	0.000	0.000	0.00	0.00	0.000	0.000
J1723+2243	4.531	46.844	0.015	not	3.983	13.02	0.07	0.040	0.003	0.00	0.00	0.000	0.000	0.00	0.00	0.000	0.000	0.00	0.00	0.000	0.000
J1723+2243	4.531	46.844	0.015	not	4.237	14.31	0.04	0.519	0.006	13.79	0.04	0.214	0.004	0.00	0.00	0.000	0.000	0.00	0.00	0.000	0.000
J1723+2243	4.531	46.844	0.015	not	4.396	13.27	0.07	0.079	0.003	0.00	0.00	0.000	0.000	0.00	0.00	0.000	0.000	0.00	0.00	0.000	0.000
J1723+2243	4.531	46.844	0.015	not	4.436	13.28	0.05	0.054	0.004	0.00	0.00	0.000	0.000	0.00	0.00	0.000	0.000	0.00	0.00	0.000	0.000
J2215-1611	3.994	46.763	0.013	not	3.702	14.05	0.03	0.356	0.247	13.77	0.04	0.359	0.005	0.00	0.00	0.000	0.000	0.00	0.00	0.000	0.000
J2215-1611	3.994	46.763	0.013	not	3.662	13.82	0.10	0.194	0.161	14.05	0.05	0.376	0.005	0.00	0.00	0.000	0.000	0.00	0.00	0.000	0.000
J2215-1611	3.994	46.763	0.013	not	3.491	13.68	0.06	0.204	0.249	0.00	0.00	0.000	0.000	0.00	0.00	0.000	0.000	0.00	0.00	0.000	0.000
J2215-1611	3.994	46.763	0.013	not	3.466	13.96	0.06	0.300	0.204	13.27	0.04	0.140	0.003	0.00	0.00	0.000	0.000	0.00	0.00	0.000	0.000
J2215-1611	3.994	46.763	0.013	not	3.985	14.05	0.04	0.278	0.004	0.00	0.00	0.000	0.000	13.98	0.04	0.171	0.003	0.00	0.00	0.000	0.000
J2215-1611	3.994	46.763	0.013	not	3.978	13.68	0.06	0.181	0.005	0.00	0.00	0.000	0.000	14.37	0.06	0.435	0.005	0.00	0.00	0.000	0.000
J2215-1611	3.994	46.763	0.013	not	2.955	13.97	0.07	0.286	0.004	0.00	0.00	0.000	0.000	0.00	0.00	0.000	0.000	0.00	0.00	0.000	0.000
J2215-1611	3.994	46.763	0.013	not	3.007	13.21	0.04	0.060	0.002	0.00	0.00	0.000	0.000	0.00	0.00	0.000	0.000	0.00	0.00	0.000	0.000
J2215-1611	3.994	46.763	0.013	not	3.896	13.19	0.05	0.059	0.005	0.00	0.00	0.000	0.000	0.00	0.00	0.000	0.000	0.00	0.00	0.000	0.000
J2215-1611	3.994	46.763	0.013	not	3.865	13.18	0.04	0.059	0.005	0.00	0.00	0.000	0.000	0.00	0.00	0.000	0.000	0.00	0.00	0.000	0.000
J2215-1611	3.994	46.763	0.013	not	3.033	13.29	0.03	0.073	0.004	0.00	0.00	0.000	0.000	0.00	0.00	0.000	0.000	0.00	0.00	0.000	0.000
J2215-1611	3.994	46.763	0.013	not	3.227	13.59	0.05	0.141	0.005	0.00	0.00	0.000	0.000	0.00	0.00	0.000	0.000	0.00	0.00	0.000	0.000
J2215-1611	3.994	46.763	0.013	not	3.306	13.79	0.05	0.203	0.005	0.00	0.00	0.000	0.000	0.00	0.00	0.000	0.000	0.00	0.00	0.000	0.000
J2239-0552	4.556	47.081	0.007	RQ	3.832	14.43	0.05	0.433	0.004	0.00	0.00	0.000	0.000	0.00	0.00	0.000	0.000	0.00	0.00	0.000	0.000
J2239-0552	4.556	47.081	0.007	RQ	3.978	13.52	0.04	0.126	0.005	0.00	0.00	0.000	0.000	0.00	0.00	0.000	0.000	0.00	0.00	0.000	0.000
J2239-0552	4.556	47.081	0.007	RQ	4.030	12.99	0.06	0.038	0.002	0.00	0.00	0.000	0.000	0.00	0.00	0.000	0.000	0.00	0.00	0.000	0.000
J2239-0552	4.556	47.081	0.007	RQ	4.080	13.77	0.04	0.195	0.005	0.00	0.00	0.178	0.004	0.00	0.00	0.000	0.000	0.00	0.00	0.000	0.000
J2239-0552	4.556	47.081	0.007	RQ	4.201	13.18	0.05	0.055	0.003	0.00	0.00	0.000	0.000	0.00	0.00	0.000	0.000	0.00	0.00	0.000	0.000
J2239-0552	4.556	47.081	0.007	RQ	4.231	13.33	0.03	0.077	0.003	0.00	0.00	0.000	0.000	0.00	0.00	0.000	0.000	0.00	0.00	0.000	0.000
J2239-0552	4.556	47.081	0.007	RQ	4.247	13.45	0.04	0.108	0.004	13.31	0.04	0.085	0.004	0.00	0.00	0.000	0.000	0.00	0.00	0.000	0.000
J2239-0552	4.556	47.081	0.007	RQ	4.286	13.68	0.05	0.152	0.003	0.00	0.00	0.000	0.000	0.00	0.00	0.000	0.000	0.00	0.00	0.000	0.000
J2239-0552	4.556	47.081	0.007	RQ	4.362	14.17	0.06	0.462	0.005	14.15	0.03	0.454	0.004	0.00	0.00	0.000	0.000	0.00	0.00	0.000	0.000
J2239-0552	4.556	47.081	0.007	RQ	4.390	13.09	0.02	0.069	0.005	0.00	0.00	0.000	0.000	0.00	0.00	0.000	0.000	0.00	0.00	0.000	0.000
J2251-1227	4.157	46.700	0.014	not	3.493	13.04	0.03	0.053	0.005	0.00	0.00	0.000	0.000	0.00	0.00	0.000	0.000	0.00	0.00	0.000	0.000
J2251-1227	4.157	46.700	0.014	not	3.456	14.39	0.03	0.533	0.008	0.00	0.00	0.000	0.000	0.00	0.00	0.000	0.000	0.00	0.00	0.000	0.000

Tab. A.1 — Continued.

Quasar	z_{em}	L_{bol}	σL_{bol}	Radio type	z_{abs}	N CIV	σ N CIV	W CIV	σ W CIV	N SiIV	σ N SiIV	W SiIV	σ W SiIV	N NV	σ N NV	W NV	σW NV	N CII	σ N CII	W CII	σW CII
(1)	(2)	(3)	(4)	(5)	(6)	(7)	(8)	(9)	(10)	(11)	(12)	(13)	(14)	(15)	(16)	(17)	(18)	(19)	(20)	(21)	(22)
J2251-1227	4.157	46.700	0.014	not	3.411	13.13	0.04	0.053	0.005	0.00	0.00	0.000	0.000	0.00	0.00	0.000	0.000	0.00	0.00	0.000	0.000
J2251-1227	4.157	46.700	0.014	not	3.763	12.97	0.04	0.037	0.004	0.00	0.00	0.000	0.000	0.00	0.00	0.000	0.000	0.00	0.00	0.000	0.000
J2251-1227	4.157	46.700	0.014	not	3.838	13.24	0.05	0.067	0.005	0.00	0.00	0.000	0.000	0.00	0.00	0.000	0.000	0.00	0.00	0.000	0.000
J2251-1227	4.157	46.700	0.014	not	3.849	13.32	0.05	0.080	0.007	0.00	0.00	0.000	0.000	0.00	0.00	0.000	0.000	0.00	0.00	0.000	0.000
J2251-1227	4.157	46.700	0.014	not	3.879	13.01	0.06	0.039	0.004	0.00	0.00	0.000	0.000	0.00	0.00	0.000	0.000	0.00	0.00	0.000	0.000
J2251-1227	4.157	46.700	0.014	not	3.979	12.92	0.04	0.032	0.003	0.00	0.00	0.000	0.000	0.00	0.00	0.000	0.000	0.00	0.00	0.000	0.000
J2251-1227	4.157	46.700	0.014	not	4.127	14.48	0.05	0.355	0.003	13.24	0.03	0.114	0.004	13.80	0.06	0.113	0.004	0.00	0.00	0.000	0.000
J2251-1227	4.157	46.700	0.014	not	4.066	12.94	0.05	0.036	0.004	0.00	0.00	0.000	0.000	0.00	0.00	0.000	0.000	0.00	0.00	0.000	0.000
J2251-1227	4.157	46.700	0.014	not	4.020	14.17	0.05	0.453	0.007	11.80	0.25	0.097	0.006	0.00	0.00	0.000	0.000	0.00	0.00	0.000	0.000
J2344+0342	4.248	46.258	0.017	RQ	3.220	14.74	0.03	0.621	0.007	0.00	0.00	0.000	0.000	0.00	0.00	0.000	0.000	0.00	0.00	0.000	0.000
J2344+0342	4.248	46.258	0.017	RQ	3.368	13.24	0.04	0.066	0.004	0.00	0.00	0.000	0.000	0.00	0.00	0.000	0.000	0.00	0.00	0.000	0.000
J2344+0342	4.248	46.258	0.017	RQ	3.495	13.20	0.05	0.060	0.005	0.00	0.00	0.000	0.000	0.00	0.00	0.000	0.000	0.00	0.00	0.000	0.000
J2344+0342	4.248	46.258	0.017	RQ	3.489	13.52	0.06	0.117	0.007	0.00	0.00	0.000	0.000	0.00	0.00	0.000	0.000	0.00	0.00	0.000	0.000
J2344+0342	4.248	46.258	0.017	RQ	3.570	13.18	0.06	0.058	0.006	0.00	0.00	0.000	0.000	0.00	0.00	0.000	0.000	0.00	0.00	0.000	0.000
J2344+0342	4.248	46.258	0.017	RQ	3.847	13.58	0.07	0.135	0.006	0.00	0.00	0.000	0.000	0.00	0.00	0.000	0.000	0.00	0.00	0.000	0.000
J2344+0342	4.248	46.258	0.017	RQ	3.885	14.23	0.06	0.477	0.008	13.67	0.03	0.300	0.006	0.00	0.00	0.000	0.000	0.00	0.00	0.000	0.000
J2344+0342	4.248	46.258	0.017	RQ	4.010	13.06	0.05	0.046	0.005	0.00	0.00	0.000	0.000	0.00	0.00	0.000	0.000	0.00	0.00	0.000	0.000
J2344+0342	4.248	46.258	0.017	RQ	4.094	13.01	0.06	0.038	0.005	0.00	0.00	0.000	0.000	0.00	0.00	0.000	0.000	0.00	0.00	0.000	0.000
J2344+0342	4.248	46.258	0.017	RQ	4.225	13.29	0.05	0.072	0.005	0.00	0.00	0.000	0.000	13.54	0.06	0.068	0.004	0.00	0.00	0.000	0.000
J2344+0342	4.248	46.258	0.017	RQ	4.137	13.49	0.06	0.110	0.006	12.90	0.03	0.066	0.005	0.00	0.00	0.000	0.000	0.00	0.00	0.000	0.000
J2216-6714	4.479	46.810	0.012	not	4.098	14.17	0.04	0.257	0.010	0.00	0.00	0.000	0.000	0.00	0.00	0.000	0.000	0.00	0.00	0.000	0.000
J2216-6714	4.479	46.810	0.012	not	3.371	13.85	0.06	0.248	0.005	0.00	0.00	0.000	0.000	0.00	0.00	0.000	0.000	0.00	0.00	0.000	0.000
J2216-6714	4.479	46.810	0.012	not	4.014	13.03	0.06	0.040	0.004	0.00	0.00	0.000	0.000	0.00	0.00	0.000	0.000	0.00	0.00	0.000	0.000
J2216-6714	4.479	46.810	0.012	not	3.995	13.47	0.05	0.108	0.006	11.66	0.12	0.091	0.004	0.00	0.00	0.000	0.000	0.00	0.00	0.000	0.000
J2216-6714	4.479	46.810	0.012	not	3.979	13.28	0.05	0.073	0.005	13.06	0.06	0.121	0.005	0.00	0.00	0.000	0.000	0.00	0.00	0.000	0.000
J2216-6714	4.479	46.810	0.012	not	4.391	12.60	0.06	0.019	0.007	0.00	0.00	0.000	0.000	0.00	0.00	0.000	0.000	0.00	0.00	0.000	0.000
J2216-6714	4.479	46.810	0.012	not	4.320	13.40	0.04	0.096	0.004	13.16	0.04	0.114	0.004	0.00	0.00	0.000	0.000	0.00	0.00	0.000	0.000
J2216-6714	4.479	46.810	0.012	not	3.730	13.76	0.05	0.210	0.007	0.00	0.00	0.000	0.000	0.00	0.00	0.000	0.000	0.00	0.00	0.000	0.000
J2216-6714	4.479	46.810	0.012	not	4.287	13.63	0.06	0.146	0.005	13.42	0.05	0.192	0.008	0.00	0.00	0.000	0.000	0.00	0.00	0.000	0.000
J2216-6714	4.479	46.810	0.012	not	4.135	13.49	0.07	0.058	0.004	0.00	0.00	0.000	0.000	0.00	0.00	0.000	0.000	0.00	0.00	0.000	0.000
J2216-6714	4.479	46.810	0.012	not	3.592	13.14	0.03	0.052	0.004	0.00	0.00	0.000	0.000	0.00	0.00	0.000	0.000	0.00	0.00	0.000	0.000
J2216-6714	4.479	46.810	0.012	not	3.841	13.65	0.06	0.160	0.006	13.49	0.06	0.088	0.003	0.00	0.00	0.000	0.000	0.00	0.00	0.000	0.000
J2349-3712	4.219	46.352	0.015	not	3.230	13.49	0.04	0.114	0.006	0.00	0.00	0.000	0.000	0.00	0.00	0.000	0.000	0.00	0.00	0.000	0.000
J2349-3712	4.219	46.352	0.015	not	3.260	14.22	0.06	0.366	0.006	0.00	0.00	0.000	0.000	0.00	0.00	0.000	0.000	0.00	0.00	0.000	0.000
J2349-3712	4.219	46.352	0.015	not	3.580	13.68	0.04	0.175	0.009	0.00	0.00	0.000	0.000	0.00	0.00	0.000	0.000	0.00	0.00	0.000	0.000
J2349-3712	4.219	46.352	0.015	not	3.686	13.09	0.06	0.048	0.007	0.00	0.00	0.000	0.000	0.00	0.00	0.000	0.000	0.00	0.00	0.000	0.000
J2349-3712	4.219	46.352	0.015	not	3.759	14.05	0.05	0.350	0.010	13.19	0.06	0.122	0.007	0.00	0.00	0.000	0.000	0.00	0.00	0.000	0.000
J2349-3712	4.219	46.352	0.015	not	3.964	13.87	0.03	0.231	0.007	0.00	0.00	0.000	0.000	0.00	0.00	0.000	0.000	0.00	0.00	0.000	0.000
J2349-3712	4.219	46.352	0.015	not	4.090	13.25	0.05	0.062	0.006	0.00	0.00	0.000	0.000	0.00	0.00	0.000	0.000	0.00	0.00	0.000	0.000
J0003-2603	4.125	47.304	0.005	not	3.053	13.13	0.05	0.053	0.002	0.00	0.00	0.000	0.000	0.00	0.00	0.000	0.000	0.00	0.00	0.000	0.000
J0003-2603	4.125	47.304	0.005	not	3.819	13.04	0.06	0.042	0.002	12.58	0.05	0.032	0.001	0.00	0.00	0.000	0.000	0.00	0.00	0.000	0.000

Tab. A.1 — Continued.

Quasar	z_{em}	L_{bol}	σL_{bol}	Radio type	z_{abs}	N CIV	σN CIV	W CIV	σW CIV	N SiIV	σN SiIV	W SiIV	σW SiIV	N NV	σN NV	W NV	σW NV	N CII	σN CII	W CII	σW CII
(1)	(2)	(3)	(4)	(5)	(6)	(7)	(8)	(9)	(10)	(11)	(12)	(13)	(14)	(15)	(16)	(17)	(18)	(19)	(20)	(21)	(22)
J0003-2603	4.125	47.304	0.005	not	3.798	12.75	0.06	0.022	0.002	0.00	0.00	0.000	0.000	0.00	0.00	0.000	0.000	0.00	0.00	0.000	0.000
J0003-2603	4.125	47.304	0.005	not	3.748	13.41	0.04	0.096	0.003	12.82	0.06	0.053	0.002	0.00	0.00	0.000	0.000	0.00	0.00	0.000	0.000
J0003-2603	4.125	47.304	0.005	not	3.595	13.55	0.06	0.132	0.003	0.00	0.00	0.000	0.000	0.00	0.00	0.000	0.000	0.00	0.00	0.000	0.000
J0003-2603	4.125	47.304	0.005	not	3.536	13.74	0.04	0.188	0.003	12.85	0.04	0.059	0.002	0.00	0.00	0.000	0.000	0.00	0.00	0.000	0.000
J0003-2603	4.125	47.304	0.005	not	3.390	14.80	0.05	0.967	0.003	14.44	0.08	0.849	0.002	0.00	0.00	0.000	0.000	0.00	0.00	0.000	0.000
J0003-2603	4.125	47.304	0.005	not	4.089	13.08	0.03	0.056	0.002	0.00	0.00	0.000	0.000	0.00	0.00	0.000	0.000	0.00	0.00	0.000	0.000
J0003-2603	4.125	47.304	0.005	not	4.133	14.92	0.05	1.093	0.003	13.28	0.06	0.156	0.003	13.76	0.04	0.115	0.003	0.00	0.00	0.000	0.000
J0003-2603	4.125	47.304	0.005	not	4.101	13.14	0.06	0.076	0.002	12.54	0.04	0.030	0.001	0.00	0.00	0.000	0.000	0.00	0.00	0.000	0.000
J0003-2603	4.125	47.304	0.005	not	4.009	13.61	0.04	0.094	0.003	12.21	0.05	0.015	0.002	0.00	0.00	0.000	0.000	0.00	0.00	0.000	0.000
J0003-2603	4.125	47.304	0.005	not	4.004	13.52	0.05	0.087	0.003	0.00	0.00	0.000	0.000	0.00	0.00	0.000	0.000	0.00	0.00	0.000	0.000
J0003-2603	4.125	47.304	0.005	not	4.062	13.79	0.03	0.206	0.002	0.00	0.00	0.000	0.000	0.00	0.00	0.000	0.000	0.00	0.00	0.000	0.000
J0003-2603	4.125	47.304	0.005	not	3.138	12.92	0.04	0.033	0.002	0.00	0.00	0.000	0.000	0.00	0.00	0.000	0.000	0.00	0.00	0.000	0.000
J0003-2603	4.125	47.304	0.005	not	3.162	13.58	0.05	0.143	0.004	0.00	0.00	0.000	0.000	0.00	0.00	0.000	0.000	0.00	0.00	0.000	0.000
J0006-6208	4.440	46.508	0.020	not	3.415	13.05	0.06	0.060	0.008	0.00	0.00	0.000	0.000	0.00	0.00	0.000	0.000	0.00	0.00	0.000	0.000
J0006-6208	4.440	46.508	0.020	not	3.460	14.09	0.05	0.346	0.008	0.00	0.00	0.000	0.000	0.00	0.00	0.000	0.000	0.00	0.00	0.000	0.000
J0006-6208	4.440	46.508	0.020	not	3.590	14.25	0.06	0.523	0.010	0.00	0.00	0.000	0.000	0.00	0.00	0.000	0.000	0.00	0.00	0.000	0.000
J0006-6208	4.440	46.508	0.020	not	4.357	14.11	0.05	1.112	0.016	13.37	0.06	0.179	0.009	0.00	0.00	0.000	0.000	0.00	0.00	0.000	0.000
J0006-6208	4.440	46.508	0.020	not	3.648	13.98	0.04	0.320	0.010	0.00	0.00	0.000	0.000	0.00	0.00	0.000	0.000	0.00	0.00	0.000	0.000
J0006-6208	4.440	46.508	0.020	not	3.798	14.00	0.06	0.326	0.009	0.00	0.00	0.000	0.000	0.00	0.00	0.000	0.000	0.00	0.00	0.000	0.000
J0006-6208	4.440	46.508	0.020	not	3.543	14.09	0.04	0.417	0.013	0.00	0.00	0.000	0.000	0.00	0.00	0.000	0.000	0.00	0.00	0.000	0.000
J0006-6208	4.440	46.508	0.020	not	3.694	13.86	0.07	0.230	0.007	0.00	0.00	0.000	0.000	0.00	0.00	0.000	0.000	0.00	0.00	0.000	0.000
J0030-5129	4.173	46.314	0.021	not	3.502	13.47	0.06	0.117	0.009	0.00	0.00	0.000	0.000	0.00	0.00	0.000	0.000	0.00	0.00	0.000	0.000
J0030-5129	4.173	46.314	0.021	not	3.467	13.90	0.04	0.241	0.009	0.00	0.00	0.000	0.000	0.00	0.00	0.000	0.000	0.00	0.00	0.000	0.000
J0030-5129	4.173	46.314	0.021	not	3.437	14.46	0.05	0.508	0.010	0.00	0.00	0.000	0.000	0.00	0.00	0.000	0.000	0.00	0.00	0.000	0.000
J0030-5129	4.173	46.314	0.021	not	3.315	13.85	0.05	0.206	0.008	0.00	0.00	0.000	0.000	0.00	0.00	0.000	0.000	0.00	0.00	0.000	0.000
J0030-5129	4.173	46.314	0.021	not	3.783	13.98	0.06	0.307	0.013	13.22	0.07	0.133	0.009	0.00	0.00	0.000	0.000	0.00	0.00	0.000	0.000
J0030-5129	4.173	46.314	0.021	not	4.036	13.37	0.07	0.077	0.008	12.81	0.06	0.051	0.006	0.00	0.00	0.000	0.000	0.00	0.00	0.000	0.000
J0030-5129	4.173	46.314	0.021	not	3.577	13.41	0.05	0.088	0.006	0.00	0.00	0.000	0.000	0.00	0.00	0.000	0.000	0.00	0.00	0.000	0.000
J0030-5129	4.173	46.314	0.021	not	3.557	13.80	0.05	0.207	0.010	12.11	0.05	0.014	0.005	0.00	0.00	0.000	0.000	0.00	0.00	0.000	0.000
J0030-5129	4.173	46.314	0.021	not	3.355	14.06	0.04	0.384	0.012	0.00	0.00	0.000	0.000	0.00	0.00	0.000	0.000	0.00	0.00	0.000	0.000
J0034+1639	4.292	46.834	0.016	not	3.480	14.24	0.05	0.517	0.007	0.00	0.00	0.000	0.000	0.00	0.00	0.000	0.000	0.00	0.00	0.000	0.000
J0034+1639	4.292	46.834	0.016	not	3.428	13.83	0.04	0.261	0.007	0.00	0.00	0.000	0.000	0.00	0.00	0.000	0.000	0.00	0.00	0.000	0.000
J0034+1639	4.292	46.834	0.016	not	3.402	14.46	0.05	0.661	0.005	0.00	0.00	0.000	0.000	0.00	0.00	0.000	0.000	0.00	0.00	0.000	0.000
J0034+1639	4.292	46.834	0.016	not	3.684	13.34	0.06	0.078	0.006	0.00	0.00	0.000	0.000	0.00	0.00	0.000	0.000	0.00	0.00	0.000	0.000
J0034+1639	4.292	46.834	0.016	not	3.754	13.80	0.04	0.215	0.007	0.00	0.00	0.000	0.000	0.00	0.00	0.000	0.000	0.00	0.00	0.000	0.000
J0034+1639	4.292	46.834	0.016	not	3.656	13.29	0.01	0.070	0.005	0.00	0.00	0.000	0.000	0.00	0.00	0.000	0.000	0.00	0.00	0.000	0.000
J0034+1639	4.292	46.834	0.016	not	3.361	12.85	0.04	0.028	0.004	0.00	0.00	0.000	0.000	0.00	0.00	0.000	0.000	0.00	0.00	0.000	0.000
J0034+1639	4.292	46.834	0.016	not	3.204	14.63	0.06	0.886	0.007	0.00	0.00	0.000	0.000	0.00	0.00	0.000	0.000	0.00	0.00	0.000	0.000
J0034+1639	4.292	46.834	0.016	not	4.252	14.02	0.05	0.357	0.007	13.18	0.04	0.111	0.005	0.00	0.00	0.000	0.000	14.30	0.05	0.231	0.006
J0034+1639	4.292	46.834	0.016	not	4.283	14.28	0.05	0.343	0.003	13.47	0.05	0.198	0.005	0.00	0.00	0.000	0.000	0.00	0.00	0.600	0.004
J0034+1639	4.292	46.834	0.016	not	4.227	14.42	0.05	0.739	0.005	13.53	0.05	0.245	0.008	0.00	0.00	0.000	0.000	0.00	0.00	0.000	0.000

Tab. A.1 — Continued.

Quasar	z_{em}	L_{bol}	σL_{bol}	Radio type	z_{abs}	N CIV	σN CIV	W CIV	σW CIV	N SiIV	σN SiIV	W SiIV	σW SiIV	N NV	σN NV	W NV	σW NV	N CII	σN CII	W CII	σW CII
(1)	(2)	(3)	(4)	(5)	(6)	(7)	(8)	(9)	(10)	(11)	(12)	(13)	(14)	(15)	(16)	(17)	(18)	(19)	(20)	(21)	(22)
J0042-1020	3.863	46.991	0.009	RQ	2.852	13.31	0.04	0.076	0.003	0.00	0.00	0.000	0.000	0.00	0.00	0.000	0.000	0.00	0.00	0.000	0.000
J0042-1020	3.863	46.991	0.009	RQ	2.876	13.19	0.03	0.057	0.003	0.00	0.00	0.000	0.000	0.00	0.00	0.000	0.000	0.00	0.00	0.000	0.000
J0042-1020	3.863	46.991	0.009	RQ	3.028	13.89	0.06	0.264	0.006	0.00	0.00	0.000	0.000	0.00	0.00	0.000	0.000	0.00	0.00	0.000	0.000
J0042-1020	3.863	46.991	0.009	RQ	3.237	13.11	0.05	0.051	0.003	0.00	0.00	0.000	0.000	0.00	0.00	0.000	0.000	0.00	0.00	0.000	0.000
J0042-1020	3.863	46.991	0.009	RQ	3.334	12.75	0.06	0.022	0.003	0.00	0.00	0.000	0.000	0.00	0.00	0.000	0.000	0.00	0.00	0.000	0.000
J0042-1020	3.863	46.991	0.009	RQ	3.386	13.60	0.04	0.141	0.004	13.14	0.03	0.099	0.003	0.00	0.00	0.000	0.000	0.00	0.00	0.000	0.000
J0042-1020	3.863	46.991	0.009	RQ	3.521	13.50	0.06	0.060	0.004	0.00	0.00	0.000	0.000	0.00	0.00	0.000	0.000	0.00	0.00	0.000	0.000
J0042-1020	3.863	46.991	0.009	RQ	3.501	12.95	0.04	0.035	0.003	0.00	0.00	0.000	0.000	0.00	0.00	0.000	0.000	0.00	0.00	0.000	0.000
J0042-1020	3.863	46.991	0.009	RQ	3.629	14.53	0.06	0.705	0.004	14.10	0.07	0.629	0.005	0.00	0.00	0.000	0.000	0.00	0.00	0.000	0.000
J0042-1020	3.863	46.991	0.009	RQ	3.694	13.43	0.06	0.103	0.004	12.57	0.04	0.033	0.003	0.00	0.00	0.000	0.000	0.00	0.00	0.000	0.000
J0042-1020	3.863	46.991	0.009	RQ	3.787	13.87	0.04	0.257	0.004	12.73	0.05	0.044	0.003	0.00	0.00	0.000	0.000	0.00	0.00	0.000	0.000
J0042-1020	3.863	46.991	0.009	RQ	3.804	12.80	0.06	0.025	0.002	0.00	0.00	0.000	0.000	0.00	0.00	0.000	0.000	0.00	0.00	0.000	0.000
J0042-1020	3.863	46.991	0.009	RQ	3.810	13.62	0.04	0.126	0.003	0.00	0.00	0.000	0.000	0.00	0.00	0.000	0.000	0.00	0.00	0.000	0.000
J0048-2442	4.083	46.443	0.020	not	3.447	13.64	0.04	0.328	0.013	0.00	0.00	0.000	0.000	0.00	0.00	0.000	0.000	0.00	0.00	0.000	0.000
J0048-2442	4.083	46.443	0.020	not	3.156	14.66	0.03	0.837	0.012	0.00	0.00	0.000	0.000	0.00	0.00	0.000	0.000	0.00	0.00	0.000	0.000
J0048-2442	4.083	46.443	0.020	not	3.371	13.08	0.08	0.043	0.007	0.00	0.00	0.000	0.000	0.00	0.00	0.000	0.000	0.00	0.00	0.000	0.000
J0048-2442	4.083	46.443	0.020	not	3.758	13.58	0.05	0.139	0.009	13.11	0.05	0.103	0.009	0.00	0.00	0.000	0.000	0.00	0.00	0.000	0.000
J0048-2442	4.083	46.443	0.020	not	4.058	13.53	0.04	0.062	0.005	0.00	0.00	0.000	0.000	0.00	0.00	0.000	0.000	0.00	0.00	0.000	0.000
J0048-2442	4.083	46.443	0.020	not	3.737	13.79	0.20	0.197	0.010	0.00	0.00	0.000	0.000	0.00	0.00	0.000	0.000	0.00	0.00	0.000	0.000
J0048-2442	4.083	46.443	0.020	not	4.101	14.83	0.12	1.292	0.011	13.37	0.04	0.168	0.008	14.45	0.04	0.459	0.009	13.86	0.05	0.119	0.006
J0056-2808	3.635	46.509	0.017	not	2.729	14.56	0.05	1.082	0.011	0.00	0.00	0.000	0.000	0.00	0.00	0.000	0.000	0.00	0.00	0.000	0.000
J0056-2808	3.635	46.509	0.017	not	2.872	13.90	0.04	0.263	0.010	0.00	0.00	0.000	0.000	0.00	0.00	0.000	0.000	0.00	0.00	0.000	0.000
J0056-2808	3.635	46.509	0.017	not	3.057	13.46	0.05	0.100	0.006	0.00	0.00	0.000	0.000	0.00	0.00	0.000	0.000	0.00	0.00	0.000	0.000
J0056-2808	3.635	46.509	0.017	not	3.132	13.58	0.04	0.127	0.006	0.00	0.00	0.000	0.000	0.00	0.00	0.000	0.000	0.00	0.00	0.000	0.000
J0056-2808	3.635	46.509	0.017	not	3.313	13.52	0.05	0.124	0.008	0.00	0.00	0.000	0.000	0.00	0.00	0.000	0.000	0.00	0.00	0.000	0.000
J0056-2808	3.635	46.509	0.017	not	3.380	13.28	0.06	0.071	0.006	0.00	0.00	0.000	0.000	0.00	0.00	0.000	0.000	0.00	0.00	0.000	0.000
J0056-2808	3.635	46.509	0.017	not	3.505	13.08	0.05	0.044	0.005	0.00	0.00	0.000	0.000	0.00	0.00	0.000	0.000	0.00	0.00	0.000	0.000
J0056-2808	3.635	46.509	0.017	not	3.237	14.03	0.03	0.183	0.007	12.85	0.06	0.128	0.009	0.00	0.00	0.000	0.000	0.00	0.00	0.000	0.000
J0056-2808	3.635	46.509	0.017	not	3.620	14.21	0.05	0.485	0.004	13.13	0.03	0.121	0.009	0.00	0.00	0.000	0.000	0.00	0.00	0.000	0.000
J0056-2808	3.635	46.509	0.017	not	3.558	13.11	0.03	0.049	0.005	0.00	0.00	0.000	0.000	0.00	0.00	0.000	0.000	0.00	0.00	0.000	0.000
J0056-2808	3.635	46.509	0.017	not	3.580	14.46	0.05	0.658	0.007	13.95	0.06	0.393	0.010	0.00	0.00	0.000	0.000	14.62	0.06	0.330	0.007
J0057-2643	3.661	47.079	0.010	not	2.946	13.14	0.04	0.052	0.005	0.00	0.00	0.000	0.000	0.00	0.00	0.000	0.000	0.00	0.00	0.000	0.000
J0057-2643	3.661	47.079	0.010	not	2.951	14.27	0.06	0.326	0.007	0.00	0.00	0.000	0.000	0.00	0.00	0.000	0.000	0.00	0.00	0.000	0.000
J0057-2643	3.661	47.079	0.010	not	3.039	12.94	0.03	0.035	0.005	0.00	0.00	0.000	0.000	0.00	0.00	0.000	0.000	0.00	0.00	0.000	0.000
J0057-2643	3.661	47.079	0.010	not	3.086	13.31	0.06	0.074	0.005	12.46	0.05	0.024	0.002	0.00	0.00	0.000	0.000	0.00	0.00	0.000	0.000
J0057-2643	3.661	47.079	0.010	not	3.192	14.66	0.04	0.786	0.006	13.46	0.05	0.225	0.006	0.00	0.00	0.000	0.000	0.00	0.00	0.000	0.000
J0057-2643	3.661	47.079	0.010	not	3.527	13.58	0.06	0.141	0.006	0.00	0.00	0.000	0.000	0.00	0.00	0.000	0.000	0.00	0.00	0.000	0.000
J0057-2643	3.661	47.079	0.010	not	3.556	13.51	0.03	0.115	0.004	0.00	0.00	0.000	0.000	0.00	0.00	0.000	0.000	0.00	0.00	0.000	0.000
J0057-2643	3.661	47.079	0.010	not	3.573	13.38	0.06	0.096	0.005	0.00	0.00	0.000	0.000	0.00	0.00	0.000	0.000	0.00	0.00	0.000	0.000
J0057-2643	3.661	47.079	0.010	not	3.602	14.14	0.04	0.435	0.004	12.93	0.04	0.073	0.005	0.00	0.00	0.000	0.000	0.00	0.00	0.000	0.000
J0100-2708	3.546	46.508	0.016	not	2.555	13.87	0.06	0.238	0.012	0.00	0.00	0.000	0.000	0.00	0.00	0.000	0.000	0.00	0.00	0.000	0.000

Tab. A.1 — Continued.

Quasar	z_{em}	L_{bol}	σL_{bol}	Radio type	z_{abs}	N CIV	σ N CIV	W CIV	σ W CIV	N SiIV	σ N SiIV	W SiIV	σ W SiIV	N NV	σ N NV	W NV	σW NV	N CII	σ N CII	W CII	σW CII
(1)	(2)	(3)	(4)	(5)	(6)	(7)	(8)	(9)	(10)	(11)	(12)	(13)	(14)	(15)	(16)	(17)	(18)	(19)	(20)	(21)	(22)
J0100-2708	3.546	46.508	0.016	not	2.647	13.02	0.07	0.039	0.005	0.00	0.00	0.000	0.000	0.00	0.00	0.000	0.000	0.00	0.00	0.000	0.000
J0100-2708	3.546	46.508	0.016	not	2.636	14.72	0.04	0.719	0.010	0.00	0.00	0.000	0.000	0.00	0.00	0.000	0.000	0.00	0.00	0.000	0.000
J0100-2708	3.546	46.508	0.016	not	3.084	13.08	0.07	0.044	0.006	0.00	0.00	0.000	0.000	0.00	0.00	0.000	0.000	0.00	0.00	0.000	0.000
J0100-2708	3.546	46.508	0.016	not	3.356	13.42	0.04	0.098	0.007	0.00	0.00	0.000	0.000	0.00	0.00	0.000	0.000	0.00	0.00	0.000	0.000
J0100-2708	3.546	46.508	0.016	not	3.243	13.11	0.06	0.049	0.007	0.00	0.00	0.000	0.000	0.00	0.00	0.000	0.000	0.00	0.00	0.000	0.000
J0100-2708	3.546	46.508	0.016	not	3.468	13.59	0.05	0.122	0.006	12.99	0.05	0.081	0.008	0.00	0.00	0.000	0.000	0.00	0.00	0.000	0.000
J0113-2803	4.314	47.225	0.013	not	3.729	13.49	0.03	0.117	0.007	0.00	0.00	0.000	0.000	0.00	0.00	0.000	0.000	0.00	0.00	0.000	0.000
J0113-2803	4.314	47.225	0.013	not	3.830	13.58	0.04	0.144	0.007	0.00	0.00	0.118	0.007	0.00	0.00	0.000	0.000	0.00	0.00	0.000	0.000
J0113-2803	4.314	47.225	0.013	not	3.890	14.57	0.05	0.791	0.011	0.00	0.00	0.705	0.008	0.00	0.00	0.000	0.000	0.00	0.00	0.000	0.000
J0113-2803	4.314	47.225	0.013	not	4.071	13.59	0.03	0.138	0.005	0.00	0.00	0.000	0.000	0.00	0.00	0.000	0.000	0.00	0.00	0.000	0.000
J0113-2803	4.314	47.225	0.013	not	4.122	13.11	0.06	0.048	0.005	0.00	0.00	0.000	0.000	0.00	0.00	0.000	0.000	0.00	0.00	0.000	0.000
J0113-2803	4.314	47.225	0.013	not	4.273	13.98	0.06	0.287	0.005	0.00	0.00	0.000	0.000	14.64	0.04	0.401	0.007	0.00	0.00	0.000	0.000
J0113-2803	4.314	47.225	0.013	not	4.333	14.17	0.07	0.367	0.005	0.00	0.00	0.000	0.000	0.00	0.00	0.000	0.000	0.00	0.00	0.000	0.000
J0117+1552	4.243	46.812	0.012	not	3.646	14.54	0.08	0.352	0.004	13.55	0.06	0.130	0.003	0.00	0.00	0.000	0.000	0.00	0.00	0.000	0.000
J0117+1552	4.243	46.812	0.012	not	3.696	13.36	0.04	0.119	0.005	0.00	0.00	0.000	0.000	0.00	0.00	0.000	0.000	0.00	0.00	0.000	0.000
J0117+1552	4.243	46.812	0.012	not	3.251	12.83	0.06	0.028	0.003	0.00	0.00	0.000	0.000	0.00	0.00	0.000	0.000	0.00	0.00	0.000	0.000
J0117+1552	4.243	46.812	0.012	not	3.231	14.13	0.05	0.235	0.005	0.00	0.00	0.000	0.000	0.00	0.00	0.000	0.000	0.00	0.00	0.000	0.000
J0117+1552	4.243	46.812	0.012	not	3.275	13.31	0.06	0.079	0.004	0.00	0.00	0.000	0.000	0.00	0.00	0.000	0.000	0.00	0.00	0.000	0.000
J0117+1552	4.243	46.812	0.012	not	4.033	13.70	0.07	0.179	0.005	0.00	0.00	0.000	0.000	0.00	0.00	0.000	0.000	0.00	0.00	0.000	0.000
J0117+1552	4.243	46.812	0.012	not	4.071	13.29	0.05	0.072	0.004	12.76	0.05	0.046	0.003	0.00	0.00	0.000	0.000	0.00	0.00	0.000	0.000
J0117+1552	4.243	46.812	0.012	not	4.127	12.76	0.07	0.022	0.003	0.00	0.00	0.000	0.000	0.00	0.00	0.000	0.000	0.00	0.00	0.000	0.000
J0117+1552	4.243	46.812	0.012	not	4.146	13.79	0.06	0.188	0.005	12.50	0.03	0.027	0.004	0.00	0.00	0.000	0.000	0.00	0.00	0.000	0.000
J0117+1552	4.243	46.812	0.012	not	4.096	12.93	0.04	0.035	0.004	0.00	0.00	0.000	0.000	0.00	0.00	0.000	0.000	0.00	0.00	0.000	0.000
J0117+1552	4.243	46.812	0.012	not	3.495	13.24	0.06	0.065	0.004	0.00	0.00	0.000	0.000	0.00	0.00	0.000	0.000	0.00	0.00	0.000	0.000
J0121+0347	4.125	46.689	0.020	RL	3.362	14.04	0.05	0.343	0.009	0.00	0.00	0.000	0.000	0.00	0.00	0.000	0.000	0.00	0.00	0.000	0.000
J0121+0347	4.125	46.689	0.020	RL	3.426	13.38	0.03	0.085	0.005	0.00	0.00	0.000	0.000	0.00	0.00	0.000	0.000	0.00	0.00	0.000	0.000
J0121+0347	4.125	46.689	0.020	RL	3.528	13.28	0.04	0.069	0.005	0.00	0.00	0.000	0.000	0.00	0.00	0.000	0.000	0.00	0.00	0.000	0.000
J0121+0347	4.125	46.689	0.020	RL	3.570	13.86	0.06	0.263	0.008	0.00	0.00	0.000	0.000	0.00	0.00	0.000	0.000	0.00	0.00	0.000	0.000
J0121+0347	4.125	46.689	0.020	RL	3.800	13.22	0.03	0.060	0.006	0.00	0.00	0.000	0.000	0.00	0.00	0.000	0.000	0.00	0.00	0.000	0.000
J0121+0347	4.125	46.689	0.020	RL	3.794	12.96	0.04	0.035	0.005	0.00	0.00	0.000	0.000	0.00	0.00	0.000	0.000	0.00	0.00	0.000	0.000
J0121+0347	4.125	46.689	0.020	RL	4.105	13.03	0.06	0.042	0.004	0.00	0.00	0.000	0.000	13.79	0.05	0.120	0.005	0.00	0.00	0.000	0.000
J0121+0347	4.125	46.689	0.020	RL	3.806	13.55	0.04	0.123	0.007	0.00	0.00	0.000	0.000	0.00	0.00	0.000	0.000	0.00	0.00	0.000	0.000
J0124+0044	3.837	46.853	0.015	RQ	2.834	13.89	0.04	0.278	0.006	0.00	0.00	0.000	0.000	0.00	0.00	0.000	0.000	0.00	0.00	0.000	0.000
J0124+0044	3.837	46.853	0.015	RQ	2.910	13.92	0.07	0.284	0.004	0.00	0.00	0.000	0.000	0.00	0.00	0.000	0.000	0.00	0.00	0.000	0.000
J0124+0044	3.837	46.853	0.015	RQ	2.987	14.44	0.05	0.509	0.008	0.00	0.00	0.000	0.000	0.00	0.00	0.000	0.000	0.00	0.00	0.000	0.000
J0124+0044	3.837	46.853	0.015	RQ	3.065	14.18	0.04	0.410	0.007	0.00	0.00	0.000	0.000	0.00	0.00	0.000	0.000	0.00	0.00	0.000	0.000
J0124+0044	3.837	46.853	0.015	RQ	3.077	13.85	0.05	0.254	0.008	0.00	0.00	0.000	0.000	0.00	0.00	0.000	0.000	0.00	0.00	0.000	0.000
J0124+0044	3.837	46.853	0.015	RQ	3.188	13.07	0.07	0.045	0.004	0.00	0.00	0.000	0.000	0.00	0.00	0.000	0.000	0.00	0.00	0.000	0.000
J0124+0044	3.837	46.853	0.015	RQ	3.393	14.00	0.05	0.296	0.005	13.19	0.05	0.119	0.006	0.00	0.00	0.000	0.000	0.00	0.00	0.000	0.000
J0124+0044	3.837	46.853	0.015	RQ	3.474	12.93	0.06	0.045	0.004	0.00	0.00	0.000	0.000	0.00	0.00	0.000	0.000	0.00	0.00	0.000	0.000
J0124+0044	3.837	46.853	0.015	RQ	3.500	13.45	0.03	0.188	0.008	0.00	0.00	0.000	0.000	0.00	0.00	0.000	0.000	0.00	0.00	0.000	0.000

Tab. A.1 — Continued.

Quasar	z_{em}	L_{bol}	σL_{bol}	Radio type	z_{abs}	N CIV	σ N CIV	W CIV	σ W CIV	N SiIV	σ N SiIV	W SiIV	σ W SiIV	N NV	σ N NV	W NV	σW NV	N CII	σ N CII	W CII	σW CII
(1)	(2)	(3)	(4)	(5)	(6)	(7)	(8)	(9)	(10)	(11)	(12)	(13)	(14)	(15)	(16)	(17)	(18)	(19)	(20)	(21)	(22)
J0124+0044	3.837	46.853	0.015	RQ	3.549	14.12	0.05	0.427	0.008	13.61	0.04	0.259	0.005	0.00	0.00	0.000	0.000	0.00	0.00	0.000	0.000
J0124+0044	3.837	46.853	0.015	RQ	3.675	14.35	0.07	0.420	0.008	13.88	0.06	0.428	0.007	0.00	0.00	0.000	0.000	0.00	0.00	0.000	0.000
J0124+0044	3.837	46.853	0.015	RQ	3.766	13.71	0.05	0.193	0.007	13.08	0.05	0.102	0.007	0.00	0.00	0.000	0.000	0.00	0.00	0.000	0.000
J0132+1341	4.152	46.828	0.012	not	3.968	14.54	0.04	0.684	0.007	14.12	0.06	0.745	0.009	0.00	0.00	0.000	0.000	0.00	0.00	0.000	0.000
J0132+1341	4.152	46.828	0.012	not	3.100	14.57	0.05	0.823	0.008	0.00	0.00	0.000	0.000	0.00	0.00	0.000	0.000	0.00	0.00	0.000	0.000
J0132+1341	4.152	46.828	0.012	not	3.837	13.01	0.06	0.039	0.004	0.00	0.00	0.000	0.000	0.00	0.00	0.000	0.000	0.00	0.00	0.000	0.000
J0132+1341	4.152	46.828	0.012	not	4.056	14.24	0.07	0.467	0.007	12.89	0.03	0.064	0.006	0.00	0.00	0.000	0.000	0.00	0.00	0.000	0.000
J0132+1341	4.152	46.828	0.012	not	4.078	14.44	0.04	0.822	0.010	13.85	0.05	0.498	0.008	0.00	0.00	0.000	0.000	14.19	0.05	0.220	0.007
J0132+1341	4.152	46.828	0.012	not	4.104	14.10	0.05	0.406	0.007	13.47	0.05	0.213	0.006	0.00	0.00	0.000	0.000	0.00	0.00	0.000	0.000
J0132+1341	4.152	46.828	0.012	not	3.885	13.34	0.07	0.081	0.005	0.00	0.00	0.000	0.000	0.00	0.00	0.000	0.000	0.00	0.00	0.000	0.000
J0134+0400	4.185	46.901	0.008	RQ	3.088	14.17	0.05	0.441	0.003	0.00	0.00	0.000	0.000	0.00	0.00	0.000	0.000	0.00	0.00	0.000	0.000
J0134+0400	4.185	46.901	0.008	RQ	3.138	14.52	0.04	0.816	0.004	0.00	0.00	0.000	0.000	0.00	0.00	0.000	0.000	0.00	0.00	0.000	0.000
J0134+0400	4.185	46.901	0.008	RQ	3.229	13.81	0.07	0.221	0.004	0.00	0.00	0.000	0.000	0.00	0.00	0.000	0.000	0.00	0.00	0.000	0.000
J0134+0400	4.185	46.901	0.008	RQ	3.302	13.17	0.07	0.056	0.004	0.00	0.00	0.000	0.000	0.00	0.00	0.000	0.000	0.00	0.00	0.000	0.000
J0134+0400	4.185	46.901	0.008	RQ	3.501	14.18	0.08	0.425	0.004	0.00	0.00	0.000	0.000	0.00	0.00	0.000	0.000	0.00	0.00	0.000	0.000
J0134+0400	4.185	46.901	0.008	RQ	3.598	13.41	0.06	0.096	0.004	0.00	0.00	0.000	0.000	0.00	0.00	0.000	0.000	0.00	0.00	0.000	0.000
J0134+0400	4.185	46.901	0.008	RQ	3.620	14.24	0.05	0.463	0.003	13.67	0.05	0.319	0.004	0.00	0.00	0.000	0.000	0.00	0.00	0.000	0.000
J0134+0400	4.185	46.901	0.008	RQ	3.772	14.36	0.05	0.620	0.006	13.89	0.06	0.482	0.005	0.00	0.00	0.000	0.000	0.00	0.00	0.000	0.000
J0134+0400	4.185	46.901	0.008	RQ	3.798	12.95	0.03	0.034	0.002	0.00	0.00	0.000	0.000	0.00	0.00	0.000	0.000	0.00	0.00	0.000	0.000
J0134+0400	4.185	46.901	0.008	RQ	4.048	13.37	0.05	0.085	0.003	0.00	0.00	0.000	0.000	0.00	0.00	0.000	0.000	0.00	0.00	0.000	0.000
J0134+0400	4.185	46.901	0.008	RQ	4.025	14.10	0.06	0.237	0.005	0.00	0.00	0.000	0.000	0.00	0.00	0.000	0.000	0.00	0.00	0.000	0.000
J0134+0400	4.185	46.901	0.008	RQ	4.168	12.95	0.06	0.034	0.002	0.00	0.00	0.000	0.000	0.00	0.00	0.000	0.000	0.00	0.00	0.000	0.000
J0134+0400	4.185	46.901	0.008	RQ	4.117	0.00	0.00	1.240	0.004	13.96	0.06	0.515	0.006	0.00	0.00	0.000	0.000	13.75	0.04	0.110	0.006
J0134+0400	4.185	46.901	0.008	RQ	3.986	13.81	0.03	0.120	0.005	0.00	0.00	0.000	0.000	0.00	0.00	0.000	0.000	0.00	0.00	0.000	0.000
J0134+0400	4.185	46.901	0.008	RQ	3.999	13.80	0.06	0.207	0.004	13.84	0.04	0.249	0.004	0.00	0.00	0.000	0.000	0.00	0.00	0.000	0.000
J0137-4224	3.971	46.372	0.021	not	2.970	14.22	0.04	0.288	0.006	0.00	0.00	0.000	0.000	0.00	0.00	0.000	0.000	0.00	0.00	0.000	0.000
J0137-4224	3.971	46.372	0.021	not	3.064	13.51	0.06	0.116	0.008	0.00	0.00	0.000	0.000	0.00	0.00	0.000	0.000	0.00	0.00	0.000	0.000
J0137-4224	3.971	46.372	0.021	not	3.031	13.54	0.03	0.125	0.009	0.00	0.00	0.000	0.000	0.00	0.00	0.000	0.000	0.00	0.00	0.000	0.000
J0137-4224	3.971	46.372	0.021	not	3.074	14.33	0.05	0.456	0.009	0.00	0.00	0.000	0.000	0.00	0.00	0.000	0.000	0.00	0.00	0.000	0.000
J0137-4224	3.971	46.372	0.021	not	3.102	13.85	0.04	0.244	0.012	0.00	0.00	0.000	0.000	0.00	0.00	0.000	0.000	0.00	0.00	0.000	0.000
J0137-4224	3.971	46.372	0.021	not	3.817	13.50	0.03	0.113	0.007	0.00	0.00	0.000	0.000	0.00	0.00	0.000	0.000	0.00	0.00	0.000	0.000
J0137-4224	3.971	46.372	0.021	not	3.238	13.22	0.06	0.065	0.007	0.00	0.00	0.000	0.000	0.00	0.00	0.000	0.000	0.00	0.00	0.000	0.000
J0153-0011	4.195	46.713	0.030	RL	3.570	13.26	0.02	0.062	0.008	0.00	0.00	0.000	0.000	0.00	0.00	0.000	0.000	0.00	0.00	0.000	0.000
J0153-0011	4.195	46.713	0.030	RL	3.370	13.32	0.03	0.076	0.009	0.00	0.00	0.000	0.000	0.00	0.00	0.000	0.000	0.00	0.00	0.000	0.000
J0153-0011	4.195	46.713	0.030	RL	3.324	13.67	0.04	0.167	0.013	0.00	0.00	0.000	0.000	0.00	0.00	0.000	0.000	0.00	0.00	0.000	0.000
J0153-0011	4.195	46.713	0.030	RL	4.193	13.51	0.05	0.117	0.006	0.00	0.00	0.000	0.000	0.00	0.00	0.000	0.000	0.00	0.00	0.000	0.000
J0153-0011	4.195	46.713	0.030	RL	4.169	14.83	0.04	1.116	0.013	0.00	0.00	0.000	0.000	15.07	0.07	1.151	0.011	0.00	0.00	0.000	0.000
J0153-0011	4.195	46.713	0.030	RL	3.873	13.80	0.07	0.206	0.011	0.00	0.00	0.000	0.000	0.00	0.00	0.000	0.000	0.00	0.00	0.000	0.000
J0153-0011	4.195	46.713	0.030	RL	3.100	13.09	0.06	0.046	0.005	0.00	0.00	0.000	0.000	0.00	0.00	0.000	0.000	0.00	0.00	0.000	0.000

Bibliography

Aguirre, A., Dow-Hygelund, C., Schaye, J., and Theuns, T. (2008). Metallicity of the Intergalactic Medium Using Pixel Statistics. IV. Oxygen. *The Astrophysical Journal*, 689:851–864.

Aguirre, A., Schaye, J., Kim, T.-S., Theuns, T., Rauch, M., and Sargent, W. L. W. (2004). Metallicity of the Intergalactic Medium Using Pixel Statistics. III. Silicon. *The Astrophysical Journal*, 602:38–50.

Alexander, D. M. and Hickox, R. C. (2012). What drives the growth of black holes? *nar*, 56:93–121.

Anderson, S. F., Weymann, R. J., Foltz, C. B., and Chaffee, Jr., F. H. (1987). Associated C IV absorption in radio-loud QSOs - The '3C mini-survey'. *Astronomic. J.*, 94:278–288.

Antonucci, R. (1993). Unified models for active galactic nuclei and quasars. *Annu. Rev. Astron. Astrophys.*, 31:473–521.

Arav, N., Borguet, B., Chamberlain, C., Edmonds, D., and Danforth, C. (2013). Quasar outflows and AGN feedback in the extreme UV: HST/COS observations of HE 0238-1904. *MNRAS*, 436:3286–3305.

Arnaud, M. and Rothenflug, R. (1985). An updated evaluation of recombination and ionization rates. *Astron. Astrophys. Supp. Series*, 60:425–457.

Baade, W. and Minkowski, R. (1954). Identification of the Radio Sources in Cassiopeia, Cygnus A, and Puppis A. *The Astrophysical Journal*, 119:206.

Baes, M., Buyle, P., Hau, G. K. T., and Dejonghe, H. (2003). Observational evidence for a connection between supermassive black holes and dark matter haloes. *MNRAS*, 341:L44–L48.

Bahcall, J. N. and Salpeter, E. E. (1965). On the Interaction of Radiation from Distant Sources with the Intervening Medium. *The Astrophysical Journal*, 142:1677–1680.

Baker, J. C., Hunstead, R. W., Athreya, R. M., Barthel, P. D., de Silva, E., Lehnert, M. D., and Saunders, R. D. E. (2002). Associated Absorption in Radio Quasars.

I. C IV Absorption and the Growth of Radio Sources. *The Astrophysical Journal*, 568:592–609.

Baldwin, J. A., Phillips, M. M., and Terlevich, R. (1981). Classification parameters for the emission-line spectra of extragalactic objects. *pasp*, 93:5–19.

Balick, B. and Heckman, T. M. (1982). Extranuclear clues to the origin and evolution of activity in galaxies. *Annu. Rev. Astron. Astrophys.*, 20:431–468.

Barlow, T. A. and Sargent, W. L. W. (1997). Keck High Resolution Spectroscopy of PKS 0123+257: Intrinsic Absorption in a Radio-Loud Quasar. *Astronomic. J.*, 113:136.

Barvainis, R. (1987). Hot dust and the near-infrared bump in the continuum spectra of quasars and active galactic nuclei. *The Astrophysical Journal*, 320:537–544.

Barvainis, R. (1993). Free-free emission and the big blue bump in active galactic nuclei. *The Astrophysical Journal*, 412:513–523.

Bechtold, J. (2001). Quasar Absorption Lines. *ArXiv Astrophysics e-prints*.

Becker, R. H., White, R. L., Gregg, M. D., Brotherton, M. S., Laurent-Muehleisen, S. A., and Arav, N. (2000). Properties of Radio-selected Broad Absorption Line Quasars from the First Bright Quasar Survey. *The Astrophysical Journal*, 538:72–82.

Becker, R. H., White, R. L., Gregg, M. D., Laurent-Muehleisen, S. A., Brotherton, M. S., Impey, C. D., Chaffee, F. H., Richards, G. T., Helfand, D. J., Lacy, M., Courbin, F., and Proctor, D. D. (2001). The FIRST Bright Quasar Survey. III. The South Galactic Cap. *apjs*, 135:227–262.

Becker, R. H., White, R. L., and Helfand, D. J. (1995). The FIRST Survey: Faint Images of the Radio Sky at Twenty Centimeters. *The Astrophysical Journal*, 450:559.

Beifiori, A., Courteau, S., Corsini, E. M., and Zhu, Y. (2012). On the correlations between galaxy properties and supermassive black hole mass. *MNRAS*, 419:2497–2528.

Benson, A. J., Bower, R. G., Frenk, C. S., Lacey, C. G., Baugh, C. M., and Cole, S. (2003). What Shapes the Luminosity Function of Galaxies? *The Astrophysical Journal*, 599:38–49.

Berg, T. A. M. and et al. (2016). . *(submitted)*.

Bergeron, J. and Herbert-Fort, S. (2005). Highly ionised absorbers at high redshift. In Williams, P., Shu, C.-G., and Menard, B., editors, *IAU Colloq. 199: Probing Galaxies through Quasar Absorption Lines*, pages 265–280.

Blandford, R. D. and Begelman, M. C. (2004). Two-dimensional adiabatic flows on to a black hole - I. Fluid accretion. *MNRAS*, 349:68–86.

Blandford, R. D. and Payne, D. G. (1982). Hydromagnetic flows from accretion discs and the production of radio jets. *MNRAS*, 199:883–903.

Boksenberg, A. and Sargent, W. L. W. (2015). Properties of QSO Metal-line Absorption Systems at High Redshifts: Nature and Evolution of the Absorbers and New Evidence on Escape of Ionizing Radiation from Galaxies. *apjs*, 218:7.

Booth, C. M. and Schaye, J. (2009). Cosmological simulations of the growth of supermassive black holes and feedback from active galactic nuclei: method and tests. *MNRAS*, 398:53–74.

Booth, C. M. and Schaye, J. (2010). Dark matter haloes determine the masses of supermassive black holes. *MNRAS*, 405:L1–L5.

Bourne, M. A., Nayakshin, S., and Hobbs, A. (2014). Black hole feedback in a multiphase interstellar medium. *MNRAS*, 441:3055–3064.

Bower, R. G., Benson, A. J., and Crain, R. A. (2012). What shapes the galaxy mass function? Exploring the roles of supernova-driven winds and active galactic nuclei. *MNRAS*, 422:2816–2840.

Bower, R. G., Benson, A. J., Malbon, R., Helly, J. C., Frenk, C. S., Baugh, C. M., Cole, S., and Lacey, C. G. (2006). Breaking the hierarchy of galaxy formation. *MNRAS*, 370:645–655.

Bowler, R. A. A., Hewett, P. C., Allen, J. T., and Ferland, G. J. (2014). Line-driven radiative outflows in luminous quasars. *MNRAS*, 445:359–377.

Brotherton, M. S., van Breugel, W., Smith, R. J., Boyle, B. J., Shanks, T., Croom, S. M., Miller, L., and Becker, R. H. (1998). Discovery of Radio-Loud Broad Absorption Line Quasars Using Ultraviolet Excess and Deep Radio Selection. *The Astrophysical Journal Letters*, 505:L7–L10.

Burbidge, G. R., Burbidge, M., Hoyle, F., and Lynds, C. R. (1966). On the Interpretation of the Line Spectra of Quasi-Stellar Objects. *Nature*, 210:774–778.

Burkert, A. and Tremaine, S. (2010). A Correlation Between Central Supermassive Black Holes and the Globular Cluster Systems of Early-type Galaxies. *The Astrophysical Journal*, 720:516–521.

Calura, F. and Menci, N. (2009). Chemical evolution of local galaxies in a hierarchical model. *MNRAS*, 400:1347–1365.

Cano-Díaz, M., Maiolino, R., Marconi, A., Netzer, H., Shemmer, O., and Cresci, G. (2012). Observational evidence of quasar feedback quenching star formation at high redshift. *Astron. Astrophys.*, 537:L8.

Capellupo, D. M., Hamann, F., Shields, J. C., Barlow, T. A., and Rodriguez, P. (2010). Variability in Quasar Broad Absorption Line Outflows. In Peterson, B. M., Somerville, R. S., and Storchi-Bergmann, T., editors, *Co-Evolution of Central Black Holes and Galaxies*, volume 267 of *IAU Symposium*, pages 394–394.

Carswell, R. F. and Rees, M. J. (1987). Constraints on voids at high redshifts from Ly-alpha absorbers. *MNRAS*, 224:13P–16P.

Charlton, J. and Churchill, C. (2000). *Quasistellar Objects: Intervening Absorption Lines*.

Chartas, G., Charlton, J., Eracleous, M., Giustini, M., Hidalgo, P. R., Ganguly, R., Hamann, F., Misawa, T., and Tytler, D. (2009). High velocity outflows in narrow absorption line quasars. *nar*, 53:128–132.

Churchill, C. W., Schneider, D. P., Schmidt, M., and Gunn, J. E. (1999). An Unusual "Mini-BAL" Quasar at Z=4.59. *Astronomic. J.*, 117:2573–2581.

Cicone, C., Maiolino, R., Sturm, E., Graciá-Carpio, J., Feruglio, C., Neri, R., Aalto, S., Davies, R., Fiore, F., Fischer, J., García-Burillo, S., González-Alfonso, E., Hailey-Dunsheath, S., Piconcelli, E., and Veilleux, S. (2014). Massive molecular outflows and evidence for AGN feedback from CO observations. *Astron. Astrophys.*, 562:A21.

Ciotti, L. and Ostriker, J. P. (1997). Cooling Flows and Quasars: Different Aspects of the Same Phenomenon? I. Concepts. *The Astrophysical Journal Letters*, 487:L105–L108.

Colberg, J. M. and Di Matteo, T. (2008). Supermassive black holes and their environments. *MNRAS*, 387:1163–1178.

Costa, T., Sijacki, D., and Haehnelt, M. G. (2014). Feedback from active galactic nuclei: energy- versus momentum-driving. *MNRAS*, 444:2355–2376.

Cowie, L. L. and Songaila, A. (1998). Heavy-element enrichment in low-density regions of the intergalactic medium. *Nature*, 394:44–46.

Cowie, L. L., Songaila, A., Kim, T.-S., and Hu, E. M. (1995). The metallicity and internal structure of the Lyman-alpha forest clouds. *Astronomic. J.*, 109:1522–1530.

Crenshaw, D. M., Kraemer, S. B., Boggess, A., Maran, S. P., Mushotzky, R. F., and Wu, C.-C. (1999). Intrinsic Absorption Lines in Seyfert 1 Galaxies. I. Ultraviolet Spectra from the Hubble Space Telescope. *The Astrophysical Journal*, 516:750–768.

Crenshaw, D. M., Kraemer, S. B., and George, I. M. (2003). Mass Loss from the Nuclei of Active Galaxies. *Annu. Rev. Astron. Astrophys.*, 41:117–167.

Croton, D. J., Springel, V., White, S. D. M., De Lucia, G., Frenk, C. S., Gao, L., Jenkins, A., Kauffmann, G., Navarro, J. F., and Yoshida, N. (2006). The many lives of active galactic nuclei: cooling flows, black holes and the luminosities and colours of galaxies. *MNRAS*, 365:11–28.

Dai, X., Shankar, F., and Sivakoff, G. R. (2008). 2MASS Reveals a Large Intrinsic Fraction of BALQSOs. *The Astrophysical Journal*, 672:108–114.

Dai, X., Shankar, F., and Sivakoff, G. R. (2012). The Intrinsic Fractions and Radio Properties of Low-ionization Broad Absorption Line Quasars. *The Astrophysical Journal*, 757:180.

Debuhr, J., Quataert, E., and Ma, C.-P. (2011). The growth of massive black holes in galaxy merger simulations with feedback by radiation pressure. *MNRAS*, 412:1341–1360.

Debuhr, J., Quataert, E., and Ma, C.-P. (2012). Galaxy-scale outflows driven by active galactic nuclei. *MNRAS*, 420:2221–2231.

Debuhr, J., Quataert, E., Ma, C.-P., and Hopkins, P. (2010). Self-regulated black hole growth via momentum deposition in galaxy merger simulations. *MNRAS*, 406:L55–L59.

Di Matteo, T., Colberg, J., Springel, V., Hernquist, L., and Sijacki, D. (2008). Direct Cosmological Simulations of the Growth of Black Holes and Galaxies. *The Astrophysical Journal*, 676:33–53.

Di Matteo, T., Croft, R. A. C., Springel, V., and Hernquist, L. (2003). Black Hole Growth and Activity in a Λ Cold Dark Matter Universe. *The Astrophysical Journal*, 593:56–68.

Di Matteo, T., Springel, V., and Hernquist, L. (2005). Energy input from quasars regulates the growth and activity of black holes and their host galaxies. *Nature*, 433:604–607.

Dietrich, M., Hamann, F., Shields, J. C., Constantin, A., Heidt, J., Jäger, K., Vestergaard, M., and Wagner, S. J. (2003). Quasar Elemental Abundances at High Redshifts. *The Astrophysical Journal*, 589:722–732.

D'Odorico, V., Calura, F., Cristiani, S., and Viel, M. (2010). The rise of the CIV mass density at z $<$ 2.5. *MNRAS*, 401:2715–2721.

D'Odorico, V., Calura, F., Cristiani, S., and Viel, M. (2016). Metals in the $z \sim 3$ intergalactic medium: results from an ultra-high signal-to-noise ratio UVES quasar spectrum. *(MNRAS submitted)*.

D'Odorico, V., Cristiani, S., Romano, D., Granato, G. L., and Danese, L. (2004). Chemical abundances in QSO host galaxies and environments from narrow absorption line systems. *MNRAS*, 351:976–988.

Dubois, Y., Devriendt, J., Slyz, A., and Teyssier, R. (2012). Self-regulated growth of supermassive black holes by a dual jet-heating active galactic nucleus feedback mechanism: methods, tests and implications for cosmological simulations. *MNRAS*, 420:2662–2683.

Dyson, J. E. and Williams, D. A. (1997). *The physics of the interstellar medium*.

Ellison, S. L., Songaila, A., Schaye, J., and Pettini, M. (2000). The Enrichment History of the Intergalactic Medium-Measuring the C IV/H I Ratio in the Lyα Forest. *Astronomic. J.*, 120:1175–1191.

Elvis, M. (2000). A Structure for Quasars. *The Astrophysical Journal*, 545:63–76.

Elvis, M. (2006). Quasar structure and cosmological feedback. *memsai*, 77:573.

Elvis, M., Wilkes, B. J., McDowell, J. C., Green, R. F., Bechtold, J., Willner, S. P., Oey, M. S., Polomski, E., and Cutri, R. (1994). Atlas of quasar energy distributions. *apjs*, 95:1–68.

Everett, J. E. (2005). Radiative Transfer and Acceleration in Magnetocentrifugal Winds. *The Astrophysical Journal*, 631:689–706.

Fabian, A. C. (1999). The obscured growth of massive black holes. *MNRAS*, 308:L39–L43.

Fabian, A. C. (2012). Observational Evidence of Active Galactic Nuclei Feedback. *Annu. Rev. Astron. Astrophys.*, 50:455–489.

Fabian, A. C. and Iwasawa, K. (1999). The mass density in black holes inferred from the X-ray background. *MNRAS*, 303:L34–L36.

Fardal, M. A., Katz, N., Weinberg, D. H., and Davé, R. (2007). On the evolutionary history of stars and their fossil mass and light. *MNRAS*, 379:985–1002.

Farina, E. P., Falomo, R., Decarli, R., Treves, A., and Kotilainen, J. K. (2013). On the cool gaseous haloes of quasars. *MNRAS*, 429:1267–1277.

Farina, E. P., Falomo, R., Scarpa, R., Decarli, R., Treves, A., and Kotilainen, J. K. (2014). The extent of the Mg II absorbing circumgalactic medium of quasars. *MNRAS*, 441:886–899.

Farrah, D., Lacy, M., Priddey, R., Borys, C., and Afonso, J. (2007). Evidence that FeLoBALs May Signify the Transition between an Ultraluminous Infrared Galaxy and a Quasar. *The Astrophysical Journal Letters*, 662:L59–L62.

Faucher-Giguère, C.-A. and Quataert, E. (2012). The physics of galactic winds driven by active galactic nuclei. *MNRAS*, 425:605–622.

Fechner, C. and Richter, P. (2009). The nature of N V absorbers at high redshift. *Astron. Astrophys.*, 496:31–44.

Ferland, G. J., Porter, R. L., van Hoof, P. A. M., Williams, R. J. R., Abel, N. P., Lykins, M. L., Shaw, G., Henney, W. J., and Stancil, P. C. (2013). The 2013 Release of Cloudy. *rmxaa*, 49:137–163.

Ferrarese, L. (2002). Beyond the Bulge: A Fundamental Relation between Supermassive Black Holes and Dark Matter Halos. *The Astrophysical Journal*, 578:90–97.

Ferrarese, L. and Merritt, D. (2000). A Fundamental Relation between Supermassive Black Holes and Their Host Galaxies. *The Astrophysical Journal Letters*, 539:L9–L12.

Foltz, C. B., Chaffee, F. H., Hewett, P. C., Weymann, R. J., Anderson, S. F., and MacAlpine, G. M. (1989). The large, bright QSO survey. II - QSOs in three equatorial fields. *Astronomic. J.*, 98:1959–1988.

Foltz, C. B., Weymann, R. J., Morris, S. L., and Turnshek, D. A. (1987). The complex absorption spectrum of the broad absorption line QSO 1303 + 308. *The Astrophysical Journal*, 317:450–459.

Foltz, C. B., Weymann, R. J., Peterson, B. M., Sun, L., Malkan, M. A., and Chaffee, Jr., F. H. (1986). C IV absorption systems in QSO spectra - Is the character of systems with Z(abs) = about Z(em) different from those with Z(abs) much less than Z(em)? *The Astrophysical Journal*, 307:504–534.

Fontana, A. and Ballester, P. (1995). FITLYMAN: a Midas tool for the analysis of absorption spectra. *The Messenger*, 80:37–41.

Fox, A. J., Prochaska, J. X., Ledoux, C., Petitjean, P., Wolfe, A. M., and Srianand, R. (2009). Metal-enriched plasma in protogalactic halos. A survey of N V absorption in high-z damped and sub-damped Lyman-α systems. *Astron. Astrophys.*, 503:731–746.

Fox, A. J., Savage, B. D., and Wakker, B. P. (2005). Measurement of Noisy Absorption Lines Using the Apparent Optical Depth Technique. *Astronomic. J.*, 130:2418–2423.

Frank, S., Mathur, S., Pieri, M., and York, D. G. (2010). A Survey of Metal Lines at High Redshift. II. SDSS Absorption Line Studies O VI Line Density, Space Density, and Gas Metallicity at z $_{abs}$ ˜ 3.0. *Astronomic. J.*, 140:835–843.

Fransson, C. and Epstein, R. (1982). Winds from dwarf galaxies and Lyman-alpha absorption features in quasar spectra. *MNRAS*, 198:1127–1141.

Fumagalli, M., Prochaska, J. X., Kasen, D., Dekel, A., Ceverino, D., and Primack, J. R. (2011). Absorption-line systems in simulated galaxies fed by cold streams. *MNRAS*, 418:1796–1821.

Gabel, J. R., Arav, N., and Kim, T.-S. (2006). The AGN Outflow in the HDF-S Target QSO J2233-606 from a High-Resolution VLT UVES Spectrum. *The Astrophysical Journal*, 646:742–753.

Ganguly, R., Bond, N. A., Charlton, J. C., Eracleous, M., Brandt, W. N., and Churchill, C. W. (2001). On the Origin of Intrinsic Narrow Absorption Lines in $z \lesssim 1$ QSOS. *The Astrophysical Journal*, 549:133–154.

Ganguly, R. and Brotherton, M. S. (2008). On the Fraction of Quasars with Outflows. *The Astrophysical Journal*, 672:102–107.

Ganguly, R., Brotherton, M. S., Cales, S., Scoggins, B., Shang, Z., and Vestergaard, M. (2007). Outflows and the Physical Properties of Quasars. *The Astrophysical Journal*, 665:990–1003.

Ganguly, R., Lynch, R. S., Charlton, J. C., Eracleous, M., Tripp, T. M., Palma, C., Sembach, K. R., Misawa, T., Masiero, J. R., Milutinovic, N., Lackey, B. D., and Jones, T. M. (2013). A census of quasar-intrinsic absorption in the Hubble Space Telescope archive: systems from high-resolution echelle spectra. *MNRAS*, 435:1233–1264.

Ganguly, R., Masiero, J., Charlton, J. C., and Sembach, K. R. (2003). An Intrinsic Absorption Complex toward RX J1230.8+0115: Geometry and Photoionization Conditions. *The Astrophysical Journal*, 598:922–934.

Gebhardt, K., Bender, R., Bower, G., Dressler, A., Faber, S. M., Filippenko, A. V., Green, R., Grillmair, C., Ho, L. C., Kormendy, J., Lauer, T. R., Magorrian, J., Pinkney, J., Richstone, D., and Tremaine, S. (2000). A Relationship between Nuclear Black Hole Mass and Galaxy Velocity Dispersion. *The Astrophysical Journal Letters*, 539:L13–L16.

George, I. M. and Fabian, A. C. (1991). X-ray reflection from cold matter in active galactic nuclei and X-ray binaries. *MNRAS*, 249:352–367.

Gibson, R. R., Brandt, W. N., Gallagher, S. C., Hewett, P. C., and Schneider, D. P. (2010). The Evolution of Quasar C IV and Si IV Broad Absorption Lines over Multi-year Timescales. *The Astrophysical Journal*, 713:220–231.

Gibson, R. R., Brandt, W. N., Schneider, D. P., and Gallagher, S. C. (2008). Quasar Broad Absorption Line Variability on Multiyear Timescales. *The Astrophysical Journal*, 675:985–1001.

Goodrich, R. W. (1997). On the Fraction of Broad Absorption Line Quasi-stellar Objects. *The Astrophysical Journal*, 474:606–611.

Goodrich, R. W. and Miller, J. S. (1995). Polarization Clues to the Structure of Broad Absorption Line Quasi-stellar Objects. *The Astrophysical Journal Letters*, 448:L73.

Graham, A. W. and Driver, S. P. (2007). A Log-Quadratic Relation for Predicting Supermassive Black Hole Masses from the Host Bulge Sérsic Index. *The Astrophysical Journal*, 655:77–87.

Graham, A. W., Erwin, P., Caon, N., and Trujillo, I. (2001). A Correlation between Galaxy Light Concentration and Supermassive Black Hole Mass. *The Astrophysical Journal Letters*, 563:L11–L14.

Graham, A. W., Onken, C. A., Athanassoula, E., and Combes, F. (2011). An expanded M_{bh}-σ diagram, and a new calibration of active galactic nuclei masses. *MNRAS*, 412:2211–2228.

Granato, G. L., De Zotti, G., Silva, L., Bressan, A., and Danese, L. (2004). A Physical Model for the Coevolution of QSOs and Their Spheroidal Hosts. *The Astrophysical Journal*, 600:580–594.

Greene, J. E., Zakamska, N. L., Ho, L. C., and Barth, A. J. (2011). Feedback in Luminous Obscured Quasars. *The Astrophysical Journal*, 732:9.

Gregg, M. D., Becker, R. H., and de Vries, W. (2006). FR II Broad Absorption Line Quasars and the Life Cycle of Quasars. *The Astrophysical Journal*, 641:210–216.

Grier, C. J., Martini, P., Watson, L. C., Peterson, B. M., Bentz, M. C., Dasyra, K. M., Dietrich, M., Ferrarese, L., Pogge, R. W., and Zu, Y. (2013). Stellar Velocity Dispersion Measurements in High-luminosity Quasar Hosts and Implications for the AGN Black Hole Mass Scale. *The Astrophysical Journal*, 773:90.

Gültekin, K., Richstone, D. O., Gebhardt, K., Lauer, T. R., Tremaine, S., Aller, M. C., Bender, R., Dressler, A., Faber, S. M., Filippenko, A. V., Green, R., Ho, L. C., Kormendy, J., Magorrian, J., Pinkney, J., and Siopis, C. (2009). The M-σ and M-L Relations in Galactic Bulges, and Determinations of Their Intrinsic Scatter. *The Astrophysical Journal*, 698:198–221.

Gunn, J. E. and Peterson, B. A. (1965). On the Density of Neutral Hydrogen in Intergalactic Space. *The Astrophysical Journal*, 142:1633–1641.

Haehnelt, M. G., Natarajan, P., and Rees, M. J. (1998). High-redshift galaxies, their active nuclei and central black holes. *MNRAS*, 300:817–827.

Hall, P. B., Anderson, S. F., Strauss, M. A., York, D. G., Richards, G. T., Fan, X., Knapp, G. R., Schneider, D. P., Vanden Berk, D. E., Geballe, T. R., Bauer, A. E., Becker, R. H., Davis, M., Rix, H.-W., Nichol, R. C., Bahcall, N. A., Brinkmann, J., Brunner, R., Connolly, A. J., Csabai, I., Doi, M., Fukugita, M., Gunn, J. E., Haiman, Z., Harvanek, M., Heckman, T. M., Hennessy, G. S., Inada, N., Ivezić, Ž., Johnston, D., Kleinman, S., Krolik, J. H., Krzesinski, J., Kunszt, P. Z., Lamb, D. Q., Long, D. C., Lupton, R. H., Miknaitis, G., Munn, J. A., Narayanan, V. K., Neilsen, E., Newman, P. R., Nitta, A., Okamura, S., Pentericci, L., Pier, J. R., Schlegel, D. J., Snedden, S., Szalay, A. S., Thakar, A. R., Tsvetanov, Z., White, R. L., and Zheng, W. (2002). Unusual Broad Absorption Line Quasars from the Sloan Digital Sky Survey. *apjs*, 141:267–309.

Hamann, F., Barlow, T. A., and Junkkarinen, V. (1997a). Time-variable Intrinsic Absorption Lines in the Quasi-stellar Object Q2343+125. *The Astrophysical Journal*, 478:87–93.

Hamann, F., Barlow, T. A., Junkkarinen, V., and Burbidge, E. M. (1997b). High-Resolution Spectra of Intrinsic Absorption Lines in the Quasi-stellar Object UM 675. *The Astrophysical Journal*, 478:80–86.

Hamann, F., Beaver, E. A., Cohen, R. D., Junkkarinen, V., Lyons, R. W., and Burbidge, E. M. (1997c). The Nature and Origin of $z_a \tilde{} z_e$ Absorption Lines in the Redshift 0.20 Quasar, PKS 2135-147. *The Astrophysical Journal*, 488:155–163.

Hamann, F. and Ferland, G. (1999). Elemental Abundances in Quasistellar Objects: Star Formation and Galactic Nuclear Evolution at High Redshifts. *Annu. Rev. Astron. Astrophys.*, 37:487–531.

Hamann, F., Kaplan, K. F., Rodríguez Hidalgo, P., Prochaska, J. X., and Herbert-Fort, S. (2008). Emergence of a quasar outflow. *MNRAS*, 391:L39–L43.

Hamann, F., Korista, K. T., and Morris, S. L. (1993). On the Geometry, Covering Factor, and Scattering-Emission Properties of QSO Broad Absorption-Line Regions. *The Astrophysical Journal*, 415:541.

Hamann, F. and Sabra, B. (2004). The Diverse Nature of Intrinsic Absorbers in AGNs. In Richards, G. T. and Hall, P. B., editors, *AGN Physics with the Sloan Digital Sky Survey*, volume 311 of *Astronomical Society of the Pacific Conference Series*, page 203.

Hamann, F., Simon, L., Capellupo, D., Barlow, T., Ellison, S., Junkkarinen, V., Kanekar, N., Malec, A. L., Milutinovic, N., Murphy, M. T., Pettini, M.,

Prochaska, J. X., Shields, J., and Ubachs, W. (2011). Quasar Absorption Lines as Probes of Quasar-SMBH-Host Galaxy Coevolution. In *Galaxy Formation*, page P148.

Hamann, F., Simon, L., Rodriguez Hidalgo, P., and Capellupo, D. (2012). Narrow UV Absorption Line Outflows from Quasars. In Chartas, G., Hamann, F., and Leighly, K. M., editors, *AGN Winds in Charleston*, volume 460 of *Astronomical Society of the Pacific Conference Series*, page 47.

Hamann, F. W., Netzer, H., and Shields, J. C. (2000). The Nature of Associated Absorption and the Ultraviolet-X-Ray Connection in 3C 288.1. *The Astrophysical Journal*, 536:101–111.

Häring, N. and Rix, H.-W. (2004). On the Black Hole Mass-Bulge Mass Relation. *The Astrophysical Journal Letters*, 604:L89–L92.

Harris, D. W., Jensen, T. W., Suzuki, N., Bautista, J. E., Dawson, K. S., Vivek, M., Brownstein, J. R., Ge, J., Hamann, F., Herbst, H., Jiang, L., Moran, S. E., Myers, A. D., Olmstead, M. D., and Schneider, D. P. (2016). The Composite Spectrum of BOSS Quasars Selected for Studies of the Lyα Forest. *Astronomic. J.*, 151:155.

Harris, G. L. H. and Harris, W. E. (2011). The globular cluster/central black hole connection in galaxies. *MNRAS*, 410:2347–2352.

Harrison, C. M., Alexander, D. M., Mullaney, J. R., and Swinbank, A. M. (2014). Kiloparsec-scale outflows are prevalent among luminous AGN: outflows and feedback in the context of the overall AGN population. *MNRAS*, 441:3306–3347.

Hennawi, J. F., Prochaska, J. X., Burles, S., Strauss, M. A., Richards, G. T., Schlegel, D. J., Fan, X., Schneider, D. P., Zakamska, N. L., Oguri, M., Gunn, J. E., Lupton, R. H., and Brinkmann, J. (2006). Quasars Probing Quasars. I. Optically Thick Absorbers near Luminous Quasars. *The Astrophysical Journal*, 651:61–83.

Hewett, P. C. and Foltz, C. B. (2003). The Frequency and Radio Properties of Broad Absorption Line Quasars. *Astronomic. J.*, 125:1784–1794.

Hewett, P. C., Foltz, C. B., and Chaffee, F. H. (1995). The large bright quasar survey. 6: Quasar catalog and survey parameters. *Astronomic. J.*, 109:1498–1521.

Hewett, P. C., Foltz, C. B., Chaffee, F. H., Francis, P. J., Weymann, R. J., Morris, S. L., Anderson, S. F., and MacAlpine, G. M. (1991). The large, bright QSO survey. III - QSOs in six equatorial fields. *Astronomic. J.*, 101:1121–1182.

Hjerting, F. (1938). Tables Facilitating the Calculation of Line Absorption Coefficients. *The Astrophysical Journal*, 88:508.

Ho, L. C. (2008). Nuclear Activity in Nearby Galaxies. *Annu. Rev. Astron. Astrophys.*, 46:475–539.

Ho, L. C. and Kim, M. (2014). The Black Hole Mass Scale of Classical and Pseudo Bulges in Active Galaxies. *The Astrophysical Journal*, 789:17.

Hopkins, A. M. and Beacom, J. F. (2006). On the Normalization of the Cosmic Star Formation History. *The Astrophysical Journal*, 651:142–154.

Hopkins, P. F. and Elvis, M. (2010). Quasar feedback: more bang for your buck. *MNRAS*, 401:7–14.

Hopkins, P. F., Hernquist, L., Cox, T. J., Di Matteo, T., Robertson, B., and Springel, V. (2006). A Unified, Merger-driven Model of the Origin of Starbursts, Quasars, the Cosmic X-Ray Background, Supermassive Black Holes, and Galaxy Spheroids. *apjs*, 163:1–49.

Hopkins, P. F., Hernquist, L., Cox, T. J., and Kereš, D. (2008). A Cosmological Framework for the Co-Evolution of Quasars, Supermassive Black Holes, and Elliptical Galaxies. I. Galaxy Mergers and Quasar Activity. *apjs*, 175:356–389.

Horan, D. and Weekes, T. C. (2004). Extragalactic sources of TeV gamma rays: a summary. *nar*, 48:527–535.

Hu, E. M., Kim, T.-S., Cowie, L. L., Songaila, A., and Rauch, M. (1995). The Distribution of Column Densities and B Values in the Lyman-Alpha Forest. *Astronomic. J.*, 110:1526.

Hu, J. (2008). The black hole mass-stellar velocity dispersion correlation: bulges versus pseudo-bulges. *MNRAS*, 386:2242–2252.

Hubble, E. P. (1925). NGC 6822, a remote stellar system. *The Astrophysical Journal*, 62.

Ivezić, Ž., Lupton, R. H., Schlegel, D., Boroski, B., Adelman-McCarthy, J., Yanny, B., Kent, S., Stoughton, C., Finkbeiner, D., Padmanabhan, N., Rockosi, C. M., Gunn, J. E., Knapp, G. R., Strauss, M. A., Richards, G. T., Eisenstein, D., Nicinski, T., Kleinman, S. J., Krzesinski, J., Newman, P. R., Snedden, S., Thakar, A. R., Szalay, A., Munn, J. A., Smith, J. A., Tucker, D., and Lee, B. C. (2004). SDSS data management and photometric quality assessment. *Astronomische Nachrichten*, 325:583–589.

Jannuzi, B. T., Hartig, G. F., Kirhakos, S., Sargent, W. L. W., Turnshek, D. A., Weymann, R. J., Bahcall, J. N., Bergeron, J., Boksenberg, A., Savage, B. D., Schneider, D. P., and Wolfe, A. M. (1996). The Hubble Space Telescope Quasar Absorption Line Key Project: The Unusual Absorption-Line System in the

Spectrum of PG 2302+029—Ejected or Intervening? *The Astrophysical Journal Letters*, 470:L11.

Jeans, J. H. (1929). *Astronomy and Cosmogony.*

Jenkins, E. B. (1996). A Procedure for Correcting the Apparent Optical Depths of Moderately Saturated Interstellar Absorption Lines. *The Astrophysical Journal*, 471:292.

Juarez, Y., Maiolino, R., Mujica, R., Pedani, M., Marinoni, S., Nagao, T., Marconi, A., and Oliva, E. (2009). The metallicity of the most distant quasars. *Astron. Astrophys.*, 494:L25–L28.

Kauffmann, G. and Haehnelt, M. (2000). A unified model for the evolution of galaxies and quasars. *MNRAS*, 311:576–588.

Kauffmann, G., Heckman, T. M., Tremonti, C., Brinchmann, J., Charlot, S., White, S. D. M., Ridgway, S. E., Brinkmann, J., Fukugita, M., Hall, P. B., Ivezić, Ž., Richards, G. T., and Schneider, D. P. (2003). The host galaxies of active galactic nuclei. *MNRAS*, 346:1055–1077.

Kellermann, K. I. (2014). The discovery of quasars and its aftermath. *Journal of Astronomical History and Heritage*, 17:267–282.

Kewley, L. J., Dopita, M. A., Sutherland, R. S., Heisler, C. A., and Trevena, J. (2001). Theoretical Modeling of Starburst Galaxies. *The Astrophysical Journal*, 556:121–140.

Kim, T.-S., Carswell, R. F., Cristiani, S., D'Odorico, S., and Giallongo, E. (2002). The physical properties of the Lyα forest at z $>$ 1.5. *MNRAS*, 335:555–573.

Kim, T.-S., Carswell, R. F., Mongardi, C., Partl, A. M., Mücket, J. P., Barai, P., and Cristiani, S. (2016). Triple-ionized carbon associated with the low-density neutral hydrogen gas at 1.7 $<$ z $<$ 3.3: the integrated N $_{H_{I}$}-N $_{C_{IV}$} relation. *MNRAS*, 457:2005–2028.

Kim, T.-S., Cristiani, S., and D'Odorico, S. (2001). The Lyalpha forest at 1.5 $<$ z $<$ 4. *Astron. Astrophys.*, 373:757–781.

Kim, T.-S., Hu, E. M., Cowie, L. L., and Songaila, A. (1997). The Redshift Evolution of the Ly alpha Forest. *Astronomic. J.*, 114:1–13.

King, A. (2003). Black Holes, Galaxy Formation, and the M_{BH}-σ Relation. *The Astrophysical Journal Letters*, 596:L27–L29.

King, A. (2005). The AGN-Starburst Connection, Galactic Superwinds, and M_{BH}-σ. *The Astrophysical Journal Letters*, 635:L121–L123.

King, A. and Pounds, K. (2015). Powerful Outflows and Feedback from Active Galactic Nuclei. *Annu. Rev. Astron. Astrophys.*, 53:115–154.

King, A. R., Zubovas, K., and Power, C. (2011). Large-scale outflows in galaxies. *MNRAS*, 415:L6–L10.

Kirkman, D., Tytler, D., Suzuki, N., Melis, C., Hollywood, S., James, K., So, G., Lubin, D., Jena, T., Norman, M. L., and Paschos, P. (2005). The HI opacity of the intergalactic medium at redshifts $1.6 < z < 3.2$. *MNRAS*, 360:1373–1380.

Kormendy, J. and Bender, R. (2009). Correlations between Supermassive Black Holes, Velocity Dispersions, and Mass Deficits in Elliptical Galaxies with Cores. *The Astrophysical Journal Letters*, 691:L142–L146.

Kormendy, J. and Bender, R. (2011). Supermassive black holes do not correlate with dark matter haloes of galaxies. *Nature*, 469:377–380.

Kormendy, J. and Gebhardt, K. (2001). Supermassive black holes in galactic nuclei. In Wheeler, J. C. and Martel, H., editors, *20th Texas Symposium on relativistic astrophysics*, volume 586 of *American Institute of Physics Conference Series*, pages 363–381.

Kormendy, J. and Ho, L. C. (2013). Coevolution (Or Not) of Supermassive Black Holes and Host Galaxies. *Annu. Rev. Astron. Astrophys.*, 51:511–653.

Kormendy, J. and Richstone, D. (1995). Inward Bound—The Search For Supermassive Black Holes In Galactic Nuclei. *Annu. Rev. Astron. Astrophys.*, 33:581.

Krogager, J.-K., Fynbo, J. P. U., Noterdaeme, P., Zafar, T., Møller, P., Ledoux, C., Krühler, T., and Stockton, A. (2016). A quasar reddened by a sub-parsec-sized, metal-rich and dusty cloud in a damped Lyman α absorber at $z = 2.13$. *MNRAS*, 455:2698–2711.

Krolik, J. H. and Kriss, G. A. (2001). Warm Absorbers in Active Galactic Nuclei: A Multitemperature Wind. *The Astrophysical Journal*, 561:684–690.

Krolik, J. H. and Voit, G. M. (1998). What Is the True Covering Factor of Absorbing Matter in BALQSOs? *The Astrophysical Journal Letters*, 497:L5–L8.

Kuraszkiewicz, J. K. and Green, P. J. (2002). Evidence of a Strong N V/C IV Correlation between Emission and Absorption Lines in Active Galactic Nuclei. *The Astrophysical Journal Letters*, 581:L77–L80.

Lacey, C. G., Baugh, C. M., Frenk, C. S., Benson, A. J., Bower, R. G., Cole, S., Gonzalez-Perez, V., Helly, J. C., Lagos, C. D. P., and Mitchell, P. D. (2015). A unified multi-wavelength model of galaxy formation. *ArXiv e-prints*.

Lau, M. W., Prochaska, J. X., and Hennawi, J. F. (2015). Quasars Probing Quasars VIII. The Physical Properties of the Cool Circumgalactic medium Surrounding z ~ 2-3 Massive Galaxies. *ArXiv e-prints*.

Lauer, T. R., Faber, S. M., Richstone, D., Gebhardt, K., Tremaine, S., Postman, M., Dressler, A., Aller, M. C., Filippenko, A. V., Green, R., Ho, L. C., Kormendy, J., Magorrian, J., and Pinkney, J. (2007). The Masses of Nuclear Black Holes in Luminous Elliptical Galaxies and Implications for the Space Density of the Most Massive Black Holes. *The Astrophysical Journal*, 662:808–834.

Lawther, D., Paarup, T., Schmidt, M., Vestergaard, M., Hjorth, J., and Malesani, D. (2012). Constraints on the relative sizes of intervening Mg II-absorbing clouds and quasar emitting regions. *Astron. Astrophys.*, 546:A67.

Lebofsky, M. J. and Rieke, G. H. (1980). Variations in the thermal emission of Seyfert galaxies. *Nature*, 284:410–412.

Leighly, K. M., Hamann, F., Casebeer, D. A., and Grupe, D. (2009). Emergence of a Broad Absorption Line Outflow in the Narrow-line Seyfert 1 Galaxy WPVS 007. *The Astrophysical Journal*, 701:176–199.

Liang, E. P. T. (1979). Electron-positron pair production in hot unsaturated Compton accretion models around black holes. *The Astrophysical Journal*, 234:1105–1112.

Lopez, S. (2006). The source of metals in the high-redshift Lyman-α forest. In *Revista Mexicana de Astronomia y Astrofisica Conference Series*, volume 26 of *Revista Mexicana de Astronomia y Astrofisica, vol. 27*, pages 117–118.

Lopez, S., D'Odorico, S., Ellison, S. L., and Kim, T.-S. (2004). Clues to the Origin of Metals in the Lyα Forest. *Origin and Evolution of the Elements*.

Lopez, S., D'Odorico, V., Ellison, S. L., Becker, G. D., Christensen, L., Cupani, G., Denney, K. D., Paris, I., Worseck, G., Berg, T. A. M., Cristiani, S., Dessauges-Zavadsky, M., Haehnelt, M., Hamann, F., Hennawi, J., Irsic, V., Kim, T.-S., Lopez, P., Saust, R. L., Menard, B., Perrotta, S., Prochaska, J. X., Sanchez-Ramirez, R., Vestergaard, M., Viel, M., and Wisotzki, L. (2016). XQ-100: A legacy survey of one hundred $3.5 < z < 4.5$ quasars observed with VLT/XSHOOTER. *ArXiv e-prints*.

Lu, L., Sargent, W. L. W., Barlow, T. A., and Rauch, M. (1998). The Metal Contents of Very Low Column Density Lyman-alpha Clouds: Implications for the Origin of Heavy Elements in the Intergalactic Medium. *ArXiv Astrophysics e-prints*.

Lynden-Bell, D. (1969). Galactic Nuclei as Collapsed Old Quasars. *Nature*, 223:690–694.

Lynds, R. (1971). The Absorption-Line Spectrum of 4c 05.34. *The Astrophysical Journal Letters*, 164:L73.

Magorrian, J., Tremaine, S., Richstone, D., Bender, R., Bower, G., Dressler, A., Faber, S. M., Gebhardt, K., Green, R., Grillmair, C., Kormendy, J., and Lauer, T. (1998). The Demography of Massive Dark Objects in Galaxy Centers. *Astronomic. J.*, 115:2285–2305.

Maiolino, R. (2009). Early metal enrichment in high-redshift quasars. In Giobbi, G., Tornambe, A., Raimondo, G., Limongi, M., Antonelli, L. A., Menci, N., and Brocato, E., editors, *American Institute of Physics Conference Series*, volume 1111 of *American Institute of Physics Conference Series*, pages 160–167.

Maiolino, R., Gallerani, S., Neri, R., Cicone, C., Ferrara, A., Genzel, R., Lutz, D., Sturm, E., Tacconi, L. J., Walter, F., Feruglio, C., Fiore, F., and Piconcelli, E. (2012). Evidence of strong quasar feedback in the early Universe. *MNRAS*, 425:L66–L70.

Malbon, R. K., Baugh, C. M., Frenk, C. S., and Lacey, C. G. (2007). Black hole growth in hierarchical galaxy formation. *MNRAS*, 382:1394–1414.

Malkan, M. A. and Sargent, W. L. W. (1982). The ultraviolet excess of Seyfert 1 galaxies and quasars. *The Astrophysical Journal*, 254:22–37.

Marconi, A. and Hunt, L. K. (2003). The Relation between Black Hole Mass, Bulge Mass, and Near-Infrared Luminosity. *The Astrophysical Journal Letters*, 589:L21–L24.

McConnell, N. J. and Ma, C.-P. (2013). Revisiting the Scaling Relations of Black Hole Masses and Host Galaxy Properties. *The Astrophysical Journal*, 764:184.

McConnell, N. J., Ma, C.-P., Gebhardt, K., Wright, S. A., Murphy, J. D., Lauer, T. R., Graham, J. R., and Richstone, D. O. (2011). Two ten-billion-solar-mass black holes at the centres of giant elliptical galaxies. *Nature*, 480:215–218.

McGill, C. (1990). The redshift projection. II - Caustics and the Lyman alpha forest. *MNRAS*, 242:544–554.

McLure, R. J. and Dunlop, J. S. (2002). On the black hole-bulge mass relation in active and inactive galaxies. *MNRAS*, 331:795–804.

McNamara, B. R. and Nulsen, P. E. J. (2007). Heating Hot Atmospheres with Active Galactic Nuclei. *Annu. Rev. Astron. Astrophys.*, 45:117–175.

McNamara, B. R. and Nulsen, P. E. J. (2012). Mechanical feedback from active galactic nuclei in galaxies, groups and clusters. *New Journal of Physics*, 14(5):055023.

McQuinn, M. (2015). The Evolution of the Intergalactic Medium. *ArXiv e-prints*.

Meiksin, A. (1994). The structure and evolution of Lyman-alpha forest clouds in the minihalo model. *The Astrophysical Journal*, 431:109–122.

Ménard, B., Nestor, D., Turnshek, D., Quider, A., Richards, G., Chelouche, D., and Rao, S. (2008). Lensing, reddening and extinction effects of MgII absorbers from z = 0.4 to 2. *MNRAS*, 385:1053–1066.

Menci, N., Fontana, A., Giallongo, E., Grazian, A., and Salimbeni, S. (2006). The Abundance of Distant and Extremely Red Galaxies: The Role of AGN Feedback in Hierarchical Models. *The Astrophysical Journal*, 647:753–762.

Merloni, A., Bongiorno, A., Bolzonella, M., Brusa, M., Civano, F., Comastri, A., Elvis, M., Fiore, F., Gilli, R., Hao, H., Jahnke, K., Koekemoer, A. M., Lusso, E., Mainieri, V., Mignoli, M., Miyaji, T., Renzini, A., Salvato, M., Silverman, J., Trump, J., Vignali, C., Zamorani, G., Capak, P., Lilly, S. J., Sanders, D., Taniguchi, Y., Bardelli, S., Carollo, C. M., Caputi, K., Contini, T., Coppa, G., Cucciati, O., de la Torre, S., de Ravel, L., Franzetti, P., Garilli, B., Hasinger, G., Impey, C., Iovino, A., Iwasawa, K., Kampczyk, P., Kneib, J.-P., Knobel, C., Kovač, K., Lamareille, F., Le Borgne, J.-F., Le Brun, V., Le Fèvre, O., Maier, C., Pello, R., Peng, Y., Perez Montero, E., Ricciardelli, E., Scodeggio, M., Tanaka, M., Tasca, L. A. M., Tresse, L., Vergani, D., and Zucca, E. (2010). On the Cosmic Evolution of the Scaling Relations Between Black Holes and Their Host Galaxies: Broad-Line Active Galactic Nuclei in the zCOSMOS Survey. *The Astrophysical Journal*, 708:137–157.

Merritt, D. and Ferrarese, L. (2001). The M_{BH}-σ Relation for Supermassive Black Holes. *The Astrophysical Journal*, 547:140–145.

Meyer, D. M. and York, D. G. (1987). Observations of weak C IV absorption toward the QSOs 2000-330 and 2126-158. *The Astrophysical Journal Letters*, 315:L5–L9.

Misawa, T., Charlton, J. C., Eracleous, M., Ganguly, R., Tytler, D., Kirkman, D., Suzuki, N., and Lubin, D. (2007). A Census of Intrinsic Narrow Absorption Lines in the Spectra of Quasars at z = 2-4. *apjs*, 171:1–28.

Moll, R., Schindler, S., Domainko, W., Kapferer, W., Mair, M., van Kampen, E., Kronberger, T., Kimeswenger, S., and Ruffert, M. (2007). Simulations of metal enrichment in galaxy clusters by AGN outflows. *Astron. Astrophys.*, 463:513–518.

Monaco, P., Salucci, P., and Danese, L. (2000). Joint cosmological formation of QSOs and bulge-dominated galaxies. *MNRAS*, 311:279–296.

Morton, D. C. (2003). Atomic Data for Resonance Absorption Lines. III. Wavelengths Longward of the Lyman Limit for the Elements Hydrogen to Gallium. *apjs*, 149:205–238.

Murray, N. and Chiang, J. (1995). Active Galactic Nuclei Disk Winds, Absorption Lines, and Warm Absorbers. *The Astrophysical Journal Letters*, 454:L105.

Murray, N., Quataert, E., and Thompson, T. A. (2005). On the Maximum Luminosity of Galaxies and Their Central Black Holes: Feedback from Momentum-driven Winds. *The Astrophysical Journal*, 618:569–585.

Nagao, T., Maiolino, R., and Marconi, A. (2006). Gas metallicity diagnostics in star-forming galaxies. *Astron. Astrophys.*, 459:85–101.

Nandra, K. and Pounds, K. A. (1994). GINGA Observations of the X-Ray Spectra of Seyfert Galaxies. *MNRAS*, 268:405.

Narayanan, D., Hamann, F., Barlow, T., Burbidge, E. M., Cohen, R. D., Junkkarinen, V., and Lyons, R. (2004). Variability Tests for Intrinsic Absorption Lines in Quasar Spectra. *The Astrophysical Journal*, 601:715–722.

Nestor, D., Hamann, F., and Rodriguez Hidalgo, P. (2008). The quasar-frame velocity distribution of narrow CIV absorbers. *MNRAS*, 386:2055–2064.

Nesvadba, N. P. H., Boulanger, F., Salomé, P., Guillard, P., Lehnert, M. D., Ogle, P., Appleton, P., Falgarone, E., and Pineau Des Forets, G. (2010). Energetics of the molecular gas in the H_2 luminous radio galaxy 3C 326: Evidence for negative AGN feedback. *Astron. Astrophys.*, 521:A65.

Nesvadba, N. P. H., Lehnert, M. D., De Breuck, C., Gilbert, A. M., and van Breugel, W. (2008). Evidence for powerful AGN winds at high redshift: dynamics of galactic outflows in radio galaxies during the "Quasar Era". *Astron. Astrophys.*, 491:407–424.

Nesvadba, N. P. H., Lehnert, M. D., Eisenhauer, F., Gilbert, A., Tecza, M., and Abuter, R. (2006). Extreme Gas Kinematics in the z=2.2 Powerful Radio Galaxy MRC 1138-262: Evidence for Efficient Active Galactic Nucleus Feedback in the Early Universe? *The Astrophysical Journal*, 650:693–705.

Nesvadba, N. P. H., Polletta, M., Lehnert, M. D., Bergeron, J., De Breuck, C., Lagache, G., and Omont, A. (2011). The dynamics of the ionized and molecular interstellar medium in powerful obscured quasars at z$>$ 3.5. *MNRAS*, 415:2359–2372.

Oemler, Jr., A. and Lynds, C. R. (1975). The absorption spectrum of 4C 25.05. *The Astrophysical Journal*, 199:558–564.

Okamoto, T., Nemmen, R. S., and Bower, R. G. (2008). The impact of radio feedback from active galactic nuclei in cosmological simulations: formation of disc galaxies. *MNRAS*, 385:161–180.

Osterbrock, D. E. (1989). *Astrophysics of gaseous nebulae and active galactic nuclei*.

Padovani, P. and Giommi, P. (1995). The connection between x-ray- and radio-selected BL Lacertae objects. *The Astrophysical Journal*, 444:567–581.

Pentericci, L., Fan, X., Rix, H.-W., Strauss, M. A., Narayanan, V. K., Richards, G. T., Schneider, D. P., Krolik, J., Heckman, T., Brinkmann, J., Lamb, D. Q., and Szokoly, G. P. (2002). VLT Optical and Near-Infrared Observations of the z = 6.28 Quasar SDSS J1030+0524. *Astronomic. J.*, 123:2151–2158.

Perrotta, S., D'Odorico, V., Prochaska, J. X., Cristiani, S., Cupani, G., Ellison, S., Lòpez, S., Becker, G. D., Berg, T. A. M., Christensen, L., Denney, K. D., Hamann, F., Pâris, I., Vestergaard, M., and Worseck, G. (2016). Nature and statistical properties of quasar associated absorption systems in the XQ-100 Legacy Survey. *ArXiv e-prints*.

Peterson, B. M. (1993). Reverberation mapping of active galactic nuclei. *pasp*, 105:247–268.

Petitjean, P. (1998). QSO Absorption Line Systems. *ArXiv Astrophysics e-prints*.

Pieri, M. M., Frank, S., Weinberg, D. H., Mathur, S., and York, D. G. (2010). The Composite Spectrum of Strong Lyα Forest Absorbers. *The Astrophysical Journal Letters*, 724:L69–L73.

Pieri, M. M. and Haehnelt, M. G. (2004). Pixel correlation searches for OVI in the Lyman α forest and the volume filling factor of metals in the intergalactic medium at z˜ 2-3.5. *MNRAS*, 347:985–993.

Pieri, M. M., Schaye, J., and Aguirre, A. (2006). The Spatial Distribution of Metals in the Intergalactic Medium. *The Astrophysical Journal*, 638:45–51.

Planck Collaboration, Ade, P. A. R., Aghanim, N., Armitage-Caplan, C., Arnaud, M., Ashdown, M., Atrio-Barandela, F., Aumont, J., Baccigalupi, C., Banday, A. J., and et al. (2014). Planck 2013 results. XVI. Cosmological parameters. *Astron. Astrophys.*, 571:A16.

Pounds, K. A. and Page, K. L. (2006). Confirming the high velocity outflow in PG1211+143. *MNRAS*, 372:1275–1278.

Power, C., Nayakshin, S., and King, A. (2011). The accretion disc particle method for simulations of black hole feeding and feedback. *MNRAS*, 412:269–276.

Prochaska, J. X. and Hennawi, J. F. (2009). Quasars Probing Quasars. III. New Clues to Feedback, Quenching, and the Physics of Massive Galaxy Formation. *The Astrophysical Journal*, 690:1558–1584.

Prochaska, J. X., Hennawi, J. F., Lee, K.-G., Cantalupo, S., Bovy, J., Djorgovski, S. G., Ellison, S. L., Lau, M. W., Martin, C. L., Myers, A., Rubin, K. H. R., and Simcoe, R. A. (2013). Quasars Probing Quasars. VI. Excess H I Absorption within One Proper Mpc of z ˜ 2 Quasars. *The Astrophysical Journal*, 776:136.

Prochaska, J. X., Lau, M. W., and Hennawi, J. F. (2014). Quasars Probing Quasars. VII. The Pinnacle of the Cool Circumgalactic Medium Surrounds Massive z ˜ 2 Galaxies. *The Astrophysical Journal*, 796:140.

Prochaska, J. X. and Wolfe, A. M. (1997). On the Kinematics of the Damped Lyman-α Protogalaxies. *The Astrophysical Journal*, 487:73–95.

Proga, D. (2000). Winds from Accretion Disks Driven by Radiation and Magneto-centrifugal Force. *The Astrophysical Journal*, 538:684–690.

Proga, D., Rodriguez-Hidalgo, P., and Hamann, F. (2012). On Time Variability and Other Complications in Studying the UV Broad Absorption Lines of Quasars: Results from Numerical Simulations of Radiation Driven Disk Winds. In Chartas, G., Hamann, F., and Leighly, K. M., editors, *AGN Winds in Charleston*, volume 460 of *Astronomical Society of the Pacific Conference Series*, page 171.

Proga, D., Stone, J. M., and Kallman, T. R. (2000). Dynamics of Line-driven Disk Winds in Active Galactic Nuclei. *The Astrophysical Journal*, 543:686–696.

Rauch, M. (1998). The Lyman Alpha Forest in the Spectra of QSOs. *Annu. Rev. Astron. Astrophys.*, 36:267–316.

Rauch, M., Sargent, W. L. W., Womble, D. S., and Barlow, T. A. (1996). Temperature and Kinematics of C IV Absorption Systems. *The Astrophysical Journal Letters*, 467:L5.

Rees, M. J. (1984). Black Hole Models for Active Galactic Nuclei. *Annu. Rev. Astron. Astrophys.*, 22:471–506.

Rees, M. J., Silk, J. I., Werner, M. W., and Wickramasinghe, N. C. (1969). Infrared Radiation from Dust in Seyfert Galaxies. *Nature*, 223:788–791.

Reeves, J. N., O'Brien, P. T., Braito, V., Behar, E., Miller, L., Turner, T. J., Fabian, A. C., Kaspi, S., Mushotzky, R., and Ward, M. (2009). A Compton-thick Wind in the High-luminosity Quasar, PDS 456. *The Astrophysical Journal*, 701:493–507.

Reichard, T. A., Richards, G. T., Schneider, D. P., Hall, P. B., Tolea, A., Krolik, J. H., Tsvetanov, Z., Vanden Berk, D. E., York, D. G., Knapp, G. R., Gunn, J. E., and Brinkmann, J. (2003). A Catalog of Broad Absorption Line Quasars from the Sloan Digital Sky Survey Early Data Release. *Astronomic. J.*, 125:1711–1728.

Rodríguez Hidalgo, P., Hamann, F., and Hall, P. (2011). The extremely high velocity outflow in quasar PG0935+417. *MNRAS*, 411:247–259.

Rodriguez Hidalgo, P., Hamann, F., Nestor, D., and Shields, J. (2007). High-velocity Outflows in Quasars. In Ho, L. C. and Wang, J.-W., editors, *The Central Engine of Active Galactic Nuclei*, volume 373 of *Astronomical Society of the Pacific Conference Series*, page 287.

Romano, D., Silva, L., Matteucci, F., and Danese, L. (2002). Chemical evolution in a model for the joint formation of quasars and spheroids. *MNRAS*, 334:444–458.

Romano, D. and Starkenburg, E. (2013). Chemical evolution of Local Group dwarf galaxies in a cosmological context - I. A new modelling approach and its application to the Sculptor dwarf spheroidal galaxy. *MNRAS*, 434:471–487.

Roos, O., Juneau, S., Bournaud, F., and Gabor, J. M. (2015). Thermal and Radiative Active Galactic Nucleus Feedback have a Limited Impact on Star Formation in High-redshift Galaxies. *The Astrophysical Journal*, 800:19.

Runnoe, J. C., Brotherton, M. S., and Shang, Z. (2012). Updating quasar bolometric luminosity corrections. *MNRAS*, 422:478–493.

Rupke, D. S. N. and Veilleux, S. (2011). Integral Field Spectroscopy of Massive, Kiloparsec-scale Outflows in the Infrared-luminous QSO Mrk 231. *The Astrophysical Journal Letters*, 729:L27.

Sadoun, R. and Colin, J. (2012). M_{BH}-σ relation between supermassive black holes and the velocity dispersion of globular cluster systems. *MNRAS*, 426:L51–L55.

Salpeter, E. E. (1964). Accretion of Interstellar Matter by Massive Objects. *The Astrophysical Journal*, 140:796–800.

Sánchez-Ramírez, R., Ellison, S. L., Prochaska, J. X., Berg, T. A. M., López, S., D'Odorico, V., Becker, G. D., Christensen, L., Cupani, G., Denney, K. D., Pâris, I., Worseck, G., and Gorosabel, J. (2016). The evolution of neutral gas in damped Lyman α systems from the XQ-100 survey. *MNRAS*, 456:4488–4505.

Sandage, A. (1965). The Existence of a Major New Constituent of the Universe: the Quasistellar Galaxies. *The Astrophysical Journal*, 141:1560.

Sani, E., Marconi, A., Hunt, L. K., and Risaliti, G. (2011). The Spitzer/IRAC view of black hole-bulge scaling relations. *MNRAS*, 413:1479–1494.

Sargent, W. L. W., Boksenberg, A., and Steidel, C. C. (1988). C IV absorption in a new sample of 55 QSOs - Evolution and clustering of the heavy-element absorption redshifts. *apjs*, 68:539–641.

Savage, B. D. and Sembach, K. R. (1991a). The analysis of apparent optical depth profiles for interstellar absorption lines. *The Astrophysical Journal*, 379:245–259.

Savage, B. D. and Sembach, K. R. (1991b). The analysis of apparent optical depth profiles for interstellar absorption lines. *The Astrophysical Journal*, 379:245–259.

Savaglio, S., Cristiani, S., D'Odorico, S., Fontana, A., Giallongo, E., and Molaro, P. (1997). The shape of the ionizing UV background at z˜3.7 from the metal absorption systems of Q 0000-2619. *Astron. Astrophys.*, 318:347–360.

Scannapieco, E. and Oh, S. P. (2004). Quasar Feedback: The Missing Link in Structure Formation. *The Astrophysical Journal*, 608:62–79.

Schaye, J., Aguirre, A., Kim, T.-S., Theuns, T., Rauch, M., and Sargent, W. L. W. (2003). Metallicity of the Intergalactic Medium Using Pixel Statistics. II. The Distribution of Metals as Traced by C IV. *The Astrophysical Journal*, 596:768–796.

Schaye, J., Crain, R. A., Bower, R. G., Furlong, M., Schaller, M., Theuns, T., Dalla Vecchia, C., Frenk, C. S., McCarthy, I. G., Helly, J. C., Jenkins, A., Rosas-Guevara, Y. M., White, S. D. M., Baes, M., Booth, C. M., Camps, P., Navarro, J. F., Qu, Y., Rahmati, A., Sawala, T., Thomas, P. A., and Trayford, J. (2015). The EAGLE project: simulating the evolution and assembly of galaxies and their environments. *MNRAS*, 446:521–554.

Schaye, J., Rauch, M., Sargent, W. L. W., and Kim, T.-S. (2000). The Detection of Oxygen in the Low-Density Intergalactic Medium. *The Astrophysical Journal Letters*, 541:L1–L4.

Schmidt, M. (1963). 3C 273 : A Star-Like Object with Large Red-Shift. *Nature*, 197:1040.

Schneider, D. P., Hall, P. B., Richards, G. T., Vanden Berk, D. E., Anderson, S. F., Fan, X., Jester, S., Stoughton, C., Strauss, M. A., SubbaRao, M., Brandt, W. N., Gunn, J. E., Yanny, B., Bahcall, N. A., Barentine, J. C., Blanton, M. R., Boroski, W. N., Brewington, H. J., Brinkmann, J., Brunner, R., Csabai, I., Doi, M., Eisenstein, D. J., Frieman, J. A., Fukugita, M., Gray, J., Harvanek, M., Heckman, T. M., Ivezić, Ž., Kent, S., Kleinman, S. J., Knapp, G. R., Kron, R. G., Krzesinski, J., Long, D. C., Loveday, J., Lupton, R. H., Margon, B., Munn, J. A., Neilsen, E. H., Newberg, H. J., Newman, P. R., Nichol, R. C., Nitta, A., Pier, J. R., Rockosi, C. M., Saxe, D. H., Schlegel, D. J., Snedden, S. A., Szalay,

A. S., Thakar, A. R., Uomoto, A., Voges, W., and York, D. G. (2005). The Sloan Digital Sky Survey Quasar Catalog. III. Third Data Release. *Astronomic. J.*, 130:367–380.

Schulze, A. and Gebhardt, K. (2011). Effect of a Dark Matter Halo on the Determination of Black Hole Masses. *The Astrophysical Journal*, 729:21.

Sembach, K. R. and Savage, B. D. (1992). Observations of highly ionized gas in the Galactic halo. *apjs*, 83:147–201.

Seyfert, C. K. (1943). Nuclear Emission in Spiral Nebulae. *The Astrophysical Journal*, 97:28.

Shang, Z., Brotherton, M. S., Green, R. F., Kriss, G. A., Scott, J., Quijano, J. K., Blaes, O., Hubeny, I., Hutchings, J., Kaiser, M. E., Koratkar, A., Oegerle, W., and Zheng, W. (2005). Quasars and the Big Blue Bump. *The Astrophysical Journal*, 619:41–59.

Shankar, F., Weinberg, D. H., and Miralda-Escudé, J. (2009). Self-Consistent Models of the AGN and Black Hole Populations: Duty Cycles, Accretion Rates, and the Mean Radiative Efficiency. *The Astrophysical Journal*, 690:20–41.

Shields, G. A. (1978). Thermal continuum from acretion disks in quasars. *Nature*, 272:706–708.

Sijacki, D., Springel, V., Di Matteo, T., and Hernquist, L. (2007). A unified model for AGN feedback in cosmological simulations of structure formation. *MNRAS*, 380:877–900.

Sijacki, D., Vogelsberger, M., Genel, S., Springel, V., Torrey, P., Snyder, G. F., Nelson, D., and Hernquist, L. (2015). The Illustris simulation: the evolving population of black holes across cosmic time. *MNRAS*, 452:575–596.

Silk, J. (2013). Unleashing Positive Feedback: Linking the Rates of Star Formation, Supermassive Black Hole Accretion, and Outflows in Distant Galaxies. *The Astrophysical Journal*, 772:112.

Silk, J. and Rees, M. J. (1998). Quasars and galaxy formation. *Astron. Astrophys.*, 331:L1–L4.

Simcoe, R. A., Sargent, W. L. W., and Rauch, M. (2004). The Distribution of Metallicity in the Intergalactic Medium at z˜2.5: O VI and C IV Absorption in the Spectra of Seven QSOs. *The Astrophysical Journal*, 606:92–115.

Skrutskie, M. F., Cutri, R. M., Stiening, R., Weinberg, M. D., Schneider, S., Carpenter, J. M., Beichman, C., Capps, R., Chester, T., Elias, J., Huchra, J., Liebert, J., Lonsdale, C., Monet, D. G., Price, S., Seitzer, P., Jarrett, T.,

Kirkpatrick, J. D., Gizis, J. E., Howard, E., Evans, T., Fowler, J., Fullmer, L., Hurt, R., Light, R., Kopan, E. L., Marsh, K. A., McCallon, H. L., Tam, R., Van Dyk, S., and Wheelock, S. (2006). The Two Micron All Sky Survey (2MASS). *Astronomic. J.*, 131:1163–1183.

Somerville, R. S., Hopkins, P. F., Cox, T. J., Robertson, B. E., and Hernquist, L. (2008). A semi-analytic model for the co-evolution of galaxies, black holes and active galactic nuclei. *MNRAS*, 391:481–506.

Songaila, A. and Cowie, L. L. (1996). Metal enrichment and Ionization Balance in the Lyman Alpha Forest at Z = 3. *Astronomic. J.*, 112:335.

Springel, V., White, S. D. M., Jenkins, A., Frenk, C. S., Yoshida, N., Gao, L., Navarro, J., Thacker, R., Croton, D., Helly, J., Peacock, J. A., Cole, S., Thomas, P., Couchman, H., Evrard, A., Colberg, J., and Pearce, F. (2005). Simulations of the formation, evolution and clustering of galaxies and quasars. *Nature*, 435:629–636.

Sramek, R. A. and Weedman, D. W. (1980). The radio properties of optically discovered quasars. *The Astrophysical Journal*, 238:435–444.

Srianand, R., Petitjean, P., Ledoux, C., and Hazard, C. (2002). A collimated flow driven by radiative pressure from the nucleus of quasar Q1511 + 091. *MNRAS*, 336:753–758.

Sturm, E., González-Alfonso, E., Veilleux, S., Fischer, J., Graciá-Carpio, J., Hailey-Dunsheath, S., Contursi, A., Poglitsch, A., Sternberg, A., Davies, R., Genzel, R., Lutz, D., Tacconi, L., Verma, A., Maiolino, R., and de Jong, J. A. (2011). Massive Molecular Outflows and Negative Feedback in ULIRGs Observed by Herschel-PACS. *The Astrophysical Journal Letters*, 733:L16.

Suzuki, N., Tytler, D., Kirkman, D., O'Meara, J. M., and Lubin, D. (2005). Predicting QSO Continua in the Lyα Forest. *The Astrophysical Journal*, 618:592–600.

Tody, D. (1986). The IRAF Data Reduction and Analysis System. In Crawford, D. L., editor, *Instrumentation in astronomy VI*, volume 627 of *Society of Photo-Optical Instrumentation Engineers (SPIE) Conference Series*, page 733.

Tombesi, F., Cappi, M., Reeves, J. N., and Braito, V. (2012). Evidence for ultrafast outflows in radio-quiet AGNs - III. Location and energetics. *MNRAS*, 422:1–5.

Torricelli-Ciamponi, G., Pietrini, P., and Orr, A. (2005). Non-thermal emission from AGN coronae. *Astron. Astrophys.*, 438:55–69.

Tozzi, P., Gilli, R., Mainieri, V., Norman, C., Risaliti, G., Rosati, P., Bergeron, J., Borgani, S., Giacconi, R., Hasinger, G., Nonino, M., Streblyanska, A., Szokoly,

G., Wang, J. X., and Zheng, W. (2006). X-ray spectral properties of active galactic nuclei in the Chandra Deep Field South. *Astron. Astrophys.*, 451:457–474.

Tremaine, S., Gebhardt, K., Bender, R., Bower, G., Dressler, A., Faber, S. M., Filippenko, A. V., Green, R., Grillmair, C., Ho, L. C., Kormendy, J., Lauer, T. R., Magorrian, J., Pinkney, J., and Richstone, D. (2002). The Slope of the Black Hole Mass versus Velocity Dispersion Correlation. *The Astrophysical Journal*, 574:740–753.

Tripp, T. M., Sembach, K. R., Bowen, D. V., Savage, B. D., Jenkins, E. B., Lehner, N., and Richter, P. (2008). A High-Resolution Survey of Low-Redshift QSO Absorption Lines: Statistics and Physical Conditions of O VI Absorbers. *apjs*, 177:39–102.

Trump, J. R., Hall, P. B., Reichard, T. A., Richards, G. T., Schneider, D. P., Vanden Berk, D. E., Knapp, G. R., Anderson, S. F., Fan, X., Brinkman, J., Kleinman, S. J., and Nitta, A. (2006). A Catalog of Broad Absorption Line Quasars from the Sloan Digital Sky Survey Third Data Release. *apjs*, 165:1–18.

Turnshek, D. A. (1984). Properties of the broad absorption-line QSOs. *The Astrophysical Journal*, 280:51–65.

Turnshek, D. A. (1988). BAL QSOs: Observations, Models and Implications for Narrow Absorption Line Systems. In Blades, J. C., Turnshek, D. A., and Norman, C. A., editors, *QSO Absorption Lines: Probing the Universe*, page 17.

Vernaleo, J. C. and Reynolds, C. S. (2006). AGN Feedback and Cooling Flows: Problems with Simple Hydrodynamic Models. *The Astrophysical Journal*, 645:83–94.

Vernet, J., Dekker, H., D'Odorico, S., Kaper, L., Kjaergaard, P., Hammer, F., Randich, S., Zerbi, F., Groot, P. J., Hjorth, J., Guinouard, I., Navarro, R., Adolfse, T., Albers, P. W., Amans, J.-P., Andersen, J. J., Andersen, M. I., Binetruy, P., Bristow, P., Castillo, R., Chemla, F., Christensen, L., Conconi, P., Conzelmann, R., Dam, J., de Caprio, V., de Ugarte Postigo, A., Delabre, B., di Marcantonio, P., Downing, M., Elswijk, E., Finger, G., Fischer, G., Flores, H., François, P., Goldoni, P., Guglielmi, L., Haigron, R., Hanenburg, H., Hendriks, I., Horrobin, M., Horville, D., Jessen, N. C., Kerber, F., Kern, L., Kiekebusch, M., Kleszcz, P., Klougart, J., Kragt, J., Larsen, H. H., Lizon, J.-L., Lucuix, C., Mainieri, V., Manuputy, R., Martayan, C., Mason, E., Mazzoleni, R., Michaelsen, N., Modigliani, A., Moehler, S., Møller, P., Norup Sørensen, A., Nørregaard, P., Péroux, C., Patat, F., Pena, E., Pragt, J., Reinero, C., Rigal, F., Riva, M., Roelfsema, R., Royer, F., Sacco, G., Santin, P., Schoenmaker, T., Spano, P., Sweers, E., Ter Horst, R., Tintori, M., Tromp, N., van Dael, P.,

van der Vliet, H., Venema, L., Vidali, M., Vinther, J., Vola, P., Winters, R., Wistisen, D., Wulterkens, G., and Zacchei, A. (2011). X-shooter, the new wide band intermediate resolution spectrograph at the ESO Very Large Telescope. *Astron. Astrophys.*, 536:A105.

Vestergaard, M. (2003). Occurrence and Global Properties of Narrow C IV λ1549 Å Absorption Lines in Moderate-Redshift Quasars. *The Astrophysical Journal*, 599:116–139.

Volonteri, M., Haardt, F., and Madau, P. (2003). The Assembly and Merging History of Supermassive Black Holes in Hierarchical Models of Galaxy Formation. *The Astrophysical Journal*, 582:559–573.

Volonteri, M., Natarajan, P., and Gültekin, K. (2011). How Important is the Dark Matter Halo for Black Hole Growth? *The Astrophysical Journal*, 737:50.

Wang, B. (1995). Ly-alpha forests and cooling outflow from dwarf galaxies. *The Astrophysical Journal Letters*, 444:L17–L20.

Weaver, R., McCray, R., Castor, J., Shapiro, P., and Moore, R. (1977). Interstellar bubbles. II - Structure and evolution. *The Astrophysical Journal*, 218:377–395.

Webb, J. K. (1987). Clustering of LYα Absorbing Clouds at High Redshift /. In Hewitt, A., Burbidge, G., and Fang, L. Z., editors, *Observational Cosmology*, volume 124 of *IAU Symposium*, page 803.

Weisheit, J. C. (1978). On the use of line shapes in the analysis of QSO absorption spectra. *The Astrophysical Journal*, 219:829–835.

Weymann, R. J., Carswell, R. F., and Smith, M. G. (1981). Absorption lines in the spectra of quasistellar objects. *Annu. Rev. Astron. Astrophys.*, 19:41–76.

Weymann, R. J., Morris, S. L., Foltz, C. B., and Hewett, P. C. (1991). Comparisons of the emission-line and continuum properties of broad absorption line and normal quasi-stellar objects. *The Astrophysical Journal*, 373:23–53.

Weymann, R. J., Scott, J. S., Schiano, A. V. R., and Christiansen, W. A. (1982). A thermal wind model for the broad emission line region of quasars. *The Astrophysical Journal*, 262:497–510.

Weymann, R. J., Williams, R. E., Peterson, B. M., and Turnshek, D. A. (1979). Results of a homogeneous survey of absorption lines in QSOs of small and intermediate emission redshift. *The Astrophysical Journal*, 234:33–46.

Wild, V., Kauffmann, G., White, S., York, D., Lehnert, M., Heckman, T., Hall, P. B., Khare, P., Lundgren, B., Schneider, D. P., and vanden Berk, D. (2008). Narrow associated quasi-stellar object absorbers: clustering, outflows and the line-of-sight proximity effect. *MNRAS*, 388:227–241.

Woo, J.-H., Schulze, A., Park, D., Kang, W.-R., Kim, S. C., and Riechers, D. A. (2013). Do Quiescent and Active Galaxies Have Different M $_{BH}$-σ_* Relations? *The Astrophysical Journal*, 772:49.

Wu, J., Charlton, J. C., Misawa, T., Eracleous, M., and Ganguly, R. (2010). The Physical Conditions of the Intrinsic N V Narrow Absorption Line Systems of Three Quasars. *The Astrophysical Journal*, 722:997–1012.

Wurster, J. and Thacker, R. J. (2013). A comparative study of AGN feedback algorithms. *MNRAS*, 431:2513–2534.

York, D. G., Adelman, J., Anderson, Jr., J. E., Anderson, S. F., Annis, J., Bahcall, N. A., Bakken, J. A., Barkhouser, R., Bastian, S., Berman, E., Boroski, W. N., Bracker, S., Briegel, C., Briggs, J. W., Brinkmann, J., Brunner, R., Burles, S., Carey, L., Carr, M. A., Castander, F. J., Chen, B., Colestock, P. L., Connolly, A. J., Crocker, J. H., Csabai, I., Czarapata, P. C., Davis, J. E., Doi, M., Dombeck, T., Eisenstein, D., Ellman, N., Elms, B. R., Evans, M. L., Fan, X., Federwitz, G. R., Fiscelli, L., Friedman, S., Frieman, J. A., Fukugita, M., Gillespie, B., Gunn, J. E., Gurbani, V. K., de Haas, E., Haldeman, M., Harris, F. H., Hayes, J., Heckman, T. M., Hennessy, G. S., Hindsley, R. B., Holm, S., Holmgren, D. J., Huang, C.-h., Hull, C., Husby, D., Ichikawa, S.-I., Ichikawa, T., Ivezić, Ž., Kent, S., Kim, R. S. J., Kinney, E., Klaene, M., Kleinman, A. N., Kleinman, S., Knapp, G. R., Korienek, J., Kron, R. G., Kunszt, P. Z., Lamb, D. Q., Lee, B., Leger, R. F., Limmongkol, S., Lindenmeyer, C., Long, D. C., Loomis, C., Loveday, J., Lucinio, R., Lupton, R. H., MacKinnon, B., Mannery, E. J., Mantsch, P. M., Margon, B., McGehee, P., McKay, T. A., Meiksin, A., Merelli, A., Monet, D. G., Munn, J. A., Narayanan, V. K., Nash, T., Neilsen, E., Neswold, R., Newberg, H. J., Nichol, R. C., Nicinski, T., Nonino, M., Okada, N., Okamura, S., Ostriker, J. P., Owen, R., Pauls, A. G., Peoples, J., Peterson, R. L., Petravick, D., Pier, J. R., Pope, A., Pordes, R., Prosapio, A., Rechenmacher, R., Quinn, T. R., Richards, G. T., Richmond, M. W., Rivetta, C. H., Rockosi, C. M., Ruthmansdorfer, K., Sandford, D., Schlegel, D. J., Schneider, D. P., Sekiguchi, M., Sergey, G., Shimasaku, K., Siegmund, W. A., Smee, S., Smith, J. A., Snedden, S., Stone, R., Stoughton, C., Strauss, M. A., Stubbs, C., SubbaRao, M., Szalay, A. S., Szapudi, I., Szokoly, G. P., Thakar, A. R., Tremonti, C., Tucker, D. L., Uomoto, A., Vanden Berk, D., Vogeley, M. S., Waddell, P., Wang, S.-i., Watanabe, M., Weinberg, D. H., Yanny, B., Yasuda, N., and SDSS Collaboration (2000). The Sloan Digital Sky Survey: Technical Summary. *Astronomic. J.*, 120:1579–1587.

Young, P., Sargent, W. L. W., and Boksenberg, A. (1982). C IV absorption in an unbiased sample of 33 QSOs - Evidence for the intervening galaxy hypothesis. *apjs*, 48:455–505.

Young, P. J., Sargent, W. L. W., Boksenberg, A., Carswell, R. F., and Whelan, J. A. J. (1979). A high-resolution study of the absorption spectrum of PKS 2126-158. *The Astrophysical Journal*, 229:891–908.

Zasov, A. V., Petrochenko, L. N., and Cherepashchuk, A. M. (2005). Supermassive Black Holes: Relation to Dark Halos. *Astronomy Reports*, 49:362–367.

Zubovas, K. and King, A. (2012). Clearing Out a Galaxy. *The Astrophysical Journal Letters*, 745:L34.